



Thèse

2022

Open Access

This version of the publication is provided by the author(s) and made available in accordance with the copyright holder(s).

---

## Oxic Methane Production Dynamics in Lakes

---

Ordóñez Valdebenito, Cesar Fernando

### How to cite

ORDÓÑEZ VALDEBENITO, Cesar Fernando. Oxic Methane Production Dynamics in Lakes. Doctoral Thesis, 2022. doi: 10.13097/archive-ouverte/unige:162115

This publication URL: <https://archive-ouverte.unige.ch/unige:162115>

Publication DOI: [10.13097/archive-ouverte/unige:162115](https://doi.org/10.13097/archive-ouverte/unige:162115)

# Oxic Methane Production Dynamics in Lakes

THÈSE

présenté à la Faculté de Sciences de l'Université de Genève  
pour obtenir le grade de Docteur ès Sciences, mention Science de l'Environnement

par

**César ORDÓÑEZ**

de

Chile

Thèse N° 5655

GENÈVE

Atelier d'impression ReproMail

2022



**UNIVERSITÉ  
DE GENÈVE**

**FACULTÉ DES SCIENCES**

**DOCTORAT ÈS SCIENCES, MENTION SCIENCES DE  
L'ENVIRONNEMENT**

**Thèse de Monsieur César Fernando ORDONEZ VALDEBENITO**

intitulée :

**«Oxic Methane Production Dynamics  
in Lakes»**

La Faculté des sciences, sur le préavis de Monsieur D. F. MCGINNIS, professeur associé et directeur de thèse (Département F.-A. Forel des sciences de l'environnement et de l'eau), Monsieur B. W. IBELINGS, professeur ordinaire (Département F.-A. Forel des sciences de l'environnement et de l'eau), Monsieur A. LORKE, professeur (Institute for Environmental Sciences, Natural and Environmental Sciences, The University of Koblenz-Landau, Landau, Germany), autorise l'impression de la présente thèse, sans exprimer d'opinion sur les propositions qui y sont énoncées.

Genève, le 30 mai 2022

**Thèse - 5655 -**

**Le Doyen**

*Las cosas solo son puras si uno las mira desde lejos*

– Jorge Drexler





## Summary

Over the last decades, methane ( $\text{CH}_4$ ) oversaturation in surface oxic waters in the ocean and inland waters has been widely reported, contrasting the paradigms that  $\text{CH}_4$  is only produced in anoxic conditions (called "The methane paradox"). During the last decade, several studies have shown that different organisms are able to produce  $\text{CH}_4$  in oxic conditions, however the contribution of oxic methane production (OMP) to  $\text{CH}_4$  emissions from lakes versus the  $\text{CH}_4$  produced in anoxic sediment has been hotly debated. Recent estimates show that  $\text{CH}_4$  is responsible for about 20 % of the radiative force and that emissions from freshwaters are about 30 to 60 % of the global  $\text{CH}_4$  budget. Since OMP occurs in surface waters, it can be rapidly emitted to the atmosphere. Therefore, to be able to predict  $\text{CH}_4$  emissions from lakes, it is crucial to understand the OMP dynamics and its contribution to emissions in different lakes and at different time scales. In this doctoral thesis, modelling approaches are used to quantify the net production rate ( $P_{\text{net}}$ ), which is defined as the balance between OMP (adds  $\text{CH}_4$ ) and  $\text{CH}_4$  oxidation ( $\text{MOx}$ , removes  $\text{CH}_4$ ) in the lake surface mixed layer. I investigated the main physical and biochemical lake features that drive  $P_{\text{net}}$  rates and its contribution to diffusive  $\text{CH}_4$  emissions over the stratified season in five natural lakes. Chapter 1 provides an overview of the state of the art on OMP and the  $\text{CH}_4$  cycle in lakes.

Using an extensive dataset across trophic state gradients, Chapter 2 studies the occurrence and OMP contribution to diffusive  $\text{CH}_4$  emissions in four pre-alpine lakes. With both a 0-D full-scale mass balance model and a 1-D lateral transport model,  $P_{\text{net}}$  rates in the surface mixed layer (SML) are quantified during three different times over the stratified season. In previous studies, these two models showed contradictory results mainly due to the use of parameterizations to estimate surface diffusive  $\text{CH}_4$  emissions. Nevertheless, Chapter 2 results show a good agreement between the two models when correct boundary conditions are utilized. The conclusions illustrate that eutrophic lakes have higher  $P_{\text{net}}$  rates than oligotrophic lakes and the rates tended to be higher in late spring and decrease towards the end of the summer. Including literature data from additional lakes, light climate, Secchi disk depth and chlorophyll-*a* concentrations were identified as the main drivers of  $P_{\text{net}}$ , suggesting that photoautotrophs play an important role in  $\text{CH}_4$  production in surface oxic waters. Using these data, an empirical up-scaling method is proposed to estimate  $P_{\text{net}}$  rates in different lake ecosystems. Chapter 2

concludes that OMP can be the dominant source of  $\text{CH}_4$  in the pre-alpine lakes during the stratified season, but it highly depends on the physical and biochemical conditions in each lake.

So far, only one investigation reported the same trend that I observed in Chapter 2 using one year of data on Lake Stechlin (Germany). To further investigate the seasonal cycle of  $P_{\text{net}}$  rates, Chapter 3 analyzes data collected over four years in a small eutrophic lake (Soppensee, Switzerland). Using the same approaches from Chapter 2,  $P_{\text{net}}$  rates were estimated in the SML. The results confirm that  $P_{\text{net}}$  seasonal dynamics observed previously tend to occur every year. The stable isotopic signature ( $\delta^{13}\text{C}_{\text{CH}_4}$ ) suggest that MOx dominated over OMP at the end of the summer as the residual  $\text{CH}_4$  concentration became highly  $^{13}\text{C}$  enriched. Chapter 3 also corroborates the role of photoautotrophs in OMP and highlights the importance of including the temporal seasonal variation to estimate the OMP contribution to the  $\text{CH}_4$  atmospheric budget.

Using different phytoplankton cultures, it was shown that OMP was higher under light compared to dark conditions. In addition to the results observed in Chapter 2 and Chapter 3 regarding the role of phytoplankton on  $P_{\text{net}}$  rates, Chapter 4 investigates the diurnal variation of  $P_{\text{net}}$  rates in a small eutrophic lake located in the pre-alpine region (Lac de Bretaye, Switzerland). Using day and night measurements over three days, it is demonstrated that the variation of  $\text{CH}_4$  concentration in time was only explained when  $P_{\text{net}}$  was included as an additional sources/sink in the SML. OMP tended to dominate over MOx during the day while during the night MOx dominated over OMP. Until now, all reported OMP studies were conducted during the day, therefore Chapter 4 concludes that OMP contribution to  $\text{CH}_4$  emissions from lakes may be overestimated due to the lack of nighttime data and illustrates the importance of including the temporal diurnal cycle of  $P_{\text{net}}$  in the  $\text{CH}_4$  budget.

Finally, Chapter 5 gathers the implications of this doctoral thesis on the role of OMP in the atmospheric  $\text{CH}_4$  budget, the impact of the feedback between climate change, lake eutrophication and  $\text{CH}_4$  emissions from lakes, and discusses potential future research. This doctoral thesis mainly focusses on OMP and its contribution to  $\text{CH}_4$  emissions from lakes at different temporal scales and with varying physico-chemical conditions. However, more research is needed to validate the upscaling approach proposed to predict  $P_{\text{net}}$  rates in different lake ecosystems. Understanding the main sources of  $\text{CH}_4$  emissions from freshwaters and identifying

their contribution on a global scale is necessary to be able to predict, adapt and mitigate future changes in the CH<sub>4</sub> cycle in inland waters.



## Résumé

Au cours des dernières décennies, la sursaturation en méthane ( $\text{CH}_4$ ) des eaux de surface oxygènes de l'océan et des eaux intérieures a été largement signalée, contrastant avec les paradigmes selon lesquels le  $\text{CH}_4$  n'est produit que dans des conditions anoxiques. Cette observation est appelée "le paradoxe du méthane". Ces dernières années, plusieurs études ont montré que différents organismes sont capables de produire du  $\text{CH}_4$  dans des conditions oxygènes, mais la contribution de la production de méthane oxygène (PMO) aux émissions de  $\text{CH}_4$  des lacs par rapport au  $\text{CH}_4$  produit dans des sédiments anoxiques a été largement débattue. Des estimations récentes montrent que le  $\text{CH}_4$  est responsable d'environ 20 % du forçage radiatif et les émissions provenant des eaux douces représentent environ 30 à 60 % du budget global du  $\text{CH}_4$ . Comme la PMO est produite dans les eaux de surface, il peut être rapidement émis dans l'atmosphère. Par conséquent, pour être en mesure de prédire les émissions de  $\text{CH}_4$  des lacs, il est crucial de comprendre la dynamique de la PMO et sa contribution aux émissions dans différents lacs et à différentes échelles de temps. Dans cette thèse de doctorat, des approches de modélisation sont utilisées pour quantifier le taux de production net ( $P_{\text{net}}$ ), qui est défini comme l'équilibre entre la PMO (qui ajoute du  $\text{CH}_4$ ) et l'oxydation du  $\text{CH}_4$  ( $\text{MOx}$ , qui élimine le  $\text{CH}_4$ ) dans la couche mixte de surface du lac. J'ai étudié les principales caractéristiques physiques et biochimiques des lacs qui déterminent les taux de  $P_{\text{net}}$  et sa contribution aux émissions diffusives de  $\text{CH}_4$  pendant la saison stratifiée dans cinq lacs naturels. Le chapitre 1 donne une vue d'ensemble de l'état de l'art sur le  $P_{\text{net}}$  et le cycle du  $\text{CH}_4$  dans les lacs.

En utilisant un grand ensemble de données avec un gradient d'état trophique, le chapitre 2 étudie l'occurrence et la contribution de la PMO aux émissions diffusives de  $\text{CH}_4$  dans quatre lacs préalpins. Avec un modèle 0-D de bilan de masse à l'échelle réelle et un modèle 1-D de transport latéral, les taux de  $P_{\text{net}}$  dans la couche mélangée de surface (CMS) sont quantifiés à trois moments différents de la saison stratifiée. Dans les études précédentes, ces deux modèles ont montré des résultats contradictoires, principalement en raison de l'utilisation de paramétrages pour estimer les émissions diffuses de  $\text{CH}_4$  à la surface. Néanmoins, les résultats du chapitre 2 montrent un bon accord entre les deux modèles lorsque les conditions correctes aux limites sont utilisées. Les conclusions montrent que les lacs eutrophes ont des taux de  $P_{\text{net}}$  plus élevés que les lacs oligotrophes et que les taux ont tendance à être plus importants à la fin du printemps et

à diminuer vers la fin de l'été. En incluant des données bibliographiques provenant d'autres lacs, des facteurs tel que le climat lumineux, la profondeur du disque de Secchi et les concentrations de chlorophylle-a sont identifiés comme les principaux facteurs de  $P_{\text{net}}$ , ce qui suggère que les photoautotrophes jouent un rôle important dans la production de  $\text{CH}_4$  dans les eaux oxiques de surface. En utilisant ces données, une méthode empirique à grande échelle est proposée pour estimer les taux de  $P_{\text{net}}$  dans différents écosystèmes lacustres. Le chapitre 2 conclut que la PMO peut être la source dominante de  $\text{CH}_4$  dans les lacs préalpins pendant la saison stratifiée, mais cela dépend fortement des conditions physiques et biochimiques de chaque lac.

Jusqu'à présent, une seule étude rapporté la même tendance que celle observée dans le chapitre 2 en utilisant les données d'une année sur le lac Stechlin (Allemagne). Pour approfondir le cycle saisonnier des taux de  $P_{\text{net}}$ , le chapitre 3 analyse quatre ans de données provenant d'un petit lac eutrophique (Soppensee, Suisse). En utilisant les mêmes approches que dans le chapitre 2, les taux de  $P_{\text{net}}$  ont été estimés dans la CMS. Les résultats confirment que la dynamique saisonnière observée précédemment a tendance à se produire chaque année. La signature isotopique stable ( $\delta^{13}\text{C}_{\text{CH}_4}$ ) suggère que le MOx a dominé sur la PMO à la fin de l'été lorsque la concentration résiduelle de  $\text{CH}_4$  est devenue fortement enrichie en  $^{13}\text{C}$ . Le chapitre 3 corrobore également le rôle des photoautotrophes dans la PMO et souligne l'importance d'inclure la variation saisonnière temporelle pour estimer la contribution de la PMO au bilan total du  $\text{CH}_4$  atmosphérique.

En utilisant différentes cultures de phytoplancton, il a été démontré que la  $P_{\text{net}}$  était plus élevée dans des conditions lumineuses que dans des conditions d'obscurité. En plus des résultats observés dans les chapitres 2 et 3 concernant le rôle du phytoplancton sur les taux de  $P_{\text{net}}$ , le chapitre 4 étudie la variation diurne des taux de  $P_{\text{net}}$  dans un petit lac eutrophe situé dans la région pré-alpine (Lac de Bretaye, Suisse). En utilisant des mesures diurnes et nocturnes sur trois jours, il a été démontré que la variation de la concentration de  $\text{CH}_4$  dans le temps est expliquée lorsque  $P_{\text{net}}$  est inclus comme source/puits supplémentaire dans la CMS. La PMO a eu tendance à dominer le MOx pendant la journée alors que, pendant la nuit, le MOx a dominé la PMO. Par conséquent, le chapitre 4 conclut que la contribution de la PMO aux émissions de  $\text{CH}_4$  des lacs peut être surestimée en raison du manque de données nocturnes et illustre l'importance d'inclure le cycle temporel diurne de  $P_{\text{net}}$  dans le bilan de  $\text{CH}_4$ .

Enfin, le chapitre 5 rassemble les implications de cette thèse de doctorat sur le rôle de la PMO sur le bilan atmosphérique du  $\text{CH}_4$ , l'impact de la rétroaction entre le changement climatique, l'eutrophisation des lacs et les émissions de  $\text{CH}_4$  des lacs, et discute des recherches futures potentielles. Cette thèse de doctorat se concentre principalement sur l'étude de la PMO et sa contribution aux émissions de  $\text{CH}_4$  des lacs à différentes échelles temporelles et à plusieurs conditions physico-chimiques. Cependant, des recherches supplémentaires sont nécessaires pour valider l'approche de mise à l'échelle proposée pour prédire les taux de  $P_{\text{net}}$  dans différents écosystèmes lacustres. La compréhension des principales sources d'émissions de  $\text{CH}_4$  des eaux douces et l'identification de leur contribution à l'échelle mondiale sont nécessaires pour pouvoir prévoir, adapter et atténuer les changements futurs du cycle du  $\text{CH}_4$  dans les eaux intérieures.





## Acknowledgements

This doctoral thesis is the final result of 5 years of investigation, and across this journey I have received the valuable support of many people.

First, I would like to thank my PhD supervisor Daniel F. McGinnis for giving me the opportunity to be part of the Aphys group in the University of Geneva. I am very grateful for his constant support, the possibility to develop myself as a researcher and teacher and, it is worth mention it, for many beers shared together as he said “it is where science happens”. Without a doubt, I hope to continue working with him in the next years.

I would like to thank Tonya DelSontro, who co-supervised my research. I want to thank her, not only the very interesting discussion about my research, but for all the fun that we had in our fieldwork, and those memorable conversations where she advised me to regard my scientific career. I will keep those advices with me for the uncertain times ahead. At the same time, I would like to acknowledge the incredible support of Daphne Donis. I will always be grateful for her help after the problematic incident that I had when I arrived to Geneva. I want to thank her for all the laughs in our conversation in “Chilean Spanish”. I had great times with her.

I would like to thank, as well, to Andreas Lorke and Bastiaan Ibelings for being part of my Defense Committee and to be interested in my research and results.

Most important, I want to thank my family, because without their support I could have not reached the stage where I am now. First to my parents, whom even when they do not fully understand my research topic, they have been always willing to hear me and encourage me to continue and pursue my dreams. (Muchas gracias mamá y papá por todo su cariño, soy quien soy gracias a ustedes). Likewise, I would like to say thanks to my brothers and sisters, their kind words, many calls and messages were a constant fuel over these years. Finally, I want to thank specially to my lovely wife, Daniela. There are many things to thank her for, but can be summarized in that she always encourage me, and was my most important pillar during these 5 years.

I had great times at UNIGE because I met incredible people, who became really good friends. I would like to thank Ena for our friendship during these years. She helped me a lot during the writing period of my thesis, and our fun conversation and dancing kept me mentally sane during the last weeks of this process. Also, thanks to Timon for being a good friend and great co-worker and for his constant cooperation and friendliness. Likewise, I am deeply grateful to Joren, apart from the very interesting talks we had together, I have to thank him for introducing me to the show “The Office”, oh man, he has no idea how this show was a psychological tool during the times of lockdown for Covid. I want to thank Alonso, and our many memorable talks, he brought a little of South America to my life when I needed it the most. Finally, I want to thank João, Julio, Jorrit, Evi, Mridul, Fabio, Roxane and Xujian for bringing a great environment to this institute. It was a pleasure to work with them.

One of the most important experiences during my PhD was to guide master students on their thesis. I would like to thank Alexandrine, Anja, Amelie and Aurora (the A-team) as well as Iga, Caroline, Leila and Fabio, for all their patience with me and all the great times we had together. I wish them the all best, for sure they are going to do excellent with their career.

I also want to thank my friends from Chile. Even though we are in different places around the world I want to thanks to Alfonso, Karel, Hugo and Cristóbal for being there every time that I need a good conversation in Spanish, a good laugh and many nerdy talks. I want to thank Oscar and Hugo for your advice and great moments we had during my PhD. Many thanks, also, to Joaquín for making these 5 years funnier, not only for the great tennis matches but also for the nice moments we spent together. I learned from him to relax and take things more easily.

Furthermore, thanks to many people at UNIGE that helped to develop my work. Thanks to Alexandra who always was there to help me with administrative paperwork and Katia with IT stuff. Thanks to Philippe and Roxane for their help with all my measurements in the laboratory and also in fieldwork. Also, I would like to thank Dominic, Sabine and Kam who helped me with their guidance and collection of data during my research.

In addition, I want to thank to two persons that supported and encouraged me to pursue this PhD. Thanks to Andreas and Nicolás, even though I “betrayed them” by changing

the research topic, I expect to come back to work with them and share new ideas while we're drinking some beers.

Finally, this thesis would have not been possible without the support of the funding provided by Swiss National Science Foundation (SNSF) Grants No. 200021\_169899 (Methane Paradox) and 200021\_160018 (Bubble Flux), and European Union's Horizon 2020 research and innovation programme under the Marie Skłodowska-Curie grant agreement No 788612 (TRIAGE). I would also thank to Canton of Vaud, Canton Lucerne, Direction générale de l'environnement (DGE) and the Municipalité d'Ormont-Dessous for providing access to all sampled lakes. Thanks to Mr. Bernhard Pfyffer for his support of this study on Soppensee, giving us access to the lake and infrastructure.

*Geneva, May 2022*



# Contents

<b>Summary</b>	<b>i</b>
<b>Résumé</b>	<b>v</b>
<b>Acknowledgements</b>	<b>ix</b>
<b>1 Introduction</b>	<b>1</b>
1.1 Climate crisis . . . . .	1
1.2 Methane in the atmosphere . . . . .	3
1.3 Global methane sources and sinks . . . . .	4
1.4 Methane pathways in lakes . . . . .	6
1.5 The methane paradox . . . . .	7
1.5.1 OMP controversy . . . . .	8
1.6 Climate change and eutrophication impacts on CH <sub>4</sub> cycle . . . . .	9
1.7 Objectives . . . . .	10
1.8 Chapter organization . . . . .	11
<b>2 Towards a global scaling of oxic methane production: evaluation of the methane paradox in four Swiss pre-alpine lakes</b>	<b>13</b>
2.1 Introduction . . . . .	14
2.2 Results . . . . .	17
2.2.1 Study sites. . . . .	18
2.2.2 Surface methane concentration and isotopic signature. . . . .	18
2.2.3 Diffusive CH <sub>4</sub> emissions to the atmosphere. . . . .	20
2.2.4 Diffusive CH <sub>4</sub> fluxes from littoral sediments. . . . .	20

2.2.5	CH <sub>4</sub> ebullition rates and bubble dissolution. . . . .	21
2.2.6	Vertical diffusive fluxes from/to the epilimnion. . . . .	21
2.2.7	Horizontal dispersion. . . . .	22
2.2.8	Surface mass balances. . . . .	22
2.2.9	Sensitivity analysis of surface diffusive emission to the atmosphere. . . .	24
2.2.10	Contribution of methane sources to atmospheric diffusive emissions. . .	27
2.3	Discussion . . . . .	28
2.4	Methods . . . . .	34
2.4.1	Study sites. . . . .	34
2.4.2	Limnological measurements. . . . .	34
2.4.3	Mass balance. . . . .	35
2.4.4	Full-scale mass balance. . . . .	35
2.4.5	Lateral transport model. . . . .	35
2.4.6	Monte Carlo Simulation . . . . .	36
2.4.7	Water column CH <sub>4</sub> and $\delta^{13}\text{C}_{\text{CH}_4}$ signature. . . . .	37
2.4.8	CH <sub>4</sub> diffusive fluxes to the atmosphere. . . . .	37
2.4.9	Sediment sampling. . . . .	38
2.4.10	Porewater CH <sub>4</sub> concentration and $\delta^{13}\text{C}_{\text{CH}_4}$ signature. . . . .	38
2.4.11	Methane benthic fluxes. . . . .	39
2.4.12	CH <sub>4</sub> bubble dissolution and ebullition rates. . . . .	40
2.4.13	Vertical diffusive CH <sub>4</sub> flux from/to hypolimnion. . . . .	41
2.4.14	Sources contribution to diffusive CH <sub>4</sub> emissions. . . . .	42
<b>3</b>	<b>Temporal dynamics of oxic methane production in a hypertrophic Swiss lake</b>	<b>43</b>
3.1	Introduction . . . . .	44
3.2	Methods . . . . .	46
3.2.1	Study site and sampling. . . . .	46
3.2.2	Surface mass balance . . . . .	47
3.2.3	Full-scale mass balance . . . . .	47
3.2.4	Wind-based mass balance . . . . .	49
3.2.5	Lateral transport model . . . . .	49
3.2.6	Water column CH <sub>4</sub> concentration and $\delta^{13}\text{C}_{\text{CH}_4}$ signature . . . . .	50

3.2.7	CH <sub>4</sub> diffusive fluxes to the atmosphere . . . . .	51
3.2.8	Sediment cores extraction . . . . .	51
3.2.9	Porewater CH <sub>4</sub> concentration and $\delta^{13}\text{C}_{\text{CH}_4}$ signature . . . . .	51
3.2.10	Methane diffusive fluxes from littoral sediments . . . . .	52
3.2.11	Bubble CH <sub>4</sub> dissolution and ebullition rates . . . . .	53
3.2.12	Vertical CH <sub>4</sub> diffusive fluxes from/to the SML . . . . .	53
3.2.13	Monte Carlo simulation . . . . .	54
3.2.14	Sources contribution to CH <sub>4</sub> diffusive fluxes to the atmosphere . . . . .	54
3.3	Results . . . . .	54
3.3.1	Limnological measurements . . . . .	54
3.3.2	Surface CH <sub>4</sub> concentration and isotopic signature . . . . .	55
3.3.3	Diffusive CH <sub>4</sub> emissions to the atmosphere . . . . .	55
3.3.4	Diffusive CH <sub>4</sub> fluxes from littoral sediment . . . . .	56
3.3.5	CH <sub>4</sub> ebullition rate and bubble dissolution . . . . .	57
3.3.6	Vertical diffusive fluxes from/to the SML . . . . .	57
3.3.7	Surface mass balance . . . . .	57
3.3.8	Contribution of CH <sub>4</sub> sources to atmospheric diffusive emissions . . . . .	58
3.4	Discussion . . . . .	59
3.4.1	P <sub>net</sub> seasonal variability . . . . .	60
3.4.2	Effect of methane oxidation and OMP on $\delta^{13}\text{C}_{\text{CH}_4}$ in the SML . . . . .	60
3.4.3	Oxic methane contribution to diffusive emissions . . . . .	61
3.4.4	OMP key drivers and upscaling approach evaluation . . . . .	62
3.4.5	Uncertainty assessment . . . . .	63
3.4.6	Conclusions . . . . .	64
<b>4</b>	<b>Diurnal cycle of oxic methane production in a pre-alpine lake (Lac de Bretaye)</b>	<b>67</b>
4.1	Introduction . . . . .	68
4.2	Methods . . . . .	70
4.2.1	Study site . . . . .	70
4.2.2	Limnological measurements . . . . .	70
4.2.3	Meteorological data . . . . .	72
4.2.4	Water CH <sub>4</sub> concentrations and its isotopic signature . . . . .	72



4.2.5	Diffusive CH <sub>4</sub> emissions . . . . .	73
4.2.6	Vertical diffusive flux to/from the SML . . . . .	73
4.2.7	Mass balance in the SML . . . . .	74
4.2.8	Sources contribution to CH <sub>4</sub> diffusive fluxes to the atmosphere . . . . .	75
4.3	Results . . . . .	75
4.3.1	Study site general features . . . . .	75
4.3.2	Meteorological data . . . . .	75
4.3.3	Vertical profiles . . . . .	76
4.3.4	Surface CH <sub>4</sub> concentrations and $\delta^{13}\text{C}_{\text{CH}_4}$ signature . . . . .	77
4.3.5	Diffusive CH <sub>4</sub> emissions to the atmosphere . . . . .	77
4.3.6	Vertical diffusive CH <sub>4</sub> flux through the bottom the SML . . . . .	79
4.3.7	Mass balance in the SML . . . . .	80
4.3.8	Sources contribution to diffusive CH <sub>4</sub> emissions . . . . .	80
4.4	Discussion . . . . .	80
4.4.1	Is $P_{\text{net}}$ an artefact of the methodology? . . . . .	81
4.4.2	Can we explain $\frac{\partial C_{\text{SML}}^{\text{V}}}{\partial t}$ if we do not consider $P_{\text{net}}$ ? . . . . .	83
4.4.3	Modeled sediment flux estimation. . . . .	84
4.4.4	Effect of choosing a constant or variable mixed layer depth on $P_{\text{net}}$ . . . . .	85
4.4.5	Drivers of $P_{\text{net}}$ and isotopic analysis in the SML. . . . .	87
4.4.6	Conclusion and implications . . . . .	89
<b>5</b>	<b>Conclusions and Perspective</b>	<b>91</b>
5.1	Interaction between OMP, eutrophication and climate change . . . . .	93
5.2	Determination of the boundary conditions in the SML . . . . .	94
5.3	Final remarks . . . . .	96
<b>A</b>	<b>Supplementary Information Chapter 2</b>	<b>97</b>
<b>B</b>	<b>Supplementary Information Chapter 3</b>	<b>111</b>
<b>C</b>	<b>Supplementary Information Chapter 4</b>	<b>121</b>
	<b>Bibliography</b>	<b>127</b>

*CONTENTS*

xvii

**Curriculum Vitae**

**145**



# Introduction

## 1.1 Climate crisis

The global average surface temperature during 2011 - 2020 was 1.09 °C higher than the 1850 - 1900 time period (Fig. 1.1) and each of the last four decades have been successively warmer than the preceding decade since 1850 (IPCC 2021). Anthropogenic greenhouse gases (GHG) emissions are the main drivers of this tropospheric warming (Eyring *et al.* 2021). We are already experiencing several changes around the world caused by global warming, for example the increase by 0.2 m of the sea level between 1901 and 2018, the retreat of Arctic Sea ice, the acidification of the ocean and the increase on average global precipitation (Gulev *et al.* 2021).

Changes in global surface temperature relative to 1850-1900

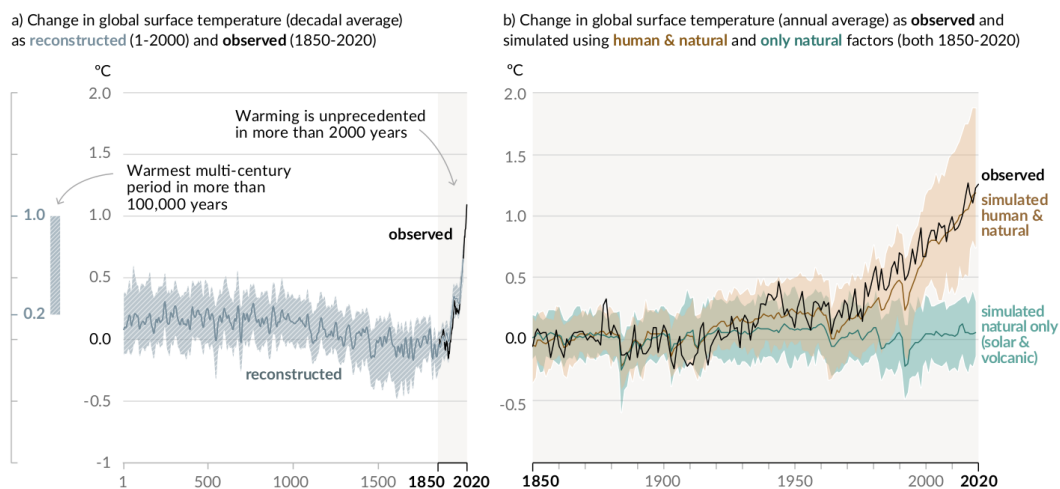


Figure 1.1. Change of global temperature relative to 1850-1900. Figure from: (IPCC 2021).

Gulev *et al.* 2021 showed that most of these changes are unprecedented. The rate of warming of the global air temperature since 1970 has not been observed for at least the last 2000 years (Fig. 1.1). During the summer of 2020, the sea ice area in the Arctic was the smallest in last 1000 years and in the last 2 million years, the ocean was not as acid as it is today.

The Intergovernmental Panel on Climate Change (IPCC) established that “It is unequivocal that human influence has warmed the atmosphere, ocean and land.” (IPCC 2021). Global warming will continue with every emission scenario until at least 2050 and with every increment of global warming the environmental changes will be larger (Gulev *et al.* 2021). The ocean acidification and deoxygenation, the retreat of mountain and polar glaciers, and the sea level rise are irreversible for centuries to millennia (Lee *et al.* 2021).

**Projected global GHG emissions from NDCs announced prior to COP26 would make it likely that warming will exceed 1.5°C and also make it harder after 2030 to limit warming to below 2°C.**

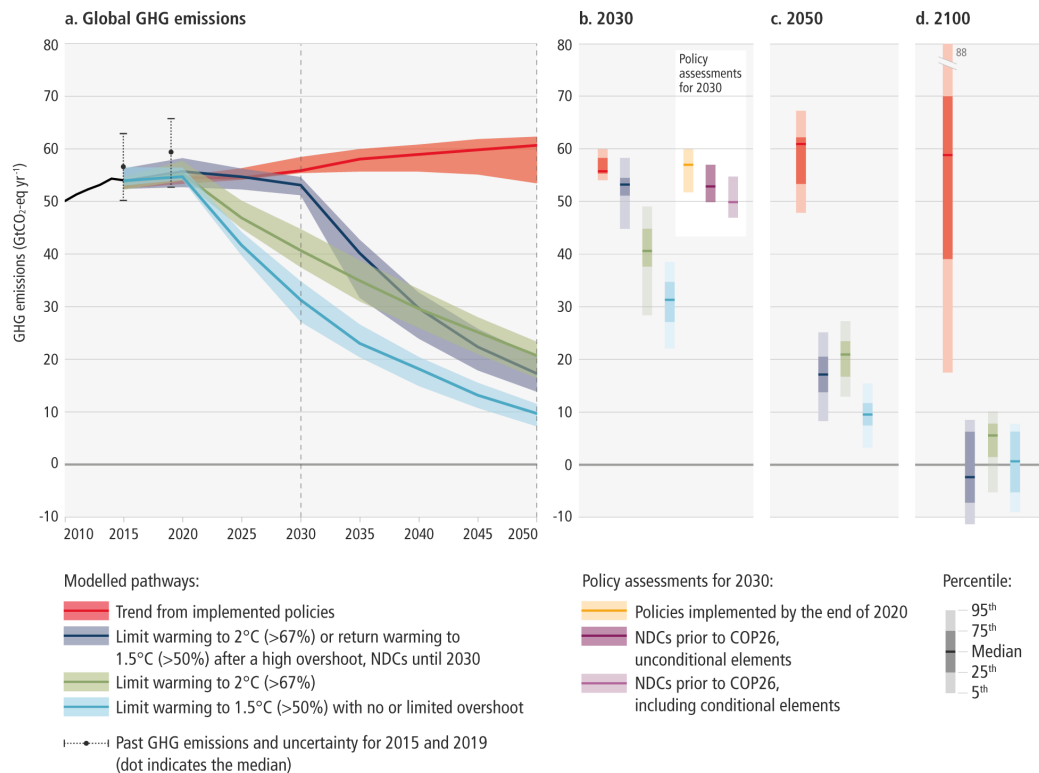


Figure 1.2. Global GHG emissions of modelled pathways (funnels in Panel a and associated bars in Panels b, c, d) and projected emission outcomes from near-term policy assessments for 2030 (Panel b). Panel a shows global GHG emissions over 2015-2050 for four types of assessed modelled global pathways. Figure from: IPCC 2022.

A decrease in the anthropogenic CO<sub>2</sub> emissions to at least net-zero and a rapid reduction

in CH<sub>4</sub> and other GHGs emissions are needed to limit the effect of global warming on the climate system (Fig. 1.2).

## 1.2 Methane in the atmosphere

A greenhouse gas is a gas that absorbs and emits radiation within the range of the radiation emitted by the Earth's surface, by the atmosphere and by clouds, causing the greenhouse effect. The primary GHGs are water vapor (H<sub>2</sub>O), carbon dioxide (CO<sub>2</sub>), nitrous oxide (N<sub>2</sub>O), methane (CH<sub>4</sub>), and ozone (O<sub>3</sub>). After CO<sub>2</sub>, CH<sub>4</sub> is the second most important carbon-based GHG contributing about 16 - 23 % of the additional radiative forcing to date (Fig. 1.3). Despite its low atmospheric concentration compared to CO<sub>2</sub>, its global warming potential (GWP) is ~84 times greater than CO<sub>2</sub> in a 20-yr timescale (Myhre *et al.* 2013).

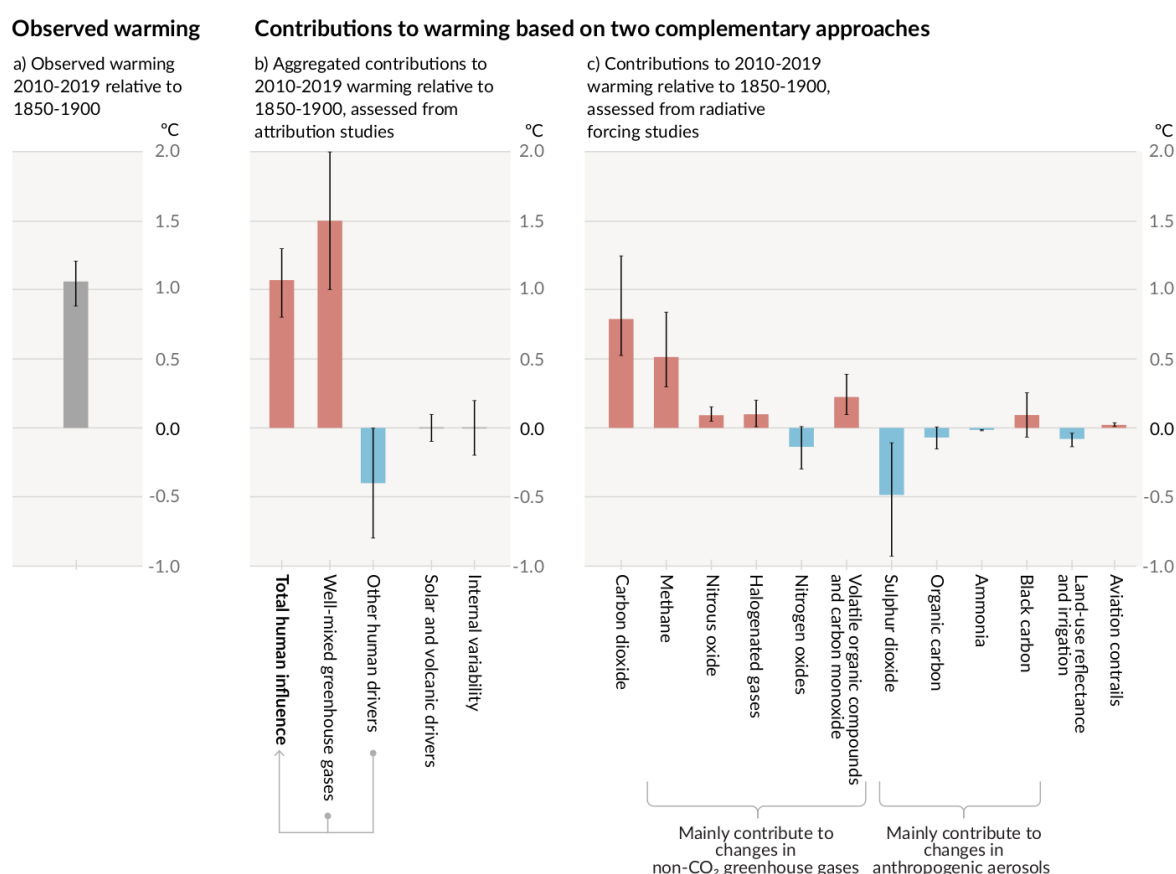


Figure 1.3. Contribution to observed warming in 2010 to 2019 relative to 1850 to 1900. Figure from: (IPCC 2021).

The atmospheric CH<sub>4</sub> concentration has nearly tripled from the pre-industrial era in

1750 to the current average value of  $\sim 1.89$  part per million (ppm) in 2021 (Fig. 1.4). Data analysis from ice cores shows that this concentration level is unprecedented on the last 800,000 years (Meure *et al.* 2006; Louergue *et al.* 2008). After a temporary pause in the increment of the  $\text{CH}_4$  concentrations between late 1990s to 2006, they have been continuously increasing again at a rate of  $7 \pm 3$  ppb/yr between 2006 to 2019 (Saunois *et al.* 2020). The renewed growth of  $\text{CH}_4$  concentration after 2006 is due to an imbalance of about 3.5 % ( $20 \text{ Tg yr}^{-1}$ ) between the global sources and sinks. Currently, the uncertainty in the different components of the  $\text{CH}_4$  budget greatly exceed this value. Therefore, the causes of the change in the trends over the last 30 years is highly debated (Turner *et al.* 2019).

Since the lifetime of  $\text{CH}_4$  in the atmosphere is about 12.4 yr (Myhre *et al.* 2013), the radiative forcing caused by the increase of  $\text{CH}_4$  in the atmosphere can be slowed down by reducing  $\text{CH}_4$  emissions (Nisbet *et al.* 2021).

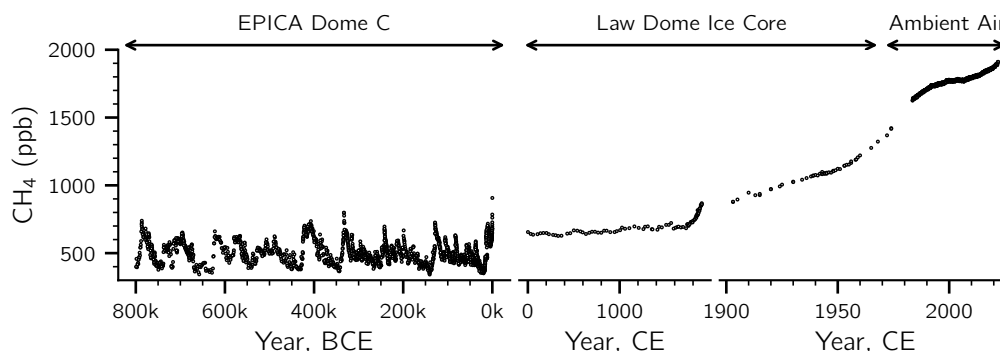


Figure 1.4. Atmospheric  $\text{CH}_4$  concentration of the last 800,000 years. The BCE period (800,000 – 0 BCE) are from Vostok, EPICA Dome C ice cores (Louergue *et al.* 2008). The data from 0 year CE are taken from Law Dome ice core analysis (Meure *et al.* 2006). And the ambient air concentration are taken from NOAA ([www.esrl.noaa.gov/gmd/ccgg/trends\\_ch4](http://www.esrl.noaa.gov/gmd/ccgg/trends_ch4), retrieved 26 April 2022). BCE = before current era, CE = current era.

### 1.3 Global methane sources and sinks

During 2000 - 2017, the global  $\text{CH}_4$  emissions to the atmosphere estimated based on top-down and bottom-up methodologies are about 737 and 576  $\text{Tg CH}_4 \text{ yr}^{-1}$  respectively (Fig. 1.5). The top-down methodology estimates  $\text{CH}_4$  emissions based on satellite observations and inverse modelling whereas the bottom-up is the result of global anthropogenic inventories, land surface models for wetland emissions, and literature inventories from other natural sources (Saunois *et al.*

2020). About 50 to 60 % of  $\text{CH}_4$  emissions come from anthropogenic sources, where agricultural and waste activity are the largest contributors (about  $211 \text{ Tg CH}_4 \text{ yr}^{-1}$ ). The major natural sources are aquatic ecosystems such as wetlands and lakes (Saunois *et al.* 2020; Rosentreter *et al.* 2021). Chemical loss in the atmosphere (mainly by reaction with OH radicals) is the major sink of  $\text{CH}_4$  with a minor contribution by oxidation in soils. The current imbalance between sources and sinks in the atmosphere is about  $110 \text{ Tg CH}_4 \text{ yr}^{-1}$  for the top-down and  $13 \text{ Tg CH}_4 \text{ yr}^{-1}$  for the bottom-up methodology. Lakes, rivers, reservoirs and wetlands are the greatest sources of uncertainty in the global  $\text{CH}_4$  emissions to the atmosphere and therefore it is necessary to improve these estimates (Saunois *et al.* 2020).

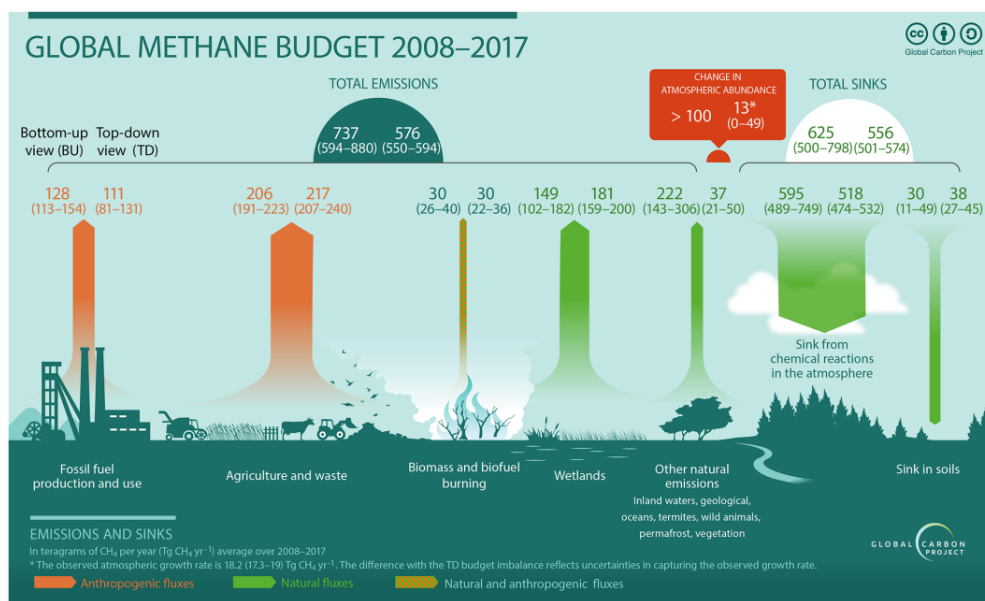


Figure 1.5. Global  $\text{CH}_4$  budget between 2008 – 2017. Both bottom-up (left) and top-down (right) estimates ( $\text{Tg CH}_4 \text{ yr}^{-1}$ ). Figure from: (Saunois *et al.* 2020).

Methane emissions from lakes and reservoirs range about  $69$  to  $179 \text{ Tg CH}_4\text{-C yr}^{-1}$  (Bastviken *et al.* 2008; DelSontro *et al.* 2018b; Rosentreter *et al.* 2021). The major sources of uncertainty are linked to the understanding of how  $\text{CH}_4$  is produced and consumed in these ecosystems, the different transport pathways (ebullition, diffusion, plant mediation), the temporal and spatial variability, and statistical up-scaling methods (Bastviken *et al.* 2008; Rosentreter *et al.* 2021). To decrease the high variability of these data and predict future  $\text{CH}_4$  emissions, further research is needed to understand the mechanisms of  $\text{CH}_4$  productions and emissions in lakes.



## 1.4 Methane pathways in lakes

In lakes, CH<sub>4</sub> is generally produced under anaerobic conditions in the sediment as a final step of organic matter decomposition after other electron acceptors have been exhausted (Wetzel 2001). There are two dominant methanogenic pathways: acetoclastic methanogenesis using acetate as a substrate and hydrogenotrophic methanogenesis using CO<sub>2</sub> and H<sub>2</sub> as substrates (Conrad 2005).



During these metabolic processes, CH<sub>4</sub> producing bacteria (methanogens) prefer lighter <sup>12</sup>C over heavier <sup>13</sup>C which alters the stable isotopic signature  $\delta^{13}\text{C}$  (Mach *et al.* 2015). Methane oxidation (i.e., consumption of CH<sub>4</sub>) in lake sediments and the water column is primarily attributed to aerobic pathways (King 1992). Aerobic CH<sub>4</sub> oxidizers preferentially utilize light carbon, leaving behind a CH<sub>4</sub> pool with a heavier residual  $\delta^{13}\text{C}_{\text{CH}_4}$  signature (Whiticar 1999). Therefore, knowing the stable-C isotopes can help determine the origin and fate of CH<sub>4</sub> in aquatic systems.

In stratified lakes, CH<sub>4</sub> that is produced in the sediment is transported by diffusion to the water column ( $F_s$ ) and can also be introduced by sediment-released bubbles (McGinnis *et al.* 2006). Methane is ~27 times less soluble than CO<sub>2</sub> (Sander 2015), and when its production is faster than CH<sub>4</sub> oxidation (MOx) and diffusion, bubbles can be formed (Schmid *et al.* 2017). These bubbles efficiently pass through the diffusive barrier at the sediment-water interface and depending on the depth of the lake, CH<sub>4</sub> in bubbles can bypass oxidation and reach the atmosphere with some fraction of the CH<sub>4</sub> partially dissolving into the water column ( $R_{\text{dis}}$ ) (McGinnis *et al.* 2006).

Dissolved CH<sub>4</sub> in the water column is transported vertically by turbulent diffusion ( $F_z$ ). This flux is directly proportional to the vertical concentration gradient of CH<sub>4</sub> and turbulent diffusivity ( $K_z$ ), which depends on the kinetic energy in the water column and the stratification strength (Imboden & Wüest 1995). Right below the oxycline/thermocline dissolved CH<sub>4</sub> is mainly oxidized in a narrow zone (Rudd *et al.* 1976; Oswald *et al.* 2015; Thottathil *et al.* 2019).

In stratified lakes with anoxic hypolimnia,  $\text{CH}_4$  is stored in the hypolimnion until turnover when a portion is released to the atmosphere (Schubert *et al.* 2010; Vachon *et al.* 2019).

Once  $\text{CH}_4$  reaches the surface it is emitted to the atmosphere via diffusion ( $F_a$ ), which depends on the surface water concentration and the gas transfer velocity ( $k_{\text{CH}_4}$ ). The latter is mainly controlled by the turbulence level at the surface layer (MacIntyre *et al.* 2010), and potentially enhanced by microbubbles (Melack & Kilham 1974; McGinnis *et al.* 2015). Fig. 1.6 shows the classical scheme of the components of the  $\text{CH}_4$  budget in lakes considering only anoxic sources during the stratified season.

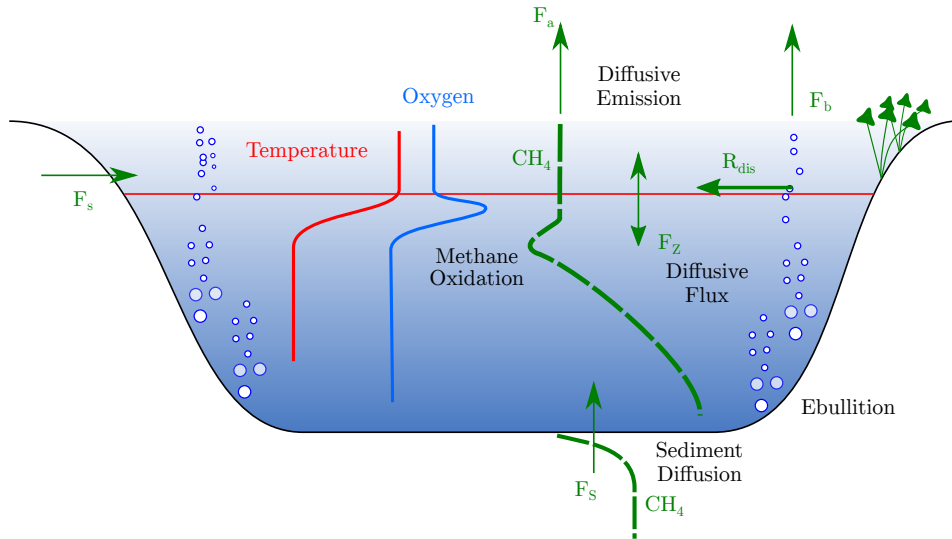


Figure 1.6. Schematic of  $\text{CH}_4$  budget in lakes during the stratified period with typical profiles of temperature, oxygen ( $\text{O}_2$ ) and  $\text{CH}_4$  concentrations considering only anoxic sources.  $\text{CH}_4$  mass balance components: diffusive  $\text{CH}_4$  emissions to the atmosphere ( $F_a$ ), vertical turbulent diffusion ( $F_z$ ),  $\text{CH}_4$  diffusive flux from littoral sediments ( $F_s$ ), bubbles emissions ( $F_b$ ),  $\text{CH}_4$  oxidation and  $\text{CH}_4$  dissolution from bubbles ( $R_{\text{dis}}$ ).

## 1.5 The methane paradox

The paradigm that  $\text{CH}_4$  is only produced in anoxic conditions has been challenged by measurements showing widespread  $\text{CH}_4$  oversaturation in oxic surface water in the ocean and inland waters (Karl *et al.* 2008; Tang *et al.* 2016). Using laboratory lake water incubations, Grossart *et al.* 2011 were the first to demonstrate that  $\text{CH}_4$  production in oxic conditions (also called oxic methane production or OMP) could occur in lakes and could substantially contribute to epilimnetic  $\text{CH}_4$  oversaturation and thus emissions. Subsequently, Bogard *et al.* 2014 showed

that a new source of  $\text{CH}_4$  needed to be included in the epilimnion using an in-lake mesocosm experiment. Tang *et al.* 2014 demonstrated the  $\text{CH}_4$  concentration peak found in the thermocline in Lake Stechlin did not originate from anoxic sources ( $\text{CH}_4$  production in littoral or bottom sediments, or anoxic microniches) and in-situ  $\text{CH}_4$  production needed to be included. Donis *et al.* 2017, using a full-scale mass balance, illustrated that OMP rates were higher in the surface mixed layer (SML) than in the metalimnion in Lake Hallwil (Switzerland). This new recognized source of  $\text{CH}_4$  in lakes surface waters can therefore be rapidly emitted to the atmosphere (Tang *et al.* 2016).

Numerous mechanisms have been proposed for OMP in lakes and oceans such as archaeal methanogenesis in anoxic micro-niches (Oremland 1979; Grossart *et al.* 2011), associations between methanogens and photoautotrophs (Grossart *et al.* 2011; Bogard *et al.* 2014; Tang *et al.* 2014; Yao *et al.* 2016b) and dissolved organic matter photoproduction (Xie *et al.* 2019; Li *et al.* 2020). Moreover, OMP has been shown to be produced by methylphosphonate (MPn) biodegradation in phosphorus limited environments (Karl *et al.* 2008; Repeta *et al.* 2016; Wang *et al.* 2017; Khatun *et al.* 2019) and microbial  $\text{CH}_4$  formation as a product of nitrogen fixation (Zheng *et al.* 2018; Luxem *et al.* 2020).

Recent studies show strong evidence that  $\text{CH}_4$  can be produced by several phytoplankton species (Bižić *et al.* 2020; Günthel *et al.* 2020; Hartmann *et al.* 2020; Morana *et al.* 2020). Correlations between  $\text{CH}_4$  concentrations and light, oxygen and phytoplankton concentrations suggest a direct role of metabolic processes in the production of  $\text{CH}_4$ . These processes might be linked with the ability that all organisms may have to produce  $\text{CH}_4$  based on the combined reactions between reactive oxygen species, iron species and methyl donors (Ernst *et al.* 2022).

### 1.5.1 OMP controversy

Donis *et al.* 2017 and Günthel *et al.* 2019 showed, for the first time, that during the stratified season OMP could contribute up to  $\sim 70\%$  to the diffusive  $\text{CH}_4$  emissions from lakes. Both studies performed a mass balance assuming the SML of the lake as a well-mixed reactor and measured sources and sinks of  $\text{CH}_4$ . These results contrast with other investigations that show using water incubations (Morana *et al.* 2020) and 1-D lateral transport model (Peeters *et al.* 2019) that  $\text{CH}_4$  diffusive flux from littoral sediments was enough to compensate the losses of

CH<sub>4</sub> in the SML.

The CH<sub>4</sub> concentration in the SML is mostly defined by the lateral inputs from littoral sediments, OMP and MOx which can be affected by environmental factors in the lake. For example, the presence of oxygen on top of littoral sediment may decrease the CH<sub>4</sub> flux release to the water column (Damgaard *et al.* 1998; Liikanen *et al.* 2002). Conversely, warmer temperatures can increase CH<sub>4</sub> production in the sediment (Nozhevnikova *et al.* 1997) potentially increasing F<sub>s</sub>. In the water column, laboratory water incubations experiments have shown that MOx can be inhibited by light (Shelley *et al.* 2017; Morana *et al.* 2020) and by elevated oxygen concentrations (Thottathil *et al.* 2019). However, only a few studies have so far focused on the effect of environmental conditions on OMP. Recent studies showed that OMP rates follow the dark/light cycle (Bižić *et al.* 2020; Hartmann *et al.* 2020) and increase at warmer temperatures (Klintzsch *et al.* 2020). Nevertheless, the drivers, temporal dynamics and contribution to diffusive CH<sub>4</sub> emissions are still unknown.

## 1.6 Climate change and eutrophication impacts on CH<sub>4</sub> cycle

Climate change and eutrophication are the two mayor threat to lakes and inland waters. The increase of air temperature due to climate change will lead to warmer surface water temperatures in lakes (Adrian *et al.* 2009; Woolway *et al.* 2020). Since it has been shown that both methanogenesis and ebullition exponentially increase with temperature (Nozhevnikova *et al.* 1997; DelSontro *et al.* 2010), the littoral zone will be highly impacted by the increase of surface temperature. MOx also increases with temperature, but slower than CH<sub>4</sub> production rates (Thottathil *et al.* 2019). Longer stratification periods are also projected (Woolway *et al.* 2021) promoting anoxia in the hypolimnion (Hadley *et al.* 2014) which could potentially increase methanogenesis in pelagic sediments and hypolimnetic CH<sub>4</sub> storage (Vachon *et al.* 2019). Global warming will also increase the ice free period, allowing CH<sub>4</sub> to be emitted for a longer time. The projected increase of human population will also enhance the loadings of agricultural fertilizers and sewage to inland waters (Beaulieu *et al.* 2019 and references therein). Moreover, heavier rainfall would enhance the load of dissolved organic matter and nutrients in aquatic ecosystems. The combination of increased nutrient loading and higher temperatures will promote the growth of algae in inland waters (Rigosi *et al.* 2014). Correlations between CH<sub>4</sub> emissions

and chlorophyll-*a* concentrations (DelSontro *et al.* 2018a) suggest an increase of CH<sub>4</sub> emissions from lakes as a result of lake eutrophication (Beaulieu *et al.* 2019).

High uncertainties remain as to the magnitude of the impact that climate change and eutrophication may simultaneously have on the CH<sub>4</sub> cycle in lakes. Numerical models considering physical and biochemical processes have been developed to investigate the fate of CH<sub>4</sub> concentrations in lakes (Tan *et al.* 2015; Stepanenko *et al.* 2016; Schmid *et al.* 2017). Nevertheless, several parameters used in these models are often unknown or poorly constrained. Moreover, processes such as OMP need to be included to be able to project CH<sub>4</sub> emissions from lakes in a changing environment. Therefore, further research needs to be conducted to understand the mechanisms behind the CH<sub>4</sub> cycle in lakes.

## 1.7 Objectives

Most of the CH<sub>4</sub> investigations have been focused on CH<sub>4</sub> emissions from lakes and less research has been done to understand the basic processes driving those emissions and their interaction with environmental changes (Soued & Prairie 2021). OMP is a newly recognize source of CH<sub>4</sub> to the atmosphere but its importance in the CH<sub>4</sub> cycle and its occurrence remain uncertain. This doctoral thesis investigates the CH<sub>4</sub> sources and sinks using in-situ measurements and modelling approaches with focus on the physical aspects.

This thesis was conducted in five natural lakes, four in the Swiss pre-alpine region and one in the Swiss plateau. Detailed information about the study sites can be found on each individual chapters.

This doctoral thesis addresses the following research goals:

1. Use mass balance approaches to determine  $P_{\text{net}}$  in the surface mixed layer and its contribution to diffusive CH<sub>4</sub> emissions in five natural lakes.
2. Use a multi-lake survey to investigate the occurrence of OMP and its main drivers.
3. Determine the seasonal and diel  $P_{\text{net}}$  cycle during the stratified season.

## 1.8 Chapter organization

The investigations of the PhD thesis are organized in three individual manuscripts (Chapters 2 to 4) and conclusions and perspective can be found in Chapter 5.

**Chapter 2** Towards a global scaling of oxic methane production: evaluation of the methane paradox in four Swiss pre-alpine lakes.

*First author publication. Ordóñez, C., DelSontro, T., Langenegger, T., Donis, D., Suarez, E. L. & McGinnis, D. F. Towards a Global Scaling of Oxic Methane Production: Evaluation of the Methane Paradox in Four Swiss Pre-Alpine Lakes. Nature Communications (submitted) (2022)*

**Chapter 3** Temporal dynamics of oxic methane production in a hypertrophic Swiss lake.

*First author publication. Ordóñez, C., Massot, A., DelSontro, T., Langenegger, T. & McGinnis, D. F. Temporal Dynamic of Oxic Methane Production in a Hypereutrophic Swiss Lake. Frontiers in Environmental Science (submitted) (2022)*

**Chapter 4** Diurnal cycle of oxic methane production in a pre-alpine lake (Lac de Bretaye).

*First author manuscript to be submitted for publication 2022.*

**Chapter 5** Conclusions and Perspective



---

# Towards a global scaling of oxic methane production: evaluation of the methane paradox in four Swiss pre-alpine lakes

---

César Ordóñez<sup>1</sup>, Tonya DelSontro<sup>1, 2</sup>, Timon Langenegger<sup>1</sup>, Daphne Donis<sup>1</sup>, Ena L. Suarez<sup>1</sup>, and Daniel F. McGinnis<sup>1</sup>

<sup>1</sup>Aquatic Physics Group, Department F.-A. Forel for Environmental and Aquatic Sciences (DEFSE), Faculty of Science, University of Geneva, Uni Carl Vogt, 66 Boulevard Carl-Vogt, 1211 Geneva, Switzerland

<sup>1, 2</sup> Now at Department of Earth and Environmental Sciences, University of Waterloo, Ontario, Canada

Content of Chapter 2 was submitted in:

Ordóñez, C., DelSontro, T., Langenegger, T., Donis, D., Suarez, E. L. & McGinnis, D. F. Towards a Global Scaling of Oxic Methane Production: Evaluation of the Methane Paradox in Four Swiss Pre-Alpine Lakes. *Nature Communications (submitted)* (2022)



## Abstract

Oxic methane production (OMP) in freshwaters is more widely accepted, but the mechanisms behind it and its contribution to local and global methane ( $\text{CH}_4$ ) emissions are not well constrained. We use a full-scale mass balance and a lateral transport model to analyze sources and sinks of  $\text{CH}_4$  in the surface mixed layer of four pre-alpine lakes in the Swiss Alps. With the appropriate parameterizations, we find that these two approaches agree well, suggesting that OMP occurs in the studied lakes and is often the dominant source of total  $\text{CH}_4$  emissions. Correlations between OMP versus algal concentration, Secchi depth and mixed layer depth suggest a link between photosynthesis and  $\text{CH}_4$  production that provides an empirical approach to upscale OMP rates globally. OMP is a newly recognized direct  $\text{CH}_4$  source in surface waters that is rapidly emitted to the atmosphere. The extent of OMP and drivers need better understanding, especially considering the potential positive feedback between climate change, phytoplankton production, OMP and  $\text{CH}_4$  emissions to the atmosphere.

## 2.1 Introduction

The widely reported methane ( $\text{CH}_4$ ) oversaturation in surface oxic waters in oceans (Karl *et al.* 2008) and lakes (also referred to as "the methane paradox"; Tang *et al.* 2014) contrasts with the current understanding that biogenic  $\text{CH}_4$  formation occurs exclusively under anoxic conditions (Conrad 2009). Methane production in oxic conditions (also called oxic methane production or OMP) has been reported for an increasing number of lakes (Grossart *et al.* 2011; Bogard *et al.* 2014; Tang *et al.* 2014; Donis *et al.* 2017; Günthel *et al.* 2019; Hartmann *et al.* 2020). While recent studies have shown that OMP may contribute up to 80% of the lake diffusive  $\text{CH}_4$  emissions (Donis *et al.* 2017; Günthel *et al.* 2019), other researchers argued that  $\text{CH}_4$  produced in anoxic littoral sediments is enough to resolve the methane paradox (Hofmann *et al.* 2010; Encinas Fernández *et al.* 2016; Peeters *et al.* 2019; Morana *et al.* 2020). Thus, the OMP contribution to global lake  $\text{CH}_4$  emissions thus remains unclear and hotly debated (Günthel *et al.* 2021; Peeters & Hofmann 2021).

Atmospheric  $\text{CH}_4$  concentrations have more than doubled since the industrial era (Hartmann, D. L. *et al.* 2013; Nisbet *et al.* 2019). Although  $\text{CH}_4$  is less abundant in the

atmosphere than carbon dioxide ( $\text{CO}_2$ ), its global warming potential (GWP) is about 81 times higher than carbon dioxide ( $\text{CO}_2$ ) in a 20-year period (Forster *et al.* [In Press](#)). Its GWP combined with its  $\sim 12$  year lifetime means that reducing  $\text{CH}_4$  emissions is a priority for mitigating climate change (Nisbet *et al.* [2021](#)). Lakes represent between 20 to 50 % of natural  $\text{CH}_4$  atmospheric sources, but large uncertainties remain about the contribution of internal sources and sinks (Bastviken *et al.* [2011](#); Saunio *et al.* [2020](#); Rosentreter *et al.* [2021](#)). Methane in lakes can be emitted to the atmosphere through bubbles (ebullition) and diffusive fluxes at the air-water interface (AWI) (Bastviken *et al.* [2011](#)). Ebullition is mainly driven by high  $\text{CH}_4$  production rates in anoxic sediments (Langenegger *et al.* [2019](#)) and the diffusive fluxes at the AWI are driven by  $\text{CH}_4$  concentrations and turbulence level in surface waters (MacIntyre *et al.* [2010](#)). Unlike anoxic  $\text{CH}_4$  sources in sediments and bottom waters, OMP occurs in oxic surface waters where is quickly emitted to the atmosphere (Tang *et al.* [2014](#)); however, the processes behind OMP and its drivers remain unconstrained.

Several mechanisms have been proposed for OMP such as archaeal methanogenesis in anoxic micro-niches (Oremland [1979](#); Grossart *et al.* [2011](#)), associations of methanogens with photoautotrophs (Grossart *et al.* [2011](#); Bogard *et al.* [2014](#); Tang *et al.* [2014](#); Yao *et al.* [2016a](#)), dissolved organic matter photoproduction (Xie *et al.* [2019](#); Li *et al.* [2020](#)), biodegradation of methylphosphonate (MPn) in phosphorus limited environments (Karl *et al.* [2008](#); Repeta *et al.* [2016](#); Wang *et al.* [2017](#); Khatun *et al.* [2019](#)) and  $\text{CH}_4$  as a byproduct of nitrogen fixation (Zheng *et al.* [2018](#); Luxem *et al.* [2020](#)). However, recent studies have shown strong evidence pointing to a direct role of phytoplankton in OMP (Bižić *et al.* [2020](#); Günthel *et al.* [2020](#); Hartmann *et al.* [2020](#)) indicated by positive correlations between  $\text{CH}_4$ , oxygen and phytoplankton concentrations (Grossart *et al.* [2011](#); Hartmann *et al.* [2020](#)). Moreover, it has been shown that OMP follows light-dark cycles in different phytoplankton cultures (Bižić *et al.* [2020](#); Günthel *et al.* [2020](#)), but the processes behind photosynthesis-derived  $\text{CH}_4$  are unclear. It is likely that multiple pathways produce  $\text{CH}_4$  in oxic lake environments, and that these may vary from lake-to-lake and seasonally on the basis of trophic properties and light conditions.

OMP rates have been reported using different methodologies, such as laboratory and in situ water incubations (Grossart *et al.* [2011](#); Bižić *et al.* [2020](#); Günthel *et al.* [2020](#)), in-lake mesocosms (Bogard *et al.* [2014](#); Günthel *et al.* [2019](#)), a physical lateral transport model

(DelSontro *et al.* 2018b), and lake mass balances (Donis *et al.* 2017; Günthel *et al.* 2019). OMP has been reported from different freshwater environments, including both temperate and arctic regions (DelSontro *et al.* 2018a; Li *et al.* 2019), high altitudes lakes (above 2500 m.a.s.l) (Perez-Coronel & Beman 2020) and across a range of trophic states (DelSontro *et al.* 2018a; Khatun *et al.* 2020; Ye *et al.* 2020). While these studies show the occurrence of OMP in lakes across a geographic and trophic gradient, OMP has so far not been investigated in pre-alpine lakes.

Although not typically thought to promote CH<sub>4</sub> emissions (Beaulieu *et al.* 2019), pre-alpine lakes (from 1300 to 2000 m.a.s.l) have been shown to be sources of CH<sub>4</sub> to the atmosphere (Rinta *et al.* 2017; Pighini *et al.* 2018). Pre-alpine lakes are also disproportionately experiencing climate change (Thompson *et al.* 2005; Råman Vinnå *et al.* 2021) with air temperature increasing two times faster in the European Alps than the global mean (Cannone *et al.* 2008). Such an increase in air temperature can induce the following changes in pre-alpine lakes with implications for aquatic CH<sub>4</sub> emissions (Thompson *et al.* 2005; Råman Vinnå *et al.* 2021; Sharma *et al.* 2021): (1) a longer ice-free season that allows CH<sub>4</sub> to be emitted for a longer period (Guo *et al.* 2020); (2) an increase in surface water temperature that enhances littoral production rates of CH<sub>4</sub> (Bastviken *et al.* 2008); (3) a longer stratified season that allows for more CH<sub>4</sub> accumulation in the hypolimnion (Vachon *et al.* 2020). These impacts, however, will differ across lakes depending on the light regime and trophic state (Flaim *et al.* 2016), therefore the precise impact of climate change on the CH<sub>4</sub> budget in pre-alpine lakes needs further investigation.

This study focuses on four adjacent pre-alpine lakes ( $\sim 1700$  m.a.s.l) with identical climate forcing but different trophic states. We quantified net CH<sub>4</sub> production ( $P_{\text{net}}$ , Fig. 2.1), which is defined as the balance between OMP (that adds CH<sub>4</sub>) and CH<sub>4</sub> oxidation (MOx, that removes CH<sub>4</sub>) from the surface mixed layer (SML) (King 1992; Bastviken *et al.* 2002; Thottathil *et al.* 2019).  $P_{\text{net}}$  in the SML was estimated using two independent approaches: a 0-D full-scale mass balance following Donis *et al.* 2017 and a 1-D lateral transport model similar to Peeters *et al.* 2019. In the full-scale 0-D model, we used CH<sub>4</sub> bulk sources and sinks in the oxic SML. The lateral transport model of Peeters *et al.* 2019 was modified to include additional relevant terms, such as diffusive CH<sub>4</sub> flux across the thermocline and CH<sub>4</sub> bubble dissolution. In this model, we included all of the CH<sub>4</sub> sources in the SML and the loss to the atmosphere

to determine  $P_{\text{net}}$  when the simulated concentrations were best-fit to the  $\text{CH}_4$  concentrations measured across the lake.

In previous studies, these two models have shown contradictory results mainly due to the use of literature parameterizations to estimate surface diffusive emissions (e.g. Donis *et al.* 2017; Günthel *et al.* 2019; Peeters *et al.* 2019; Günthel *et al.* 2021; Peeters & Hofmann 2021). We used direct flux measurements from floating chambers and we found an excellent agreement between the two models. The results indicate that OMP substantially contributes to diffusive emissions during the stratified period of pre-alpine lakes with different trophic states. Moreover, we performed a sensitivity analysis using five diffusive flux literature parameterizations and surface flux measurements to analyze the impact that modeled versus measured atmospheric diffusive fluxes has on OMP estimation. Finally, we present two OMP upscaling approaches: the first based on chlorophyll a (Chla) concentrations, light penetration, and SML depth, and the second based on dissolved inorganic nitrogen (DIN) concentrations in the SML. Our findings highlight the need for OMP to be included in  $\text{CH}_4$  lake budgets and for more research to understand OMP drivers and its response to climate change.

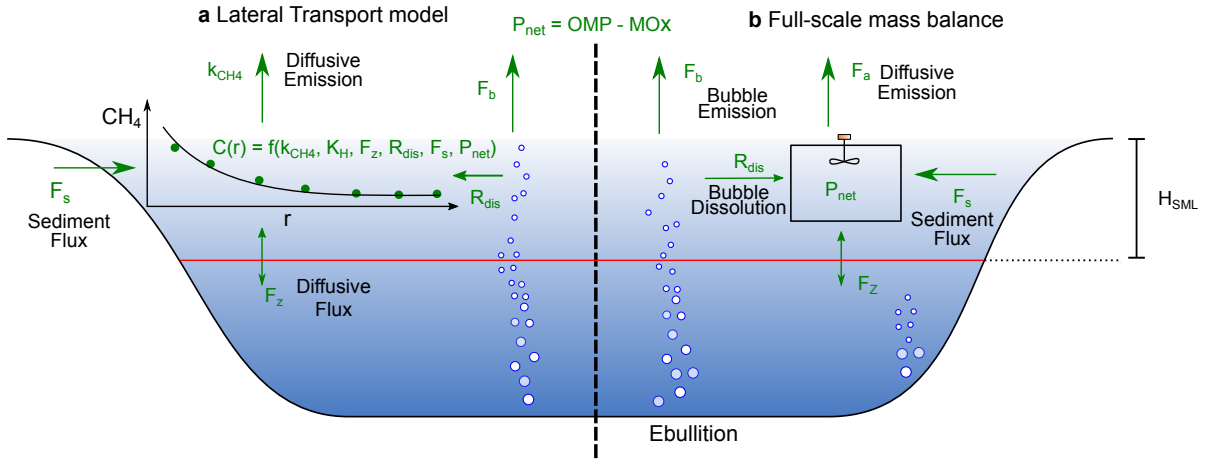


Figure 2.1. Conceptual schematic of the  $\text{CH}_4$  budget components in the SML used for the **a** Lateral transport model and the **b** Full-scale mass balance.

## 2.2 Results

Here we present results from four pre-alpine lakes using two mass balance approaches described in Eq. 2.2 and Eq. 2.3. First, we present a general description of the study sites and then the measured sources and sinks of  $\text{CH}_4$  that represent the boundary conditions for the applied

models (Fig. 2.1). We then quantify and compare the  $\text{CH}_4$  production rates in the surface mixed layer (SML) obtained from both models.

### 2.2.1 Study sites.

The four pre-alpine lakes studied - Lac Bretaye (BRE), Lac Noir (NOI), Lac des Chavonnes (CHA) and Lac Lioson (LIO) - are located between 1650 to 1850 m.a.s.l in the Swiss Alps and are hypereutrophic, eutrophic, mesotrophic and oligotrophic, respectively (Table S.A.1). NOI and BRE are small lakes with a maximum depth of  $\sim 9$  m, while CHA and LIO have a maximum depth of  $\sim 28$  m (Fig. S.A.1 and Table S.A.1). Throughout the three sampling campaigns conducted in June 2018, September 2018 and July 2019, the surface waters of all four lakes were oxic but oversaturated in  $\text{CH}_4$  (Fig. S.A.2; Table 2.1). Temperature and  $\text{CH}_4$  concentration profiles at the deepest point of the lakes show that all the lakes were stratified with a SML thickness between 1 - 6 m. Secchi disc depths, dissolved inorganic nitrogen (DIN), dissolved phosphorus (DP) and  $\text{Chl}a$  concentrations in the SML are summarized in Table 2.1.

Table 2.1. Spatial average of surface  $\text{CH}_4$  concentration and its stable isotopic signature ( $\delta^{13}\text{C}_{\text{CH}_4}$ ) along each transect. Average dissolved inorganic nitrogen (DIN),  $\text{Chl}a$ , and dissolved phosphorus (DP) concentrations in the SML. Secchi and SML depth ( $H_{\text{SML}}$ ) at each sampling campaign in each lake.  $\Delta\text{CH}_4/\text{CH}_4_{\text{shore}}$  is the percentage variation of the  $\text{CH}_4$  concentration at center and the shore. The values marked with \* signify there is a significant difference between shore and center as determined with an ANOVA analysis.

Lake	Date	$\text{CH}_4$ ( $\text{mmol m}^{-3}$ )	$\delta^{13}\text{C}_{\text{CH}_4}$ (‰)	$\Delta\text{CH}_4/\text{CH}_4_{\text{shore}}$ (%)	Secchi depth (m)	$H_{\text{SML}}$ (m)	$\text{Chl}a$ ( $\text{mg m}^{-3}$ )	DIN ( $\text{mg m}^{-3}$ )	DP ( $\text{mg m}^{-3}$ )
Bretaye	June 2018	$6.7 \pm 2.3$	-52.0	54	3.7	1.3	3.01	18	9.0
	Sept 2018	$3.5 \pm 0.5$	-38.0	22*	3.0	5.2	4.08	29	7.3
	July 2019	$2.8 \pm 1.6$	-48.8	4	4.7	2.6	4.05	4	57
Noir	June 2018	$1.4 \pm 0.1$	-54.5	18*	2.8	0.9	8.81	18	2.3
	Sept 2018	$1.8 \pm 0.4$	-45.5	19	6.1	5.4	4.71	13	2.7
	July 2019	$3.9 \pm 0.3$	-49.9	23	3.8	1.9	8.48	BD	BD
Chavonnes	June 2018	$0.1 \pm 0.1$	-62.3	59*	4.6	1.3	3.73	235	2.0
	Sept 2018	$0.2 \pm 0.1$	-62.4	22	5.2	4.6	2.51	167	1.0
	July 2019	$0.1 \pm 0.0$	-61.2	120	3.8	2.0	5.02	189	BD
Lioson	June 2018	$0.1 \pm 0.0$	-50.9	33*	9.0	0.9	1.52	126	2.0
	Sept 2018	$0.4 \pm 0.6$	-50.1	12*	10.5	6.1	3.01	45	1.0
	July 2019	$0.2 \pm 0.2$	-54.0	14	5.5	2.2	4.64	71	BD

### 2.2.2 Surface methane concentration and isotopic signature.

For each lake, surface  $\text{CH}_4$  concentrations and their stable isotopic signatures ( $\delta^{13}\text{C}_{\text{CH}_4}$ ) were measured at the deepest point of the lake and along a transect from shore to shore to resolve the spatial variability (Fig. 2.2 and Fig. S.A.3). All four lakes were oversaturated with  $\text{CH}_4$  values near the shore  $33 \pm 32\%$  higher than in the center, although only 40% of the time this difference

was significant (Table 2.1). The eutrophic lakes BRE and NOI, on average, had one order of magnitude higher surface concentrations ( $3.13 \pm 2.09 \text{ mmol m}^{-3}$ ) than the oligo/mesotrophic lakes LIO and CHA ( $0.15 \pm 0.13 \text{ mmol m}^{-3}$ ) (Table 2.1). The spatial average  $\delta^{13}\text{C}_{\text{CH}_4}$  signature ranged between  $-62$  to  $-38 \text{ ‰}$  (Table 2.1). Isotopically enriched  $\text{CH}_4$  ( $\delta^{13}\text{C}_{\text{CH}_4} \sim -40 \text{ ‰}$ ) was observed at the end of summer in the SML of the eutrophic lakes, while in the oligotrophic lakes  $\delta^{13}\text{C}_{\text{CH}_4}$  was relatively consistent between sampling dates (Table S.A.4). Relatively constant  $\delta^{13}\text{C}_{\text{CH}_4}$  values were observed along the transect for most of the lakes, except for CHA in June 2018 when lighter  $\delta^{13}\text{C}_{\text{CH}_4}$  was observed at the shore ( $\sim -65 \text{ ‰}$ ) than in the center of the lake ( $\sim -60 \text{ ‰}$ ) (Fig. S.A.3).

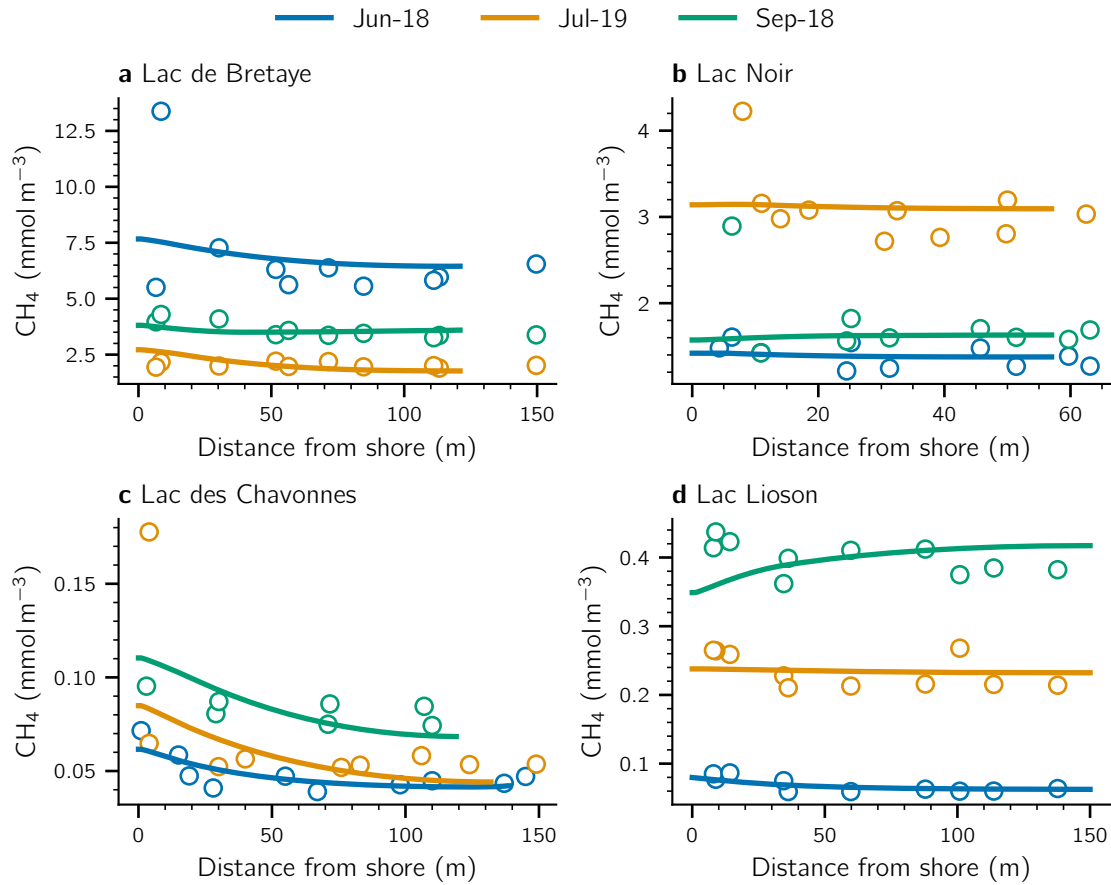


Figure 2.2. Surface  $\text{CH}_4$  concentrations along the transects sampled in each lake. Lines represent the  $\text{CH}_4$  concentration simulated using the lateral transport model and dots are the measured values. Since the lateral transport model assumes that the  $\text{CH}_4$  concentrations in the SML are radially symmetric, the concentrations are shown from shore to center.

### 2.2.3 Diffusive CH<sub>4</sub> emissions to the atmosphere.

Diffusive CH<sub>4</sub> emissions ( $F_a$ ) at the air-water interface (AWI) were measured in each lake using a floating chamber (McGinnis *et al.* 2015) at the deepest point of the lake and along the CH<sub>4</sub> concentration transects. Average surface fluxes (mean  $\pm$  SD) measured in eutrophic NOI and BRE ( $3.24 \pm 0.88 \text{ mmol m}^{-2} \text{ d}^{-1}$ ) were an order of magnitude higher than in LIO and CHA ( $0.29 \pm 0.43 \text{ mmol m}^{-2} \text{ d}^{-1}$ ). Surface diffusive fluxes of CH<sub>4</sub> remained relatively similar between sampling dates in each lake (Table 2.2).

Surface diffusive CH<sub>4</sub> fluxes can be estimated using Fick's 1st Law using (Prairie & del Giorgio 2013; McGinnis *et al.* 2015)

$$\begin{aligned} F_a &= k_{\text{CH}_4} (C_w - H_{cp} \cdot p\text{CH}_{4,\text{atm}}); & [\text{mmol/m}^2/\text{d}] \\ k_{\text{CH}_4} &= k_{600}(600/\text{Sc})^n; & [\text{m d}^{-1}] \end{aligned} \quad (2.1)$$

where  $C_w$  is the CH<sub>4</sub> concentration in the surface water,  $p\text{CH}_{4,\text{atm}}$  is the partial pressure of atmospheric CH<sub>4</sub>,  $H_{cp}$  is the Henry constant of CH<sub>4</sub> dissolution at in situ temperature, Sc is the Schmidt number for CH<sub>4</sub> and the exponent is taken as  $n = 2/3$  for wind speed  $< 3.7 \text{ m s}^{-1}$  and  $n = 1/2$  for wind  $> 3.7 \text{ m s}^{-1}$ . Several parameterizations have been proposed for the mass transfer coefficient ( $k_{600}$ ) to estimate diffusive emission to the atmosphere (Klaus & Vachon 2020 and references therein). We compared chamber-based CH<sub>4</sub> mass transfer coefficients ( $k_{600}^{\text{cb}}$ ) based on our chamber flux data to five  $k_{600}$  parameterizations: CC98 based on Cole & Caraco 1998; MA10-NP (negative buoyancy), MA10-MB (mixed buoyancy), and MA10-PB (positive buoyancy) based on MacIntyre *et al.* 2010; and VP13 based on Vachon & Prairie 2013 (Fig. S.A.4). These parameterizations weakly correlated with  $k_{600}^{\text{cb}}$  ( $r^2 = [0.01 - 0.037]$ ; (Fig. S.A.5) and all of them underestimated  $k_{600}^{\text{cb}}$  (MNB=[16 - 81 %]) (Fig. S.A.5). The best agreement was found with MA10-NB based on convective mixing ( $r^2=[0.01 - 0.37]$ , RMSE=[0.63 - 4.65  $\text{m d}^{-1}$ ], MNB=[16 - 57 %]; Fig. S.A.5).

### 2.2.4 Diffusive CH<sub>4</sub> fluxes from littoral sediments.

Diffusive CH<sub>4</sub> fluxes at the sediment-water interface (SWI) in the littoral zone ( $F_s$ ) were estimated using benthic chambers and porewater measurements of dissolved CH<sub>4</sub> (Fig. S.A.6). On average, three cores above the thermocline depth were taken in the epilimnion on September 2018 and

July 2019 (Table S.A.3) to estimate the littoral sediment fluxes at each lake (Methods). Benthic chamber fluxes were calculated based on the temporal change of  $\text{CH}_4$  concentration inside the chamber, while Fick's 1st Law was used for the porewater method (Methods). Hypereutrophic BRE showed the highest littoral sediment flux ( $8.3 \pm 6.7 \text{ mmol m}^{-2} \text{ d}^{-1}$ ), followed by NOI (eutrophic), CHA (mesotrophic) and LIO (oligotrophic) with the lowest value ( $0.3 \pm 0.1 \text{ mmol m}^{-2} \text{ d}^{-1}$ ) (Table 2.2).  $\delta^{13}\text{C}_{\text{CH}_4}$  in the upper part of the sediments ranged between  $-66$  to  $-48$  ‰ (Table S.A.4).  $\delta^{13}\text{C}_{\text{CH}_4}$  in the littoral sediment was around 20‰ lighter than in the surface waters of NOI and BRE but similar for CHA ( $-60$  ‰, Table S.A.4 and Fig. S.A.6). No porewater measurements were performed in LIO due to the rocky nature of the littoral sediments (Methods).

### 2.2.5 $\text{CH}_4$ ebullition rates and bubble dissolution.

$\text{CH}_4$  ebullition rates at the SWI were estimated using the gas composition of bubbles collected during each sampling campaign, the measured  $\text{CH}_4$  fluxes at the SWI (Table S.A.3), and modeling the dissolved porewater gas concentration in the sediments following Langenegger *et al.* 2019. Bubble dissolution rates ( $R_{\text{dis}}$ ) were calculated as the average dissolution rates in the SML obtained using a discrete bubble model (McGinnis *et al.* 2006) (see Methods). The spatially-averaged ebullition rates for BRE and NOI were  $1.06$  and  $0.56 \text{ mmol m}^{-2} \text{ d}^{-1}$ , respectively, while the bubble dissolution in the SML for BRE and NOI ranged between  $17$  -  $51 \text{ } \mu\text{mol m}^{-3} \text{ d}^{-1}$  (Table 2.2). Ebullition was not detected in CHA and LIO.

### 2.2.6 Vertical diffusive fluxes from/to the epilimnion.

The vertical transport from/to the epilimnion ( $F_z$ ) is driven by turbulent vertical diffusivity ( $K_z$ ) and concentration gradients at the bottom of the epilimnion.  $K_z$  was determined at each lake for each sampling campaign (Fig. S.A.7) using CTDs and microstructure temperature profiles following the approach from Lorke & Wüest 2002 (Methods).  $K_z$  values at the top of the thermocline ranged between  $0.03$  -  $14.4 \times 10^{-6} \text{ m s}^{-1}$  (Table 2.2).  $F_z$  was determined by Fick's 1st Law using  $K_z$  and the concentration gradient just below the SML (Table 2.2). In all lakes,  $F_z$  was typically low ( $-0.1$  -  $0.5 \text{ mmol/m}^2/\text{d}$ ), except in BRE and NOI at the end of the summer when fluxes were  $13.3$  and  $3.1 \text{ mmol/m}^2/\text{d}$ , respectively.



### 2.2.7 Horizontal dispersion.

In the lateral transport model, we estimated the horizontal dispersion coefficient ( $K_H$ ) for each lake using Peeters & Hofmann 2015 parametrization in which the length scale is equal to the equivalent radius,  $R_{eq} = \sqrt{A_a/\pi}$ , where  $A_a$  is lake surface area as a function of water level. Water level fluctuations were low in BRE, NOI and LOI. ( $\pm 1$  m). In CHA, the highest water level was observed at the beginning of summer after ice-off and slowly decreased during the summer by about 4 m (Fig. S.A.9). This water level change was accounted for when estimating horizontal dispersion in CHA on each sampling date. The calculated  $K_H$  values were 2034, 903 and  $2564 \text{ m}^2 \text{ d}^{-1}$  for BRE, NOI, and LIO, respectively, and ranged between  $2004 - 2366 \text{ m}^2 \text{ d}^{-1}$  for CHA (Table 2.2).

Table 2.2. Inputs for the lateral transport model and full-scale mass balance in the surface mixed layer (mean  $\pm$  SD).

Lake	Date	$K_H$	$C_{hyp}$	$K_z$	$\bar{k}_{CH_4}$	$F_s$	$F_a$	$F_z$	$R_{dis}$
		( $\text{m}^2 \text{ d}^{-1}$ )	( $\text{mmol m}^{-3}$ )	( $10^{-6} \text{ m s}^{-1}$ )	( $\text{m d}^{-1}$ )	(mmol $\text{m}^{-2} \text{ d}^{-1}$ )			( $\mu\text{mol m}^{-3} \text{ d}^{-1}$ )
Bretaye	June 2018		4.0	4.09	0.67	$8.3 \pm 6.7$ (n=3)	$4.6 \pm 1.8$	$0.5 \pm 0.3$	$50.6 \pm 10.2$
	Sept 2018	2034	161.8	0.96	1.00		$3.7 \pm 1.5$	$13.3 \pm 7.7$	$34.9 \pm 9$
	July 2019		2.3	0.94	2.12		$3.7 \pm 1.6$	$0.02 \pm 0.01$	$42.7 \pm 11.3$
Noir	June 2018		1.3	0.91	1.75	$1.5 \pm 0.3$ (n=4)	$2.4 \pm 0.8$	$0.03 \pm 0.02$	$17.2 \pm 1.6$
	Sept 2018	903	13.7	30.1	1.48		$2.2 \pm 1.0$	$3.1 \pm 1.8$	$24.7 \pm 8.1$
	July 2019		2.3	0.07	0.69		$2.9 \pm 1.7$	$-0.01 \pm 0$	$17.0 \pm 1.7$
Chavonnes	June 2018	2366	0.1	14.14	2.23	$0.4 \pm 0.4$ (n=3)	$0.1 \pm 0.02$	$-0.1 \pm 0.03$	$0 \pm 0$
	Sept 2018	2004	0.1	0.74	1.49		$0.2 \pm 0.1$	$0.0 \pm 0$	$0 \pm 0$
	July 2019	2246	0.4	1.02	1.12		$0.1 \pm 0.1$	$0.03 \pm 0.02$	$0 \pm 0$
Lioson	June 2018		0.1	0.89	2.22	$0.3 \pm 0.1$ (n=3)	$0.2 \pm 0.04$	$0 \pm 0$	$0 \pm 0$
	Sept 2018	2564	0.6	0.03	3.30		$1.2 \pm 0.6$	$0 \pm 0$	$0 \pm 0$
	July 2019		0.3	4.80	1.29		$0.4 \pm 0.2$	$0.01 \pm 0.01$	$0 \pm 0$

### 2.2.8 Surface mass balances.

The full-scale mass balance (0-D) proposed by Donis *et al.* 2017 and a modified version of the lateral transport model (1-D) proposed by Peeters *et al.* 2019 were used to determine  $P_{net}$  in the SML of each lake and campaign based on the input values listed in Table 2.2.  $P_{net}$  is the net result of OMP and MOx, which adds and removes  $\text{CH}_4$  to the SML, respectively. Thus, when  $P_{net}$  is positive the true OMP rate is actually higher than  $P_{net}$ .

### Full-scale mass balance.

The full-scale mass balance approach assumes that at each sampling date the surface layer can be modeled as a well-mixed reactor and  $P_{\text{net,fs}}$  can be estimated as follows:

$$\frac{\partial C}{\partial t} \forall_{\text{SML}} = A_s F_s - A_a F_a + A_z F_z + R_{\text{dis}} \forall_{\text{SML}} + P_{\text{net,fs}} \forall_{\text{SML}}; \quad [\text{mol d}^{-1}] \quad (2.2)$$

where  $C$  is surface  $\text{CH}_4$  concentration,  $\forall_{\text{SML}}$  is SML volume, and  $A_s$ ,  $A_a$  and  $A_z$  are sediment area, lake surface area, and planar area at the bottom of the SML (Table S.A.5), respectively.

### Lateral transport model.

Using a modified version of the lateral transport model presented by Peeters *et al.* 2019,  $P_{\text{net,lt}}$  rates for each lake were obtained by finding the simulated transect  $\text{CH}_4$  concentrations that best-fit to the measured  $\text{CH}_4$  concentrations. In this study, the lateral transport model includes vertical diffusive  $\text{CH}_4$  flux through the bottom of the SML and bubble dissolution:

$$\begin{aligned} \frac{\partial C}{\partial t} = & K_H \frac{1}{H(r)r} \frac{\partial}{\partial r} \left( H(r)r \frac{\partial C(r)}{\partial r} \right) + \frac{1}{H(r)} K_z \frac{C_{\text{hyp}} - C(r)}{\Delta z} - \frac{\bar{k}_{\text{CH}_4}}{H(r)} (C(r) - H_{\text{cp}} P_{\text{CH}_4, \text{atm}}) \\ & + \frac{F_s}{H(r)} + R_{\text{dis}}(r) + P_{\text{net,lt}}; \quad [\text{mol m}^{-3} \text{d}^{-1}] \end{aligned} \quad (2.3)$$

where  $H(r)$  is the spatially varying thickness of the SML. The mass transfer coefficient for  $\text{CH}_4$  was calculated based on the average gas transfer coefficient obtained from the flux chambers ( $\bar{k}_{\text{CH}_4}$ ),  $C_{\text{hyp}}$  is the  $\text{CH}_4$  concentration 1 m below the bottom of the SML and  $\Delta z = 1$  m (Table 2.2; see Methods for each term calculation).

Despite the different modeling approaches and underlying assumptions, we obtained an excellent agreement between the  $P_{\text{net}}$  rates obtained with both models assuming steady state conditions (Fig. S.A.10,  $R^2 = 0.97$ ). Monte Carlo simulations were applied to assess uncertainties in both models during the stratified period (Methods). The average  $P_{\text{net}}$  rates for the three sampling dates were 316, 1434, 12 and 223  $\mu\text{mol m}^{-3} \text{d}^{-1}$  for BRE, NOI, CHA, and LIO, respectively (Fig. 2.3).  $P_{\text{net}}$  rates in BRE and NOI were, on average, about seven times higher than CHA and LIO. A decrease of  $P_{\text{net}}$  rates from the beginning to the end of the

summer were observed in NOI and BRE, whereas in CHA and LIO  $P_{\text{net}}$  remained relatively consistent across campaigns.

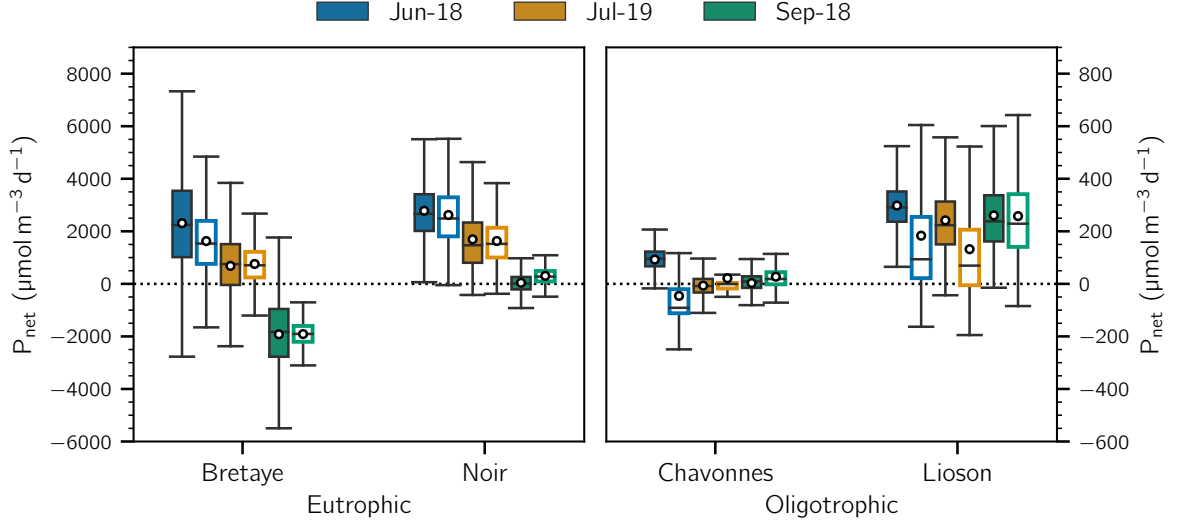


Figure 2.3.  $P_{\text{net}}$  estimation using the full-scale mass balance ( $P_{\text{net,fs}}$ ; filled boxes) and lateral transport model ( $P_{\text{net,lt}}$ ; open boxes). Boxes show the first and third quartiles with the median (line), whiskers extend to most extreme data point within 1.5 times the interquartile range from the box. The white dot represents the average of the  $P_{\text{net}}$  distribution. Note different scales on Y-axes of the two panels.

### 2.2.9 Sensitivity analysis of surface diffusive emission to the atmosphere.

Several studies have used  $k_{600}$  literature parameterization to estimate  $F_a$  (Eq. 2.1, Tan *et al.* 2021 and references there in), however other studies have shown that these estimates often do not correspond with field measurements (Klaus & Vachon 2020 and Fig. S.A.4). Therefore, we analyzed the impact of  $k_{600}$  parameterization on  $P_{\text{net}}$  as it is one of the main parameters affecting the mass balance in the epilimnion.

Since the  $P_{\text{net}}$  results from both models were similar, we used  $P_{\text{net}}$  from the full-scale mass balance in the following sensitivity analysis as it is simpler to interpret. Therefore, in the lateral transport model (Eq. 2.3), we simulated surface  $\text{CH}_4$  concentrations either with the addition of OMP (i.e.,  $P_{\text{net}}$ ), as obtained from the full-scale mass balance approach ( $P_{\text{net}}=P_{\text{net,fs}}$ ), or without any addition from OMP (i.e.,  $P_{\text{net}}=0$ ). We also used five different mass transfer coefficient parameterizations ( $k_{600}$ ) to model diffusive  $\text{CH}_4$  emission to the atmosphere in the lateral transport model (Table 2.3). Thus, the resulting surface  $\text{CH}_4$  concentrations were obtained from the combinations of  $P_{\text{net}}$  and  $k_{600}$ , as they determined different boundary conditions of the

mass balance in the SML. The analysis is focused on the best and worst mass transfer coefficient parameterizations (MA10-NB and CC98, respectively) when compared with chamber-based estimations ( $\bar{k}_{\text{CH}_4}$ ) (Figs. S.A.4 and S.A.5). The results of the three remaining parameterization comparisons are available in the Fig. S.A.11 and Table 2.3.

Table 2.3. Combinations of each simulation performed with the lateral transport model for the sensitivity analysis. Root mean square error (RMSE), correlation coefficient ( $R^2$ ) and mean normalized bias (MNB) are shown for the comparison between simulated and measured surface  $\text{CH}_4$  concentration.  $P_{\text{net,fs}}$  refers to the  $P_{\text{net}}$  rates obtained from the full-scale mass balance.  $k_{\text{CH}_4}$  were calculated from the  $k_{600}$  literature parameterizations (Eq. 2.1) to be used in (Eq. 2.3).  $U_{10}$ , wind speed at 10 m ( $\text{m s}^{-1}$ );  $A_s$ , surface lake area ( $\text{km}^2$ );  $k_{600}$ , gas transfer coefficient ( $\text{cm h}^{-1}$ ).

Configuration name	$P_{\text{net}}$	$k_{\text{CH}_4}$	RMSE	$R^2$	MNB
$P_{\text{net}}0\text{-}\bar{k}_{\text{CH}_4}$	0	$\bar{k}_{\text{CH}_4}$	2.44	0.36	-1.60
$P_{\text{net}}0\text{-CC98}$	0	$k_{600} = 2.07 + 0.215U_{10}^{1.7}$ (Cole & Caraco 1998)	4.28	0.35	-0.35
$P_{\text{net}}0\text{-MA10-NB}$	0	$k_{600} = 2.045U_{10} + 2$ (MacIntyre <i>et al.</i> 2010)	1.80	0.43	-1.27
$P_{\text{net}}0\text{-MA10-MB}$	0	$k_{600} = 2.25U_{10} + 0.16$ (MacIntyre <i>et al.</i> 2010)	1.98	0.56	-0.66
$P_{\text{net}}0\text{-MA10-PB}$	0	$k_{600} = 1.75U_{10} - 0.15$ (MacIntyre <i>et al.</i> 2010)	3.13	0.61	0.11
$P_{\text{net}}0\text{-VP13}$	0	$k_{600} = 2.51 + 1.48U_{10} + 0.39U_{10} \log_{10}(A_s)$ (Vachon & Prairie 2013)	2.54	0.36	-0.93
$P_{\text{net}}\text{-}\bar{k}_{\text{CH}_4}$	$P_{\text{net,fs}}$	$\bar{k}_{\text{CH}_4}$	0.56	0.96	0.07
$P_{\text{net}}\text{-CC98}$	$P_{\text{net,fs}}$	$k_{600} = 2.07 + 0.215U_{10}^{1.7}$ (Cole & Caraco 1998)	2.62	0.89	1.75
$P_{\text{net}}\text{-MA10-NB}$	$P_{\text{net,fs}}$	$k_{600} = 2.04U_{10} + 2$ (MacIntyre <i>et al.</i> 2010)	0.72	0.88	0.71
$P_{\text{net}}\text{-MA10-MB}$	$P_{\text{net,fs}}$	$k_{600} = 2.25U_{10} + 0.16$ (MacIntyre <i>et al.</i> 2010)	2.08	0.84	1.01
$P_{\text{net}}\text{-MA10-PB}$	$P_{\text{net,fs}}$	$k_{600} = 1.74U_{10} - 0.15$ (MacIntyre <i>et al.</i> 2010)	4.23	0.83	1.57
$P_{\text{net}}\text{-VP13}$	$P_{\text{net,fs}}$	$k_{600} = 2.51 + 1.48U_{10} + 0.39U_{10} \log_{10}(A_s)$ (Vachon & Prairie 2013)	1.06	0.9	0.72

The best agreement between measured and simulated  $\text{CH}_4$  concentrations was found using  $P_{\text{net}}$  from the full-scale mass balance ( $P_{\text{net,fs}}$ ) and the chamber-based mass transfer coefficient ( $\bar{k}_{\text{CH}_4}$ ) ( $P_{\text{net}}\text{-}\bar{k}_{\text{CH}_4}$ , Table 2.3, Fig. 2.4b). When using  $\bar{k}_{\text{CH}_4}$  with  $P_{\text{net}}$  set to zero ( $P_{\text{net}}0\text{-}\bar{k}_{\text{CH}_4}$ ), average  $\text{CH}_4$  concentrations along the transect were underestimated relative to the measured values (MNB=-1.60, Table 2.3, Fig. 2.4a). Using  $P_{\text{net,fs}}$  and MA10-NB or CC98 parameterizations ( $P_{\text{net}}\text{-MA10-NB}$  and  $P_{\text{net}}\text{-CC98}$ ) resulted in an overestimation of  $\text{CH}_4$  concentrations (Figs. 2.4d and 2.4f and Table 2.3), whereas when  $P_{\text{net}}$  was set to zero ( $P_{\text{net}}0\text{-MA10-NB}$  and  $P_{\text{net}}0\text{-CC98}$ ) using both parameterizations, the average  $\text{CH}_4$  concentrations along the transect were underestimated (Table 2.3, Figs. 2.4c and 2.4e). The lowest correlation ( $R^2=0.35$ ) and highest error (RMSE=4.28) of the all the combinations was obtained when  $P_{\text{net}}$  was set to zero and CC98 was used to estimate the  $\text{CH}_4$  diffusive flux to the atmosphere (Table 2.3).

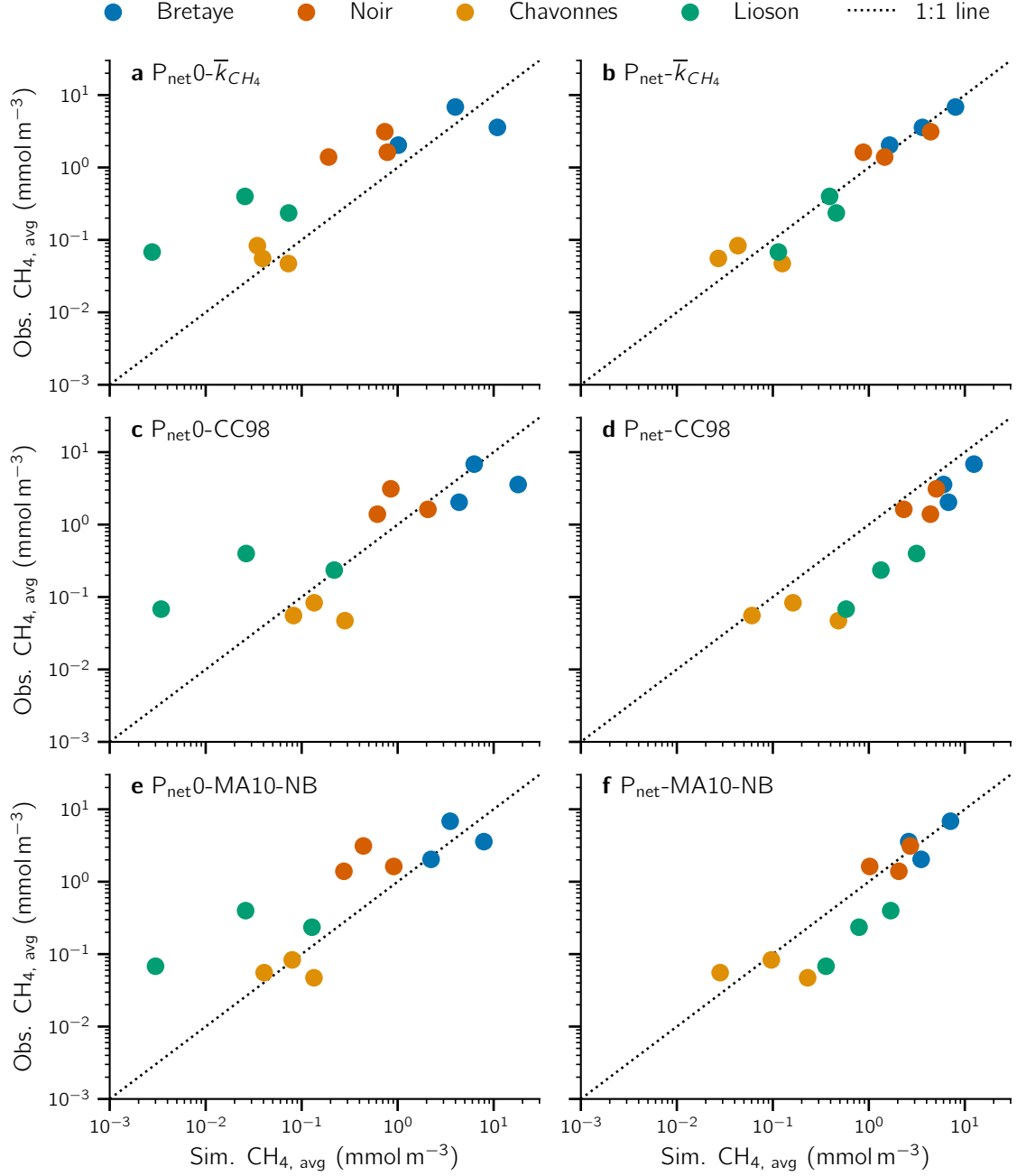


Figure 2.4. Comparison of observed and simulated average surface  $\text{CH}_4$  concentration along transects for each campaign. Simulated  $\text{CH}_4$  concentrations were obtained with the lateral transport model using  $k_{600}$  for diffusive emissions either with (panels b, d and f) or without  $P_{\text{net}}$  (panels a, c and e). The  $k_{600}$  was either the chamber-based  $k_{600}$  ( $\bar{k}_{\text{CH}_4}$ , panels a and b), Cole & Caraco 1998 (CC98, panels c and d) and MacIntyre *et al.* 2010 negative buoyancy (MA10-NB, panels e and f). The statistical results of each panel are shown in Table 2.3.

### 2.2.10 Contribution of methane sources to atmospheric diffusive emissions.

As  $P_{\text{net}}$  rates were similar from both models, we again use the  $P_{\text{net}}$  rates from the full-scale mass balance approach to calculate the contribution of each  $\text{CH}_4$  SML source to the diffusive atmospheric  $\text{CH}_4$  emissions from each lake and during each campaign (Methods).  $F_s$  and  $P_{\text{net}}$  were the two major sources of  $\text{CH}_4$  in the SML. On average,  $P_{\text{net}}$  contributed about 30% of the  $\text{CH}_4$  emissions in BRE and CHA, while it reached up to 60% and 90% for NOI and LIO, respectively (Fig. 2.5).  $P_{\text{net}}$  was a dominant source in all lakes in June and July except for CHA in July. Negligible  $P_{\text{net}}$  contributions ( $<8\%$ ) were found in all lakes in September 2019, except for LIO (91%). On average,  $F_s$  contributed about 10%, 30%, 50% and 65% to the  $\text{CH}_4$  emissions in LIO, NOI, BRE and CHA, respectively. For CHA and NOI, the  $F_s$  contribution increased at the end of the summer and reached up to 90% for CHA in September. For BRE and LIO, the  $F_s$  contribution was relatively constant during the different months. On average,  $F_s$  contributed the same in the oligotrophic and eutrophic lakes. The vertical turbulent flux ( $F_z$ ) contributed about 50% of the atmospheric  $\text{CH}_4$  from BRE and NOI in September and about 30% from CHA in July, but was negligible ( $<9\%$ ) for the other campaigns. The contribution from bubble dissolution ( $R_{\text{dis}}$ ) in BRE and NOI was also negligible ( $<4\%$ ).

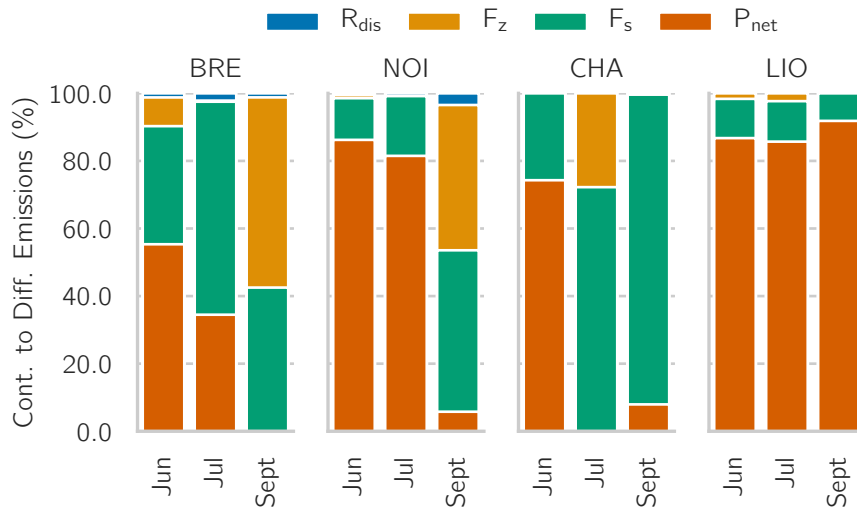


Figure 2.5. Contribution to diffusive atmospheric  $\text{CH}_4$  emissions ( $F_a$ ) from the sediment flux ( $F_s$ ), diffusive flux from hypolimnion ( $F_z$ ), bubble dissolution ( $R_{\text{dis}}$ ) and net production ( $P_{\text{net}}$ ) in the SML of Lac de Bretaye (BRE), Lac Noir (NOI), Lac des Chavannes (CHA) and Lac Lioson (LIO).

## 2.3 Discussion

In most of our study lakes during all campaigns, the  $P_{\text{net}}$  values were positive, indicating that the oxic SML acts as a  $\text{CH}_4$  source during the stratified season (Fig. 2.3).  $P_{\text{net}}$  was around zero in CHA, which is the meso-oligotrophic lake with the largest water level changes throughout the summer, in contrast to the other pre-alpine lakes in our study that maintained relatively consistent water levels. The observed average  $P_{\text{net}}$  rates were within the range of values previously reported (Günthel *et al.* 2021), except for NOI with the highest reported  $P_{\text{net}}$  ( $2308 \pm 2024 \mu\text{mol m}^{-3} \text{d}^{-1}$ ).

$P_{\text{net}}$  rates were temporally variable and across study sites. At the beginning of the summer, highly positive  $P_{\text{net}}$  rates indicated that OMP was an active source of  $\text{CH}_4$  to the atmosphere. By the end of the stratified season,  $P_{\text{net}}$  became negative indicating that MOx was dominating in surface waters of each lake except for the oligotrophic LIO (Fig. 2.3). This seasonal trend in OMP was also observed by Günthel *et al.* 2019 and may be related to the  $\text{CH}_4$  production rates of different algal species (Günthel *et al.* 2020) and their concentrations at the end of the growing season. In addition, the eutrophic lakes BRE and NOI had  $P_{\text{net}}$  rates one order magnitude higher than the meso-oligotrophic and oligotrophic lakes (CHA, LIO), suggesting that OMP may also be related to trophic state. From this perspective, productive lakes in general may experience higher OMP rates than less productive ones.

The OMP contribution to epilimnetic  $\text{CH}_4$  budgets and diffusive  $\text{CH}_4$  emissions to the atmosphere is hotly debated (Günthel *et al.* 2021; Peeters & Hofmann 2021). In our study,  $P_{\text{net}}$  is a significant contributor to atmospheric diffusive  $\text{CH}_4$  emissions. Its contribution to emissions decreased significantly by the end of the summer in the eutrophic lakes, as did  $P_{\text{net}}$  rates themselves (Figs. 2.3 and 2.5). Although higher  $P_{\text{net}}$  rates were found in the eutrophic lakes, the  $P_{\text{net}}$  contribution fraction to surface diffusive  $\text{CH}_4$  emissions was independent of the trophic status of the lake. For example, the fraction of  $P_{\text{net}}$  contribution to emissions was similar and even higher in oligotrophic LIO than that in eutrophic NOI. This was mainly due to the substantial contribution of  $\text{CH}_4$  from the littoral sediments of the eutrophic lakes to the SML. Therefore, increasing  $\text{CH}_4$  production and emission from littoral sediments will actually reduce the fractional contribution of OMP to atmospheric emissions even though OMP rates may be

higher in such productive systems.

As a first attempt at upscaling OMP, Günthel *et al.* 2019 proposed that the OMP contribution to diffusive  $\text{CH}_4$  emissions from lakes can be estimated as a function of littoral sediment area and SML volume. In our study, the  $P_{\text{net}}$  contribution to diffusive  $\text{CH}_4$  flux to the atmosphere at the AWI was highly variable and disagreed with this simple upscaling approach (Fig. S.A.14). While it is plausible that OMP contribution may partially depend on lake bathymetry (i.e., the fraction between the sediment area and the SML volume), our results indicate that OMP is a complex phenomenon more likely to be related to the lake trophic properties (e.g. productivity).

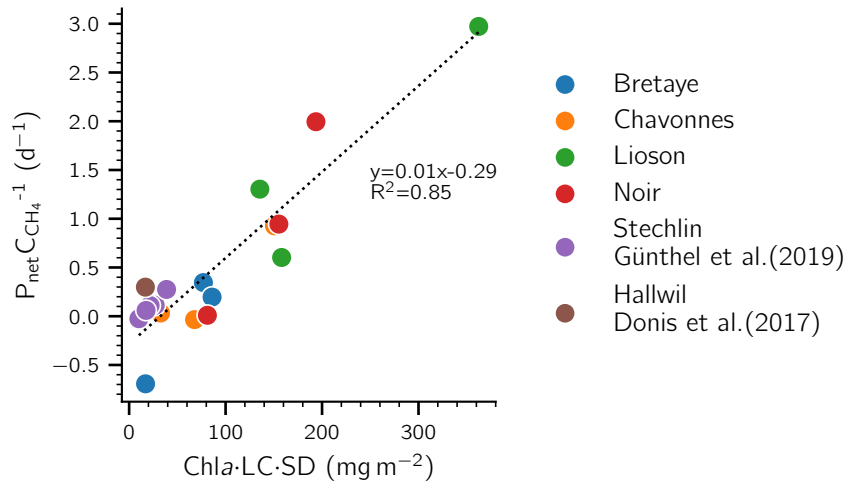


Figure 2.6. Interaction between  $P_{\text{net}}$  ( $\text{mmol m}^{-3} \text{d}^{-1}$ ) and  $\text{Chla}$  ( $\text{mg m}^{-3}$ ),  $\text{LC}$  (-) and  $\text{SD}$  (m) suggest a direct role of photosynthesis on OMP. Specific production/oxidation rate calculated as  $P_{\text{net}}$  normalized by  $\text{CH}_4$  concentration ( $\text{mmol m}^{-3}$ ) ( $P_{\text{net}} \text{C}_{\text{CH}_4}^{-1}$ ) versus  $\text{Chla} \times \text{light climate}$  ( $\text{LC} = 2.5 \frac{\text{SD}}{H_{\text{SML}}}$ )  $\times \text{SD}$ .  $\text{C}_{\text{CH}_4}$  is the average surface concentrations,  $\text{Chla}$  is the surface average concentrations obtained from CTD's profiles at the center of the lake,  $\text{SD}$  is the Secchi depth and  $H_{\text{SML}}$  is the SML depth. All the parameters were calculated at each sampling campaign.

Two primary mechanisms have been the focal points of  $\text{CH}_4$  production in oxic waters. Methylphosphonate (MPn) biodegradation has been shown to be responsible for  $\text{CH}_4$  production in oxic waters of the ocean (Karl *et al.* 2008) and lakes (Wang *et al.* 2017), specifically in phosphorus-limited environments (Karl *et al.* 2008; Wang *et al.* 2017). In our pre-alpine lakes, however, we did not observe any correlation between  $P_{\text{net}}$  and phosphorus in the SML (Fig. S.A.12). The other suggested OMP mechanism is the production of  $\text{CH}_4$  in nitrogen-limited environments via the transformation of  $\text{CO}_2$ , nitrogen gas, and hydrogen by the nitrogenase



enzyme (Zheng *et al.* 2018; Luxem *et al.* 2020) that is commonly present in cyanobacteria. While we observed that  $P_{\text{net}}$  negatively correlated with dissolved inorganic nitrogen (DIN) (Fig. S.A.13), which could indicate the use of nitrogen for OMP, to our knowledge  $\text{CH}_4$  production due to nitrogenase activity in cyanobacteria has not yet been observed. Ultimately, although our data suggests links between OMP and trophic parameters, similar to relationships found in Günthel *et al.* 2020, the underlying OMP mechanisms still need to be deciphered.

While it is premature to construct a mechanistic model to estimate OMP in lakes, based on our data we suggest an empirical approach using simple correlations between physical and biochemical parameters as a tool to identify the potential for the occurrence of  $P_{\text{net}}$  in lakes (Fig. 2.6). Higher surface  $\text{CH}_4$  concentrations were observed in eutrophic lakes (Table 2.1); therefore,  $\text{CH}_4$  concentration in the SML is used as a proxy to reflect the trophic state of each lake and to normalize  $P_{\text{net}}$  rates found in the eutrophic and oligotrophic lakes (Fig. 2.3). Although the mechanism is still unclear, recent evidence indicates that OMP could be a photosynthesis-derived process (Bižić *et al.* 2020; Günthel *et al.* 2020; Hartmann *et al.* 2020). In this approach, *Chla* is used as a proxy of phytoplankton biomass, Secchi depth as light availability for photosynthesis and MOx inhibition (Thottathil *et al.* 2019) and LC (light climate) defines the variability of light conditions that phytoplankton can be subjected to in the SML during the day (MacIntyre 1993). This interaction between  $P_{\text{net}}$  normalized by the SML  $\text{CH}_4$  concentration versus  $\text{Chla} \times \text{LC} \times \text{Secchi depth}$  indicates the direct role of phytoplankton and light availability in  $\text{CH}_4$  production under oxic conditions (Bižić *et al.* 2020; Günthel *et al.* 2020; Hartmann *et al.* 2020). Including the data from Donis *et al.* 2017 and Günthel *et al.* 2019, this parameterization explains around 85% of the dataset ( $R^2=0.85$ ). While more data are needed to understand this parameterization, it provides a step towards estimating  $P_{\text{net}}$  in the SML that would help to identify OMP dynamics across systems, identify lakes with potentially high OMP rates, and develop a global upscaling of OMP (or  $P_{\text{net}}$ ) driven emissions.

The methodologies for determining  $P_{\text{net}}$  are limited by the accuracy of the boundary conditions of the mass balance (i.e., diffusive  $\text{CH}_4$  emissions at the AWI,  $\text{CH}_4$  flux from littoral sediment, ebullition, etc.). These boundary conditions are sometimes based on very few measurement locations using uncertain methodologies and are naturally variable. The variability and uncertainty of such estimations leads to the observed range of  $P_{\text{net}}$  in mass

balance approaches obtained with the Monte Carlo simulations (Fig. 2.3). Therefore, to assess the robustness and the validity of the models used, we compared the boundary conditions components ( $F_a$  and  $F_s$ ) with literature values and examined how their variability may alter the outcome of the two mass balance models.

Diffusive  $\text{CH}_4$  emissions to the atmosphere are temporally and spatially variable. We accounted for the spatial variability by using the average of ten surface flux measurements along a lake-wide transect for each  $P_{\text{net}}$  calculation. The impact of diffusion variability at the AWI on  $P_{\text{net}}$  rates were considered in the Monte Carlo simulations conducted on both modeling approaches. In addition, the average diffusive  $\text{CH}_4$  emissions estimated for lakes NOI, CHA and BRE are well within the range reported for the stratified season of these lakes in previous studies (0.06 - 4.38 mmol/m<sup>2</sup>/d; Rinta *et al.* 2017). There are no previous data for LIO.

A large uncertainty in the estimation of diffusive  $\text{CH}_4$  emissions is the mass transfer coefficient ( $k_{600}$ ) parameterization. Therefore, we applied five alternative  $k_{600}$  parameterizations (Cole & Caraco 1998; MacIntyre *et al.* 2010; Vachon & Prairie 2013, negative, mixed and positive buoyancy) to estimate  $\text{CH}_4$  diffusion at the AWI in the four pre-alpine lakes and compared these fluxes with direct measurements using floating chambers. The comparison of  $k_{600}^{\text{cb}}$  with all the tested parameterizations resulted in a low correlation ( $R^2 < 0.38$ ) and clear underestimation of the measured  $k_{600}$  values (Fig. S.A.4), reflecting the limitations of the  $k_{600}$  models across different lakes (Klaus & Vachon 2020). The underestimation by  $k_{600}$  parameterizations has also been reported in previous studies (Tan *et al.* 2021 and references there in). We hypothesize that the presence of oxygen microbubbles produced by photosynthesis in the water column (Koschorreck *et al.* 2017) might enhance the mass transfer coefficient (McGinnis *et al.* 2015). This phenomenon would be more relevant in high altitudes lakes due to the lower air pressure and oxygen saturation concentration.

In our analysis of the  $k_{600}$  parameterizations for the lateral transport model, we observed that when using the CC98 parameterization for surface  $\text{CH}_4$  fluxes, OMP was not required to close the mass balance. Similarly, OMP seemed irrelevant when Peeters *et al.* 2019 re-analyzed the data from Donis *et al.* 2017 using the CC98  $k_{600}$  parameterization instead of the measured surface  $\text{CH}_4$  fluxes Donis *et al.* 2017. Moreover, when comparing observed surface

CH<sub>4</sub> concentrations with simulated CH<sub>4</sub> concentrations, we obtained a lower correlation and higher error using simulated CH<sub>4</sub> concentrations based on the CC98 parameterization than those based on  $k_{600}^{cb}$  or MA-NB parameterizations (Fig. 2.4). This is largely explained by the fact that the CC98 parameterization grossly underestimates  $k_{600}^{cb}$  for all lakes (MNB = [57 - 71 %]) and does not correlate well with  $k_{600}^{cb}$  ( $R^2$ =[0.01 - 0.38], Fig. S.A.5). Thus, a generalized  $k_{600}$  parameterization from a single lake (e.g. CC98) does not apply to all lakes. It is therefore much more reliable to use in situ measured fluxes to compute  $k_{600}$  in a mass balance.

The littoral diffusive sediment fluxes we measured were within the range of values reported in the literature (0.001 - 8.8 mmol m<sup>-2</sup> d<sup>-1</sup> (Huttunen *et al.* 2006; Bastviken *et al.* 2008; Peeters *et al.* 2019)). In the full-scale mass balance, we assumed that the lateral flux to the center of the lakes was equal to the diffusive CH<sub>4</sub> flux coming from the sediment in the littoral area. It has been shown that CH<sub>4</sub> production rates in sediments increase with increasing temperature (Bastviken *et al.* 2008); thus, it has been hypothesized that sediment CH<sub>4</sub> diffusion will also follow this relationship (Peeters *et al.* 2019). As most of our sediment flux measurements in the littoral zone were performed in July when the temperatures were highest in all lakes (Table S.A.3), we can assume that those observed sediment fluxes were on the higher end of possible values. Ultimately, using a presumably high sediment flux from July for the mass balance of other months would result in a conservative  $P_{net}$  estimate.

We also investigated the impact of littoral sediment flux on mass balances. Assuming that OMP does not occur (i.e.  $P_{net}=0$ ) in the full-scale mass balance, we would need littoral sediment fluxes that are two to three times higher than our measured fluxes to compensate for the diffusive CH<sub>4</sub> emissions measured at the AWI (Fig. 2.7). In oligotrophic LIO, we would need a littoral sediment flux of about  $2.23 \pm 1.12$  mmol m<sup>-2</sup> d<sup>-1</sup> which is very unlikely given that flux is an order of magnitude higher than what we measured ( $0.3 \pm 0.1$  mmol m<sup>-2</sup> d<sup>-1</sup>). In fact, in BRE we have measured one of the highest littoral sediment fluxes yet reported ( $8.3 \pm 6.7$  mmol m<sup>-2</sup> d<sup>-1</sup>) (Huttunen *et al.* 2006; Bastviken *et al.* 2008; Hardenbroek *et al.* 2012; Peeters *et al.* 2019), and we still required one of the highest  $P_{net}$  rates ever reported in the literature (June 2018:  $2314 \pm 2046$  μmol m<sup>-3</sup> d<sup>-1</sup>) to close the CH<sub>4</sub> budget in that lake. Therefore, littoral sediment CH<sub>4</sub> flux alone cannot account for the diffusive CH<sub>4</sub> emissions measured in our lakes and OMP needs to be included to close the CH<sub>4</sub> budget.

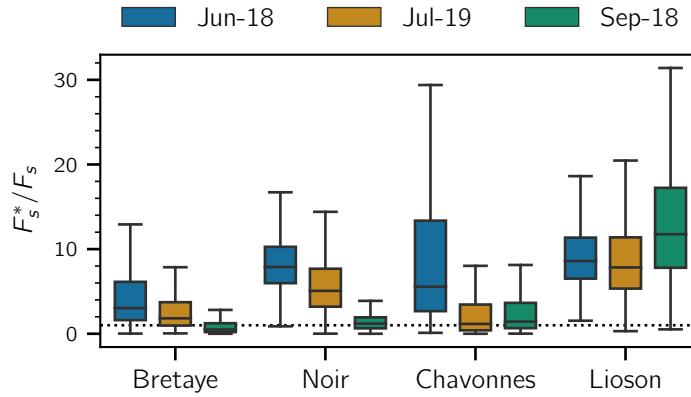


Figure 2.7. Proportion of littoral sediment flux needed ( $F_s^*$ ) to compensate the surface diffusive emissions compare to measured littoral sediment flux ( $F_s$ ) considering no OMP in the surface mixed layer.

In this study, we quantified the  $P_{\text{net}}$  rates of  $\text{CH}_4$  (i.e. net balance between OMP and  $\text{MOx}$ ) in the oxic SML of four pre-alpine lakes using two models that have previously produced contradictory results when resolving OMP in lowland lakes (Donis *et al.* 2017; Günthel *et al.* 2019; Peeters *et al.* 2019; Günthel *et al.* 2021; Peeters & Hofmann 2021). The good agreement between both approaches we found shows that there are no methodological issues with the models themselves when the appropriate boundary conditions are used to estimate OMP (or  $P_{\text{net}}$ , in our case). We also conducted thorough sensitivity analyses on the two main parameters that lead to the highest uncertainties. This analysis shows that measured surface fluxes have to be used instead on literature  $k_{600}$  parameterizations to estimate the diffusive  $\text{CH}_4$  flux to the atmosphere and an unlikely high  $\text{CH}_4$  diffusive flux from littoral sediment are need it to close the mass balance in the SML without including  $P_{\text{net}}$ . Moreover, our results indicate that in three out of four lakes a positive  $P_{\text{net}}$  (i.e. a net input of  $\text{CH}_4$  from OMP) needs to be included in the SML  $\text{CH}_4$  budget. In fact, we show that up to 85% of atmospheric  $\text{CH}_4$  emissions from these lakes at the beginning of summer results from OMP, and even in our systems with some of the highest recorded littoral sediment fluxes, we still obtained some of the highest epilimnetic  $P_{\text{net}}$  (or OMP) rates ever reported.

Finally, while the mechanisms behind OMP need further investigation, this study (in agreement with previous ones) show that nitrogen, light, and photoautotrophs may play a significant role in OMP. Consequently, future changes in light availability and temperature

may induce positive feedbacks by promoting algal species capable of producing the greenhouse gas  $\text{CH}_4$  in oxic environments at the AWI where it can easily be emitted into the atmosphere. Although the contribution of OMP to total diffusive emissions from inland waters is hotly debated, we have shown that it can be a dominant source from lakes in the pre-alpine region that is already experiencing climatic changes at higher rates than average. It is thus crucial to continue quantifying the contribution of OMP from various aquatic systems and identify the main drivers of OMP to better understand the impact of OMP on the global  $\text{CH}_4$  cycle and how to predict or even mitigate its impact in a changing climate.

## 2.4 Methods

### 2.4.1 Study sites.

Lac de Bretaye (BRE), Lac Noir (NOI), Lac des Chavonnes (CHA) and Lac Lioson (LIO) are pre-alpine lakes (above 1600 m.a.s.l) located in Canton Vaud, Switzerland (Table S.A.1). All lakes are of glacial origin and have a wide-range of trophic states (oligotrophic-hypereutrophic). BRE, NOI and CHA are  $\sim 500$  m away from each other, while LIO is located about 7 km away from the others. BRE and NOI are small and shallow lakes without inflow or outflow streams located in alpine meadows which are utilized for animal grazing (Lods-Crozet & Reymond 2008). CHA has a small inflow stream while LIO has a small creek outflow that is the origin of the Hongrin River.

### 2.4.2 Limnological measurements.

At each sampling date, water column profiles were measured at the deepest point of each lake (M1, Fig. S.A.1) with a CTD profiler (Conductivity-Temperature-Depth, Seabird SBE19plus) equipped with temperature, conductivity, oxygen, PAR, turbidity, Chl-*a* and pH sensors.

Total (TP) and dissolved phosphorus (DP), dissolved inorganic nitrogen as nitrate plus nitrite (DIN), dissolved silica (DSIL) and total carbon concentration (TC) were measured at each campaign in the upper mixed layer (from the surface to the bottom of the thermocline) and in the hypolimnion (Table S.A.2). Water samples were collected with a Niskin sampler and equal amounts of water were transferred into two 1L glass bottle (Duran, GmbH, Mainz, Germany).

50 mL of water were filtered through 0.45  $\mu\text{m}$  (PES) Syringe filters to measure dissolved nutrient fractions. An AQ2 Discrete Analyzer (SEAL Analytical) based on spectrophotometric methods was used to measure TP and DP by Acidic molybdate/antimony with ascorbic acid reduction (USEPA 1993), Nitrate-N plus Nitrite-N by Cadmium coil reduction followed by sulfanilamide reaction in the presence of N-(1-naphthylethylenediamine) (USEPA 1993) and DSIL by Acidic molybdate with ANSA reduction (USEPA 1983). A Shimadzu carbon analyzer (TOC-L<sub>CPH/CPN</sub>) measured TC.

### 2.4.3 Mass balance.

The mass balance of  $\text{CH}_4$  in the SML was calculated using two models (Eqs. 2.2 and 2.3). A sonar survey was performed to obtain the bathymetry of each lake (Fig. S.A.1). The bottom of the SML ( $H_{\text{SML}}$ ) was define when  $\partial T/\partial z$  becomes smaller than  $-1\text{ }^\circ\text{C m}^{-1}$  (Read *et al.* 2011) (Table 2.1). The SML water volume ( $\forall_{\text{SML}}$ ), the surface area ( $A_a$ ), the sediment area ( $A_s$ ) and the planar area at the bottom of the SML ( $A_z$ ) were determined using the software Surfer® (Golden Software, LCC) (Table S.A.5).

### 2.4.4 Full-scale mass balance.

The net  $\text{CH}_4$  production ( $P_{\text{net}}$ ) was estimated using a mass balance in the surface mixed layer (Eq. 2.2) assuming steady state conditions ( $\frac{\partial C}{\partial t}\forall = 0$ ). We assumed that the lateral contribution to the mass balance is equal to the littoral sediment flux times the area of the sediment. The spatial average values for the surface fluxes ( $F_a$ ), bubble dissolution rates ( $R_{\text{dis}}$ ) in the SML and hypolimnetic fluxes ( $F_z$ ) were used as boundaries conditions (Table 2.2).

### 2.4.5 Lateral transport model.

The lateral transport model simulates the transect  $\text{CH}_4$  concentrations in the SML similar to Peeters *et al.* 2019 but including the additional flux terms from bubble dissolution and diffusion across the thermocline (Eq. 2.3). This model considers that the surface layer is fully mixed in the vertical and, therefore, the vertical  $\text{CH}_4$  concentrations are homogeneous within the SML.

In the simulations of each lake, we assumed that the SML, sources and sinks are radially symmetric in the horizontal. Therefore, the development of  $\text{CH}_4$  concentration can be described

based on the radial distance  $r$  from the shore to the center of the lake ( $r_{\max} = \sqrt{A_a/\pi}$ ).

Two regions were defined in the model, the littoral zone ( $r \leq r_s = \sqrt{(A_a - A_s)/\pi}$ ) and the pelagic waters ( $r > r_s$ ). The SML thickness ( $H(r)$ ) is equal to the mixed layer depth in the pelagic region and, within the littoral zone,  $H(r)$  decreases linearly with  $r$  from the mixed layer depth to zero at the shore. The littoral sediment flux is zero in the pelagic zone ( $r < r_s$ ) and equal to the measured average littoral sediment flux ( $\overline{F_s}$ ) in the shallow region ( $r \geq r_s$ ) as:

$$F_s(r, t) = \begin{cases} \overline{F_s} & \text{for } r \geq r_s \\ 0 & \text{for } r < r_s \end{cases} \quad [\text{mmol/m}^2/\text{d}] \quad (2.4)$$

The vertical turbulent transport ( $F_z$ ) is zero in the littoral areas and in the pelagic waters  $F_z$  is calculated as:

$$F_z = K_z \frac{C_{\text{hyp}} - C(r)}{\Delta z} \quad (2.5)$$

where  $K_z$  is the turbulent vertical diffusivity,  $C_{\text{hyp}}$  is the  $\text{CH}_4$  concentration 1 m below the bottom of the SML and  $\Delta z = 1$  m. Average bubble dissolution rates ( $R_{\text{dis}}(h(r))$ ) as a function of lake depth ( $h$ ) were included in the SML. At the boundaries, horizontal fluxes were assumed as zero. To estimate the horizontal dispersion coefficient ( $K_H$ ) we used Peeters & Hofmann 2015 parameterization:

$$K_H = 1.4 \times 10^{-4} L^{1.07} \quad [\text{m}^2 \text{s}^{-1}] \quad (2.6)$$

where the length scale  $L$  [m] was calculated as  $L = r_s$  (Table S.A.5). Eq. 2.6 is the average of the results 1, 3 and 4 found on Table 2 of Peeters & Hofmann 2015.

$P_{\text{net}}$  rates were obtained using least square method optimization solver implemented with the *curve fit* function from Scipy (Virtanen *et al.* 2020) in Python.

## 2.4.6 Monte Carlo Simulation

To assess uncertainties, Monte Carlo simulation were performed (10000 iterations) when solving the full-scale mass balance model.  $P_{\text{net}}$ ,  $R_{\text{dis}}$  and  $F_z$  were selected within a normal distribution resulting from the mean ( $\mu$ ) and their standard deviation ( $\sigma$ ) retrieved from the field measure-

ments. To prevent negative values,  $F_a$  and  $F_s$  were chosen from a gamma distribution defined by shape ( $\kappa = \mu^2/\sigma^2$ ) and the scale ( $\theta^2 = \sigma^2/\mu$ ). Here the gamma distribution has the density  $f(x) = \left(x^{\kappa-1} \frac{e^{-x/\theta}}{\theta^\kappa \Gamma}\right)$  where  $\Gamma$  is the gamma function. `Random.normal` and `random.gamma` functions from the Numpy package (Harris *et al.* 2020) in Python were used for each normal and gamma distributions, respectively.

#### 2.4.7 Water column $\text{CH}_4$ and $\delta^{13}\text{C}_{\text{CH}_4}$ signature.

At each sampling campaign  $\text{CH}_4$  and  $\delta^{13}\text{C}_{\text{CH}_4}$  concentration profiles were taken at the deepest location of each lake (M1, Fig. S.A.1). A transect composed of 10 or 11 stations across the lake (shore to shore) was also performed at each lake (T1-T11, Fig. S.A.1) where surface  $\text{CH}_4$  and  $\delta^{13}\text{C}_{\text{CH}_4}$  concentrations and surface  $\text{CH}_4$  fluxes were measured.

Dissolved  $\text{CH}_4$  concentration profiles were performed at a maximum depth resolution of 0.5 m where the metalimnetic  $\text{CH}_4$  gradient was expected. For the profile, the water samples were obtained with a 5-L Niskin bottle and then gently transferred into a 1 L glass bottle (Duran GmbH, Mainz, Germany) while for the transect the samples were obtained directly with a 1 L glass bottle (Duran GmbH, Mainz, Germany). For both methodologies, the water was overflowing to replace the volume three times.  $\text{CH}_4$  concentrations and  $\delta^{13}\text{C}_{\text{CH}_4}$  were measured using the headspace method following Donis *et al.* 2017. The samples were measured on a Cavity Ring-Down Spectrometer analyzer (Picarro G220-i, Santa Clara, CA, USA) for  $\text{CH}_4$  concentrations in the gas phase (ppm) and stable isotope ratio ( $\delta^{13}\text{C}_{\text{CH}_4}$  in ‰). Water  $\text{CH}_4$  concentrations were back calculated according to Wiesenburg & Guinasso 1979 accounting for water temperature, air concentration and the headspace/water ratio in the bottle.

#### 2.4.8 $\text{CH}_4$ diffusive fluxes to the atmosphere.

Diffusive  $\text{CH}_4$  emissions to the atmosphere ( $F_a$ ) were measured using a floating chamber attached to a portable GHG analyzer (UGGA; Los Gatos Research, Inc.). Instrument-specific precision at ambient concentrations (1- $\sigma$  of 100 s average) for  $[\text{CH}_4]$  is 0.25 ppb. The floating chamber consist of an inverted plastic container with foam elements for floatation (as McGinnis *et al.* 2015). To minimize artificial turbulence effects, the buoyancy element was adjusted that only  $\sim 2$  cm of the chamber penetrated below the water level. The chamber was painted white to



minimize heating. Two gas ports (inflow and outflow) were installed at the top of the chamber via two 5 m gas-impermeable tubes (Tygon 2375) and connected to the GHG analyzer measuring the gaseous  $\text{CH}_4$  concentrations in the chamber every 1 s. Transects were performed with the chamber deployed from a boat. The chamber was allowed to freely drift to minimize artificial disturbance. Fluxes were obtained by the slopes of the resolved  $\text{CH}_4$  curves over the first  $\sim 5$  min when the slopes were approximately linear ( $R^2 > 0.97$ ).

To simulate the fluxes to the atmosphere in the lateral transport model, chamber-based mass transfer coefficient ( $k_{\text{CH}_4}^{\text{cb}}$ ) was calculated as:

$$k_{\text{CH}_4}^{\text{cb}} = \frac{F_a}{(\text{CH}_{4,w} - H_{\text{cp}} \cdot \text{pCH}_{4,\text{atm}})}; \quad [\text{mmol m}^{-2} \text{d}^{-1}] \quad (2.7)$$

where  $\text{pCH}_{4,\text{atm}}$  and  $\text{CH}_{4,w}$  are the  $\text{CH}_4$  atmospheric partial pressures and water concentration, respectively.  $H_{\text{cp}}$  is the Henry constant of  $\text{CH}_4$  dissolution at in situ temperature obtained from Sander 2015.

#### 2.4.9 Sediment sampling.

Littoral sediment cores were taken in most of the lakes, except for LIO where the rocky bottom made it impossible to take a sample. Sampling was performed with a gravity sediment corer (Uwitech, Mondsee, Austria) equipped with an acrylic liner of 70 cm in length and with an internal diameter of 6 cm. The liner had pre-drilled holes to fit 3 mL syringes at 1 cm intervals. Additionally, in-site core liners were hammered into shallow littoral sediment where benthic chambers were performed. The location and depth of each core are shown in Fig. S.A.1 and Table S.A.3.

#### 2.4.10 Porewater $\text{CH}_4$ concentration and $\delta^{13}\text{C}_{\text{CH}_4}$ signature.

3 mL of sediment was sub-sampled at 1 - 2 cm depth intervals with headless 3 mL syringes through the pre-drilled holes from the selected depths. The sediment sub-sample was immediately placed into 1 L glass bottle (Duran GmbH, Mainz, Germany) containing 500 mL of lake water previously bubbled with air to reach equilibrium with the atmosphere. The subsequent procedure followed the same as for the water column head-space method. Porewater  $\text{CH}_4$  concentrations were back calculated from the headspace concentrations accounting for dilution of sediment porewater

in the lake water (assuming that aerated lake water is in equilibrium with the atmosphere), temperature, headspace ratio, and assuming a porosity of 0.9.

#### 2.4.11 Methane benthic fluxes.

The littoral CH<sub>4</sub> sediment flux ( $F_s$ ) at each lake was determined as the average flux provided by two independent methods which are described below.

##### Porewater method.

Methane fluxes at the sediment–water interface were calculated with Fick’s 1st Law over the linear top 2 - 3 cm of the porewater concentration profile.

$$F_s = -\phi D_{\text{CH}_4} \theta^{-2} \frac{\partial C}{\partial z}; \quad [\text{mmol m}^{-2} \text{ d}^{-1}] \quad (2.8)$$

where  $F_s$  is the diffusive CH<sub>4</sub> flux at the sediment–water interface,  $\phi$  the porosity of the sediments (assumed as 0.9),  $D_{\text{CH}_4}$  the diffusion coefficient for CH<sub>4</sub> in water ( $1.5 \times 10^{-5} \text{ cm}^2 \text{ s}^{-1}$ ) (Broecker & Peng 1974),  $\theta^2$  the square of tortuosity (1.2) (Boudreau 1997) and  $\partial C/\partial z$  the measured vertical concentration gradient.

##### Benthic chamber.

Benthic chambers were deployed in situ or by sediment cores retrieved from the littoral sediment of the lake. The core was covered leaving ~5 cm of headspace and ~30 - 50 cm of water. The lid was connected to a GHG analyzer creating a closed loop where partial pressure of CH<sub>4</sub> ( $P_{\text{CH}_4}$ ) was measured over time. At the beginning and at the end of the experiment, water CH<sub>4</sub> concentration ( $C_w$ ) was also measured. Each experiment deployment lasted about 1 h while the surface water was gently stirred to increase the mass transfer coefficient ( $k_{\text{bc}}$ ) at the air–water interface without producing sediment resuspension. The sediment flux was calculated using three methods:

- Integrated mass balance:  $F_s$  is obtained using the beginning and final air and gas CH<sub>4</sub>

concentration and performing a mass balance in the water and the air phase as:

$$F_s A_{bc} = \frac{V_{air}}{RT_a} \frac{\Delta P_{CH_4}}{\Delta t} + \frac{V_w \Delta C_w}{\Delta t}; \quad [\text{mmol d}^{-1}] \quad (2.9)$$

where  $V_w$  and  $V_{air}$  are the volume of the water and air phases, respectively.  $R$  is the ideal gas constant,  $T_a$  is the air temperature and  $A_{bc}$  is the surface area of the chamber.

- Transient mass balance: solving the mass balance over time we obtain that:

$$\frac{\partial P_{CH_4}}{\partial t} = \frac{RT_a}{b} \left( w F_s - (w F_s - b k_{cb} C_0) e^{-b k_{cb} t} \right); \quad [\text{Pa d}^{-1}] \quad (2.10)$$

where  $w = A_{bc}/V_w$ ,  $a = A_{bc}/V_a$ ,  $C_0 = C_w(0) - H_{cp} P_{CH_4}$  and  $b = (w - H_{cp} R T_a a)$ . The sediment flux is estimated fitting  $k_{cb}$  and  $F_s$  to the measured  $\partial P_{CH_4}/\partial t$  using least square method optimization solver implemented on the *curve fit* function from Scipy (Virtanen *et al.* 2020) in Python. The  $k_{cb}$  boundaries were set from 0 - 40  $\text{m d}^{-1}$  for the fitting.

- Equilibrium mass balance: after  $\sim 1$  h of measurements, we assume that the exponential part of the curve of Eq. 2.10 becomes negligible. Therefore,  $F_s$  can be estimated with the last 5 min of the  $\text{CH}_4$  partial pressure as:

$$P_{CH_4} = \frac{RT_a}{b} w F_s t; \quad [\text{Pa}] \quad (2.11)$$

The flux from the benthic chamber was calculated as the average of the results of the three methods described above.

#### 2.4.12 $\text{CH}_4$ bubble dissolution and ebullition rates.

The  $\text{CH}_4$  dissolution from a single bubble released from the sediment was calculated using McGinnis *et al.* 2006. For each bubble we considered a diameter of 5 mm and the water column  $\text{CH}_4$ ,  $\text{CO}_2$  and  $\text{O}_2$  concentrations and temperature profiles at each date. The initial bubble composition at each depth was estimated from a linear interpolation from bubble content obtained following the same methodology as Langenegger *et al.* 2019. The total bubble dissolution rate ( $R_{dis}(z)$ ) was calculated considering the contribution from all bubbles released below that depth

as:

$$R_{\text{dis}}(z) = \frac{\sum_{\text{bottom}}^z r_i \frac{F_{\text{eb,SWI},i}}{n_{0,i}} \Delta A_{\text{sed},i}}{A_p(z)} \quad [\mu\text{mol m}^{-3} \text{d}^{-1}] \quad (2.12)$$

where  $r_i$  is the bubble dissolution from an individual bubble at depth  $i$  ( $\mu\text{mol bub}^{-1}$ ),  $F_{\text{eb,SWI},i}$  is the  $\text{CH}_4$  ebullition flux released at the sediment-water interface (SWI) at depth  $i$  ( $\text{mmol}/\text{m}^2/\text{d}$ ) and  $n_{0,i}$  is the initial amount of  $\text{CH}_4$  in a single bubble ( $\mu\text{mol bub}^{-1}$ ).  $\Delta A_{\text{sed},i}$  is the sediment area between the depth interval  $i$  to  $i + 1$  ( $\text{m}^2$ ).  $F_{\text{eb,SWI},i}$  was estimated using Langenegger *et al.* 2019's model. This model assumes an exponential profile for the  $\text{CH}_4$  production rates as a function of the sediment depth ( $W_{\text{CH}_4}(z) = ae^{-bz}$ ), where  $a$  and  $b$  are solved using as inputs the bubble content and the sediment flux at each depth (Langenegger *et al.* 2019). These inputs were estimated using linear and polynomial interpolation respectively from data collected at each lake.

#### 2.4.13 Vertical diffusive $\text{CH}_4$ flux from/to hypolimnion.

To estimate the transport of  $\text{CH}_4$  into the SML via turbulent diffusion we applied the Fick's First Law as:

$$F_z = -K_z \frac{\partial C}{\partial z}; \quad [\text{mmol m}^{-2} \text{d}^{-1}] \quad (2.13)$$

where  $F_z$  is the average vertical  $\text{CH}_4$  diffusive flux,  $z$  is depth (m),  $\frac{\partial C}{\partial z}$  is the vertical gradient measured at 1 m depth resolution approximately.  $K_z$  is the vertical diffusivity derived from temperature profiles (sampling rate 4 Hz) and the Osmidov method Thorpe & Deacon 1977 as:

$$K_z = \gamma_{\text{mix}} L_T^2 N; \quad [\text{m}^2 \text{d}^{-1}] \quad (2.14)$$

where  $\gamma_{\text{mix}}$  is the mixing efficiency (assumed 0.15, Wüest & Lorke 2003),  $N$  is the Brunt-Väisälä buoyancy frequency and  $L_T$  is the Thorpe scale estimated from the maximum displacement length ( $L_{\text{max}}$ ) as Lorke & Wüest 2002:

$$L_T = \frac{\sqrt{2}}{7.3} L_{\text{max}}; \quad [\text{m}] \quad (2.15)$$

This estimation was tested using microstructure profiles measured with a self-contained autonomous microstructure profiler (SCAMP; PME, Inc.) during the summer of 2021 in BRE, NOI and CHA (Fig. S.A.8), where turbulence profiles were resolved after Kreling *et al.* 2014.

#### 2.4.14 Sources contribution to diffusive CH<sub>4</sub> emissions.

We studied the importance of each source contribution (SC) to the diffusive surface flux by computing:

$$SC_i = \frac{S_i}{\sum_j S_j} \cdot 100; \quad [\%] \quad (2.16)$$

where  $S_i$  is each source term ( $\text{mol d}^{-1}$ ) such as bubble dissolution ( $R_{\text{dis}} \forall_{\text{SML}}$ ), sediment flux ( $F_s A_s$ ), net production ( $P_{\text{net}} \forall_{\text{SML}}$ ) and vertical diffusive fluxes ( $F_z A_z$ ). If  $S_i \leq 0$  then  $S_i = 0$  where  $i$  is each source term.

---

# Temporal dynamics of oxic methane production in a hypertrophic Swiss lake

---

César Ordóñez<sup>1</sup>, Alexandrine Massot<sup>1</sup>, Tonya DelSontro<sup>1, 2</sup>, Timon Langenegger<sup>1</sup>, and Daniel F. McGinnis<sup>1</sup>

<sup>1</sup>Aquatic Physics Group, Department F.-A. Forel for Environmental and Aquatic Sciences (DEFSE), Faculty of Science, University of Geneva, Uni Carl Vogt, 66 Boulevard Carl-Vogt, 1211 Geneva, Switzerland

<sup>1, 2</sup> Now at Department of Earth and Environmental Sciences, University of Waterloo, Ontario, Canada

Content of Chapter 3 was submitted in:

Ordóñez, C., Massot, A., DelSontro, T., Langenegger, T. & McGinnis, D. F. Temporal Dynamic of Oxic Methane Production in a Hypereutrophic Swiss Lake. *Frontiers in Environmental Science (submitted)* (2022)

## Abstract

The occurrence of methane production in oxic conditions (OMP) is increasingly reported in diverse aquatic ecosystems. However, its seasonal and yearly dynamics, contribution to global methane ( $\text{CH}_4$ ) emissions and key drivers, remains uncertain due to lacking measurements covering the spatial and temporal OMP variability. We used three models (full-scale mass balance, wind-based and a lateral transport) to estimate the net production of  $\text{CH}_4$  ( $P_{\text{net}}$ ) in the oxic surface mixed layer of a hypereutrophic Swiss lake. Over the stratified season, we found that OMP occurs in the studied lake, and was regularly the dominant source of  $\text{CH}_4$  diffusive emissions during the four years. Moreover, we observed a clear pattern with high  $P_{\text{net}}$  rates at the beginning of the summer and a decrease towards the end of the stratified season. Correlations between  $P_{\text{net}}$  versus Secchi depth, chlorophyll-*a* concentrations and light climate suggest that photoautotrophs play a role on  $\text{CH}_4$  production in agreement with recent findings. This work highlights that the OMP temporal variability needs to be included in  $\text{CH}_4$  lake budget to estimate the OMP contribution on a global scale.

## 3.1 Introduction

During the last decades methane ( $\text{CH}_4$ ) oversaturation in oxic waters in the ocean and lakes has been widely reported and named "The Methane Paradox" (Karl *et al.* 2008; Tang *et al.* 2014). Oxic methane production (OMP) has been proposed as an explanation for the Methane Paradox (Grossart *et al.* 2011; Bogard *et al.* 2014; Donis *et al.* 2017; Günthel *et al.* 2019), contrasting with the current understanding that  $\text{CH}_4$  is only produced in anoxic conditions (Conrad 2009). While several investigations have reported that OMP does occur in the surface mixed layer in lakes (Grossart *et al.* 2011; Bogard *et al.* 2014; Donis *et al.* 2017; Günthel *et al.* 2019; Günthel *et al.* 2020; Chapter 2), its seasonal patterns and main drivers still remain unresolved. Two main biotic mechanisms have been suggested to produce  $\text{CH}_4$  under oxic condition: dimethylation of methylphosphonate under phosphorus limited environment (Karl *et al.* 2008; Repeta *et al.* 2016; Wang *et al.* 2017; Khatun *et al.* 2019) and  $\text{CH}_4$  production as a bioproduct of nitrogen fixation (Zheng *et al.* 2018; Luxem *et al.* 2020). However, positive correlations between  $\text{CH}_4$ , oxygen and chlorophyll-*a* concentration (Chl*a*) point out to a direct role of phytoplankton on OMP (Bižić *et al.* 2020; Hartmann *et al.* 2020; Günthel *et al.* 2021). Moreover, the discovery that

OMP follows light-dark cycles (Bižić *et al.* 2020; Hartmann *et al.* 2020) and a strong positive correlation of light and temperature (Klitzsch *et al.* 2020) links OMP with photosynthesis. Since primary productivity varies seasonally and from lake to lake, it is likely that OMP also varies on the basis of the trophic properties, algae species and light conditions.

Following these insights, in Chapter 2 it was proposed an empirical upscaling approach that relates Chl<sub>a</sub>, secchi disk depth (SD) and light climate (LC) with the net production rates ( $P_{\text{net}}$ ) normalized by the surface CH<sub>4</sub> concentrations.  $P_{\text{net}}$  is defined as the balance between OMP (that adds CH<sub>4</sub>) and methane oxidation (MOx, that consume CH<sub>4</sub>). Despite that this approach was tested on seven lakes with different trophic status, more studies on seasonal OMP changes and different types of lakes are needed to verify this trend on a larger scale.

An alternative explanation of the Methane Paradox is the transport of CH<sub>4</sub> from littoral sediments (Encinas Fernández *et al.* 2016; Peeters *et al.* 2019; Morana *et al.* 2020) but this source alone cannot support the CH<sub>4</sub> diffusive emissions to the atmosphere (Chapter 2). In fact, recent studies show that OMP contribution to the diffusive CH<sub>4</sub> emissions is up to ~80 % in lakes during the stratified season (Donis *et al.* 2017; Günthel *et al.* 2019; Chapter 2). OMP occurs in surface waters (Tang *et al.* 2014; Donis *et al.* 2017) and, unlike anoxic CH<sub>4</sub> sources, can be quickly emitted to the atmosphere. Despite the limited data points on a temporal scale, Günthel *et al.* 2019 and Chapter 2 show that  $P_{\text{net}}$  rates have a tendency to decrease towards the end of the summer. However, it is not known if this is driven by an increase in MOx, a decrease of the OMP rates or both.

About 20 % of the warming of the planet can be attributed to CH<sub>4</sub>, and freshwater are responsible for about ~20 - 40 % of the total CH<sub>4</sub> emissions to the atmosphere (202 - 425 Tg CH<sub>4</sub> yr<sup>-1</sup>, Saunio *et al.* 2020; Rosentreter *et al.* 2021; Forster *et al.* In Press. Considering that 50 % of the CH<sub>4</sub> emissions by lakes results from OMP in the SML and 30 % is oxidized (Günthel *et al.* 2020), Bizic 2021 estimates that OMP from freshwater is about 47 - 210 Tg CH<sub>4</sub> yr<sup>-1</sup>. These rates highlight the potential contribution of OMP globally, however there is a large uncertainty due to lacking of sufficient measurements covering the spatial and temporal OMP variability.

In this study we estimate  $P_{\text{net}}$  for a hypertrophic lake for four years during the stratified



period. We used a full-scale mass balance, a wind-based and a lateral transport model to calculate the  $P_{\text{net}}$  and analyze its seasonal pattern during the thermal stratification period. In addition, we compared each methodology and calculated the  $P_{\text{net}}$  contribution to diffusive emissions to the atmosphere. Finally, we tested the upscaling approach proposed in Chapter 2 to estimate  $P_{\text{net}}$  rates.

## 3.2 Methods

### 3.2.1 Study site and sampling.

The study was conducted in a small hypereutrophic lake, Soppensee (47.09 °N, 8.08 °E, 596 m above the sea level) located in the Canton Lucerne, Switzerland. This glacially formed lake has a surface area of 0.24 km<sup>2</sup> and a maximal depth of 26 m. The lake watershed is about 1.6 km<sup>2</sup> and lies in an area of intense agriculture (Lotter 1989).

This study relies on data from the water column profiles of CH<sub>4</sub>,  $\delta^{13}\text{C}_{\text{CH}_4}$ , temperature, O<sub>2</sub> as well as CH<sub>4</sub> diffusive fluxes to the atmosphere and CH<sub>4</sub> ebullition rates during April 2016 to January 2018 from Vachon *et al.* 2019. Additional water column data were collected during 2018 and 2019 including surface CH<sub>4</sub> concentrations,  $\delta^{13}\text{C}_{\text{CH}_4}$  and surface diffusive fluxes to the atmosphere ( $F_a$ ) along transects performed in May and August 2018 and two transects in July 2019. Ten locations were sampled in each transect from the shore to the deepest point of the lake. The sample locations and the bathymetric map are shown in Fig. S.B.1.

In the deepest point of the lake (M1; Fig. S.B.1) a dissolved O<sub>2</sub> probe (miniDot, Precision Measurements Engineering) was installed at ~1 m depth and logged temperature, dissolved O<sub>2</sub> concentration (mgO<sub>2</sub>/L) and saturation (%) every minute from April 2016 to October 2019. In addition, manual CTD (Conductivity-Temperature-Depth) profiles were performed in M1 using a multiparameter sonde (EXO2 Yellow Spring Instrument, after May 2017 a Seabird SBE19plus CTD profiler). The EXO2 profiler was equipped with a temperature, conductivity, oxygen and pH sensor while the SBE19plus was equipped additionally with turbidity, PAR, and chlorophyll-*a* (Chl*a*) sensors. The temperature (T) profiles were used to define the bottom of the surface mixed layer (SML) when  $\frac{\partial T}{\partial z}$  becomes smaller than  $-1\text{ }^\circ\text{C m}^{-1}$  (Read *et al.* 2011). The stratified period was defined when the difference between the surface

and bottom waters density exceeded  $0.7 \text{ kg m}^{-3}$ . Water density was calculated using T and the specific conductivity at  $20^\circ\text{C}$  ( $\kappa_{20}$ ) from the CTD profiles (Imboden & Wüest 1995). In August 2016, May and Aug 2018; and July 2019 manual water profiles were performed with a spectrofluorometer (bbe Moldaenke GmbH, Schwentinental, Germany) at the deepest point of the lake to measure total Chl $a$  concentrations. Lower concentrations were found from measurements performed with the SBE19plus CTD profiler compared with the spectrofluorometer at the same time in the lake (Fig. S.B.2). Therefore, the average Chl $a$  concentration was calculated as the average value in the SML measured with the spectrofluorometer and the corrected values from SBE19plus CTD profiler using an empirical correction (Fig. S.B.2).

Diffusive  $\text{CH}_4$  fluxes from littoral sediment (see definition below) from Langenegger *et al.* 2022 were also included. Additional littoral sediment cores were also retrieved to determine  $\text{CH}_4$  diffusive fluxes using benthic chambers and Rhizons (see methods below) at the same location of the cores (a, b, and c) reported by Langenegger *et al.* 2022. Finally, the Secchi disk depth was also measured at each sampling campaign after August 2016. An overview of the periods, data, and methods used is given in Table 3.1.

### 3.2.2 Surface mass balance

The full-scale mass balance (0-D) proposed by Donis *et al.* 2017, a wind-based mass balance (0-D) and the lateral transport model (1-D) proposed in Chapter 2 were used to estimate net production rates ( $P_{\text{net}}$ ) in the SML during the stratified period from 2016 to 2019.  $P_{\text{net}}$  is the result of the OMP and MOx ( $P_{\text{net}} = \text{OMP} - \text{MOx}$ ), which adds and removes  $\text{CH}_4$  in the SML, respectively. Thus, when  $P_{\text{net}}$  is positive, the true OMP rate is actually higher than  $P_{\text{net}}$ .

### 3.2.3 Full-scale mass balance

$P_{\text{net,fs}}$  was determined using a mass balance in the SML during the stratified period (Eq. 3.1). This approach assumed that the SML can be modeled as a well-mixed reactor and the lateral contribution to the mass balance is equal to the littoral sediment flux times the sediment area. The spatial average of the measured values of the  $\text{CH}_4$  concentrations ( $C$ ),  $F_a$ ,  $R_{\text{dis}}$  and  $F_z$  were used as boundary conditions at each sampling campaign. At the beginning of the stratified

Table 3.1. Measurements, modelled derived parameters and data sources analyzed from 2016 to 2019 over the stratified season.

Description	Symbol	Eq.	Method	Period	Data Source
Water column CH <sub>4</sub>	$C$		Head Space	Apr 2016 to Jan 2018	Vachon <i>et al.</i> 2019
Water column CH <sub>4</sub>	$C$		Head Space	2018-2019	This study
Transect CH <sub>4</sub>	$C$		Head Space	May and Aug 2018 and Jul 2019	This study
Water column $\delta^{13}\text{C}_{\text{CH}_4}$	$\delta^{13}\text{C}_{\text{CH}_4}$		Head Space	Apr 2016 to Jan 2018	Vachon <i>et al.</i> 2019
Water column $\delta^{13}\text{C}_{\text{CH}_4}$	$\delta^{13}\text{C}_{\text{CH}_4}$		Head Space	2018-2019	This study
Transect $\delta^{13}\text{C}_{\text{CH}_4}$	$\delta^{13}\text{C}_{\text{CH}_4}$		Head Space	2018-2019	This study
Diff. CH <sub>4</sub> emissions	$F_a$		Floating chambers	Apr 2016 to Jan 2018	Vachon <i>et al.</i> 2019
Diff. CH <sub>4</sub> emissions	$F_a$		Floating chambers	2018-2019	This study
Diff. CH <sub>4</sub> emissions transect	$F_a$		Floating chambers	May and Aug 2018 and Jul 2019	This study
Diff. CH <sub>4</sub> flux littoral sediments	$F_s$	Eq. 3.5	Cut-syringe	2016-2019	Langenegger <i>et al.</i> 2022
Diff. CH <sub>4</sub> flux littoral sediments	$F_s$	Eq. 3.5	Rhyzons	2018-2019	This study
Diff. CH <sub>4</sub> flux littoral sediments	$F_s$		Benthic chambers	2018-2019	This study
Total CH <sub>4</sub> eb. flux below 8 m	$F_{\text{eb}}$		Inverted funnels	Apr 2016 to Jan 2018	Vachon <i>et al.</i> 2019
CH <sub>4</sub> ebullition rate at SWI	$R_{\text{eb}}$		Bubble composition	2018-2019	Langenegger <i>et al.</i> 2019 and this study
CH <sub>4</sub> flux at the bottom of SML	$F_z$	Eq. 3.8	Fick's First Law	2016-2019	This study
CH <sub>4</sub> bubble dissolution rate in the SML	$R_{\text{dis}}$		McGinnis <i>et al.</i> 2006	2016-2019	Langenegger <i>et al.</i> 2019 Vachon <i>et al.</i> 2019 and this study
Net CH <sub>4</sub> production rate	$P_{\text{net,fs}}$	Eq. 3.1	Full-scale mass balance	2016-2019	This study
Net CH <sub>4</sub> production rate	$P_{\text{net,t}}$	Eqs. 3.1 and 3.2	Wind-based mass balance	2016-2019	This study
Net CH <sub>4</sub> production rate	$P_{\text{net,lt}}$	Eq. 3.3	Lateral transport	2016-2019	This study

period at each year  $\frac{\partial C^{\forall\text{SML}}}{\partial t}$  was assumed zero.

$$\begin{aligned}
 \frac{\partial C^{\forall\text{SML}}}{\partial t} = & A_s(t)F_s - A_a F_a(t) + A_z(t)F_z(t) + R_{\text{dis}}(t)\forall_{\text{SML}}(t) \\
 & + P_{\text{net,fs}}(t)\forall_{\text{SML}}(t); \quad [\text{mol d}^{-1}]
 \end{aligned} \tag{3.1}$$

The SML volume ( $\forall_{\text{SML}}$ ), the sediment area ( $A_s$ ), lake surface area ( $A_a$ ), and planar area at the bottom of the SML ( $A_z$ ) are shown in Table S.B.1.

### 3.2.4 Wind-based mass balance

$P_{\text{net,t}}$  was determined using Eq. 3.1 and the diffusive  $\text{CH}_4$  flux to the atmosphere estimated using Fick's 1st Law (Eq. 3.2). The  $\text{CH}_4$  concentration and the sources and sinks described in Eq. 3.1 were linearly interpolated to obtain daily  $P_{\text{net}}$  rates during the stratified period.

$$F_a = k_{\text{CH}_4} (C - H_{\text{cp}} P_{\text{CH}_4}); \quad [\text{mmol m}^{-2} \text{d}^{-1}] \quad (3.2)$$

The Henry constant of  $\text{CH}_4$  dissolution at in situ temperature ( $H_{\text{cp}}$ ) was the obtained following Sander 2015. The atmospheric partial pressure of  $\text{CH}_4$  ( $P_{\text{CH}_4}$ ) was obtained from air samples taken at Soppensee and the local atmospheric pressure in each sampling campaign. The mass transfer coefficient for  $\text{CH}_4$  ( $k_{\text{CH}_4}$ ) was estimated using the standardized gas transfer coefficient ( $k_{600}$ ) following MacIntyre *et al.* 2010 for negative buoyancy, using 10 min average wind speed measured from a meteorological station situated about 12 km north of the lake (Egolzwil Station, Federal Office of Meteorology and Climatology MeteoSwiss). Then,  $k_{\text{CH}_4}$  was calculated following McGinnis *et al.* 2015, where  $\text{CH}_4$  Schmidt number was estimated from the surface water temperature (Wanninkhof 1992) and the exponent  $n = -2/3$  when  $U_{10} < 3.7 \text{ m s}^{-1}$  and  $n = 1/2$  when  $U_{10} > 3.7 \text{ m s}^{-1}$ .

### 3.2.5 Lateral transport model

The lateral transport model simulates the transect  $\text{CH}_4$  concentrations in the SML following Peeters *et al.* 2019 and modified according to Chapter 2 (Eq. 3.3). This model considers that the surface layer is fully mixed in the vertical and, therefore, the vertical  $\text{CH}_4$  concentrations are homogeneous within the SML.

$$\begin{aligned} \frac{\partial C}{\partial t} = & K_H \frac{1}{H(r)r} \frac{\partial}{\partial r} \left( H(r)r \frac{\partial C(r)}{\partial r} \right) + \frac{1}{H(r)} K_z \frac{C_{\text{hyp}} - C(r)}{\Delta z} - \frac{\bar{k}_{\text{CH}_4}}{H(r)} (C(r) - H_{\text{cp}} P_{\text{CH}_4}) \\ & + \frac{F_s}{H(r)} + R_{\text{dis}}(r) + P_{\text{net,lt}}; \quad [\text{mol m}^{-3} \text{d}^{-1}] \end{aligned} \quad (3.3)$$

The mass transfer coefficient for  $\text{CH}_4$  was calculated based on the average gas transfer coefficient obtained from the flux chambers ( $\bar{k}_{\text{CH}_4}$ ),  $C_{\text{hyp}}$  is the  $\text{CH}_4$  concentration 1 m below the bottom of the SML and  $\Delta z = 1 \text{ m}$  and  $H(r)$  is the spatially varying thickness of the SML. At the boundaries, horizontal fluxes were assumed as zero. To estimate the horizontal dispersion

coefficient ( $K_H$ ) we used Peeters & Hofmann 2015 parameterization:

$$K_H = 1.4 \times 10^{-4} L^{1.07}; \quad [\text{m}^2 \text{s}^{-1}] \quad (3.4)$$

where the length scale  $L$  [m] was calculated as  $L = r_s$ . Eq. 3.4 is the average of the results 1, 3 and 4 found in Table 2 of Peeters & Hofmann 2015.

$P_{\text{net,lt}}$  rates for each date were calculated by minimizing the root-mean-square error between the simulated transect  $\text{CH}_4$  concentrations to the measured  $\text{CH}_4$  concentrations using an optimization solver implemented with the *curve fit* function from Scipy (Virtanen *et al.* 2020) in Python. Note that the lateral transport model was only applicable to the transects measured in May and August 2018, and July 2019.

### 3.2.6 Water column $\text{CH}_4$ concentration and $\delta^{13}\text{C}_{\text{CH}_4}$ signature

The surface  $\text{CH}_4$  concentrations and  $\delta^{13}\text{C}_{\text{CH}_4}$  were measured using the methodology described by Vachon *et al.* 2019 for the water profiles and in Chapter 2 for the transect. For each sample,  $\text{CH}_4$  concentration and its  $\delta^{13}\text{C}_{\text{CH}_4}$  were measured using the headspace method following Donis *et al.* 2017. The samples were measured on a Cavity Ring-Down Spectrometer analyzer (Picarro G220-i, Santa Clara, CA, USA) for  $\text{CH}_4$  concentrations in the gas phase (ppm) and stable isotope ration ( $\delta^{13}\text{C}_{\text{CH}_4}$  in ‰). Water  $\text{CH}_4$  concentrations were back calculated according to Wiesenburg & Guinasso 1979 accounting for water temperature, air concentration and the headspace/water ratio in the bottle. Water column profiles of  $\text{CH}_4$  concentrations were measured at the deepest point of the lake (M1) and in June and August 2018 and July 2019 they were also measured at 12m deep point (M2) and along 10 surface waters points in each transect. Since several measurements were taken in the SML in M1 and M2 compared with only one value at the surface of each point in the transects, the average  $\text{CH}_4$  concentration value at the SML in M1 and M2 was assumed as part of the transect to calculate the surface average  $\text{CH}_4$  concentration for the entire lake. This procedure minimizes the bias that can be caused by the several measurements taken at M1 and M2 in comparison with only one sample for the rest of the transect. When transect data were not available, the average value for the entire lake was calculated with the  $\text{CH}_4$  concentrations measured in the SML.

### 3.2.7 CH<sub>4</sub> diffusive fluxes to the atmosphere

The diffusive fluxes to the atmosphere ( $F_a$ ) were estimated using a floating chamber attached to a portable GHG analyzer (UGGA; Los Gatos Research, Inc.). The floating chamber consist of an inverted plastic container with foam elements for floatation (as McGinnis *et al.* 2015). Fluxes were obtained by the slopes of the resolved CH<sub>4</sub> curves over  $\sim 5$  min when the slopes where approximately linear ( $R^2 > 0.97$ ).  $F_a$  was measured at M1 and, in June and August 2018 and July 2019, was also measured M2 and along the same locations where we measured the CH<sub>4</sub> concentrations transects. Since several measurements were taken at M1 and M2 compared with only one value at each point in the transects, the average value at M1 and M2 was assumed as part of the transect to calculate the average flux  $F_a$  for the entire lake. Similar to the CH<sub>4</sub> concentrations, this approach minimizes the bias that can be caused by the fact of several measurements taken at M1 and M2 compared to only one sample for the rest of the transect.

### 3.2.8 Sediment cores extraction

Additional littoral sediment cores were retrieved at the same locations as the ones presented by Langenegger *et al.* 2022 (Cores a, b, c, Table S1) where porewater concentrations were measured with Rhizons (Rhizosphere Research Products, The Netherlands). The sediment cores were retrieved with a gravity sediment corer (Uwitech, Mondsee, Austria) equipped with an acrylic liner of 70 cm in length and with an internal diameter of 6 cm. The liner had pre-drilled holes every 1 cm to fit Rhizons and 1 and 3 mL syringes respectively. Additional sediment cores were also retrieved in those same locations, where benthic chambers were performed to calculate the CH<sub>4</sub> diffusive flux from the sediment. The location and depth of each core are shown in Fig. S.B.1 and Table 3.2 respectively.

### 3.2.9 Porewater CH<sub>4</sub> concentration and $\delta^{13}\text{C}_{\text{CH}_4}$ signature

The Rhizons are porewater samplers designed to extract small volumes of water from soil and sediments in a minimally disturbing way. They are made of an inert microporous tube (0.15  $\mu\text{m}$ ) which were connected to a needle through a flexible 1 mm tube. About 2 mL of porewater was extracted using the Rhizons and transported through a needle into a septum-capped vacuumed 49 mL glass vials (Infocroma). Vials were shaken vigorously for 2 min after filling the vials with zero air to create reach equilibrium with the headspace. The headspace was extracted with a

glass syringe (Fortuna Optima) by gently injecting zero air (Synthetic air 5.6, Pangas AG) in the vial with a second glass syringe prior to flushing the headspace three times between the two syringes. The headspace was then measured with the Cavity Ring-Down Spectrometer analyzer (Picarro G220-i, Santa Clara, USA) directly from the glass syringe for  $\text{CH}_4$  and  $\delta^{13}\text{C}_{\text{CH}_4}$  concentrations in the gas phase. Water  $\text{CH}_4$  concentrations were back calculated according to Wiesenburg & Guinasso 1979 accounting for water temperature, the headspace/water ratio in the vial and the dilution from the extraction with the syringes.

### 3.2.10 Methane diffusive fluxes from littoral sediments

Using the porewater measurements from the cut-syringes used by Langenegger *et al.* 2022 and the Rhizon methods, the littoral  $\text{CH}_4$  sediment flux ( $F_s$ ) was determined using Fick's First Law over the linear top 2 - 3 cm of the porewater concentration profile.

$$F_s = -\phi D_{\text{CH}_4} \theta^{-2} \frac{\partial C}{\partial z}; \quad [\text{mmol m}^{-2} \text{ d}^{-1}] \quad (3.5)$$

where  $F_s$  is the diffusive  $\text{CH}_4$  flux at the sediment–water interface,  $\phi$  the porosity of the sediments (0.9),  $D_{\text{CH}_4}$  the diffusion coefficient for  $\text{CH}_4$  in water ( $1.5 \text{ m}^2 \text{ s}^{-1}$  (Broecker & Peng 1974)),  $\theta^2$  the square of tortuosity (1.2) (Boudreau 1997) and  $\partial C / \partial z$  the measured vertical concentration gradient.

The benthic chamber consists of a core cover with a lid leaving  $\sim 5$  cm of headspace and  $\sim 30$  - 50 cm of water. The lid was connected to a GHG analyzer (UGGA, Los Gatos Research, Inc.) creating a closed loop where the partial pressure of  $\text{CH}_4$  ( $P_{\text{CH}_4}$ ) was measured over time. Water  $\text{CH}_4$  concentration ( $C_w$ ) was measured at the beginning and at the end of the experiment. Benthic chamber fluxes were calculated based on the temporal change of  $\text{CH}_4$  concentration inside the chamber following the methodology described in Chapter 2.

The littoral sediment flux was calculated as the average flux at each location, determined as the average of all the methods (when possible). The littoral sediment flux was assumed constant during the entire period of analysis.

### 3.2.11 Bubble CH<sub>4</sub> dissolution and ebullition rates

Ebullition rates for June and September 2018 and July 2019 were obtained using measurements of bubble composition at those dates and diffusive sediment fluxes from 2016 to 2019 measurements following Langenegger *et al.* 2019. Using these results, we calculated the average proportion of total ebullition rates that is emitted above 8 m ( $\chi$ ) and we used it to estimate the total ebullition rates ( $R_{\text{eb}}$ ) from the ebullition fluxes below 8 m ( $F_{\text{eb},8\text{m}}$ ) for 2016 and 2017 reported by Vachon *et al.* 2019 as:

$$R_{\text{eb}}(t) = F_{\text{eb}, 8\text{m}}(t)A_{\text{s},8\text{m}}(1 + \chi); \quad [\text{mmol d}^{-1}] \quad (3.6)$$

where  $A_{\text{s},8\text{m}}$  is the sediment area above 8 m and  $t$  are the dates of each sampling campaign conducted during 2016 and 2017.

The temporal variation of  $R_{\text{eb}}$  for 2018 and 2019 was estimated assuming that  $R_{\text{eb}}$  for July 2018 and August 2019 are the maximum rate during each year. Next, the temporal distribution of the missing data of those years were obtained from the temporal distribution of 2016 as:

$$R_{\text{eb}, i}(t) = R_{\text{eb}, i}^{\text{max}} \frac{R_{\text{eb}, 2016}(t)}{R_{\text{eb}, 2016}^{\text{max}}}; \quad [\text{mmol d}^{-1}] \quad (3.7)$$

where  $i$  is the year 2018 or 2019 and  $t$  is each sampling campaign conducted each year.

The bubble dissolution rates ( $R_{\text{dis}}\forall_{\text{SML}}$ ) in the SML were estimated using the slope of the linear interpolation of the proportion of  $R_{\text{dis}}\forall_{\text{SML}}$  in the SML and  $R_{\text{eb}}$  at May and August 2018 and July 2019 (Fig. S.B.3). The  $R_{\text{dis}}$  rates for May and August 2018 and July 2019 were estimated following Chapter 2, where the dissolution from a single bubble released from the sediment was calculated using McGinnis *et al.* 2006 considering a 5 mm bubble diameter.

### 3.2.12 Vertical CH<sub>4</sub> diffusive fluxes from/to the SML

Diffusive fluxes to/from the SML ( $F_z$ ) were estimated using Fick's First Law:

$$F_z = K_z \frac{\partial C}{\partial z} \quad (3.8)$$

where  $\frac{\partial C}{\partial z}$  at the bottom of the SML was estimated using the water column profiles of CH<sub>4</sub> concentrations and the  $K_z$  was determined from the heat budget method (Powell & Jassby 1974)



at the bottom of the SML.

### 3.2.13 Monte Carlo simulation

Monte Carlo simulations were performed (10000 iterations) when solving both mass balance models following Chapter 2.  $P_{\text{net}}$ ,  $R_{\text{dis}}$  and  $F_z$  were selected within a normal distribution resulting from the mean ( $\mu$ ) and their standard deviation ( $\sigma$ ) retrieved from the field measurements. To avoid negative values for  $F_a$  and  $F_s$  a gamma distribution defined by the shape ( $\kappa = \mu^2/\sigma^2$ ) and the scale ( $\theta^2 = \sigma^2/\mu$ ) was chosen. Here the gamma distribution has the density  $f(x) = \left(x^{\kappa-1} \frac{e^{-x/\theta}}{\theta^\kappa \Gamma}\right)$  where  $\Gamma$  is the gamma function. `Random.normal` and `random.gamma` functions from the Numpy package (Harris *et al.* 2020) in Python were used for each normal and gamma distributions, respectively.

### 3.2.14 Sources contribution to CH<sub>4</sub> diffusive fluxes to the atmosphere

Following Chapter 2, each source contribution (SC) to the diffusive surface flux was estimated as:

$$\text{SC}_i = \frac{S_i}{\sum_j S_j} \cdot 100; \quad [\%] \quad (3.9)$$

where  $S_i$  is each source term ( $\text{mol d}^{-1}$ ) such as: bubble dissolution ( $R_{\text{dis}} \forall_{\text{SML}}$ ), sediment flux ( $F_s A_s$ ), net production ( $P_{\text{net}} \forall_{\text{SML}}$ ) and vertical diffusive fluxes ( $F_z A_z$ ). If  $S_i \leq 0$  then  $S_i = 0$  where  $i$  is each source term.

## 3.3 Results

### 3.3.1 Limnological measurements

Surface waters remained oxygenated over the four years of measurements during the stratified period (2016 - 2019; Fig. S.B.4). The surface water temperature during the stratified period was consistent between the different years with an average value of  $21 \pm 3^\circ\text{C}$ . The surface mixed layer (SML) depth ranged between 1.4 - 7.5 m during the stratified period with a clear tendency to deepen towards the end of the summer (Fig. S.B.5). The average Secchi disk depth (SD) and chlorophyll-*a* (Chl*a*) concentrations during the stratified period of the four years were  $2.4 \pm 1.1$  m and  $5.1 \pm 3.1 \text{ mg m}^{-3}$ , respectively (Table S.B.1 and Fig. S.B.6).

### 3.3.2 Surface CH<sub>4</sub> concentration and isotopic signature

The surface CH<sub>4</sub> concentrations ranged between 0.3 - 1.3 mmol/m<sup>3</sup> during stratified period with an average value of  $0.93 \pm 0.28$  mmol/m<sup>3</sup> (Fig. S.B.7). In fact, the CH<sub>4</sub> concentrations showed a general tendency to be lower in May, increased in June and July, and decrease in September. There was a slight increase CH<sub>4</sub> concentrations in October likely due to the start of convective mixing (Fig. 3.1A).  $\delta^{13}\text{C}_{\text{CH}_4}$  in the SML ranged between  $-60$  to  $-30$  ‰ with a tendency to become more enriched towards the end of the summer (Fig. 3.1B).

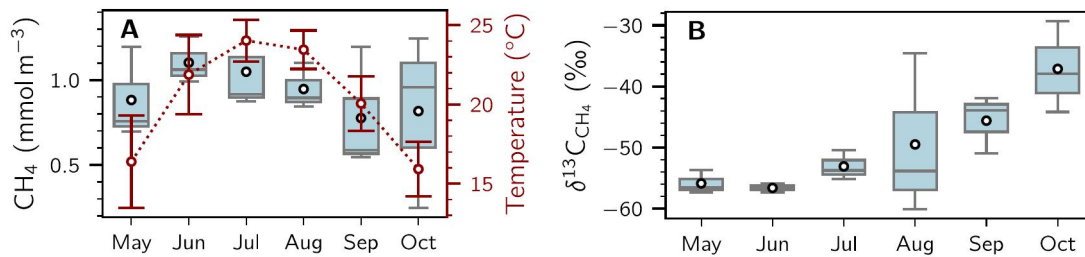


Figure 3.1. (A) Monthly average surface CH<sub>4</sub> concentrations (boxes) and surface temperature (red line) from 2016 to 2019. The error bars of the temperature represent the standard deviation for each month. (B) Monthly average of surface isotopic signature of CH<sub>4</sub> ( $\delta^{13}\text{C}_{\text{CH}_4}$ ). Each box shows the first and third quartiles with the median (line), whiskers extend to the most extreme data point within 1.5 times the interquartile range from the box. The white dot represents the average of each distribution.

Higher surface CH<sub>4</sub> concentrations were observed in the transect conducted in August 2019 compared to May and September 2018 (Fig. 3.2). On average, the CH<sub>4</sub> concentrations near the shore were 11 % higher than at the center of the lake, however the difference along each transect was not significant (ANOVA analysis). Surface  $\delta^{13}\text{C}_{\text{CH}_4}$  along the transect ranged between  $-57$  to  $-38$  ‰ (Fig. S.B.8). Lighter  $\delta^{13}\text{C}_{\text{CH}_4}$  was observed in May 2018 compared with the other two campaigns (Fig. S.B.8). Significant differences between  $\delta^{13}\text{C}_{\text{CH}_4}$  at the shore and the center of the lake were only observed on August 2019, where  $\delta^{13}\text{C}_{\text{CH}_4}$  near the shore was 8 % lighter than at the center (Fig. S.B.8).

### 3.3.3 Diffusive CH<sub>4</sub> emissions to the atmosphere

Diffuse CH<sub>4</sub> emissions ( $F_a$ ) at the air-water interface (AWI) ranged between 0.1 - 3.7 mmol/m<sup>2</sup>/d during the stratified season (Fig. S.B.9). On average, in September  $F_a$  reached its lowest value ( $1.0 \pm 0.5$  mmol/m<sup>2</sup>/d) and increased during the fall up to  $2.1 \pm 1.4$  mmol/m<sup>2</sup>/d (Fig. S.B.10a). The yearly average value of  $F_a$  during the stratified season was higher in 2016

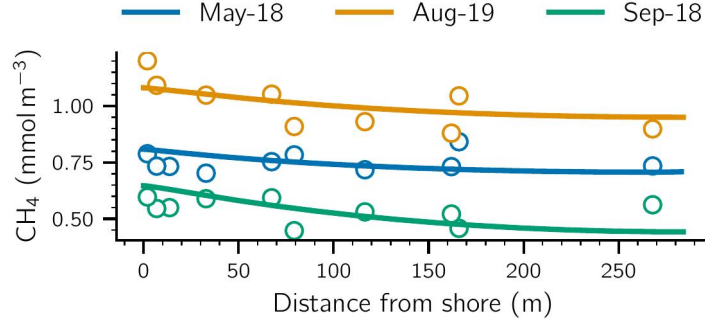


Figure 3.2. Surface  $\text{CH}_4$  concentration along the transect sampled in Soppensee. Lines represent the  $\text{CH}_4$  concentration simulated using the lateral transport model and dots are the measured values.

( $1.4 \pm 1.0 \text{ mmol/m}^2/\text{d}$ ; number of days averaged  $n=5$ ) and 2017 ( $1.8 \pm 0.8 \text{ mmol/m}^2/\text{d}$ ,  $n=6$ ) followed by a decrease during 2018 ( $1.0 \pm 1.1 \text{ mmol/m}^2/\text{d}$ ,  $n=3$ ) and 2019 ( $0.5 \pm 0.4 \text{ mmol/m}^2/\text{d}$ ,  $n=2$ ) (Fig. S.B.10b).

Five literature  $k_{600}$  parameterizations were compared with the chamber-based  $k_{600,\text{cb}}$  (Fig. S.B.11). The best fit between the  $k_{600}$  literature parameterizations and  $k_{600,\text{cb}}$  was obtained with MA10-NB (MacIntyre *et al.* 2010 negative buoyancy, Table S.B.2). The other four parameterizations underestimate  $k_{600,\text{cb}}$  ( $\text{MNB} = [0.14 - 0.5]$ ) and show a low determination coefficient ( $r^2 = [-26 \text{ to } 0.9]$ ).

Wind velocity at 10 m were used to calculate  $k_{\text{CH}_4}$  during 2016, 2017 and 2018 over the stratified period in Soppensee. Daily wind velocity at the Egolzwil meteorological station ranged between  $0.6 - 8.2 \text{ m s}^{-1}$  with an average value of  $2 \text{ m s}^{-1}$  (Fig. S.B.12). The average value of  $k_{\text{CH}_4}$  estimated with MA10-NB was  $1.3 \pm 0.3 \text{ m s}^{-1}$  from 2016 to 2018 with minimum and maximum values of  $0.68$  and  $2.8 \text{ m s}^{-1}$  respectively (Fig. S.B.12). No significant differences were found between years for the wind velocity or  $k_{\text{CH}_4}$ .

### 3.3.4 Diffusive $\text{CH}_4$ fluxes from littoral sediment

The deepest SML during the stratified season was 7.5 m, therefore sediment above the maximum SML depth was classified as littoral. Diffusive  $\text{CH}_4$  fluxes from littoral sediments ( $F_s$ ) were obtained via different methods (Table 3.2). The average  $F_s$  was  $1.56 \pm 1.19 \text{ mmol/m}^2/\text{d}$  for the entire period. About 20% lower values were obtained with the Rhizons compared to the benthic chambers and cut-syringe methods. No correlation was observed between sampled depth and  $F_s$ .

within the SML depth range.

Table 3.2. CH<sub>4</sub> diffusive flux from littoral sediments. Data from this work and previously published data from Langenegger *et al.* 2022 and Langenegger *et al.* 2019

Core	Date	Water Depth (m)	Temp (°C)	Diffusive flux (mmol m <sup>-2</sup> d <sup>-1</sup> )			
				Benthic Chamber	Rhizons	Cut-Syringe	Average
C1	08/12/19	0.80	22.40	3.23	0.29	1.27	1.60
C2	08/12/19	1.00	22.40	2.38	0.05	3.14	1.86
C3	08/12/19	1.00	22.40	0.50	0.32	1.11	0.64
C4	07/10/17	3.00	23.70	-	-	1.43	1.43
C5	09/13/16	4.00	21.00	-	-	3.64	3.64
C6	07/10/17	6.00	10.30	-	-	0.22	0.22
Average sediment flux (mmol m <sup>-2</sup> d <sup>-1</sup> )							1.56 ± 1.19

### 3.3.5 CH<sub>4</sub> ebullition rate and bubble dissolution

Monthly average ebullition rates ranged between 0.9 - 2.0 mmol/m<sup>2</sup>/d (Fig. S.B.13a). On average, the lowest and highest fluxes were found in June and September, respectively. The highest ebullitive fluxes were observed in 2018 (2.3 mmol/m<sup>2</sup>/d) and the lowest in 2016 (Fig. S.B.13b). As the CH<sub>4</sub> dissolution rates in the SML are directly related to the ebullitive fluxes, we observed the same temporal dynamics for dissolution rates as we did for ebullition. The dissolution rates into the SML layer ranged between 0.001 - 0.06 µmol/m<sup>3</sup>/d (Fig. S.B.14).

### 3.3.6 Vertical diffusive fluxes from/to the SML

The vertical diffusive flux from/to the SML is driven by the vertical turbulent diffusivity  $K_z$  and the concentration gradient just below the bottom of the SML.  $K_z$  ranged between 0.1 -  $8 \times 10^{-6} \text{ m}^2 \text{ s}^{-1}$  with a clear tendency to be lower towards the end of the summer (Figs. S.B.16a and S.B.17). During the stratified season,  $F_z$  ranged between -0.11 to 0.22 mmol/m<sup>2</sup>/d from 2016 to 2019 (Fig. S.B.17). In May, June and October the metalimnion acted as a source of CH<sub>4</sub> to the SML, and as a sink in August and September. In July of all years,  $F_z$  was negligible (Fig. S.B.18a). On a yearly average scale during the stratified period, the metalimnion was a small source of CH<sub>4</sub> to the SML except for the year 2017 (Fig. S.B.18b).

### 3.3.7 Surface mass balance

The  $P_{\text{net}}$  rates obtained with the full-scaled mass balance ( $P_{\text{net,fs}}$ ), the wind-based ( $P_{\text{net,t}}$ ) and the lateral transport ( $P_{\text{net,lt}}$ ) models ranged between -140 to 1010 µmol/m<sup>3</sup>/d (Fig. 3.3). Seasonally, a decrease of  $P_{\text{net}}$  rates was observed from the beginning towards the end of the summer where

the highest and the lowest averaged  $P_{\text{net}}$  were estimated for June ( $580 \pm 329 \mu\text{mol}/\text{m}^3/\text{d}$ ) and September ( $-44 \pm 76 \mu\text{mol}/\text{m}^3/\text{d}$ ) respectively (Fig. 3.4). On average,  $P_{\text{net}}$  rates were about 350, 500, 200 and  $-35 \mu\text{mol}/\text{m}^3/\text{d}$  for 2016, 2017, 2018 and 2019, respectively (Fig. S.B.19). Note that only three campaigns were conducted in 2018 and two at the end of the stratified period of 2019. No simulation for  $P_{\text{net},t}$  was completed for 2019 given the lack of data in the temporal scale.

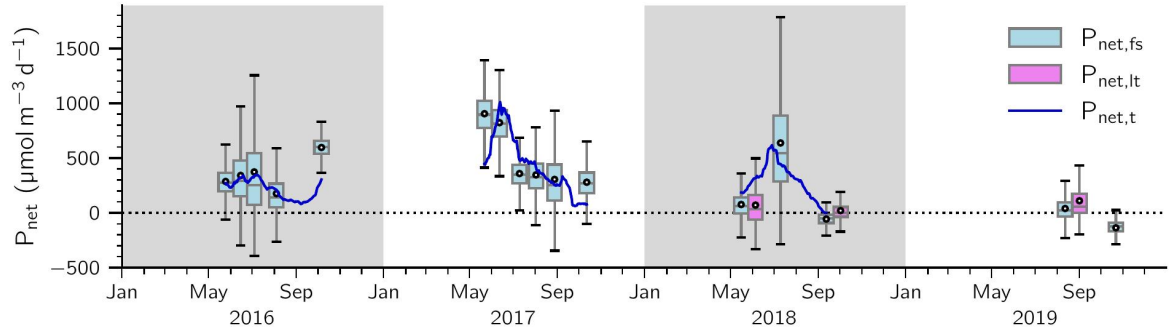


Figure 3.3.  $P_{\text{net}}$  estimation using the full-scale mass balance ( $P_{\text{net},fs}$ , light blue box), the lateral transport model ( $P_{\text{net},lt}$ , violet box) and the wind based model (two weeks moving average  $P_{\text{net},t}$ , blue line). Each box shows the first and third quartiles with the median (line), whiskers extend to the most extreme data point within 1.5 times the interquartile range from the box. The white dot represents the average of the distribution. Note that the date for  $P_{\text{net},lt}$  correspond to the date of  $P_{\text{net},fs}$  when both are calculated.

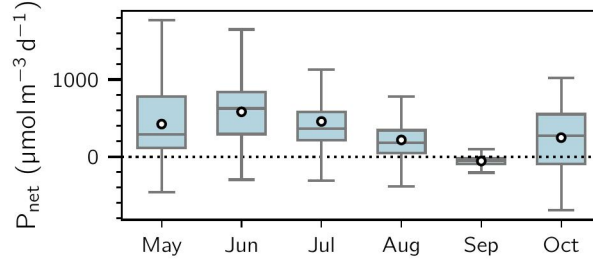


Figure 3.4. Monthly average  $P_{\text{net}}$  rates in the SML during the stratified season from 2016 to 2019 obtained with the full-scale mass balance model. Each box shows the first and third quartiles with the median (line), whiskers extend to the most extreme data point within 1.5 times the interquartile range from the box. The white dot represents the average of the distribution.

### 3.3.8 Contribution of $\text{CH}_4$ sources to atmospheric diffusive emissions

Using the  $P_{\text{net}}$  obtained from the full-scaled mass balance ( $P_{\text{net},fs}$ ), we calculated the contribution of each  $\text{CH}_4$  source to the diffusive  $\text{CH}_4$  emissions to the atmosphere during the stratified season (Fig. 3.5).  $P_{\text{net}}$  and  $F_s$  were the major sources of  $\text{CH}_4$  in the SML for most campaigns, with minor contributions from  $R_{\text{dis}}$  and  $F_z$  until the late summer campaigns of 2018 and 2019. On

average,  $P_{\text{net}}$  contributed about 64 % of the emission from 2016 to 2019 reaching up to 90 % in May 2017. Seasonally,  $P_{\text{net}}$  contributions were generally higher at the beginning of summer ( $\sim 80$  % in June) and decreased towards the end of summer ( $\sim 40$  % in September).  $P_{\text{net}}$  was the dominant source at each campaign except September 2018 and August and October 2019, when the dominant source was  $F_s$  (September 2018 and October 2019) or  $R_{\text{dis}}$  (August 2019). On average,  $F_s$  contributed about 20 % from 2016 to 2019 reaching up to about  $\sim 50$  % in September 2018. The seasonal  $F_s$  contribution mirrored the seasonal  $P_{\text{net}}$  contribution trend, i.e., lower at the beginning of summer compared to the end. The contribution of bubble dissolution in the SML ( $R_{\text{dis}}$ ) to diffusive  $\text{CH}_4$  emissions was negligible ( $< 0.1$  %) in 2016 and 2018, but was  $\sim 30$  % in 2018 and 2019. The highest  $R_{\text{dis}}$  contribution was on August 2019 (38 %). The  $F_z$  contribution was negligible during the entire period of analysis, except for May 2018 and October 2019 when it was 10 and 30 %, respectively.

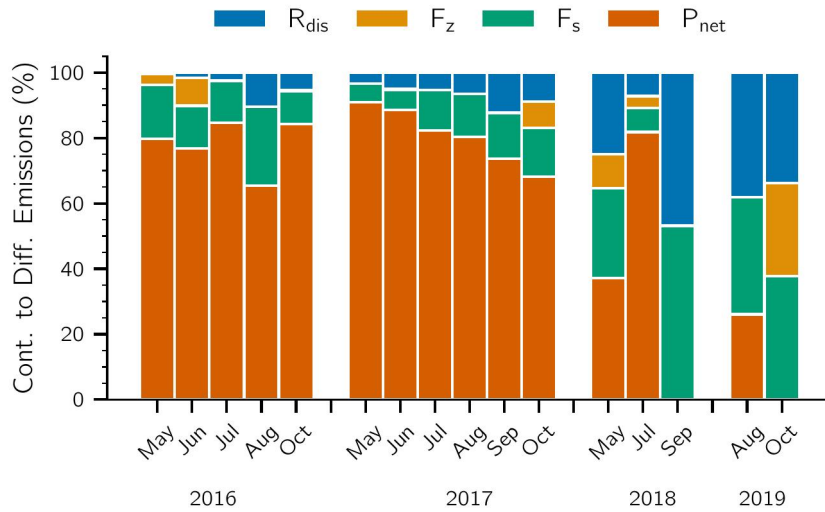


Figure 3.5. Contribution to diffusive atmospheric  $\text{CH}_4$  emissions ( $F_a$ ) from the sediment flux ( $F_s$ ), diffusive flux from hypolimnion ( $F_z$ ), bubble dissolution ( $R_{\text{dis}}$ ) and net production ( $P_{\text{net}}$ ) in the SML.

### 3.4 Discussion

In this study we quantified the rate of  $\text{CH}_4$  net production in the oxic SML during four years in a hypereutrophic Swiss lake using a full-scaled mass balance, a wind-based mass balance, and a 1-D lateral transport model. The different approaches produced similar  $P_{\text{net}}$  rates and the same temporal pattern.  $P_{\text{net}}$  rates were positive during the stratified period, indicating that OMP needs to occur to close the mass balance in the SML (except for 2019). The average  $P_{\text{net}}$

rates for the four years over the stratified season in Soppensee was  $330 \pm 290 \mu\text{mol}/\text{m}^3/\text{d}$  and is in the range of previously reported values ( $0.2 - 1434 \mu\text{mol}/\text{m}^3/\text{d}$ ; Günthel *et al.* 2021 and Chapter 2). In fact, a very similar  $P_{\text{net}}$  rate was estimated for the hypereutrophic lake Bretaye ( $316 \pm 2241 \mu\text{mol}/\text{m}^3/\text{d}$ ; Chapter 2). Moreover,  $P_{\text{net}}$  was the major contributor to diffusive atmospheric  $\text{CH}_4$  emissions from Soppensee ( $54 \pm 37 \%$ ).

### 3.4.1 $P_{\text{net}}$ seasonal variability

$P_{\text{net}}$  rates during the stratified period in Soppensee were temporally variable. The wind-based and the full-scaled mass balance models resulted in high  $P_{\text{net}}$  rates ( $\sim 800 \mu\text{mol}/\text{m}^3/\text{d}$ ) at the beginning of summer, indicating that OMP dominated over MOx in Soppensee surface waters. However, almost negligible rates were observed towards the end of the stratified season (Fig. 3.4), indicating that either the OMP rates decreased, the MOx increased or both. The same temporal trend was also observed in Chapter 2 and Günthel *et al.* 2019. The  $\delta^{13}\text{C}_{\text{CH}_4}$  signature also suggests that MOx dominated at the end of the stratified season as the residual  $\text{CH}_4$  pool became highly  $^{13}\text{C}$ -enriched, due to methane oxidation (Reeburgh 2007). Although the mechanisms behind OMP and its impact on the  $\delta^{13}\text{C}_{\text{CH}_4}$  signature of  $\text{CH}_4$  pools are not clear, our mass balance results suggest that MOx can dominate over  $P_{\text{net}}$  in the SML of Soppensee during the latter part of the stratified period (Fig. 3.1B).

### 3.4.2 Effect of methane oxidation and OMP on $\delta^{13}\text{C}_{\text{CH}_4}$ in the SML

The Keeling plot method was applied to estimate the  $\delta^{13}\text{C}_{\text{CH}_4}$  of the  $\text{CH}_4$  source in the SML (Keeling 1958). For the four years of measurements, the Keeling plot indicates that surface  $\text{CH}_4$  might be a mixture of three sources (Fig. 3.6). For August 2019 and October 2016 and 2017, a  $\delta^{13}\text{C}$  depleted source with  $\delta^{13}\text{C}_{\text{CH}_4}$  of  $-59\text{‰}$  whereas for September 2016 and 2018, and October 2019 the  $\delta^{13}\text{C}_{\text{CH}_4}$  signature of the  $\text{CH}_4$  source is less depleted in  $\delta^{13}\text{C}$  ( $-55\text{‰}$ ). The positive correlation between  $1/\text{CH}_4$  and  $\delta^{13}\text{C}_{\text{CH}_4}$  in these two groups indicates that methane oxidation occurs during those time periods due to the  $\text{CH}_4$  fractionation produced by methane oxidation. In contrast, OMP will not fractionate the  $\text{CH}_4$  pool in the SML, and it will produce  $\text{CH}_4$  with a  $\delta^{13}\text{C}_{\text{CH}_4}$  that will not show a positive correlation with  $1/\text{CH}_4$ . However, if the isotopic signature of the carbon source of OMP changes, it will be reflected in the isotopic signature associated to OMP. These features were found in May, June and July for the four

years, where we do not observe a positive correlation between  $1/\text{CH}_4$  and  $\delta^{13}\text{C}_{\text{CH}_4}$ . During those months higher  $P_{\text{net}}$  rates were estimated with no signal of methane oxidation found (Fig. 3.1B and 3.4), therefore the  $\delta^{13}\text{C}_{\text{CH}_4}$  of the main source was estimated from the average  $\delta^{13}\text{C}_{\text{CH}_4}$  signature in the SML ( $-55\text{‰}$ ). This result is agreement with Hartmann *et al.* 2020 where they found that OMP likely produces  $\text{CH}_4$  with  $\delta^{13}\text{C}_{\text{CH}_4}$  values close or higher than  $-50\text{‰}$ .

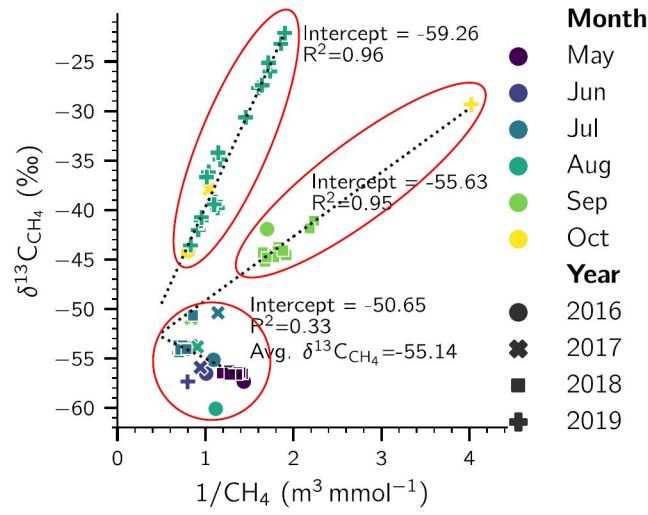


Figure 3.6. Keeling plot analysis of the surface  $\text{CH}_4$  concentration during the stratified period from 2016 to 2019.

### 3.4.3 Oxidic methane contribution to diffusive emissions

More evidence points to the occurrence of OMP across aquatic environments such as the ocean (Karl *et al.* 2008; Li *et al.* 2020), high altitude (Perez-Coronel & Beman 2020) and pre-alpine lakes (Chapter 2), as well as lakes in temperate and arctic regions (DelSontro *et al.* 2018b; Li *et al.* 2019). In addition, OMP has been observed using different methodologies, such as mesocosms (Bogard *et al.* 2014; Günthel *et al.* 2019), in-situ water incubations (Grossart *et al.* 2011; Bižić *et al.* 2020; Günthel *et al.* 2020), mass balances (Donis *et al.* 2017; Günthel *et al.* 2019; Chapter 2) and lateral transport models (Chapter 2). Despite the growing literature evidence, the OMP contribution to diffusive  $\text{CH}_4$  emissions from inland waters remains hotly debated (Günthel *et al.* 2021; Peeters & Hofmann 2021). In our study,  $P_{\text{net}}$  was the greatest contributor to diffusive  $\text{CH}_4$  fluxes to the atmosphere ( $F_a$ ), reaching up  $\sim 90\%$  in May 2017 with an average value of  $\sim 55\%$ . The temporal dynamic of the  $P_{\text{net}}$  contribution to diffusive emissions does not always follow the same trends as  $P_{\text{net}}$  rates. For example, in 2016, the



$P_{\text{net}}$  contribution to diffusive emissions was consistently around  $\sim 80\%$ , while in 2017 the  $P_{\text{net}}$  contribution decreased throughout the stratified season (Fig. 3.5). Unfortunately, we do not have enough data in 2018 and 2019 to investigate the temporal dynamic of  $P_{\text{net}}$  contribution.

### 3.4.4 OMP key drivers and upscaling approach evaluation

In Chapter 2 it was proposed an upscaling approach relating  $\text{Chl}a$ , light climate (LC) and Secchi depth (SD) to the ratio of  $P_{\text{net}}$  and surface  $\text{CH}_4$  concentration. We tested this relationship using the monthly average data from Soppensee (Fig. S.B.20) and observed a lower correlation coefficient ( $R^2 = 0.56$ ) than in Chapter 2. Nevertheless, this positive relationship between  $\text{Chl}a$  concentrations, light conditions and  $P_{\text{net}}/C_{\text{CH}_4}$  suggest that photosynthesis play a role in OMP, which is in agreement with the recent finding that photoautotrophs can produce  $\text{CH}_4$  (Bižić *et al.* 2020; Günthel *et al.* 2020; Hartmann *et al.* 2020; Klintzsch *et al.* 2020). Moreover, when we include the data from Soppensee on Fig. 3.7, a good correlation ( $R^2 = 0.83$ ) was observed (Fig. 3.7), implying that this approach could be useful as a first estimate of  $P_{\text{net}}$  rates on a global scale. As the current OMP dataset is still sparse, futures studies should be included to verify this trend on a larger scale.

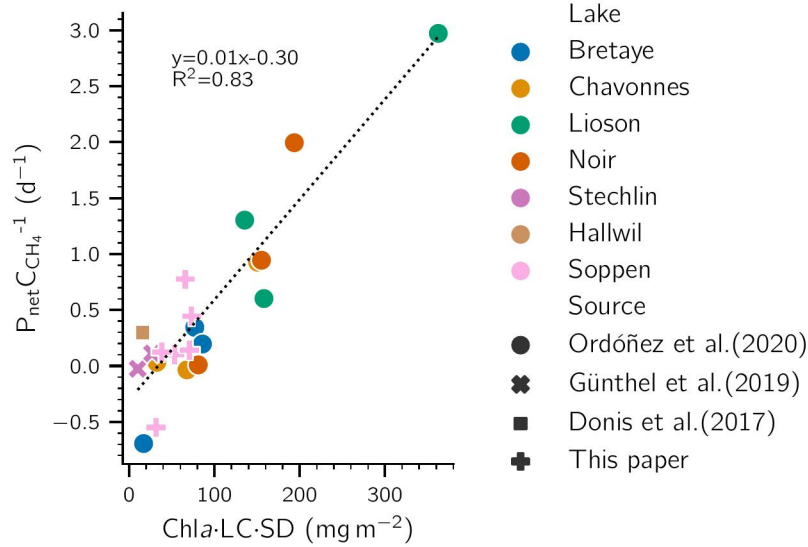


Figure 3.7. Relation between the ratio  $P_{\text{net}}$  ( $\text{mmol m}^{-3} \text{d}^{-1}$ ) and the surface  $\text{CH}_4$  concentration ( $C_{\text{CH}_4}$ ,  $\text{mmol/m}^3$ ) and chlorophyll- $a$  ( $\text{Chl}a$ ,  $\text{mg m}^{-3}$ )  $\times$  light climate ( $\text{LC} = 2.5 \frac{\text{SD}}{H_{\text{SML}}}$ , -)  $\times$  Secchi depth (SD, m) proposed in Chapter 2.  $\text{Chl}a$  is the average concentration obtained from CTD's profiles at the center of the lake corrected with Fig. S.B.2. Each point for Soppensee was calculated as the monthly average during 2016 to 2019.

### 3.4.5 Uncertainty assessment

$P_{\text{net}}$  rates were estimated using three methodologies: a full-scale mass balance, a wind-based and a lateral transport models. The major advantage of the full-scaled mass balance is that it only depends on measured values for its boundary conditions but assumes that these measurements are representative of a general trend during the residence time of  $\text{CH}_4$  in the SML ( $\sim 14$  d). It is well known that  $F_a$  varies in time and space depending on the turbulence level at the water surface due to wind velocity and convection (MacIntyre *et al.* 2010; MacIntyre *et al.* 2021), as well as the  $\text{CH}_4$  concentration in surface waters. To account for the effect of the temporal variability of  $F_a$ , we computed  $P_{\text{net}}$  with the wind-based model ( $P_{\text{net,t}}$ , Eqs. 3.1 and 3.2). In general, we observed a good agreement between the two methods, except for May and Oct 2016 and 2017 when  $P_{\text{net,t}}$  was lower than  $P_{\text{net,fs}}$  (Fig. 3.3). This discrepancy is likely because  $k_{\text{CH}_4}$  estimated via the literature parameterization was lower than that estimated via chamber on those days (Fig. S.B.12). The chamber-based  $k_{\text{CH}_4}$  may better reflect the local temporal conditions rather than the temporal average value provided by the literature parameterization (e.g., Oct 2016 data). However, this discrepancy may also point out a limitation of the  $k_{600}$  literature parameterizations that neglects different phenomena, such as diffusive flux enhancement by microbubbles (McGinnis *et al.* 2015) or buoyancy effects due to heating at low wind speeds (MacIntyre *et al.* 2021). A good agreement was found between the full-scale mass balance  $P_{\text{net,fs}}$  and the lateral transport model  $P_{\text{net,lt}}$ . This latter approach accounts for the spatial variability of surface  $\text{CH}_4$  concentrations and horizontal transport from littoral sediments using a constant  $k_{\text{CH}_4}$ . Therefore, considering these spatial changes does not have a great impact on  $P_{\text{net}}$  estimations.

The other major input that can affect  $P_{\text{net}}$  estimations is  $F_s$ . In this study, we used a constant values for  $F_s$  for all four years that was the average from using three different methods on core data from six locations in the SML taken in 2016, 2017 and 2019 (Table 3.2, Fig. S.B.1). Our resulting value ( $1.56 \pm 1.19$  mmol/m<sup>2</sup>/d) was well within the range of those reported in the literature (0.001 - 8.8 mmol/m<sup>2</sup>/d, Huttunen *et al.* 2006; Bastviken *et al.* 2008; Peeters *et al.* 2019). Using six different locations to estimate  $F_s$  in the SML provided a good representation of the average littoral sediment in Soppensee. In addition, three methods were used to estimate the average flux, minimizing the bias related with each method. For example, bubbles can

be included when taking the sediment sample in the cut-syringe method or the influence of surrounding sediments in the Rizzons methods (Seeborg-Elverfeldt *et al.* 2005).  $F_s$  can also vary by the increase of  $\text{CH}_4$  production in the sediment with increasing temperature (Nozhevnikova *et al.* 1997). However, our core measurements were conducted mostly in July and August when the highest water temperatures were measured, consequently the highest  $\text{CH}_4$  production in littoral sediment would be expected. While this means that our  $F_s$  values were in the upper range of what is expected, this translates into our  $P_{\text{net}}$  estimates being conservative, as  $F_s$  is another source of  $\text{CH}_4$  to the SML (Eqs. 3.1 and 3.3).

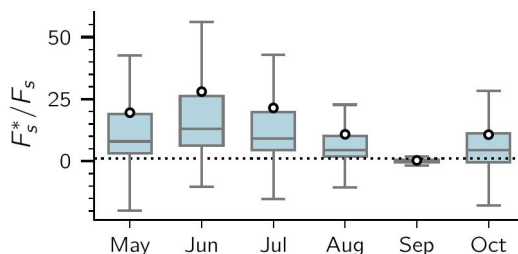


Figure 3.8. Monthly average of the proportion of littoral sediment needed ( $F_s^*$ ) to compensate the surface diffusive emissions compared to measured littoral sediment flux ( $F_s$ ) considering no  $P_{\text{net}}$  in the surface mixed layer. The boxes show the first and third quartiles with the median (line), whiskers extend to most extreme data point within 1.5 times the interquartile range from the box. The white dot represents the average of the distributions.

As  $F_s$  has been shown to be highly influential on  $P_{\text{net}}$  estimations and a source of debate regarding OMP (Donis *et al.* 2017; Peeters *et al.* 2019; Günthel *et al.* 2021; Peeters & Hofmann 2021), we used the full-scaled mass balance ( $P_{\text{net,fs}}$ ) to investigate the impact of  $F_s$  on our  $P_{\text{net}}$  estimations in Soppensee. If we assume that OMP is negligible (e.i.  $P_{\text{net}} = 0$ ), we would need up to 20 times higher sediment fluxes to account for the measured diffusive  $\text{CH}_4$  flux to the atmosphere. This means that  $F_s$  would have to approach  $F_s = \sim 30 \text{ mmol/m}^2/\text{d}$  which exceeds the highest value reported for littoral sediment  $\text{CH}_4$  fluxes by a factor of 3-4 (Peeters *et al.* 2019). We therefore conclude that the diffusive  $\text{CH}_4$  flux from littoral sediment alone cannot account for the diffusive  $\text{CH}_4$  flux to the atmosphere and that OMP needs to be included in the  $\text{CH}_4$  budget of Soppensee.

### 3.4.6 Conclusions

Substantial evidence has been gathered over the past decade suggesting that OMP is a process that occurs in most aquatic environments, however,  $P_{\text{net}}$  rates have only been reported in a few

lakes and in a short timescale. Our study of OMP over four years in a hypereutrophic temperate lake illustrates that  $P_{\text{net}}$  (i.e., the balance between OMP and MOx) needs be included in the epilimnetic  $\text{CH}_4$  lake budget. The good agreement between the three different models used to calculate  $P_{\text{net}}$  implies that there are no methodological issues with the models when the boundary conditions are properly determined.

We also showed in this study that  $P_{\text{net}}$  is the major contributor to the diffusive  $\text{CH}_4$  emissions to the atmosphere from a stratified hypereutrophic lake, further supporting observations reported by Günthel *et al.* 2019, Donis *et al.* 2017 and in Chapter 2. We, however, are the first study to show this trend over multiple years and throughout the stratified period. Our temporal datasets over the stratified periods of multiple years also highlighted the tendency of  $P_{\text{net}}$  rates to begin high in the spring and decrease to almost negligible rates at the end of the stratified season, as has been observed elsewhere (Günthel *et al.* 2019, Chapter 2). Finally, our study also corroborates the findings that photoautotrophs may play an important role in  $\text{CH}_4$  production in oxygenated waters and that the upscaling method proposed originally in Chapter 2 could be used as a first estimation of  $P_{\text{net}}$  for different lake environments. This estimation is thus useful as a first step in determining the potential for  $P_{\text{net}}$  in any system to impact surface  $\text{CH}_4$  emissions, which is important seeing as freshwater systems are responsible for about ~20 - 40 % of natural  $\text{CH}_4$  emissions to the atmosphere (Saunois *et al.* 2020; Rosentreter *et al.* 2021). Seeing as OMP is a  $\text{CH}_4$  source near the air-water interface and associated with photoautotrophs, it is crucial to continue investigating the mechanisms, rates, and drivers of OMP from various aquatic systems to be able to accurately predict future aquatic  $\text{CH}_4$  emissions in the face of global change.



---

# Diurnal cycle of oxic methane production in a pre-alpine lake (Lac de Bretaye)

---

César Ordóñez<sup>1</sup>, Héloïse Hannart<sup>2</sup>, Femke Hurtak<sup>2</sup>, Julie Seemann-Ricard<sup>1</sup>, Jannine Wetter<sup>4</sup> and Daniel F. McGinnis<sup>1</sup>

<sup>1</sup>Aquatic Physics Group, Department F.-A. Forel for Environmental and Aquatic Sciences (DEFSE), Faculty of Science, University of Geneva, Uni Carl Vogt, 66 Boulevard Carl-Vogt, 1211 Geneva, Switzerland

<sup>2</sup>Engineering of Life Sciences, École Polytechnique Fédéral de Lausanne (EPFL), Lausanne, Switzerland

<sup>3</sup>École Supérieure de Physique et de Chimie Industrielles de la Ville de Paris, Paris, France

<sup>4</sup>Institute for Atmospheric and Climate (IAC), ETH Zürich, Zürich, Switzerland

Content of Chapter 4 will be submitted for publication in 2022

## Abstract

Breaking the traditional paradigms that methane ( $\text{CH}_4$ ) is only produced by anoxic condition, evidence shows that  $\text{CH}_4$  can also be produced in presence of oxygen (also called "oxic methane production" or OMP) by almost any living organism under oxidative stress. Recent studies show that different phytoplankton cultures are able to produce methane in oxic conditions and its production rates follow the dark-light cycle. In addition, it has been observed that OMP tends to be higher at spring/early summer and decrease at the end on the stratified season in lakes, however no research have been conducted to investigate OMP changes on a daily scale. In this work, we investigated the net production rates ( $P_{\text{net}}$ ), i.e., the balance between OMP and methane oxidation, in a small eutrophic lake located in the pre-alpine region. Using day and night measurements over three days, we showed that  $P_{\text{net}}$  tends to be higher during the day while negative values during the night indicates a predominance of methane oxidation over OMP. This study highlights the importance of performing both day and night measurements to estimate the contribution of OMP in a global scale and further investigation is needed to understand the importance that photoautotrophs could play on the atmospheric  $\text{CH}_4$  budget.

## 4.1 Introduction

Methane ( $\text{CH}_4$ ) emissions from aquatic ecosystems contributes about 20 - 50 % of the global  $\text{CH}_4$  budget (Saunois *et al.* 2020; Rosentreter *et al.* 2021). Recent studies have shown high contribution of  $\text{CH}_4$  produced in oxic condition (also called oxic  $\text{CH}_4$  production or OMP) to diffusive  $\text{CH}_4$  emissions from lakes (Bogard *et al.* 2014; Donis *et al.* 2017; Günthel *et al.* 2019; Chapter 2; Chapter 3), contrasting the assumption that  $\text{CH}_4$  production was strictly an anaerobic process (Conrad 2009). It has been observed that net  $\text{CH}_4$  production ( $P_{\text{net}}$ ) follows a seasonal cycle, with higher contributions in spring/early summer than at the end of the stratified season (Günthel *et al.* 2019; Chapter 3). However, no investigations have been conducted to understand the diurnal OMP cycle in lakes.

Recent discoveries show that  $\text{CH}_4$  can be produced by any organism under oxidative stress (Ernst *et al.* 2022). Several pathways have been proposed for OMP such as dissolved organic matter photoproduction (Xie *et al.* 2019; Li *et al.* 2020), biodegradation of methylphosphonate in

phosphorus limited environments (Karl *et al.* 2008; Repeta *et al.* 2016; Wang *et al.* 2017; Khatun *et al.* 2019), archeal methanogenesis in anoxic microniches (Grossart *et al.* 2011) and bacteria conversion of methylamine to CH<sub>4</sub> (Wang *et al.* 2021). However, evidence that OMP follows the light-dark cycle in different phytoplankton cultures (Bižić *et al.* 2020; Hartmann *et al.* 2020), positive correlations between CH<sub>4</sub>, oxygen and chlorophyll-*a* concentrations (Bižić *et al.* 2020; Hartmann *et al.* 2020; León-Palmero *et al.* 2020) and higher OMP rates by photoautotrophs compared with other organisms (Ernst *et al.* 2022), indicates the important and direct role of phytoplankton on OMP in lakes. Moreover, macrophytes, usually ignored in OMP studies, can also contribute to the oversaturation of CH<sub>4</sub> in the littoral zone in lakes (Hilt *et al.* 2022). Despite that the fact OMP can be related with different processes, an important fraction could be associated to photoautotrophs production during the day.

A key component to resolve the variability of the CH<sub>4</sub> dynamics in lakes is methane oxidation (MOx). It has been shown that MOx can be inhibited by light (Shelley *et al.* 2017) and elevated oxygen concentration (Thottathil *et al.* 2019). In fact, Thottathil *et al.* 2018 hypothesized that during the day the effect of light leads to higher CH<sub>4</sub> concentration with <sup>13</sup>C-CH<sub>4</sub> depleted and during the night lower CH<sub>4</sub> concentrations and enriched <sup>13</sup>C-CH<sub>4</sub> were observed product of MOx dynamics. Nevertheless, the impact of OMP on the variation of the CH<sub>4</sub> concentrations and its stable isotopic signature ( $\delta^{13}\text{C}_{\text{CH}_4}$ ) in the surface mixed layer (SML) remains unknown.

One of the most important sources of CH<sub>4</sub> in lakes is the diffusive flux from sediments, however in surface water its contribution to emissions remain controversial (Günthel *et al.* 2021; Peeters & Hofmann 2021). Higher temperatures could CH<sub>4</sub> production rates (Nozhevnikova *et al.* 1997), however using incubations with sediments at different temperatures, Liikanen *et al.* 2002 showed no significant increase on CH<sub>4</sub> sediment fluxes under oxic conditions. Liikanen & Martikainen 2003 further demonstrated that diffusive CH<sub>4</sub> fluxes from deep sediment in with oxic overlying water decrease by ~30 times compared to those with anoxic overlying water. Moreover, Damgaard *et al.* 1998 showed that sediment CH<sub>4</sub> front in rice paddy soils deepened several millimeters in presence of oxygen produced by photosynthesis, highlighting the idea that primary production occurring in the top layer of the sediment could create a CH<sub>4</sub>-oxidizing benthic filter. Therefore, we hypothesize that the contribution of CH<sub>4</sub> diffusive flux from littoral



sediment should be higher during the night than during the day.

It has been shown that bubble dissolution and turbulent diffusive flux from the hypolimnion are usually minor contributors of  $\text{CH}_4$  to the SML (Donis *et al.* 2017; Günthel *et al.* 2019; Chapter 2; Chapter 3). However, deep convection due to the cooling of surface water during the night could increase the volume where bubbles can be dissolved, increase the sediment area included on the SML, as well as transport  $\text{CH}_4$  from the metalimnion to the SML by advection. All these processes simultaneously can change the  $\text{CH}_4$  mass balance in surface waters on a daily scale.

In this study, using a full-scale mass balance and a lateral transport model we investigate the diurnal cycle of  $P_{\text{net}}$  in a small pre-alpine eutrophic lake. Here we report, for the first time, the diurnal cycle of  $P_{\text{net}}$  rates and its effect on the observed diurnal cycle of  $\text{CH}_4$  concentrations and its  $\delta^{13}\text{C}_{\text{CH}_4}$  in the SML over two days during the stratified season. We also investigate the diurnal cycle the different inputs of the  $\text{CH}_4$  concentrations in the SML. Our study highlights the need to include night in-situ measurements to estimate OMP rates and its contribution to  $\text{CH}_4$  emissions from freshwaters ecosystems on a temporal scale.

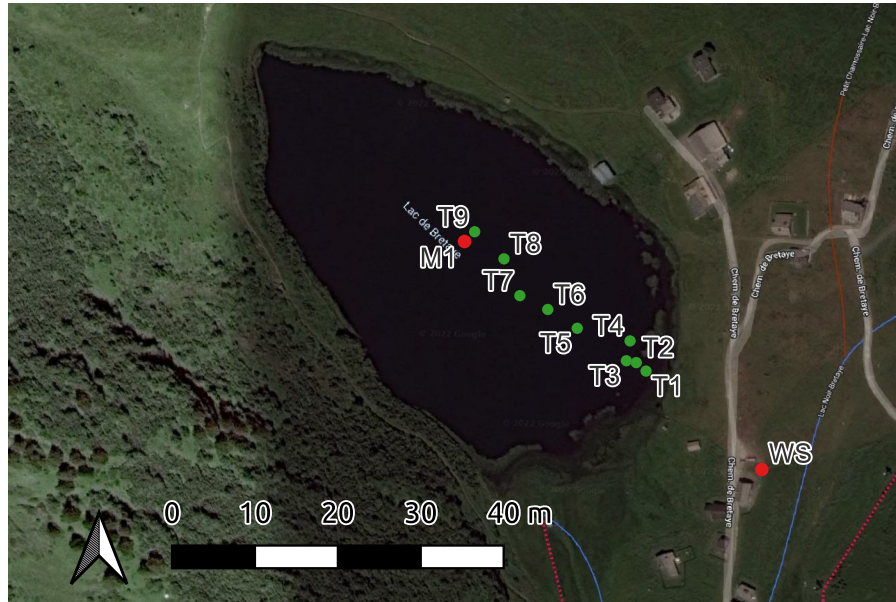
## 4.2 Methods

### 4.2.1 Study site

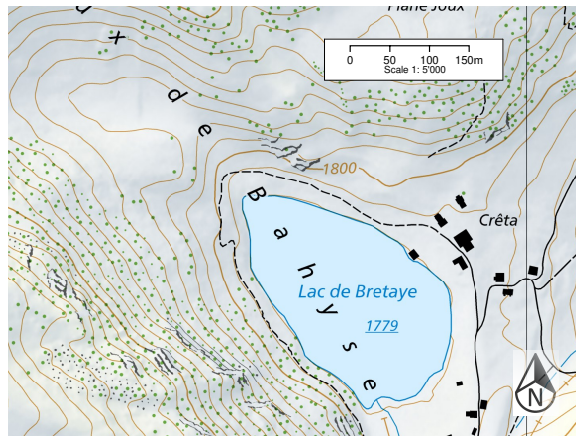
Lac de Bretaye is small pre-alpine lake located at 1785 m.a.s.l in the Swiss Alps (46.326°N, 7.072°E, Canton Vaud, Switzerland). Lac de Bretaye is a eutrophic lake, with no inflow and outflow, a maximum depth of ~9 m and a surface area of ~4 ha. Lac de Bretaye is surrounded by meadows that are used as pastures for animal grazing except for the south side that is covered mainly by *Alnus viridis* (Thöle *et al.* 2016) (Fig. 4.1c). The lake is located in a cirque with high steep slopes on north and west side of the lake (Fig. 4.1b). Abundant macrophytes are found in the north, south and west side of the lake (Fig. 4.1c).

### 4.2.2 Limnological measurements

The sampling campaign was conducted between the 5<sup>th</sup> to 9<sup>th</sup> July 2020 where Secchi disk depth (SD) and water column profiles were performed at the deepest point of Lac de Bretaye



(a) Sampling locations



(b) Topographic map



(c) Drone photography

Figure 4.1. **a** Map of Lac de Bretaye. Location of transect sampling points (T1-T9), the deepest point of the lake (M1) and weather station (WS). **b** Topographic map around Lac de Bretaye © swisstopo. **c** Drone photography over the lake on July 2019.

(M1, Fig. 4.1). The water column profiles were conducted with a CTD profiler (Conductivity-Temperature-Depth, Seabird SBEplus19) equipped with conductivity, temperature, oxygen, PAR, pH, chlorophyll-*a* and turbidity sensors. At M1 a mooring was installed during the entire sampling campaign. Dissolved O<sub>2</sub> probes (Optode, miniDOT, Precision Measurements Engineering, range=0-150% saturation, accuracy= $\pm 10 \text{ mmol m}^{-3}$ ) were installed at 0, 5 and 8 m recording every 1 min. Temperature loggers (Vemco Minilog-II-T loggers, Canada) were installed at 3, 4, 6, 7, 9 and 10 m measuring every 1 min. Temperature/light loggers (Hobo Pendant Temperature/Light Data Logger, Bourne, Ma, USA) were deployed at 4, 6, 8 and 10 m measuring every minute and a temperature/pressure logger (Levellogger Edge M100, Solinst, Canada) was installed at the bottom of the lake.

### 4.2.3 Meteorological data

Shortwave radiation, air temperature, air pressure, water vapor, wind speed and direction were measured every 10 min with a weather station (Atmos41, METER Group, USA) installed at 46.325°N, 7.074°E (WS, Fig. 4.1a). Additionally, a portable weather station (Kestrel 3000) was deployed in the center of the lake when diffusive CH<sub>4</sub> emissions were measured.

### 4.2.4 Water CH<sub>4</sub> concentrations and its isotopic signature

CH<sub>4</sub> concentrations and carbon stable isotopic signature of CH<sub>4</sub> ( $\delta^{13}\text{C}_{\text{CH}_4}$ ) profile were conducted at M1 on July 5<sup>th</sup> with 1 m vertical resolution. Two 24 hours campaign were performed at M1 where measurements were performed every four hours. The first 24h campaign started at July 5<sup>th</sup> at 18:00 CET and ended July 6<sup>th</sup> at 23:00 CET. The second was conducted from July 7<sup>th</sup> at 18:45 CET to July 8<sup>th</sup> at 19:00 CET. Additionally, a longitudinal transect composed of 9 stations was performed on July 7<sup>th</sup> from the shore to M1 (Fig. 4.1).

For the CH<sub>4</sub> concentrations and  $\delta^{13}\text{C}_{\text{CH}_4}$  water column profile, the water samples were taken with a 5-L Niskin bottle and the gently transferred into a 1 L glass bottle (Duran GmbH, Mainz, Germany), while for the transect, the water samples were taken directly with the glass bottle (Duran GmbH, Mainz, Germany). CH<sub>4</sub> and  $\delta^{13}\text{C}_{\text{CH}_4}$  were measured using the headspace method following Donis *et al.* 2017. A Cavity Ring-Down Spectrometer analyzer (Picarro G220-i, Santa Clara, CA, USA) was used to measure the CH<sub>4</sub> concentration and its

stable isotopic ratio in the gas phase. Water  $\text{CH}_4$  concentrations were back calculated following Wiesenburg & Guinasso 1979 accounting for the headspace/water ratio, air concentration and water temperature in the bottle.

#### 4.2.5 Diffusive $\text{CH}_4$ emissions

During the 24h campaigns, at each measuring point diffusive  $\text{CH}_4$  emissions ( $F_a$ ) were measured three times at station M1. At each station along the transect triplicates were also performed.  $F_a$  was measured using a floating chamber attached to a portable GHG analyzer (UGGA, Los Gatos Research, Inc.) (see McGinnis *et al.* 2015 for further details). The chamber was deployed from the boat and allowed to freely drift to minimize artificial turbulence disturbance. Fluxes were obtained by the slope of the  $\text{CH}_4$  concentration curve over the first  $\sim 5$  min when the curve was approximately linear ( $R^2 > 0.97$ ).

The mass transfer coefficient for  $\text{CH}_4$  ( $k_{\text{CH}_4}$ ) was estimated from the chamber measurements following:

$$F_a = k_{\text{CH}_4} (C_w - H_{\text{cp}} p\text{CH}_4); \quad [\text{mmol m}^{-2} \text{d}^{-1}] \quad (4.1)$$

where  $H_{\text{cp}}$  is the Henry's constant of  $\text{CH}_4$  at in situ temperature obtained from Sander 2015.  $C_w$  and  $p\text{CH}_4$  are the surface  $\text{CH}_4$  concentration and the atmospheric partial pressure of  $\text{CH}_4$ , respectively.

#### 4.2.6 Vertical diffusive flux to/from the SML

Vertical diffusive flux just below the SML was estimated using Fick's First Law as:

$$F_z = -K_z \frac{\partial C}{\partial z}; \quad [\text{mmol m}^{-2} \text{d}^{-1}] \quad (4.2)$$

where the vertical concentration gradient ( $\frac{\partial C}{\partial z}$ ) was estimated from the water column profile just below the SML. The turbulent diffusivity ( $K_z$ ) was calculated as the log-average of 13 microstructure profiles measured with a self-contained autonomous microstructure profiler

(SCAMP, PME, Inc.) considering:

$$K_z = \gamma_{mix} \frac{\epsilon}{N^2}; \quad [\text{m}^2 \text{d}^{-1}] \quad (4.3)$$

where the dissipation rate  $\epsilon$  and  $N^2$  were resolved after Kreling *et al.* 2014 and  $\gamma_{mix}$  assumed 0.15 (Wüest & Lorke 2003).

#### 4.2.7 Mass balance in the SML

The net production rate ( $P_{\text{net}}$ ) in the oxic SML was estimated using a full-scale mass balance every 4 hours during the two 24h sampling campaigns following Donis *et al.* 2017 ( $P_{\text{net,fs}}$ , Eq. 4.4). Moreover, a lateral transport model proposed in Chapter 2 ( $P_{\text{net,lt}}$ , Eq. 4.5, similar to Peeters *et al.* 2019) was used to estimate  $P_{\text{net}}$  rates fitting the simulated  $\text{CH}_4$  concentration to the measured  $\text{CH}_4$  concentrations along the transect using Eq. 4.5.

$$\frac{\partial C \forall_{\text{SML}}}{\partial t}(t) = A_s F_s - A_a F_a(t) + A_z F_z + R_{\text{dis}} \forall_{\text{SML}} + P_{\text{net,fs}}(t) \forall_{\text{SML}}; \quad [\text{mol d}^{-1}] \quad (4.4)$$

We consider a constant littoral sediment flux ( $F_s$ ) and bubble dissolution rate ( $R_{\text{dis}}$ ).  $R_{\text{dis}}$  was determined as the same rate obtained in Chapter 2 for July 2019 for the same lake. For the full-scale mass balance, we consider a constant hypolimnetic flux ( $F_z$ , Eq. 4.2) while for the lateral transport model we consider that  $\frac{\partial C}{\partial z} \sim \frac{C_{\text{hyp}} - C}{\Delta z}$  where  $C_{\text{hyp}}$  is the concentration 1 m below the bottom of the SML and  $\Delta z = 1$  m.

$$\begin{aligned} \frac{\partial C}{\partial t} = & K_H \frac{1}{H(r)r} \frac{\partial}{\partial r} \left( H(r)r \frac{\partial C(r)}{\partial r} \right) + \frac{1}{H(r)} K_z \frac{C_{\text{hyp}} - C(r)}{\Delta z} - \frac{\bar{k}_{\text{CH}_4}}{H(r)} (C(r) - H_{\text{cp}} p\text{CH}_4) \\ & + \frac{F_s}{H(r)} + R_{\text{dis}}(r) + P_{\text{net,lt}}; \quad [\text{mol m}^{-3} \text{d}^{-1}] \end{aligned} \quad (4.5)$$

For each CTD, the seasonal SML depth ( $H_{\text{SML}}$ ) was defined when  $\partial T / \partial z$  was smaller than  $-1^\circ \text{C m}^{-1}$  (Read *et al.* 2011) and assumed constant during the entire sampling campaign. The SML depth for the lateral transport model ( $H(r)$ ) was assumed equal to  $H_{\text{SML}}$  in the pelagic zone and decrease linearly to zero in the littoral region. The surface area ( $A_a$ ), the sediment area ( $A_s$ ), the planar area at the bottom of the SML ( $A_p$ ) and the SML water volume ( $V_{\text{SML}}$ ) were obtained from Chapter 2. The horizontal dispersion coefficient ( $K_h$ ) was estimated

following Peeters & Hofmann 2015. The average mass transfer coefficient ( $\bar{k}_{\text{CH}_4}$ ) was obtained from Eq. 4.1. A summary of the inputs values is shown in Table 4.1. Monte Carlo simulation were performed following Chapter 2 to calculate the uncertainty of the model.

#### 4.2.8 Sources contribution to CH<sub>4</sub> diffusive fluxes to the atmosphere

Following Chapter 2, the contribution of each source (SC) to the diffusive surface flux was estimated as:

$$\text{SC}_i = \frac{S_i}{\sum_j S_j} \cdot 100; \quad [\%] \quad (4.6)$$

where  $S_i$  is each source term ( $\text{mol d}^{-1}$ ) such as: sediment flux ( $F_s A_s$ ), bubble dissolution ( $R_{\text{dis}} \forall_{\text{SML}}$ ), net production ( $P_{\text{net}} \forall_{\text{SML}}$ ) and vertical diffusive fluxes ( $F_z A_z$ ). If  $S_i \leq 0$  then  $S_i = 0$  where  $i$  is each source term.

### 4.3 Results

#### 4.3.1 Study site general features

The average Secchi disk depth during the campaign was  $3.24 \pm 0.25$  m. The seasonal surface mixed layer (SML) depth ( $H_{\text{SML}}$ ) define by the temperature profile was  $\sim 3.10$  m. The SML remained oxic during the entire sampling period (Fig. S.C.6).  $A_a$ ,  $A_s$ ,  $A_p$  and  $\forall_{\text{SML}}$  were 45 500, 16 100 and 30 080  $\text{m}^2$ , and 112 350  $\text{m}^3$ , respectively. All the following results are presented in local time.

#### 4.3.2 Meteorological data

The air temperature ( $T_a$ ) ranged between 3.6 - 19 °C with an average value of  $11 \pm 3$  °C (Fig. 4.5b). During the afternoon of July 6<sup>th</sup> a cold front decreased the air temperature and the wind speed increased over Lac de Bretaye (Fig. 4.5b). The average wind speed at 10 m ( $U_{10}$ ) on July 7<sup>th</sup> was  $1.74 \text{ m s}^{-1}$ . After the cold front, the average temperature increased and wind speed decreased during July 8<sup>th</sup> ( $T_a=12.5$  °C and  $U_{10}=0.94 \text{ m s}^{-1}$ ). The cold front also brought cloudiness producing lower and highly variable short wave solar radiation compared to the rest of the days. Significant cloud cover also occurred on the afternoon of July 8<sup>th</sup> (Fig. 4.5a).

Table 4.1. Measurements, modelled derived parameters and data sources analyzed during the sampling campaign.

Description	Symbol	Unit	Value	Source
Surface Area	$A_a$	$\text{m}^2$	45500	Chapter 2
Sediment Area	$A_s$	$\text{m}^2$	16100	Chapter 2
Planar Area at base of SML	$A_p$	$\text{m}^2$	30080	Chapter 2
SML Volume	$V_{\text{SML}}$	$\text{m}^3$	112350	Chapter 2
SML depth	$H_{\text{SML}}$	$\text{m}$	3.10	This study
Transect average mass transfer coefficient	$\bar{k}_{\text{CH}_4}$	$\text{m d}^{-1}$	$1.51 \pm 0.51$	This study
Horizontal dispersion	$K_H$	$\text{m}^2 \text{d}^{-1}$	2034	Chapter 2
CH <sub>4</sub> concentration 1m below the bottom of the SML	$C_{\text{hyp}}$	$\text{mmol m}^{-3}$	1.59	This study
Surface CH <sub>4</sub> concentration	$C$	$\text{mmol m}^{-3}$	Fig. 4.2a	This study
Surface CH <sub>4</sub>	$\delta^{13}\text{C}_{\text{CH}_4}$	$\text{‰}$	Fig. 4.2a	This study
Water column CH <sub>4</sub>	$C$	$\text{mmol m}^{-3}$	Fig. S.C.1	This study
Water column $\delta^{13}\text{C}_{\text{CH}_4}$	$\delta^{13}\text{C}_{\text{CH}_4}$	$\text{‰}$	Fig. S.C.1	This study
Littoral sediment Flux	$F_s$	$\text{mmol m}^{-2} \text{d}^{-1}$	$3.0 \pm 6.7$	This study
Diffusive CH <sub>4</sub> emissions	$F_a$	$\text{mmol m}^{-2} \text{d}^{-1}$	Fig. 4.2b	This study
Vertical diffusive flux	$F_z$	$\text{mmol m}^{-2} \text{d}^{-1}$	$0.02 \pm 0.01$	This study
Bubble dissolution at SML	$R_{\text{dis}}$	$\mu\text{mol m}^{-3} \text{d}^{-1}$	$0.04 \pm 0.01$	Chapter 2
Net CH <sub>4</sub> Production	$P_{\text{net}}$	$\mu\text{mol m}^{-3} \text{d}^{-1}$	Fig. 4.5	This study

### 4.3.3 Vertical profiles

The average water temperature in the SML was about 18°C whereas at the bottom was about 9°C (Figs. S.C.1a and S.C.1b). Surface water remained oxic during the day and night whereas below 6 m, the water column became anoxic (Figs. S.C.1a and S.C.1b). Chlorophyll-a (Chl<sub>a</sub>) was observed along the entire water column with a peak at the base of the SML and at the bottom of the lake. During the day, lower Chl<sub>a</sub> concentrations ( $1.73 \pm 0.07 \text{ mg m}^{-3}$ , Fig. S.C.1a) were measured in the SML compare to the night period ( $4.09 \pm 0.56 \text{ mg m}^{-3}$ , Fig. S.C.1b). This difference could be explained due to transport of phytoplankton from the thermocline caused by deep convection during the night or the influence of non-photochemical quenching in our measurements during the day (Harrison *et al.* 2018).



From 0 - 4 m, the  $\text{CH}_4$  concentrations remain fairly constant ( $1.39 \pm 0.32 \text{ mmol/m}^3$ ) and then rapidly increased to  $141.17 \text{ mmol/m}^3$  at the bottom of the lake (Fig. 4.4a). The average isotopic signature ( $\delta^{13}\text{C}_{\text{CH}_4}$ ) in the SML was about  $-49.8 \text{ ‰}$ , whereas in the oxic hypolimnion  $\delta^{13}\text{C}_{\text{CH}_4}$  reached up to  $-25 \text{ ‰}$  at 6 m to then decreased to  $-64 \text{ ‰}$  at the anoxic bottom of the lake.

#### 4.3.4 Surface $\text{CH}_4$ concentrations and $\delta^{13}\text{C}_{\text{CH}_4}$ signature

The  $\text{CH}_4$  concentrations in the SML varied between  $0.8 - 1.4 \text{ mmol/m}^3$  with an average value about  $1.1 \pm 0.1 \text{ mmol/m}^3$  during the three days of measurements (Fig. 4.2a). A daily cycle was observed, where  $\text{CH}_4$  concentrations reached up to  $1.2 \text{ mmol/m}^3$  during the day followed by a decrease towards the night where  $\text{CH}_4$  concentrations decreased to about  $1.0 \text{ mmol/m}^3$  (Fig. 4.4). The average  $\text{CH}_4$  concentration along the transect was about  $1.23 \pm 0.01 \text{ mmol/m}^3$  with values near the shore 16 % higher than in the center (Fig. 4.3).

The average isotopic signature  $\delta^{13}\text{C}_{\text{CH}_4}$  in the SML were  $-52.9 \pm 1.1 \text{ ‰}$  (Fig. 4.2a). Consistent  $\delta^{13}\text{C}_{\text{CH}_4}$  of about  $-53 \text{ ‰}$  was observed from 03:00 to 18:00, then enriched  $\text{CH}_4$  was observed towards 24:00 reaching up to  $\sim -51 \text{ ‰}$  (Fig. 4.4a). The average  $\delta^{13}\text{C}_{\text{CH}_4}$  along the transect was about  $-53.0 \pm 0.5 \text{ ‰}$  without a clear difference between near the shore versus the center of the lake (Fig. S.C.3).

#### 4.3.5 Diffusive $\text{CH}_4$ emissions to the atmosphere

Diffusive  $\text{CH}_4$  emissions ( $F_a$ ) at the air-water interface (AWI) ranged between  $0.43 - 3.28 \text{ mmol/m}^2/\text{d}$  with an average value of  $1.52 \pm 0.85 \text{ mmol/m}^2/\text{d}$  (Fig. 4.2b). Between 00:00 to 6:00  $F_a$  was about  $1.14 \pm 0.75 \text{ mmol/m}^2/\text{d}$ , then increased up to about  $2.81 \pm 0.39 \text{ mmol/m}^2/\text{d}$  between 14:00 to 15:00, then finally decreased to about  $0.79 \pm 0.31 \text{ mmol/m}^2/\text{d}$  from 19:00 to 00:00. The average  $F_a$  along the transect was  $1.99 \pm 0.62 \text{ mmol/m}^2/\text{d}$  with an average mass transfer coefficient ( $\bar{k}_{\text{CH}_4}$ ) value of  $1.51 \pm 0.51 \text{ m d}^{-1}$  and during the entire campaign was  $1.29 \pm 0.68 \text{ m d}^{-1}$ .

The normalized mass transfer coefficient ( $k_{600}$ ) ranged  $0.41 - 3.06 \text{ m d}^{-1}$  (Fig. 4.4c). We observed a daily cycle of  $k_{600}$  where the maximum values were measured around 14:00



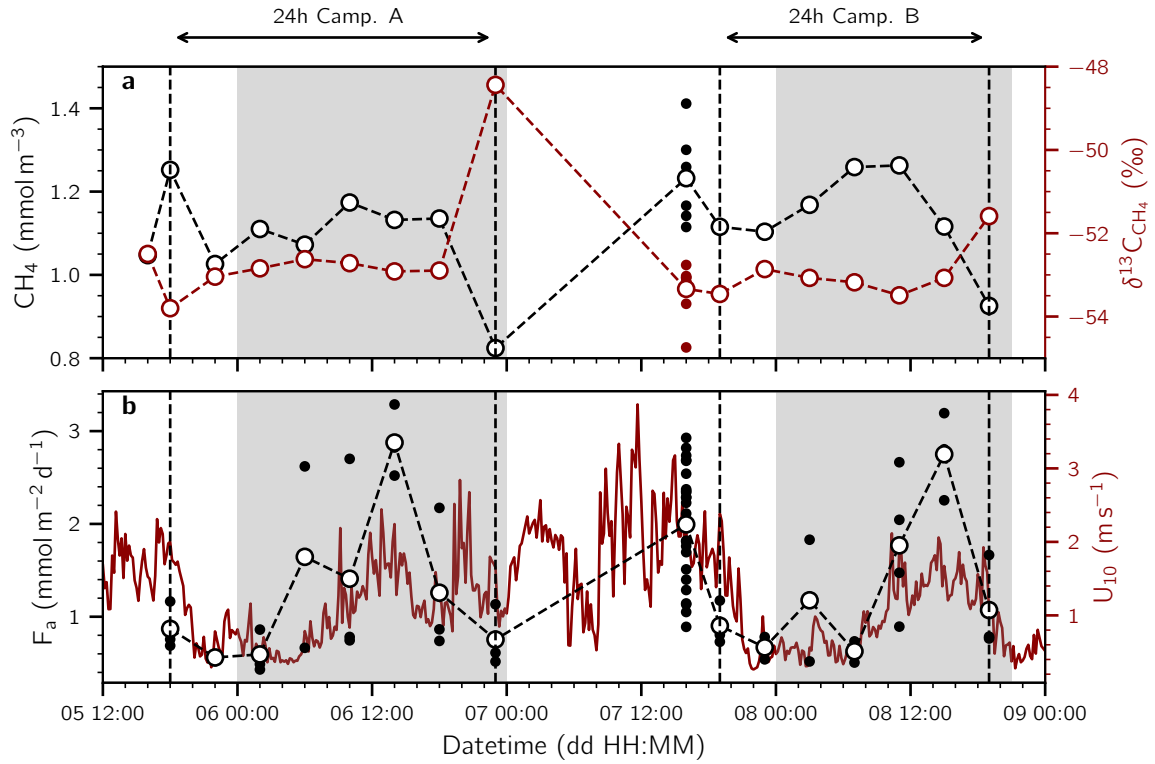


Figure 4.2. **a** Surface  $\text{CH}_4$  concentrations and its  $\delta^{13}\text{C}_{\text{CH}_4}$  isotopic signature. **b** Diffusive  $\text{CH}_4$  fluxes to the atmosphere and the wind speed at 10 m ( $U_{10}$ ). The white dots represent the average value while the filled dot are each measurement.

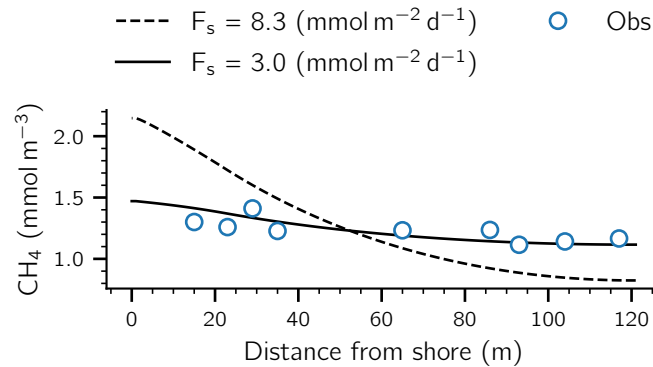


Figure 4.3. Surface  $\text{CH}_4$  concentrations along the transect. Lines represent the  $\text{CH}_4$  concentration simulated using the lateral transport model and dots are the measured values. For the dash line and the continuous line, 8.3 and 3.0  $\text{mmol/m}^2/\text{d}$  was used as a  $\text{CH}_4$  flux from littoral sediment ( $F_s$ ) respectively.

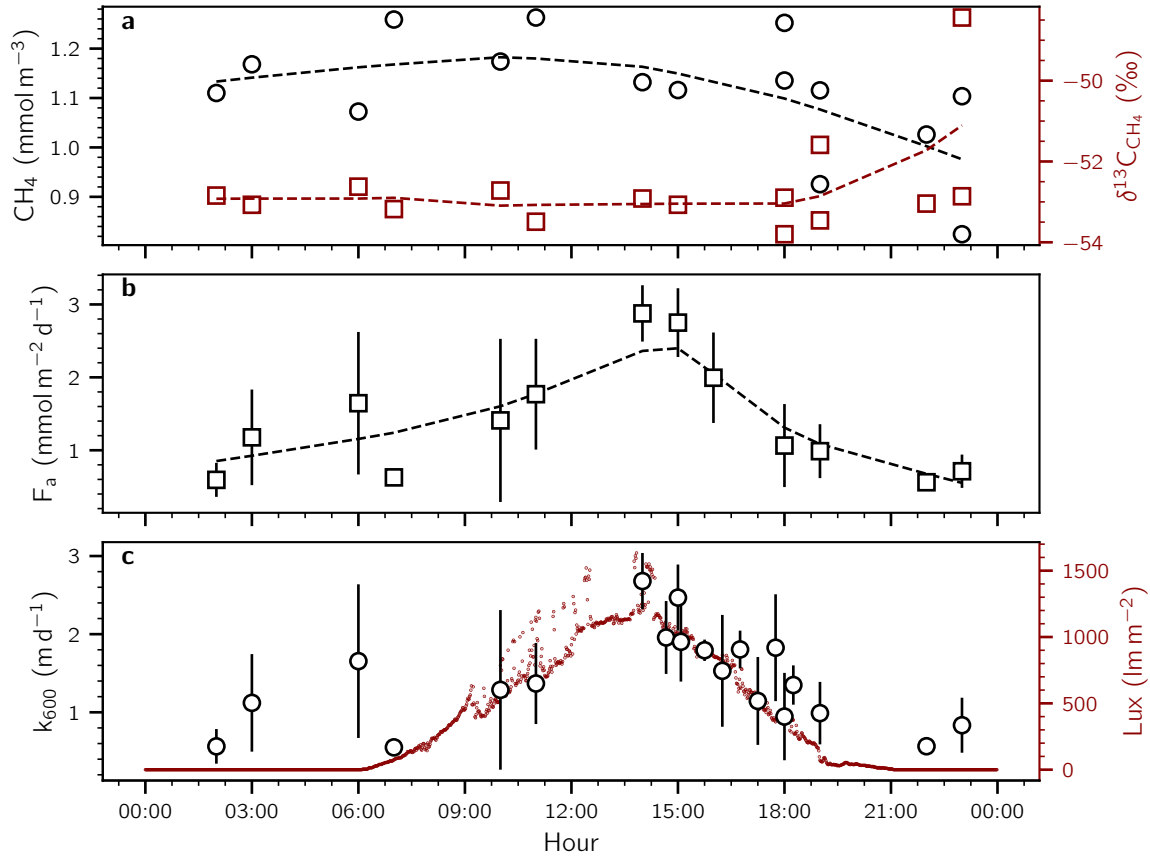


Figure 4.4. Daily cycles during the 24h campaigns for **a** surface  $\text{CH}_4$  concentrations and  $\delta^{13}\text{C}_{\text{CH}_4}$  isotopic signature and **b** diffusive  $\text{CH}_4$  fluxes to the atmosphere ( $F_a$ ) and **c** the normalized mass transfer coefficient ( $k_{600}$ ) and light intensity at 3 m. The error bars represent the standard deviation of three surface diffusive fluxes performed each time. The dashed line is the smooth data obtained with locally weighted running line smoother (LOESS method).

with a clear decrease towards the night. The average  $k_{600}$  during the sampling campaign was  $1.35 \text{ m d}^{-1}$ .

#### 4.3.6 Vertical diffusive $\text{CH}_4$ flux through the bottom the SML

The vertical diffusive fluxes through the SML is driven by the vertical turbulent diffusivity ( $K_z$ ) and the concentration gradient just below the bottom of the SML.  $K_z$  ranged between  $0.26 - 4.30 \times 10^{-6} \text{ m}^2 \text{s}^{-1}$  and at the bottom of the SML was about  $6.47 \times 10^{-6} \text{ m}^2 \text{s}^{-1}$  (Fig. S.C.1c). Using the gradient between the  $\text{CH}_4$  concentration measured at 3 and 4 m (Fig. S.C.1d), the flux through the bottom of the SML ( $F_z$ ) was  $0.02 \pm 0.01 \text{ mmol/m}^2/\text{d}$  and assumed constant during the entire sampling campaign for the full-scale mass balance.

### 4.3.7 Mass balance in the SML

The net production rates ( $P_{\text{net}} = \text{OMP} - \text{MOx}$ ) were obtained using the full-scaled mass balance ( $P_{\text{net,fs}}$ ) and the lateral transport model ( $P_{\text{net,lt}}$ ). The littoral sediment flux ( $8.3 \text{ mmol/m}^2/\text{d}$ ) and the bubble dissolution rates obtained ( $0.04 \mu\text{mol/m}^3/\text{d}$ ) in July 2019 from Chapter 2 were used on both models to calculate  $P_{\text{net}}$  (Fig. S.C.2). A large discrepancy between the model and the measured  $\text{CH}_4$  concentration near the shore was obtained using the measured  $F_s$  from Chapter 2 (Fig. 4.3). Therefore, we use the lateral transport model to estimate  $P_{\text{net}}$  and  $F_{\text{net}}$  that best fits the measured and simulated  $\text{CH}_4$  concentrations (Fig. 4.3). Following this procedure we obtained that  $F_s = 3.0 \text{ mmol/m}^2/\text{d}$  and  $P_{\text{net}} = -99.7 \pm 390.0 \mu\text{mol/m}^3/\text{d}$ . Using the estimated  $F_s$  we obtained with the lateral transport model, the  $P_{\text{net,fs}}$  ranged between  $-1636$  to  $750 \mu\text{mol/m}^3/\text{d}$  with an average value of  $-115 \mu\text{mol/m}^3/\text{d}$  (Fig. 4.5a). On average  $P_{\text{net}}$  rates were about  $534 \mu\text{mol/m}^3/\text{d}$  from 00:00 to 6:00 to then increased to  $575 \mu\text{mol/m}^3/\text{d}$  at 10:00 to then decreased to  $-994 \mu\text{mol/m}^3/\text{d}$  at 23:00 (Fig. 4.6). The average  $P_{\text{net}}$  during the day (between 7:00 to 20:00) was  $37 \pm 1119 \mu\text{mol/m}^3/\text{d}$  and  $-485 \pm 1306 \mu\text{mol/m}^3/\text{d}$  during the night (between 21:00 to 6:00).

### 4.3.8 Sources contribution to diffusive $\text{CH}_4$ emissions

We calculated the daily cycle of the contribution of each  $\text{CH}_4$  source to  $F_a$  (Fig. 4.7). The major contributor was the littoral sediment flux ( $F_s$ ) with an average value about  $69 \pm 19 \%$ . During the night (from 21:00 to 6:00)  $F_s$  contribution was  $76 \pm 18 \%$  and  $64 \pm 19 \%$  during the day (from 7:00 to 20:00). On the other hand,  $P_{\text{net}}$  contribution was about  $30 \pm 21 \%$  during the day and  $16 \pm 20 \%$  during the night, with an average value of  $24 \pm 21 \%$ . The contribution of the bubble dissolution and vertical flux at the bottom of the SML was negligible, with an average value of  $6.4 \pm 0.1 \%$  and  $0.5 \pm 0.1 \%$  respectively.

## 4.4 Discussion

On average, we observed that methane oxidation ( $\text{MOx}$ ) was predominant over OMP in the surface mixed layer of Lac de Bretaye ( $P_{\text{net}} < 0$ ). However, we observed that  $P_{\text{net}}$  rates tend towards a diurnal cycle with positive  $P_{\text{net}}$  values during the day that begin to decrease in the afternoon until they become negative around 18:00 reaching its minimum value around midnight

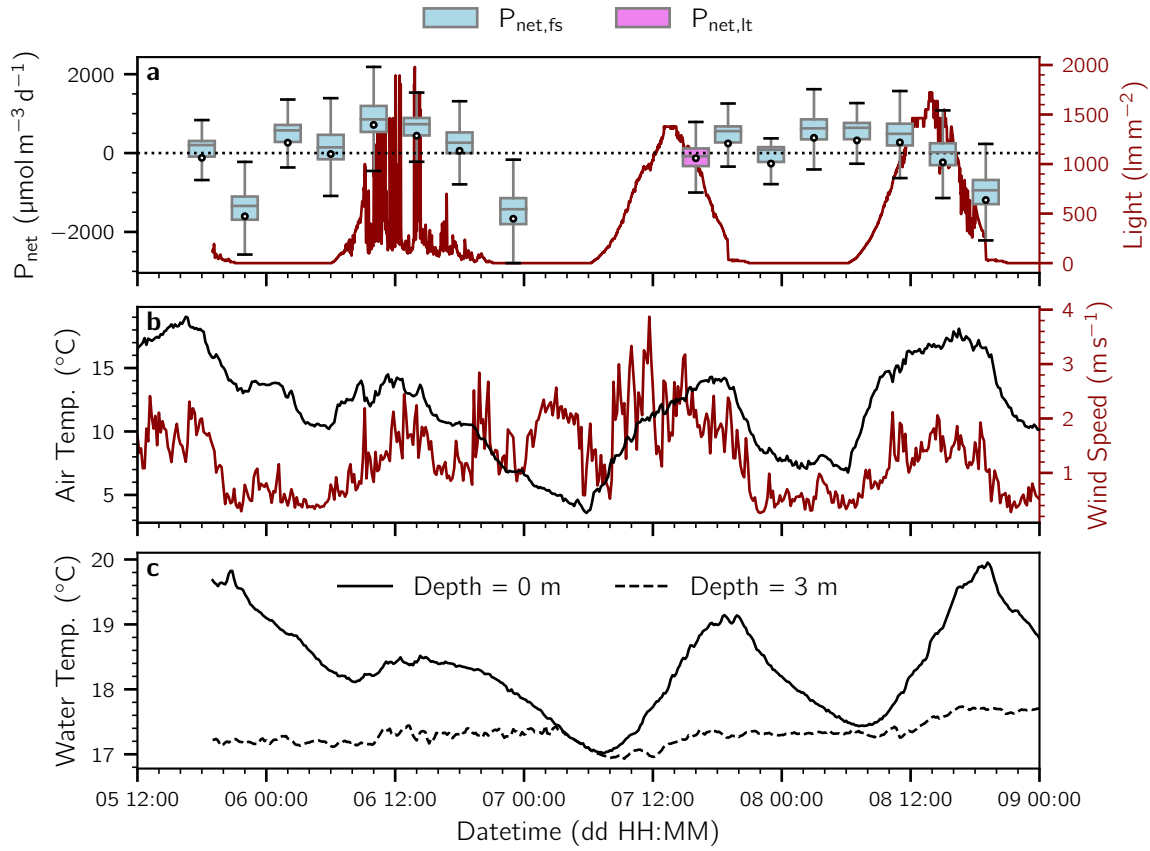


Figure 4.5. **a**  $P_{\text{net}}$  estimation using the full-scale mass balance ( $P_{\text{net,fs}}$ , light blue box) and the lateral transport model ( $P_{\text{net,lt}}$ , violet box) using  $F_s=3.0 \text{ mmol/m}^2/\text{d}$ . Each box shows the first and third quartiles with the median (line), whiskers extend to the most extreme data point within 1.5 times the interquartile range from the box. The white dot represents the average of the distribution. **b** Air temperature and wind speed measured with the Atmos 41 weather station. **c** Water temperature measured at 0 and 3 m depth at M1.

(Fig. 4.6). Here, we first investigate if  $P_{\text{net}}$  rates are an artefact of the methodology, then we analyze the impact of our model assumptions on our calculations and finally, we explore which are the different drivers to explain  $P_{\text{net}}$  temporal dynamics.

#### 4.4.1 Is $P_{\text{net}}$ an artefact of the methodology?

The diffusive  $\text{CH}_4$  emissions to the atmosphere ( $F_a$ ) and the change of mass in the SML ( $\frac{\partial CV_{\text{SML}}}{\partial t}$ ) were the only two variable parameters to estimate  $P_{\text{net}}$  with the full-scale mass balance (Eq. 4.4).  $F_a$  depends on the surface  $\text{CH}_4$  concentration and the mass transect coefficient ( $k_{\text{CH}_4}$ ) (Eq. 4.1). Strong correlations between  $k_{600}$  and the measured  $F_a$  indicate that the changes in  $F_a$  were mainly driven by  $k_{600}$  and not by the surface  $\text{CH}_4$  concentration changes (Fig. S.C.4). We

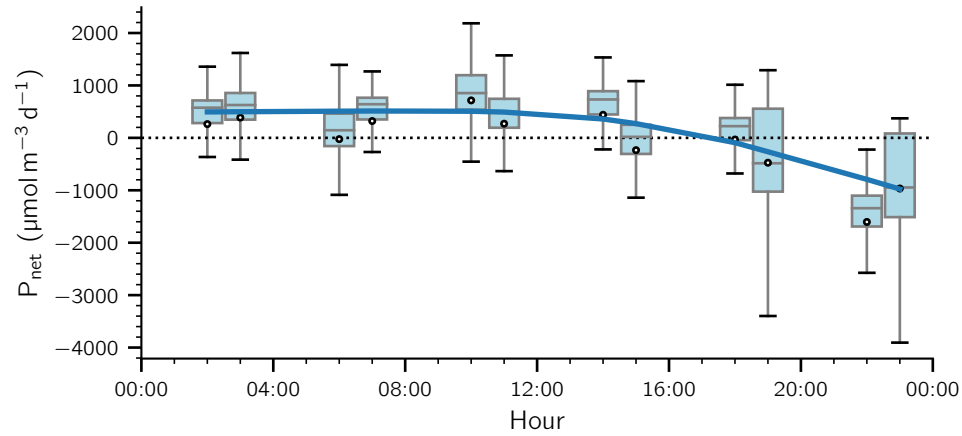


Figure 4.6. Daily cycle of  $P_{\text{net}}$  rates obtained with the full-scale mass balance model during the two 24h campaigns. Each box shows the first and third quartiles with the median (line), whiskers extend to the most extreme data point within 1.5 times the interquartile range from the box. The white dot represents the average of the distribution. The solid blue line is the smooth data obtained with locally weighted running line smoother (LOESS method).

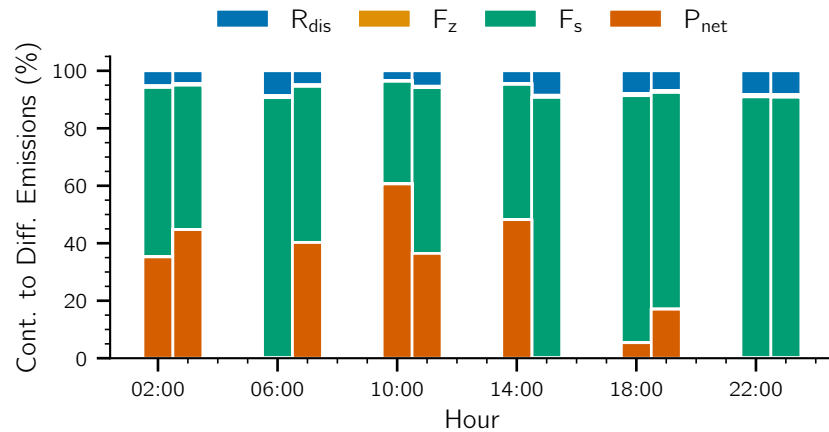


Figure 4.7. Daily cycle of contribution from bubble dissolution ( $R_{\text{dis}}$ ), littoral sediment flux ( $F_{\text{s}}$ ), vertical flux from hypolimnion ( $F_{\text{z}}$ ) and net production ( $P_{\text{net}}$ ) in the SML to the diffusive  $\text{CH}_4$  emissions ( $F_{\text{a}}$ )

observed that  $k_{600}$  has a daily cycle and correlates much higher with solar radiation ( $r^2=0.43$ ) and in-situ light ( $r^2=0.54$ ) (Figs. S.C.4c, S.C.4d and 4.4c) rather than  $U_{10}$  ( $r^2 = 0.05$ , Fig. S.C.4b). We proposed that this could be because  $k_{600}$  is enhanced by microbubbles (McGinnis *et al.* 2015) produced by photosynthesis in the water column (Melack & Kilham 1974; Koschorreck *et al.* 2017), by surface heating (MacIntyre *et al.* 2021) or both. Nevertheless, weak correlation between  $k_{600}$  and  $P_{\text{net}}$  indicates that  $k_{600}$  is not the main driver of  $P_{\text{net}}$  (Fig. 4.8) and therefore derived  $P_{\text{net}}$  rates are mainly driven by  $\frac{\partial C_{\text{SML}}^V}{\partial t}$ .

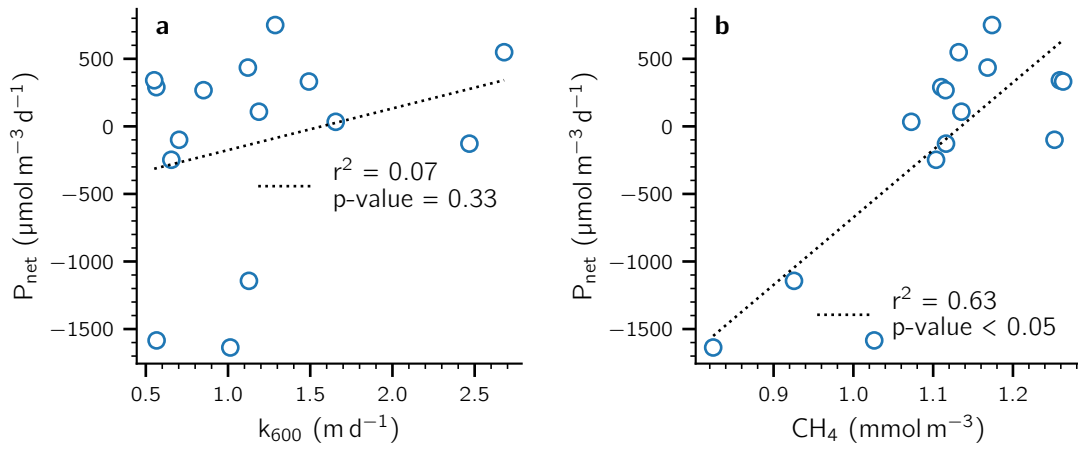


Figure 4.8.  $P_{\text{net}}$  correlations with **a** mass transfer coefficient ( $k_{600}$ ) and **b** surface  $\text{CH}_4$  concentrations.

#### 4.4.2 Can we explain $\frac{\partial C_{\text{SML}}^V}{\partial t}$ if we do not consider $P_{\text{net}}$ ?

Changes in  $F_a$  control how fast  $\text{CH}_4$  in the SML will be released to the atmosphere. However, the rapid changes of  $\text{CH}_4$  mass cannot be explained by  $F_a$  because, considering  $k_{\text{CH}_4} = 1 \text{ m d}^{-1}$  and no other  $\text{CH}_4$  sources or sinks occurring in the SML, it would take about 1.5 days to observe a 50% decrease on the surface  $\text{CH}_4$  concentration. Moreover, under the same condition,  $F_a$  would only decrease the surface  $\text{CH}_4$  concentration by  $\sim 2\%$  in an hourly scale. Therefore,  $F_a$  does not drive the rapid changes of mass in the SML.

The other major source that can drive the change of mass in the SML is the diffusive  $\text{CH}_4$  flux from littoral sediments ( $F_s$ ). Since light can reach the littoral sediment, photosynthesis on the top layer of the sediment would potentially decrease  $F_s$  during the day (Damgaard *et al.* 1998; Liikanen *et al.* 2002). Therefore, higher  $\text{CH}_4$  concentrations should be observed due to higher  $F_s$  during the night. In contrast, in Lac de Bretaye we observed an increase of  $\text{CH}_4$  during

the day compare to the night. Moreover, conducting a similar analysis as  $F_a$ , we simulated the temporal change of  $F_s$  increasing the concentration at the shore of the lake by 100 % compared to the initial condition. Without considering any other source/sink of  $CH_4$  in the SML, the changes of  $F_s$  would need more than 10 h to change by 5 % the  $CH_4$  concentration in the center of the lake (Fig. S.C.7). These results indicate that a new source or sink needs to be included in the SML to close the mass balance on an hourly scale.

#### 4.4.3 Modeled sediment flux estimation.

Accurate estimations of  $CH_4$  flux from littoral sediment are difficult to obtain.  $F_s$  based on sediment cores such as benthic chambers and pore water measurements lack spatial coverage in the littoral zone. Due to coarse vertical resolution ( $\sim 1$  cm) of pore water measurements, it might not be able to capture the decrease of  $F_s$  due to oxidation caused by the presence of oxygen at the top of the sediment (Damgaard *et al.* 1998; Liikanen *et al.* 2002). In contrast, the transect data approach estimates the overall contribution from different sources of  $CH_4$  from the littoral zone such as  $CH_4$  production by macrophytes located at the shore of the lake (Hilt *et al.* 2022) and in littoral sediments. However, this method assumes no horizontal advection of  $CH_4$  from other zones, and it could be only applicable to lakes with high horizontal  $CH_4$  gradients.

In Chapter 2,  $F_s$  in Lac de Bretaye ( $8.3 \pm 6.7$  mmol/m<sup>2</sup>/d) was estimated using benthic chambers and pore water measurements in three sediment cores taken in Sept 2018 and July 2019. This average flux, highly influenced by one high measurement of 13.5 mmol/m<sup>2</sup>/d, is one of the highest values ever reported in literature (Huttunen *et al.* 2006; Bastviken *et al.* 2008; Peeters *et al.* 2019). However, using that measured sediment flux in the lateral transport model, we observed a large discrepancy between the measured and model surface  $CH_4$  concentration (Fig. 4.3) (note that  $P_{net}$  was obtained from the best fit the model to the observed surface  $CH_4$  concentrations along the transect). To compensate for the high concentration at the shore due to the high  $F_s$ , the model finds a more negative  $P_{net}$  that underestimates the  $CH_4$  concentration at the deepest point of the lake. Therefore, we resolved Eq. 4.5 using a combination of  $P_{net}$  and  $F_{net}$  that best fit the  $CH_4$  transect concentrations at the surface. This new  $F_s$  estimated in July 2020 (3.0 mmol/m<sup>2</sup>/d) was lower compared to 2018 and 2019. The difference may be associated with more oligotrophic conditions, evidenced by the low concentrations of  $CH_4$  and Chl $a$  in the

SML observed in July 2020 during the day (Table 4.2).

Table 4.2. Summary of main drivers of net production rates ( $P_{\text{net}}$ ) during July 2020 (this study), June and September 2018, and July 2019 (Chapter 2): Light climate ( $LC=2.5SD/H_{\text{SML}}$ ), Secchi depth (SD), average chlorophyll-*a* concentration in the SML (Chl*a*), average  $\text{CH}_4$  concentration and its isotopic signature ( $\delta^{13}\text{C}_{\text{CH}_4}$ ) in the SML, and diffusive  $\text{CH}_4$  flux from littoral sediments ( $F_s$ ).

Date		LC ( $\text{m m}^{-1}$ )	SD (m)	Chl <i>a</i> ( $\text{mg m}^{-3}$ )	$\delta^{13}\text{C}_{\text{CH}_4}$ (‰)	$\text{CH}_4$ ( $\text{mmol/m}^3$ )	$F_s$ ( $\text{mmol/m}^2/\text{d}$ )	$P_{\text{net}}$ ( $\mu\text{mol/m}^3/\text{d}$ )
June 2018	Day	7.02	3.65	3.01	-52.0	$6.7 \pm 2.3$	$8.3 \pm 6.7$	$2313 \pm 1882$
Sept 2018	Day	1.42	2.95	4.08	-38.0	$3.5 \pm 0.5$	$8.3 \pm 6.7$	$-1941 \pm 1266$
July 2019	Day	4.52	4.70	4.05	-48.8	$2.8 \pm 1.6$	$8.3 \pm 6.7$	$687 \pm 1210$
July 2020	Day	2.61	3.24	1.73	-53.0	$1.2 \pm 0.1$	$3.0 \pm 6.7$	$37 \pm 1190$
July 2020	Night	-	-	4.09	-52.1	$1.1 \pm 0.1$	$3.0 \pm 6.7$	$-485 \pm 1306$
July 2020	All campaign	2.61	3.24	3.12	-52.7	$1.1 \pm 0.1$	$3.0 \pm 6.7$	$-169 \pm 1223$

#### 4.4.4 Effect of choosing a constant or variable mixed layer depth on $P_{\text{net}}$ .

Our study considers the seasonal SML depth to define the water volume for the  $\text{CH}_4$  mass balance. We analyzed the impact of choosing a variable local  $H_{\text{SML}}$  ( $P_{\text{net,mod}}$ ) instead of choosing a constant seasonal  $H_{\text{SML}}^*$  ( $P_{\text{net,0}}$ ) on  $P_{\text{net}}$  calculations. For the simulation, we considered a variable  $H_{\text{SML}}$  ranged from 50 to 150 % of  $H_{\text{SML}}^*$  (Fig. 4.9a). In addition, we considered a constant  $F_a = 1.5 \text{ mmol/m}^2/\text{d}$ ,  $R_{\text{dis}} = 0.02 \mu\text{mol/m}^3/\text{d}$  and  $\text{CH}_4$  concentration in the SML  $\text{CH}_4 = 1 \text{ mmol/m}^3$ .  $F_z$  changes were assumed negligible due to expected small changes on the  $\text{CH}_4$  concentration inside the seasonal SML (see discussion below of  $F_z$  when  $H_{\text{SML}} > H_{\text{SML}}^*$ ). When  $H_{\text{SML}} < H_{\text{SML}}^*$ ,  $P_{\text{net,0}}$  would be underestimated when  $P_{\text{net,0}}$  is positive and overestimated when  $P_{\text{net,0}}$  is negative (Fig. 4.9b, case  $F_{\text{net}} = 3 \text{ mmol/m}^3$  up to 300 % underestimation). In contrast, when the local  $H_{\text{SML}}$  is higher than  $H_{\text{SML}}^*$ ,  $P_{\text{net,0}}$  would be overestimated when  $P_{\text{net,0}}$  is positive and underestimated when  $P_{\text{net,0}}$  is negative. Note that at higher  $P_{\text{net,0}}$  rates, the impact of choosing a variable or constant  $H_{\text{SML}}$  is lower. Hence, including the change of  $H_{\text{SML}}$  in our calculations would tend to increase the difference of  $P_{\text{net}}$  during day and night considering  $P_{\text{net}} > 0$  during the day and  $P_{\text{net}} < 0$  during the night.

During our sampling campaigns we observed higher  $P_{\text{net}}$  rates during the day followed by a decrease during the evening (Fig. 4.6). However, between 00:00 to 6:00 on July 8<sup>th</sup>, we did not observe the negative  $P_{\text{net}}$  rates as we had observed during July 6<sup>th</sup> (Fig. 4.5a). To calculate  $P_{\text{net}}$  rates we assumed a constant  $F_z$  calculated from a vertical  $\text{CH}_4$  concentration profile conducted during the day and average  $K_z$  during the sampling campaigns. This assumption is based on small changes on the seasonal  $H_{\text{SML}}$  estimated based on eight CTD profiles conducted



during day and night ( $\text{STD}_{H_{\text{SML}}} = 0.13 \text{ m}$ ). However, during the nights of the 7<sup>th</sup> and 8<sup>th</sup> of July (and not on the 6<sup>th</sup>), surface water temperature was similar to the temperature at 3 m at around 6:00 – 7:00 suggesting that the SML was deeper than the seasonal  $H_{\text{SML}}$  (3.1 m, Figs. S.C.5 and 4.5c). During those nights cold air temperatures produced convection that, enhanced by wind, deepened the SML locally (Figs. S.C.4b and 4.5b). This process increases  $F_z$ , as well as the total contribution of  $F_s$  and  $R_{\text{dis}}$  due to an increase of  $A_{\text{sed}}$  and  $\forall_{\text{SML}}$  respectively. While the latter two sources will be compensated by the increase of  $\forall_{\text{SML}}$  ( $\frac{\partial A_s / \forall_{\text{SML}}}{\partial z} |_{H_{\text{SML}}} \sim 1$ ), the increase of  $F_z$  is independent of bathymetry of the lake. Therefore, deep convection could have transported  $\text{CH}_4$  from below the SML by advection, not accounted by the model, and that in addition of the increase to  $\forall_{\text{SML}}$  (discussion above), would have produced an overestimation of  $P_{\text{net}}$  during the night of July 8<sup>th</sup>.

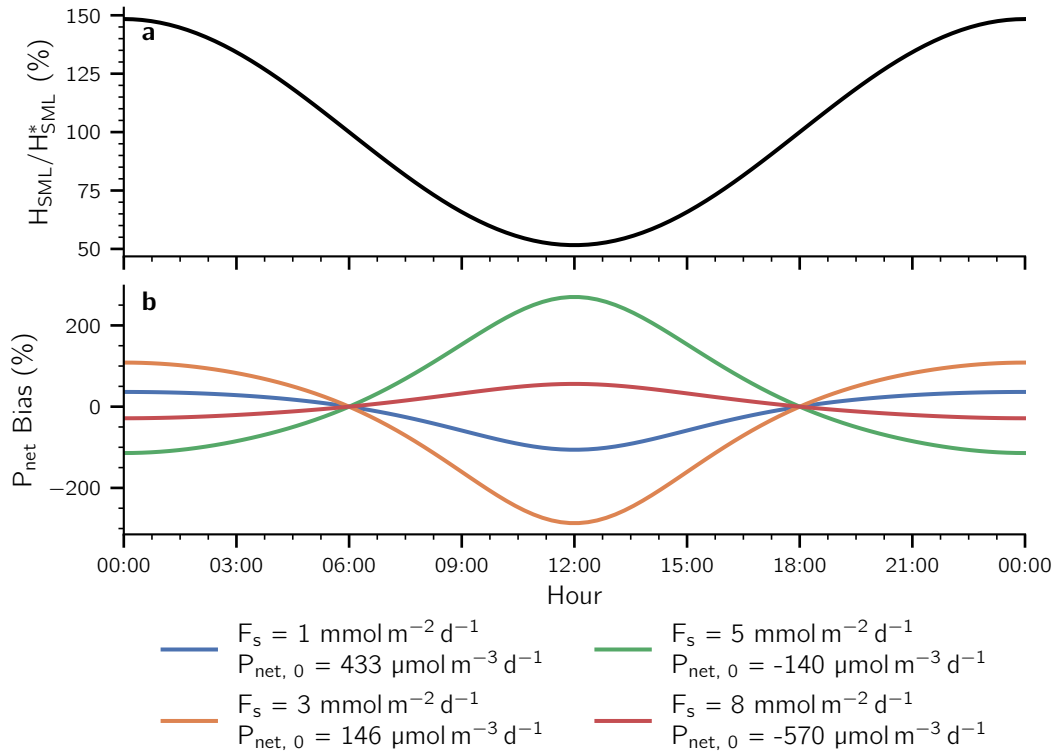


Figure 4.9. Evaluation of change on the surface mixed layer depth ( $H_{\text{SML}}$ ) on  $P_{\text{net}}$  calculations. **a** Simulated ratio between  $H_{\text{SML}}$  and the seasonal SML depth  $H_{\text{SML}}^*$  and surface  $\text{CH}_4$  concentration applied to  $P_{\text{net}}$  simulations. **b**  $P_{\text{net}}$  Bias =  $1 - P_{\text{net,mod}}/P_{\text{net,0}}$  where  $P_{\text{net,mod}}$  and  $P_{\text{net,0}}$  are the net production rate estimated with variable  $H_{\text{net}}$  and constant  $H_{\text{SML}} = 3 \text{ m}$ , respectively.

#### 4.4.5 Drivers of $P_{\text{net}}$ and isotopic analysis in the SML.

$P_{\text{net}}$  rates are the result of OMP and MOx that add and consume  $\text{CH}_4$  respectively ( $P_{\text{net}} = \text{OMP} - \text{MOx}$ ). Higher rates during the day than during the night point out that algae and cyanobacteria could be producing  $\text{CH}_4$  following the light-dark cycle as shown by Bižić *et al.* 2020 and Hartmann *et al.* 2020. It is likely that these production rates are the result of the interaction between reactive oxygen species, iron and methyl donors, enhanced by oxidative stress (Ernst *et al.* 2022). On the other hand, MOx is inhibited in the presence on light (Thottathil *et al.* 2019) and elevated  $\text{O}_2$  concentrations (Reis *et al.* 2022). Therefore, increased MOx would likely decrease  $P_{\text{net}}$  rates during the night rather than during the day. This hypothesis is supported by highly negative  $P_{\text{net}}$  rates observed during the night that were associated with heavier isotopic signature indicating that the  $\text{CH}_4$  in the SML was oxidized during those time periods (Fig. 4.10 inset).

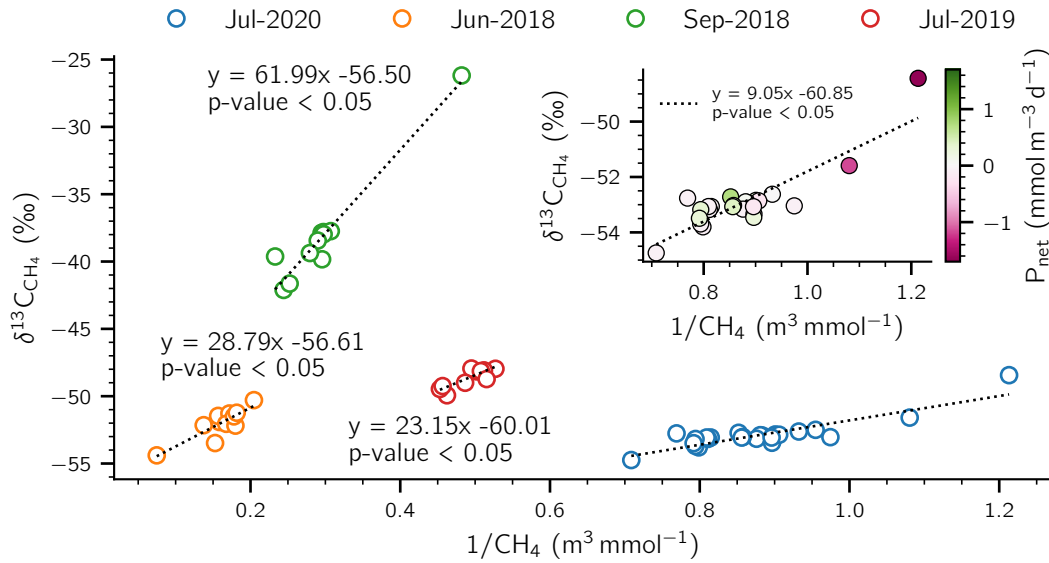


Figure 4.10. Keeling plot analysis of surface  $\text{CH}_4$  concentrations. Data from Chapter 2 was included (June and Sept 2018 and July 2019). The inset shows the Keeling plot only with the data of July 2020 where the color shows the  $P_{\text{net}}$  associated to the  $\text{CH}_4$  concentration.

To analyze the effect of methane oxidation and OMP on  $\delta^{13}\text{C}_{\text{CH}_4}$  in the SML we applied the Keeling plot method to the data from this study and Chapter 2 (June and Sept. 2018 and July 2019). The average  $P_{\text{net}}$  rates in Chapter 2 in June and Sept 2018 and July 2019 were about 2300,  $-1940$  and  $690 \mu\text{mol}/\text{m}^3/\text{d}$  respectively (Table 4.2). When  $P_{\text{net}}$  was negative, enriched  $\text{CH}_4$  was measured in the SML indicating the predominance of MOx over

OMP (Table 4.2). In addition, the  $\text{CH}_4$  fractionation caused by MOx produced  $^{13}\text{C}$  enriched  $\text{CH}_4$  at lower  $\text{CH}_4$  concentrations (case Sep-2018, Fig. 4.10). In contrast, when  $P_{\text{net}} > 0$ ,  $\delta^{13}\text{C}_{\text{CH}_4}$  was about 50 ‰ and we do not observe clear differences of  $\delta^{13}\text{C}_{\text{CH}_4}$  at different  $\text{CH}_4$  concentrations (case June and July 2018 and July 2020). This is likely because OMP will not fractionate the  $\text{CH}_4$  pool in the SML and it will produce  $\text{CH}_4$  with a constant  $\delta^{13}\text{C}_{\text{CH}_4}$ .

We observed a good agreement with the upscaling method proposed in Chapter 2 which relates  $\text{Chl}a$ , light climate (LC) and Secchi disk depth (SD) with the ratio between  $P_{\text{net}}$  and surface  $\text{CH}_4$  concentration (Fig. 4.11), suggesting that OMP can be related with photosynthetic activity by phytoplankton. We observed that from 2018 to 2020,  $P_{\text{net}}$  can be mostly explained by the changes on LC, where higher LC leads to higher  $P_{\text{net}}$  rates ( $r^2=0.9$ , Fig. S.C.8). This result shows that, despite different phytoplankton species are able to produce  $\text{CH}_4$  in oxic condition (Bižić *et al.* 2020; Hartmann *et al.* 2020), the environmental conditions are key to control the  $\text{CH}_4$  production rates by these organisms and highlight that  $\text{CH}_4$  and  $\text{Chl}a$  concentrations provide more an indication of the overall trophic condition of each lake rather than control the  $P_{\text{net}}$  rates.

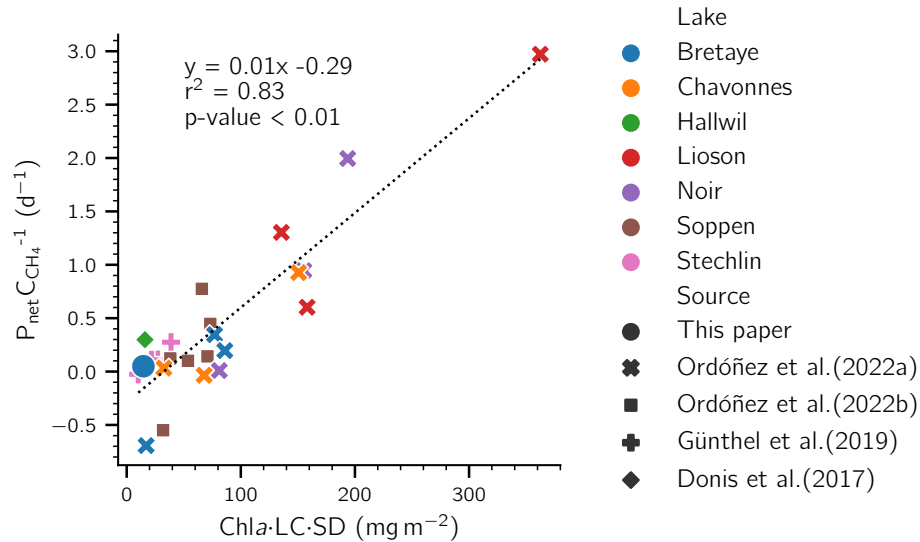


Figure 4.11. Relation between the ratio of  $P_{\text{net}}$  (mmol m<sup>-3</sup> d<sup>-1</sup>) and the surface  $\text{CH}_4$  concentration ( $C_{\text{CH}_4}$ , mmol m<sup>-3</sup>) versus chlorophylla ( $\text{Chl}a$ , mg m<sup>-3</sup>)  $\times$  light climate (LC=2.5SD/ $H_{\text{SML}}$ , -)  $\times$  Secchi depth (SD, m) proposed in Chapter 2. Only the average data during the day was included.

#### 4.4.6 Conclusion and implications

In this study, we showed that  $P_{\text{net}}$  was highly variable on a daily basis, with higher rates during the day than during the night. We demonstrated that in-situ production/consumption needs to be included to explain the change of mass of  $\text{CH}_4$  in the SML. On the other hand, the average contribution of  $P_{\text{net}}$  to the diffusive flux to the atmosphere ( $F_a$ ) was about 30 % (Fig. 4.7). However, in our study we consider the  $\text{CH}_4$  production from macrophytes in the littoral zone (Hilt *et al.* 2022) as an anoxic source included in  $F_s$  and not as OMP in  $P_{\text{net}}$ , hence the overall  $P_{\text{net}}$  contribution to  $F_a$  could be underestimated.

It is important to note that the potential contribution of  $\text{CH}_4$  by macrophytes in the littoral zone, not accounted by the recent studies, could increase the OMP contribution to lake  $\text{CH}_4$  emissions particularly in small ponds and coastal shallow zones (Hilt *et al.* 2022). While more evidence has been collected to show the high contribution of OMP to emissions in different lake environments (Bogard *et al.* 2014; Donis *et al.* 2017; Günthel *et al.* 2019; Hartmann *et al.* 2020; Chapter 2; Chapter 2), most of these studies were performed during the day when we observed the highest  $P_{\text{net}}$  rates and higher contribution to  $F_a$  (Figs. 4.6 and 4.7). As a first attempt, Bizic 2021 highlight the potential importance of OMP on the  $\text{CH}_4$  atmospheric budget. Although it has been shown that OMP can be produced by any organism under oxidative stress and not only related to photosynthesis (Bižić *et al.* 2020; Hartmann *et al.* 2020; Ernst *et al.* 2022), we hypothesize that the OMP contribution to diffusive emissions from lakes may be overestimated, and night measurements have to be performed on aquatic ecosystems to further understand OMP dynamics on both the daily and seasonal scale.



---

## Conclusions and Perspective

For the first time the Intergovernmental Panel on Climate Change (IPCC) established the unequivocal role of humanity on the warming of the atmosphere, land and ocean (IPCC 2021). It is also established that it is *very likely* that the main drivers of global warming are the greenhouse gases (GHG), methane (CH<sub>4</sub>) and carbon dioxide (CO<sub>2</sub>), and that the increase of these GHGs are unequivocally caused by human activity. The changes on the climate system are unprecedented over the last centuries, many of them are irreversible for centuries to millennia, and it will affect every region in the world. These projections mostly relied on numerical models that combine physical-chemical processes in the climatic system and GHG emissions inventories around the globe.

The interaction between the GHG inventories and the climate system depends on the physical and biochemical processes that produce those emissions. The understanding of these processes and the GHG inventories are constantly updated in the climatic models. For example, in 2007 Cole *et al.* 2007 demonstrate that inland waters were not passive conducts that simply transported carbon downstream but are active carbon transformers producing GHG emissions. That study resulted in the carbon emissions associated to inland waters to be included in the atmospheric carbon budget. These emissions have been constantly updated since then (Cole *et al.* 2007; Tranvik *et al.* 2009; DelSontro *et al.* 2018b).

After carbon dioxide (CO<sub>2</sub>), methane (CH<sub>4</sub>) is the second most important carbon based GHG contributing about 20 % to the global radiative forcing (Myhre *et al.* 2013; Sauniois

*et al.* 2020; Rosentreter *et al.* 2021). A quarter of those CH<sub>4</sub> emissions comes from inland waters, but high uncertainties remain on these estimations (Saunois *et al.* 2020; Rosentreter *et al.* 2021). In lakes, CH<sub>4</sub> can be produced in anoxic sediment and emitted through bubbles or by diffusion to the atmosphere (Bastviken *et al.* 2004). Donis *et al.* 2017 and Günthel *et al.* 2019 showed, for the first time, that oxic methane production (OMP) was the most important source of CH<sub>4</sub> emissions in Lake Hallwil contrasting the results from Peeters *et al.* 2019 where they showed that CH<sub>4</sub> produced in anoxic littoral sediment was the main contributor of the CH<sub>4</sub> emissions in that lake.

Under this context the research goals stated in Chapter 1 have been addressed as follows. In a study on four pre-alpine lakes, Chapter 2 demonstrated that the OMP controversy can be resolved when the correct boundary conditions are utilized. Furthermore, OMP occurred in three of the four studied lakes and  $P_{\text{net}}$  rates were higher in eutrophic than oligotrophic lakes. Nevertheless, no clear trend was observed regarding the  $P_{\text{net}}$  contribution to diffusive CH<sub>4</sub> emissions at different trophic states. Chapter 3 took advantage of a four-year data set on a small eutrophic Swiss lake and illustrated that  $P_{\text{net}}$  rates and its contribution were not constant during the stratified season, but had a tendency to be higher at late spring and then decrease towards the end of the summer. Chapter 4 analyzed the diel variation of  $P_{\text{net}}$  in a pre-alpine lake, and showed that OMP tended to dominate MOx during the day, and that MOx was higher than OMP during the night. So far, all OMP studies in the literature were conducted during the day, therefore Chapter 4 concludes that, due to the lack of night measurements, the OMP contribution to diffusive CH<sub>4</sub> emissions could be overestimated. Moreover, Chapters 2 to 4 highlight the role of phytoplankton on OMP and identifies light climate, Secchi disk depth, and chlorophyll-*a* as main drivers.

The following section discusses the contribution of this doctoral thesis to the understanding of the interaction between the changes in physical and biochemical processes due to climate change and their role on the CH<sub>4</sub> cycle in freshwaters. Then, the open research questions based on the findings and limitations obtained during the development of this doctoral thesis are proposed. And finally, this work concludes with a discussion on the estimations of the OMP contribution globally and final remarks.

## 5.1 Interaction between OMP, eutrophication and climate change

Lakes are sentinels for climate change due to their sensitivity to alterations in their surrounding landscape and climate (Adrian *et al.* 2009). Lakes are already experiencing rapid changes caused by climate change such as alteration on evaporation, loss of ice cover, warming surface water temperatures and variations in mixing regimes (Woolway *et al.* 2020). These changes interact with each other, making it difficult to predict their future response to climatic variations and to the direct anthropogenic pressures.

This doctoral thesis identifies light climate (i.e, light availability and SML depth) and Chl*a* as main drivers of  $P_{\text{net}}$ . As discussed in Chapter 2,  $P_{\text{net}}$  rates at each lake is driven by light climate (LC), however the different  $P_{\text{net}}$  rates between lakes are mostly controlled by is trophic states reflected by the surface  $\text{CH}_4$  and Chl*a* concentrations. This argument was complemented in Chapter 4 where light climate explained  $\sim 90\%$  of  $P_{\text{net}}$  variation in Lac de Bretaye. Changes in surface water temperature and mixing regimes will affect the SML differently depending on the trophic state of the lake. Oligotrophic lakes will experience a deepening of the SML (Flaim *et al.* 2016) that, considering no change in light availability, will decrease its light climate. However, since  $P_{\text{net}}$  becomes independent of LC in oligotrophic lakes (Fig. 5.1), no variation of  $P_{\text{net}}$  is expected under future climate scenarios. In contrast, eutrophic lakes would experience shallower SMLs with climate change that, considering no change in light conditions, will increase its LC. Since  $P_{\text{net}}$  strongly increases in eutrophic lakes as function of LC (Fig. 5.1) an increase of  $P_{\text{net}}$  would be expected in the future for these lakes.

In addition to the effect on the SML, climate warming will increase the ice-free duration in lakes allowing  $\text{CH}_4$  to be emitted for a longer period (Guo *et al.* 2020). The increase of surface water temperature will also enhance littoral production rates of  $\text{CH}_4$  in littoral sediments (Bastviken *et al.* 2008) and OMP rates (Klintzsch *et al.* 2020). Moreover, longer stratification periods (Woolway *et al.* 2021) would also allow the occurrence of OMP in the SML for a longer period. Unfortunately, the alteration of the climatic system will stay the same or increase in the next century (IPCC 2021), producing at least the changes on the  $\text{CH}_4$  cycle discussed here. As OMP it is a newly recognize source of  $\text{CH}_4$  in freshwaters in lakes and oceans, its dynamics



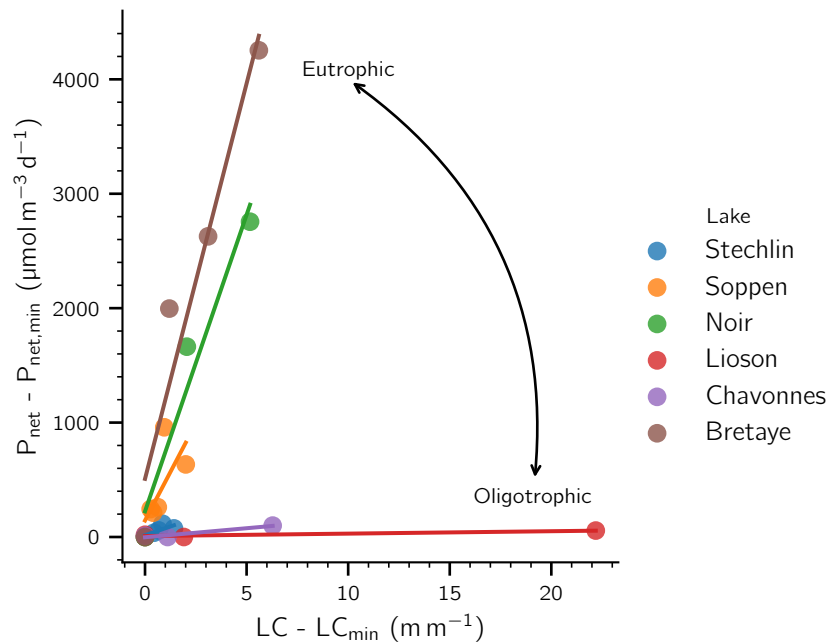


Figure 5.1. Interaction between  $P_{\text{net}}$ , light climate and eutrophication. Per each lake the minimum  $P_{\text{net}}$  rate ( $P_{\text{net,min}}$ ) and the minimum light climate ( $LC_{\text{min}}$ ) was subtracted to be able to compare the slope of each curve.  $P_{\text{net}}$  becomes more independent of LC for more oligotrophic lakes.

have not been included in the IPCC model. Despite these new insights of the OMP dynamics in lakes on different temporal scales presented in this doctoral thesis, further investigation needs to be conducted to understand the OMP associated mechanisms and the OMP dynamics in other ecosystems.

## 5.2 Determination of the boundary conditions in the SML

The methodology proposed in this thesis uses modeling approaches based on the Law of Conservation of Mass.  $P_{\text{net}}$  rates and their accuracy depend on the precision of the measurements of the sources and sinks of  $\text{CH}_4$  in the SML. The high uncertainties found on  $P_{\text{net}}$  rates calculated in this thesis mostly result from the surface diffusive emissions ( $F_a$ ) and the diffusive  $\text{CH}_4$  flux from the littoral sediments ( $F_s$ ). The excellent agreement between the two modelling approaches, the 0-D full-scale mass balance and the 1-D lateral transport model in Chapters 2 to 4, illustrate that the inclusion of the lateral transport did not substantially change the  $P_{\text{net}}$  estimations and adds robustness to our calculations. Nevertheless, the estimation of  $F_s$  remains highly uncertain due to the methodological constraints and spatial heterogeneity of the sediments.

Moreover, very little is known about how the diffusive  $\text{CH}_4$  fluxes from the sediment are affected by temperature and the presence of oxygen at the top of the sediment (Damgaard *et al.* 1998; Liikanen *et al.* 2002). To decrease the uncertainty of  $F_s$ , three different methodologies were used in Chapters 2 and 3 in different locations in each lake, but the temperature and oxygen effects were analyzed but not included in  $P_{\text{net}}$  calculations due to methodological limitations (see Chapter 4). Although these changes will be not reflected on a daily scale (Chapter 4), laboratory experiments using sediment cores incubations can be used to further investigate the effect of temperature and oxygen on  $\text{CH}_4$  fluxes and better estimate  $P_{\text{net}}$  on a seasonal scale.

Surface diffusive  $\text{CH}_4$  emissions to the atmosphere are spatially and temporally variable. Chapter 4 demonstrates that the short-term temporal variability of  $F_a$  did not affect the  $P_{\text{net}}$  calculations, however the average on a daily scale or longer is critical to perform the mass balance in the SML. For this PhD thesis,  $F_a$  was measured with the flux chambers approach (McGinnis *et al.* 2015). Vachon *et al.* 2010 showed that, using turbulence measurements inside and outside of the chambers, this methodology may overestimate  $F_a$ . Nevertheless, good agreement was found with the eddy covariance method (Schubert *et al.* 2012), which is a non-invasive methodology to estimate  $F_a$ . Moreover, flux chambers experiments on streams showed that drifting chambers had very small impact on the turbulence level below the chamber and produce reliable fluxes (Lorke *et al.* 2015). Hence, turbulence measurements in the surface layer and eddy covariance measurements need to be compared with the flux chamber method to identify key drivers for modelling the mass transfer coefficient ( $k_{600}$ ) and understand the possible bias produced by the chamber method.

Bizic 2021 highlighted the potential significance that photosynthesis-derived OMP has on global  $\text{CH}_4$  emissions. In this thesis, OMP contributions to diffusive emissions were studied across a trophic gradient and at seasonal and diurnal time scales. Chapter 4 shows that OMP did not contribute to  $F_a$  during the night. Seasonally, the OMP contribution tended to decrease at the end of the summer in eutrophic lakes, whereas in oligotrophic lakes tended to stay consistent during the stratified season (Chapter 2). Considering the temporal tendency observed in the OMP contribution during this work and that eutrophic lakes tend to emit more  $\text{CH}_4$  than the oligotrophic lakes, the OMP contribution from lakes suggested by Bizic 2021 may be overestimated. Nevertheless, most of OMP studies have been conducted in lakes or the

ocean, but the role of OMP in rivers and wetlands is still unknown. Finally, including the role of macrophytes on  $\text{CH}_4$  production in oxic conditions can increase the significance of OMP in the atmospheric  $\text{CH}_4$  budget.

### 5.3 Final remarks

This doctoral thesis resolves the OMP dynamics in lakes across trophic state gradients and different temporal scales using physical and biochemical principles. The findings of this study are of significance for resolving the "Methane paradox" globally, however some key points need to be addressed to be able to predict  $\text{CH}_4$  emissions from lakes:

- The upscaling method proposed here is a step forward to be able to predict  $P_{\text{net}}$  rates in different lake ecosystems. In this study LC climate is recognized as the main driver to predict  $P_{\text{net}}$  in each lake, however the role of trophic variables such as nutrients and algae composition play on OMP is still poorly constrained.
- To understand the  $P_{\text{net}}$  dynamics of in the SML from diurnal to seasonal scales, it is necessary to accurately isolate each OMP and  $\text{MOx}$ . This knowledge will also provide a better understanding on the isotopic signature of OMP which could help to determine the sources of  $\text{CH}_4$  in surface waters.
- Further investigation is needed regarding the spatial and temporal variations of both  $\text{CH}_4$  diffusive fluxes and ebullition from sediments. The variations caused by temperature, oxygen and carbon burial on these fluxes are key to determine its contribution to total  $\text{CH}_4$  emissions from inland waters.
- In this thesis I observed a disagreement between the flux chambers gas transfer coefficient and the literature parameterizations. Further research needs to be conducted to understand the impact of solar radiation and microbubbles to improve the parameterizations and therefore accurately estimate diffusive  $\text{CH}_4$  emissions to the atmosphere.

Resolving the issues mentioned above and including them to the existing or new numerical models of  $\text{CH}_4$  in lakes will improve the estimations of  $\text{CH}_4$  emissions from inland waters and it will be useful to predict its response to climate change and eutrophication.

# Supplementary Information

## Chapter 2

---

César Ordóñez<sup>1</sup>, Tonya DelSontro<sup>1,2</sup>, Timon Langenegger<sup>1</sup>, Daphne Donis<sup>1</sup>, Ena L. Suarez<sup>1</sup>,  
and Daniel F. McGinnis<sup>1</sup>

<sup>1</sup>Aquatic Physics Group, Department F.-A. Forel for Environmental and Aquatic Sciences (DEFSE), Faculty of Science, University of Geneva, Uni Carl Vogt, 66 Boulevard Carl-Vogt, 1211 Geneva, Switzerland

<sup>1, 2</sup> Now at Department of Earth and Environmental Sciences, University of Waterloo, Ontario, Canada

Table S.A.1. Study sites

Lake	Latitude (°N)	Longitude (°E)	Altitude (m.a.s.l)	Max. Depth (m)	Surf. Area (ha)	Trophic State
Bretaye	46.326	7.072	1785	8	4	Hypereutrophic
Chavonnes	46.333	7.085	1692	25	5	Mesotrophic
Lioson	46.386	7.128	1848	28	7	Oligotrophic
Noir	46.327	7.079	1715	9	1	Eutrophic

Table S.A.2. Total (TP) and dissolved phosphorus (DP), dissolved silica (DSIL), dissolved inorganic nitrogen as nitrate plus nitrite (DIN) and total carbon (TC) measurements in the hypolimnion and epilimnion.

Lake	Date	Region	Depth (m)	TP (mg m <sup>-3</sup> )	DP (mg m <sup>-3</sup> )	DIN (g m <sup>-3</sup> )	DSIL (g m <sup>-3</sup> )	TC (g m <sup>-3</sup> )
Bretaye	Jun-18	Epilimnion	0 to 4	20.7	9.0	0.02	0.39	19.73
		Hypolimnion	5 to 8	66.7	18.7	0.01	1.89	26.72
	Sept-18	Epilimnion	0 to 5	10.0	7.3	0.03	2.77	20.16
		Hypolimnion	5.5 to 7.5	150.0	39.3	0.02	5.29	21.00
	Jul-19	Epilimnion	0 to 5.5	33.0	-	0.00	0.83	29.13
		Hypolimnion	6 to 8.5	672.0	191.0	0.02	7.36	42.52
Noir	Jun-18	Epilimnion	0 to 5	4.0	2.3	0.02	1.02	29.52
		Hypolimnion	6 to 9.2	29.7	-	0.05	3.99	42.43
	Sept-18	Epilimnion	0 to 5	3.7	2.7	0.03	3.21	19.03
		Hypolimnion	6 to 9	13.0	2.3	0.05	7.60	51.69
	Jul-19	Epilimnion	0 to 5	8.0	BD	BD	1.22	33.11
		Hypolimnion	6 to 10	57.0	5.0	0.02	8.21	56.48
Chavonnes	Jun-18	Epilimnion	0 to 15	4.3	2.0	0.24	1.10	21.22
		Hypolimnion	18 to 26	26.3	3.0	0.18	2.61	23.99
	Sept-18	Epilimnion	0 to 10	2.7	1.0	0.17	1.70	15.91
		Hypolimnion	12 to 22	10.3	1.7	0.06	4.06	28.40
	Jul-19	Epilimnion	0 to 8	BD	BD	0.19	0.67	20.77
		Hypolimnion	10 to 25	9.0	BD	0.15	3.37	25.10
Lioson	Jun-18	Epilimnion	0 to 9	3.3	2.0	0.13	1.82	23.03
		Hypolimnion	13 to 25	5.0	2.7	0.16	2.55	24.05
	Sept-18	Epilimnion	0 to 14	3.3	1.0	0.05	1.42	7.66
		Hypolimnion	16 to 26	2.7	2.0	0.08	3.26	10.33
	Jul-19	Epilimnion	0 to 14	BD	BD	0.07	1.63	22.62
		Hypolimnion	16 to 28	BD	BD	0.10	2.71	24.47

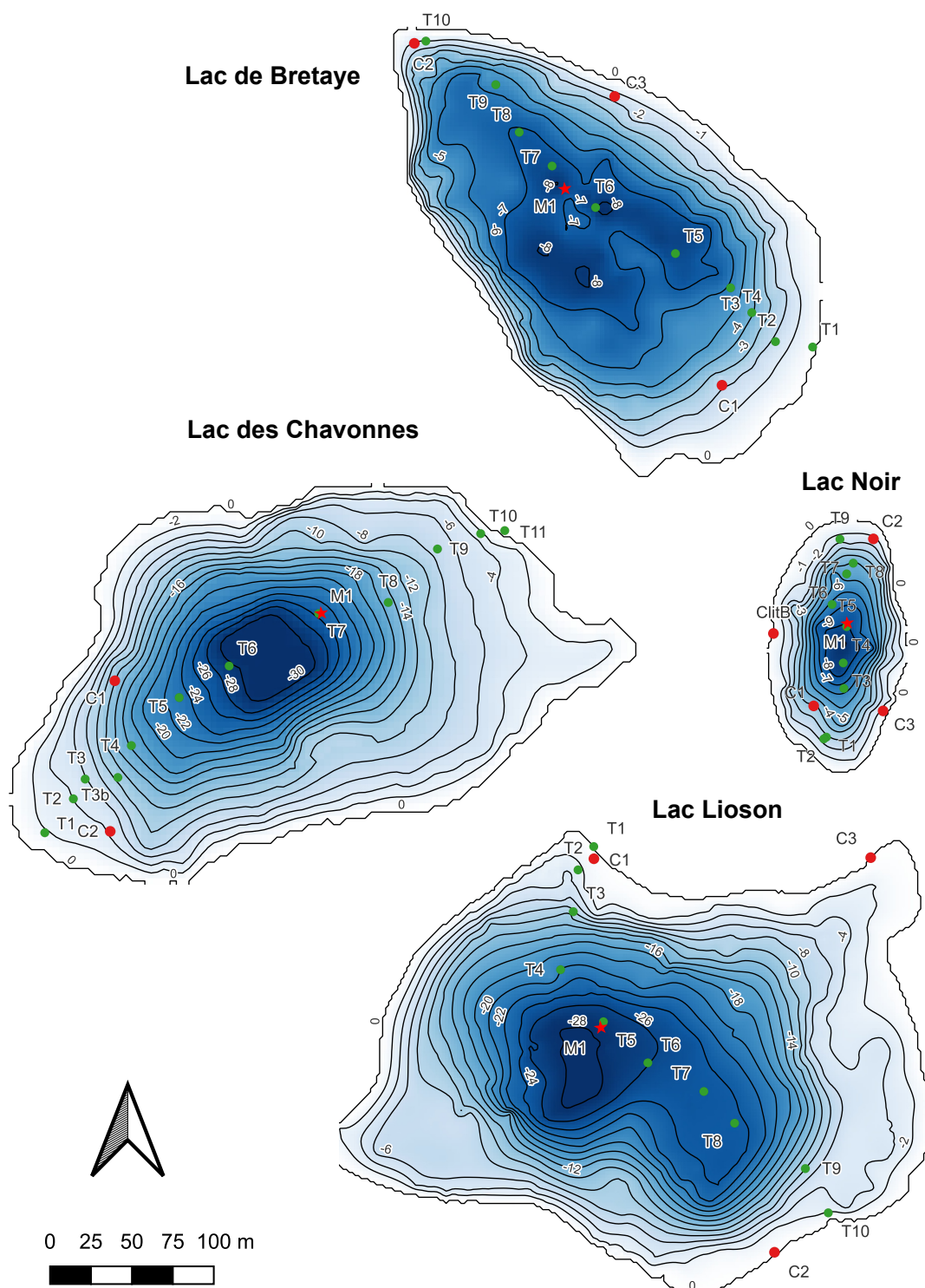


Figure S.A.1. Lake bathymetries obtained from sonar survey, sampling locations for each transect (T#; green points) and sediment sampling points (C#; red dots). M1 (red star) is the location where CTD's, nutrients sampling and CH<sub>4</sub> profiles were performed.

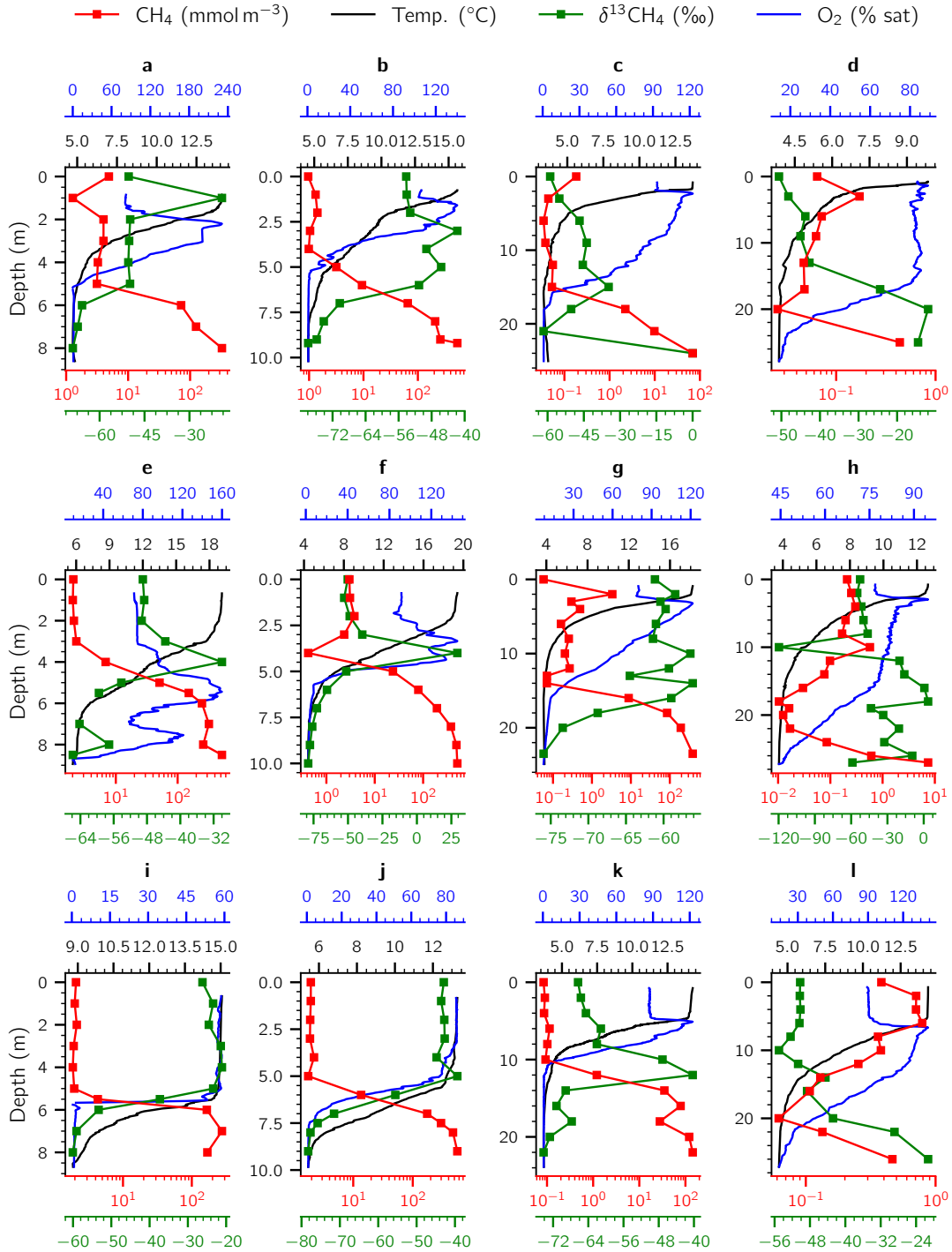


Figure S.A.2. Water column profiles of CH<sub>4</sub> concentrations (red line), temperature (black), δ<sup>13</sup>C<sub>CH<sub>4</sub></sub> (green line) and O<sub>2</sub> saturation (blue). **a-d** June 2018, **e-h** July 2019 and **i-l** Sept 2018 for Lac de Bretaye (BRE), Lac Noir (NOI), Lac des Chavonnes (CHA) and Lac Lioson (LIO).

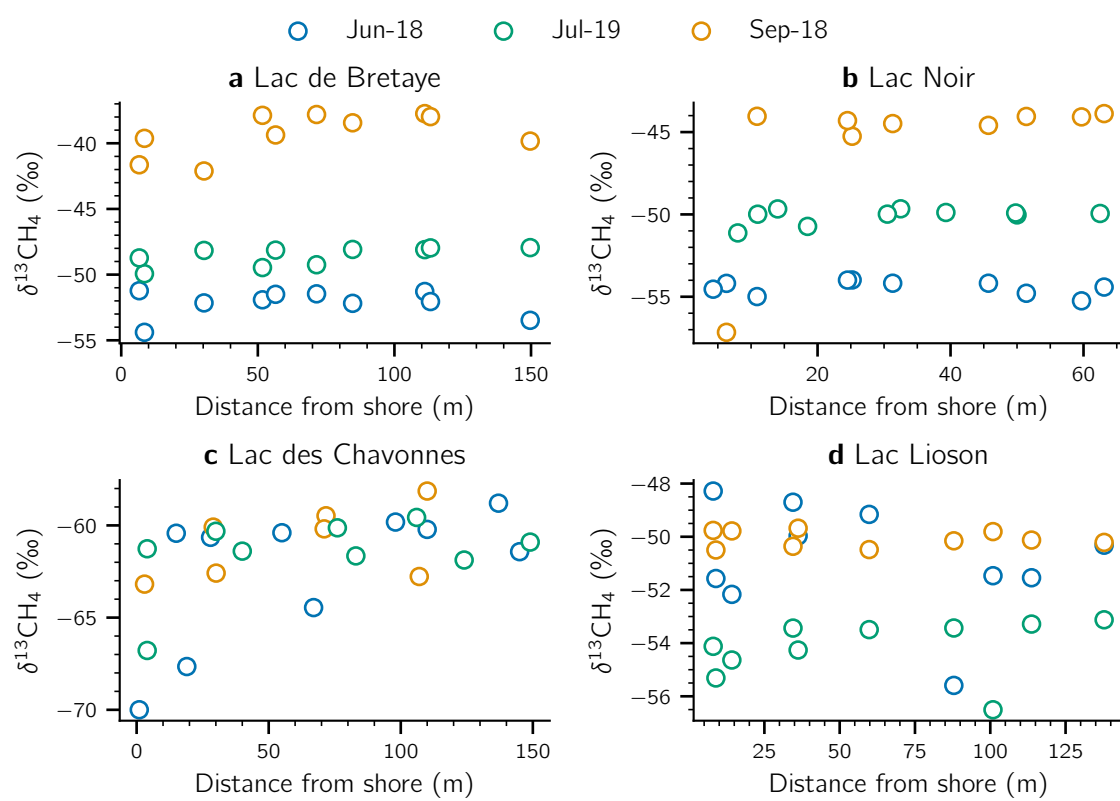


Figure S.A.3. Surface  $\delta^{13}\text{C}_{\text{CH}_4}$  along the transects from shore to the center each lake.



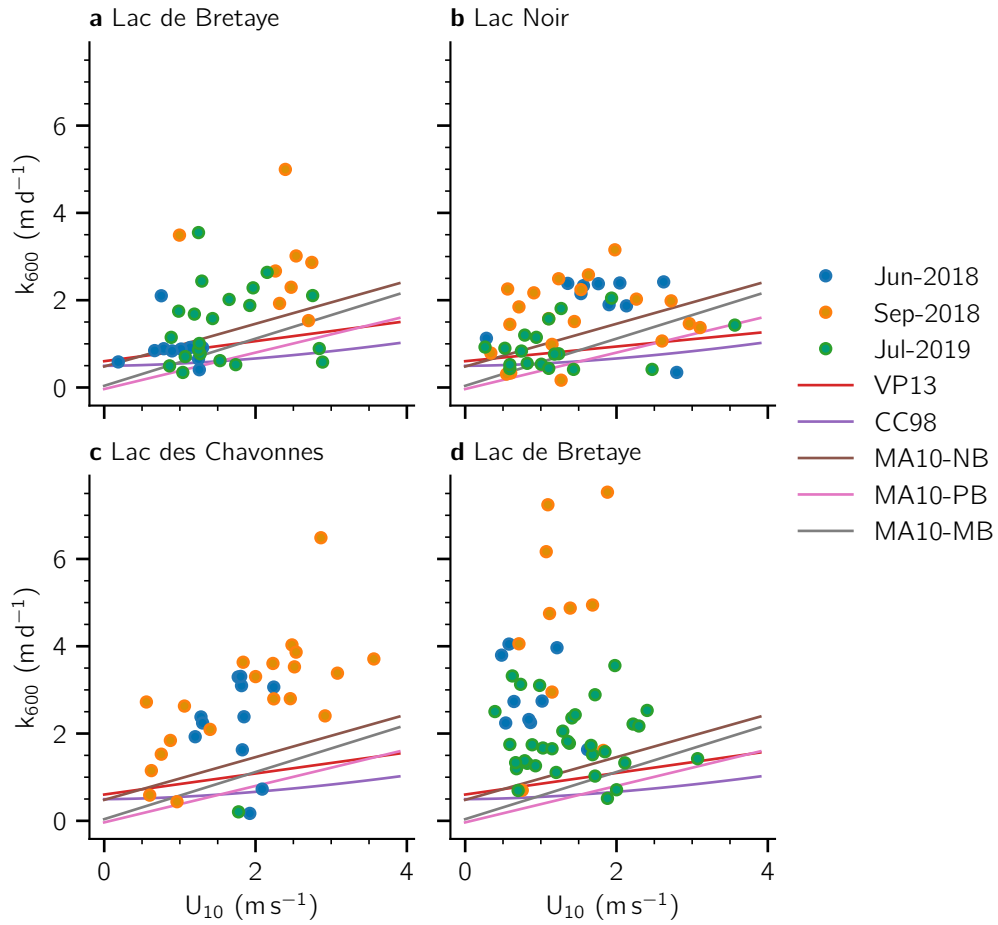


Figure S.A.4. Comparison between chamber-based  $k_{600}$  with different wind based parametrizations (CC98: Cole & Caraco 1998; MA10-NB, MA10-PB and MA10-MB: MacIntyre *et al.* 2010 Negative Buoyancy, Positive Buoyancy and Mixed Model; VP13: Vachon & Prairie 2013).

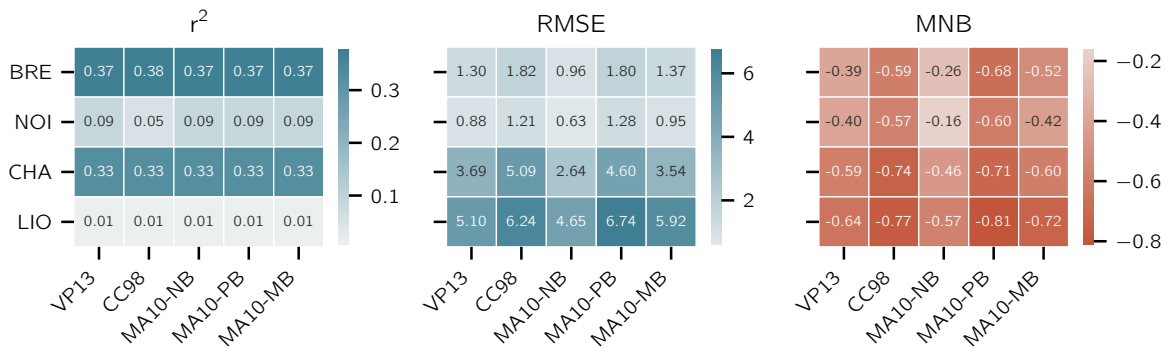


Figure S.A.5. Statistics between chamber based mass transfer coefficient and literature parameterizations. R-square ( $r^2$ ), root mean square error (RMSE) and mean normalized bias (MNB).

Table S.A.3. Summary of diffusive sediment CH<sub>4</sub> fluxes and its associated sampling depth, temperature of overlying water, type of measurement (PW: Porewater and BC: benthic chamber) and zone classification.

Lake	Date	Depth (m)	Zone	T <sub>w</sub> (°C)	Core	Type	F <sub>s</sub> (mmol m <sup>-2</sup> d <sup>-1</sup> )
Bretaye	16/06/18	9	Deep	4.8	M1	PW	5.25
	16/06/18	5.2	Deep	4.8	C1	PW	1.53
	02/09/18	9	Deep	4.8	M1	PW	5.23
	02/09/18	3.5	Shallow	15.3	C1	PW	5.76
	02/09/18	8.4	Deep	8.8	M1	PW	12.6
	20/07/19	2.7	Shallow	19.7	C1	PW	0.50
	20/07/19	1.7	Shallow	19.7	C3	BC	12.65
	20/07/19	2.6	Shallow	19.7	C2	BC	12.48
Noir	20/06/18	10.9	Deep	4.5	M1	PW	8.54
	20/06/18	5.5	Deep	5.6	C1	PW	0.22
	03/09/18	10.5	Deep	5.4	M1	PW	6.54
	03/09/18	4.7	Shallow	13.5	C1	PW	2.18
	24/07/19	0.75	Shallow	22.3	ClitB	PW	2.50
	24/07/19	0.75	Shallow	22.3	ClitB	BC	1.62
	24/07/19	0.5	Shallow	22.3	C2	BC	1.33
	24/07/19	1	Shallow	22.3	C3	BC	1.33
	25/07/19	8	Deep	4.4	M1	PW	5.62
Chavonnes	23/07/19	0.5	Shallow	21.2	C1	PW	0.01
	23/07/19	0.6	Shallow	21.2	C1	BC	0.82
	23/07/19	0.5	Shallow	21.2	C2	BC	0.39
Lioson	23/07/19	0.2	Shallow	14.7	C1	BC	0.31
	23/07/19	0.3	Shallow	14.7	C2	BC	0.16
	23/07/19	0.45	Shallow	14.7	C3	BC	0.27

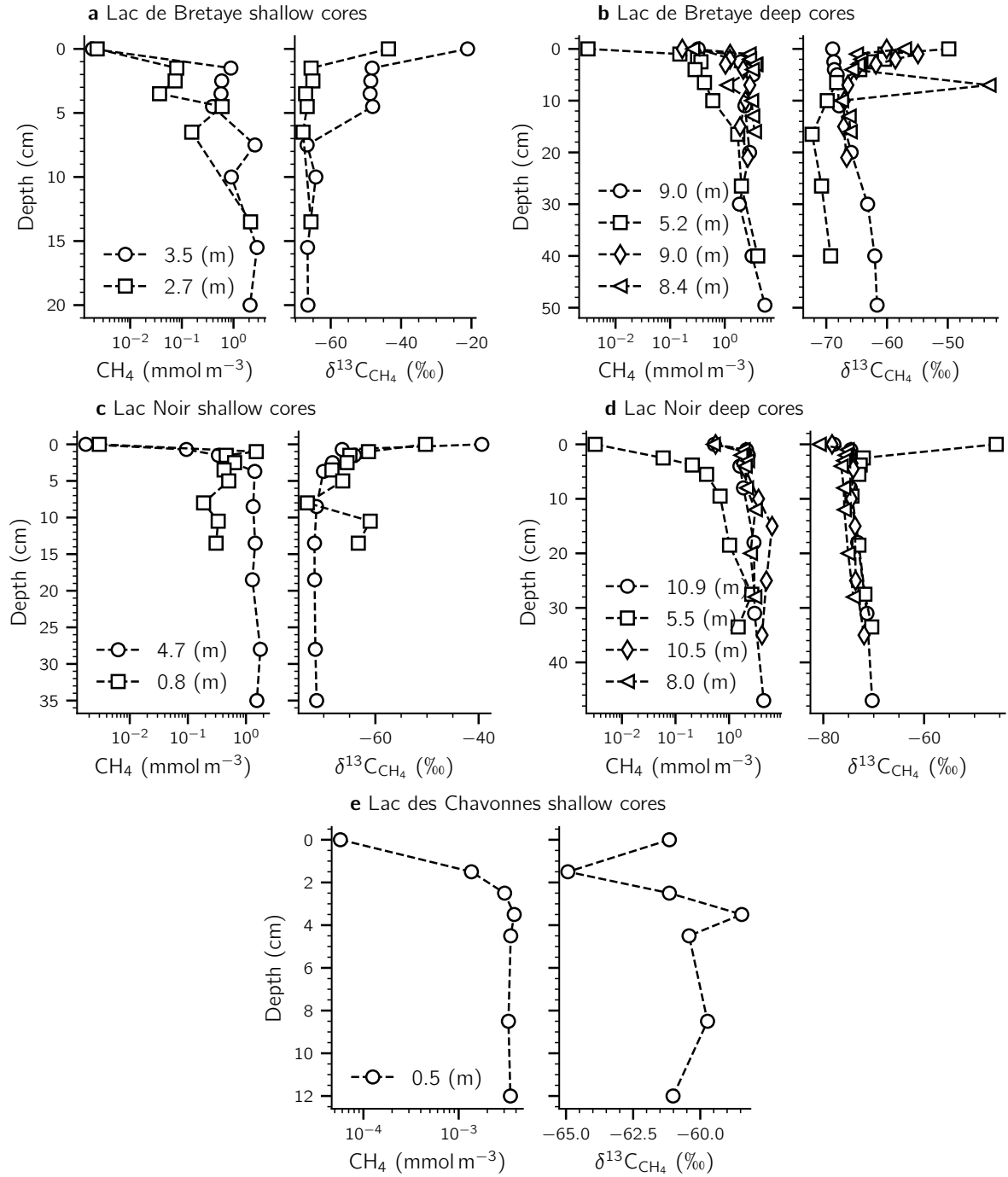
Figure S.A.6. Porewater  $\text{CH}_4$  concentration (log scale) and  $\delta^{13}\text{C}_{\text{CH}_4}$  signature profiles.

Table S.A.4. Comparison between average  $\delta^{13}\text{C}_{\text{CH}_4}$  at the surface water and  $\delta^{13}\text{C}_{\text{CH}_4}$  at the top and bottom of the porewater measurement at each lake.

Lake	Date	Surface Water	Sediment	
		$\delta^{13}\text{C}_{\text{CH}_4}$ (‰)	$\delta^{13}\text{C}_{\text{CH}_4}$ top (‰)	$\delta^{13}\text{C}_{\text{CH}_4}$ bottom (‰)
Bretaye	June 2018	-52.0		
	July 2019	-48.8	-66.0	-66.5
	Sept 2018	-38.8	-48.4	-65.7
Noir	June 2018	-54.5		
	July 2019	-49.9	-63.9	-65.9
	Sept 2018	-45.5	-66.2	-71.6
Chavonnes	June 2018	-62.3		
	July 2019	-61.2	-62.0	-60.0
	Sept 2018	-62.4		
Lioson	June 2018	-50.9		
	July 2019	-54.0		
	Sept 2018	-50.1		

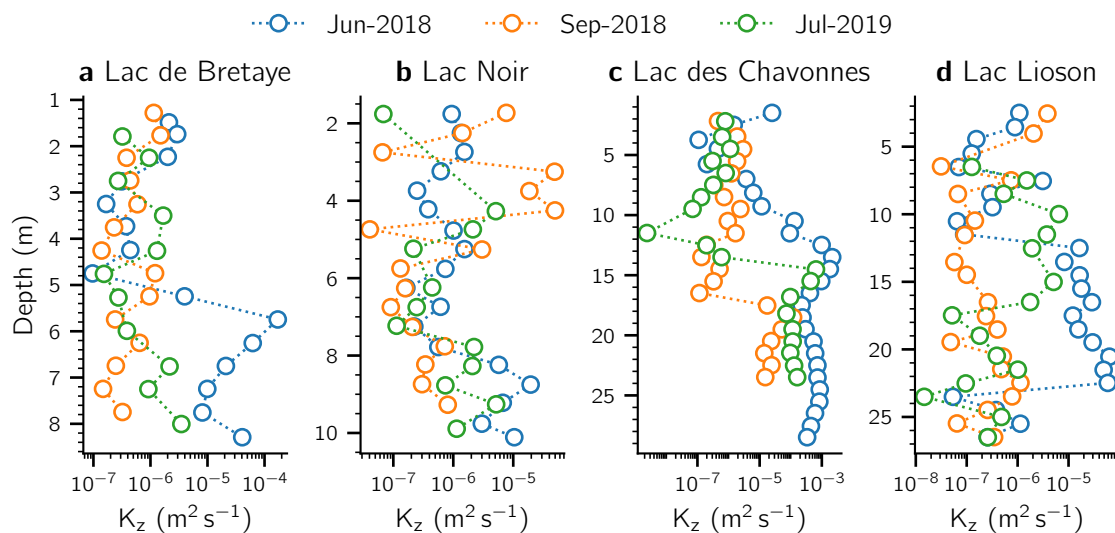


Figure S.A.7. Vertical diffusivity ( $K_z$ ) for each lake and sampling campaign.

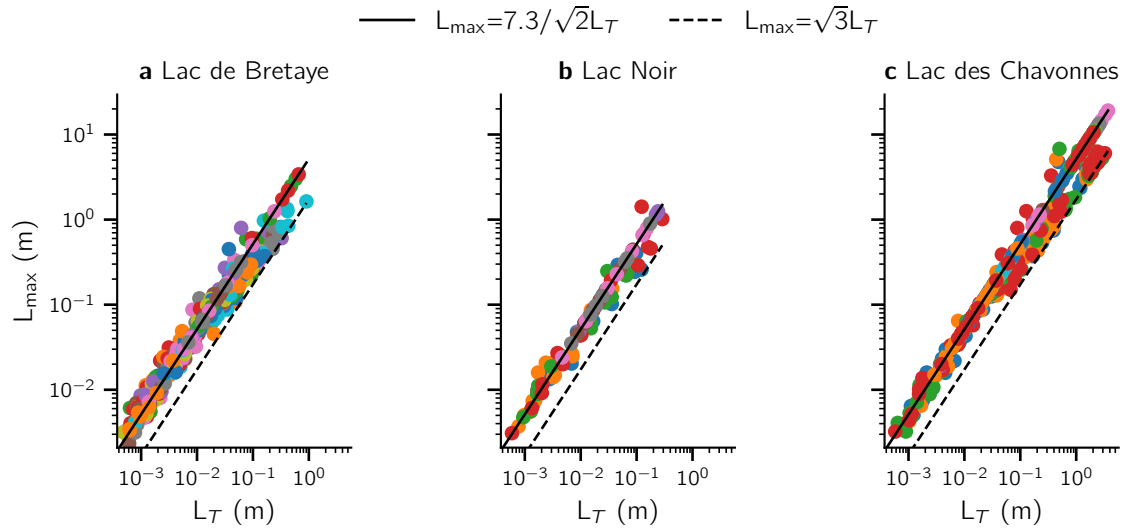


Figure S.A.8. Maximum ( $L_{\max}$ ) versus root-mean square ( $L_T$ ) displacement length scales within segments of temperatures microstructure profiles from a) Lac de Bretaye, b) Lac Noir and c) Lac des Chavonnes. Each color represent one profile performed on July 2020.

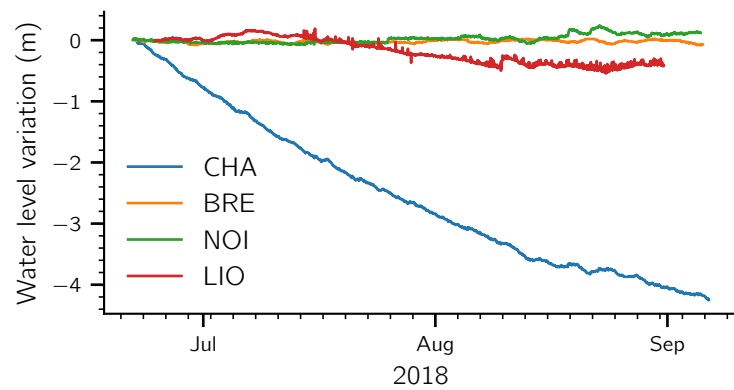


Figure S.A.9. Water level variations from the beginning of 2018 sampling campaign of 2018 for Lac de Bretaye (BRE), Lac Noir (NOI), Lac des Chavonnes (CHA), Lac Lioson (LIO).

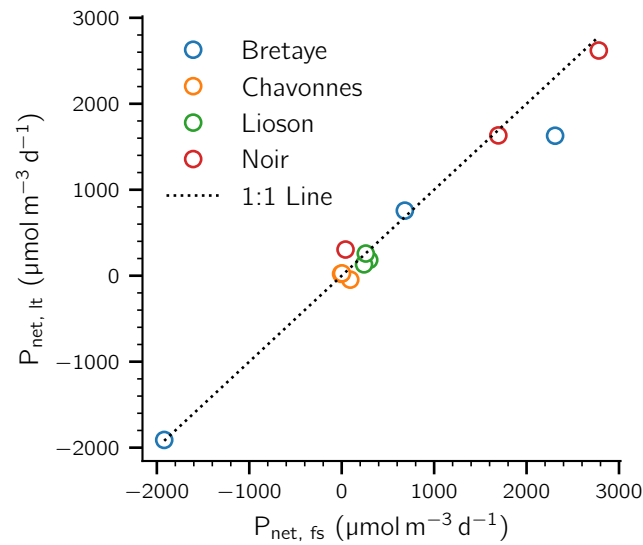


Figure S.A.10. Comparison between  $P_{\text{net}}$  rates calculated for the full scale mass balance ( $P_{\text{net,fs}}$ ) and the lateral transport model ( $P_{\text{net,lt}}$ ) for each lake at every sampling date.

Table S.A.5. Volumes and areas used in the full-scale mass balance model.  $A_z$ ,  $A_a$ ,  $A_s$  are the planar area at the bottom of the surface mixed layer, the surface area and sediment area respectively.  $V_{\text{SML}}$  is the volume of the surface mixed layer (SML).  $L$  is the length scale used to estimate the horizontal dispersion coefficient for the lateral transport model.

Lake	Date	$A_z$ ( $\text{m}^2$ )	$A_a$ ( $\text{m}^2$ )	$A_s$ ( $\text{m}^2$ )	$V_{\text{SML}}$ ( $\text{m}^3$ )	$L$ (m)
Bretaye	Jun 2018	36443	45449	8688	49380	120.28
	Sept 2018	20609	45449	24820	165770	120.28
	July 2019	32832	45449	12552	83425	120.28
Noir	Jun 2018	8012	9960	2026	7509	56.31
	Sept 2018	3057	9960	7139	30778	56.21
	July 2019	6566	9960	3511	14063	56.31
Chavonnes	Jun 2018	54267	60311	5700	71935	138.55
	Sept 2018	28949	44233	14958	166037	118.65
	July 2019	47681	54716	8236	97588	131.97
Lioson	Jun 2018	64659	70052	5129	31557	149.32
	Sept 2018	43222	70052	27800	295316	149.32
	July 2019	57722	70052	12385	89918	149.32

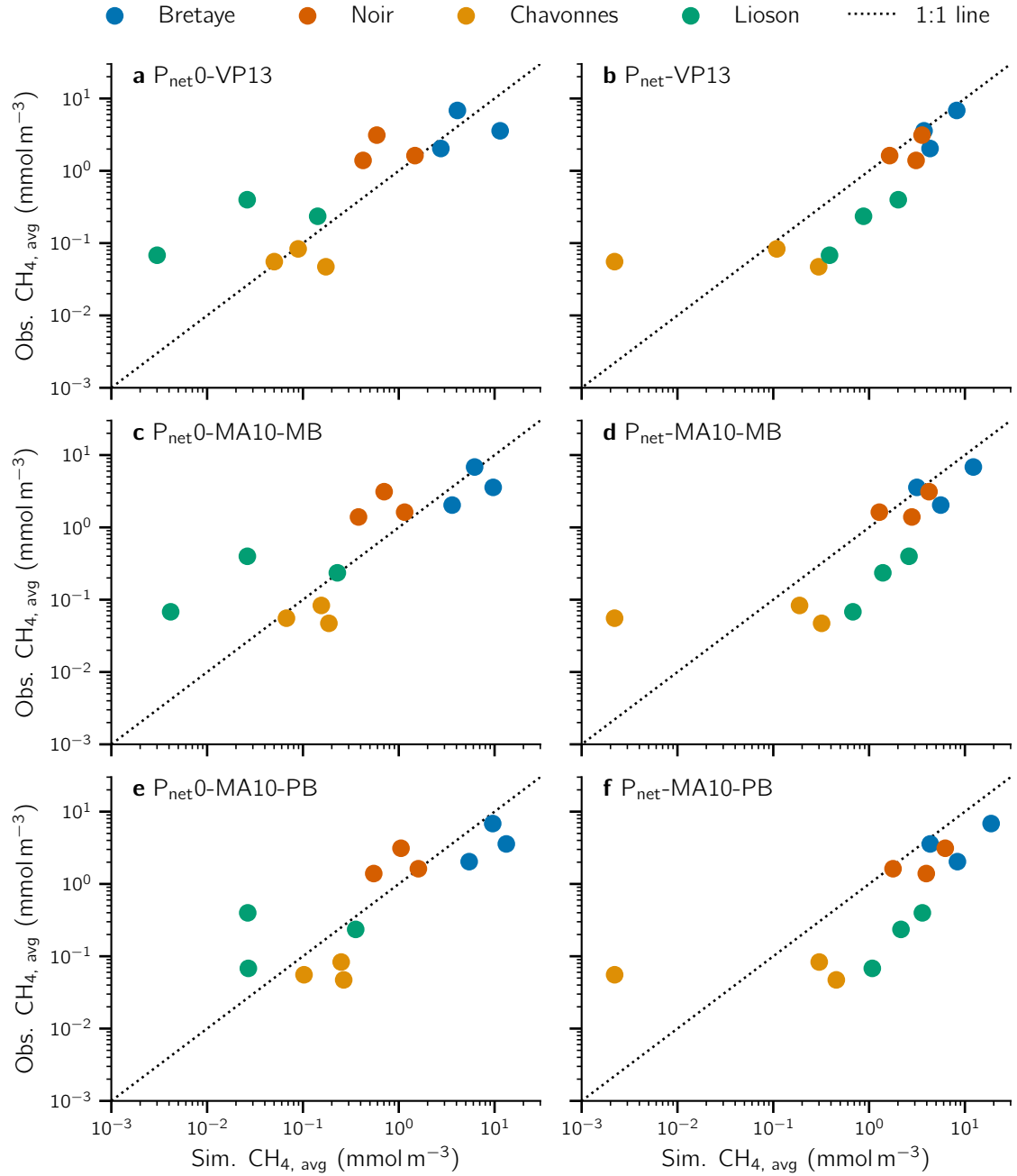


Figure S.A.11. Comparison of observed and simulated average surface  $\text{CH}_4$  concentration along transects for each campaign. Simulated  $\text{CH}_4$  concentrations were obtained with the lateral transport model using  $k_{600}$  for diffusive emissions either with (panels b, d and f) or without  $P_{\text{net}}$  (panels a, c and e). The  $k_{600}$  was either estimated by Vachon & Prairie 2013 (VP13, panels a and b), MacIntyre *et al.* 2010 mixed buoyancy (MA10-MB, panels c and d) and MacIntyre *et al.* 2010 positive buoyancy (MA10-PB, panels e and f). The statistical results of each panel are shown in Table 2.3.

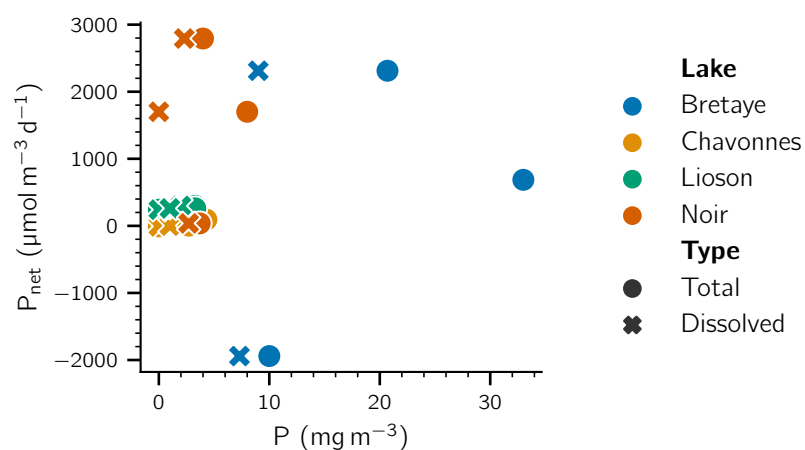


Figure S.A.12.  $P_{\text{net}}$  rates versus total and dissolved phosphorus concentration ( $P$ ) at the SML for each lake and sampling campaign.

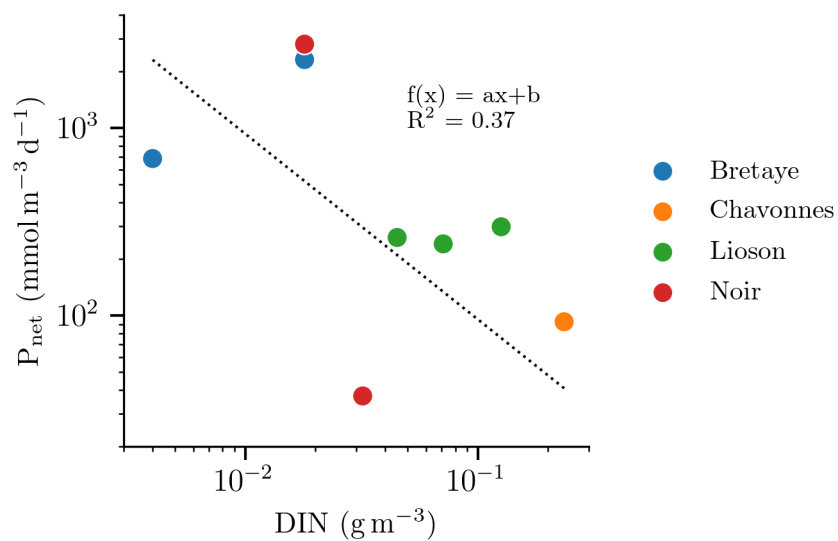


Figure S.A.13.  $P_{\text{net}}$  versus dissolved inorganic nitrogen (DIN) concentration in the SML for each lake and sampling campaign.



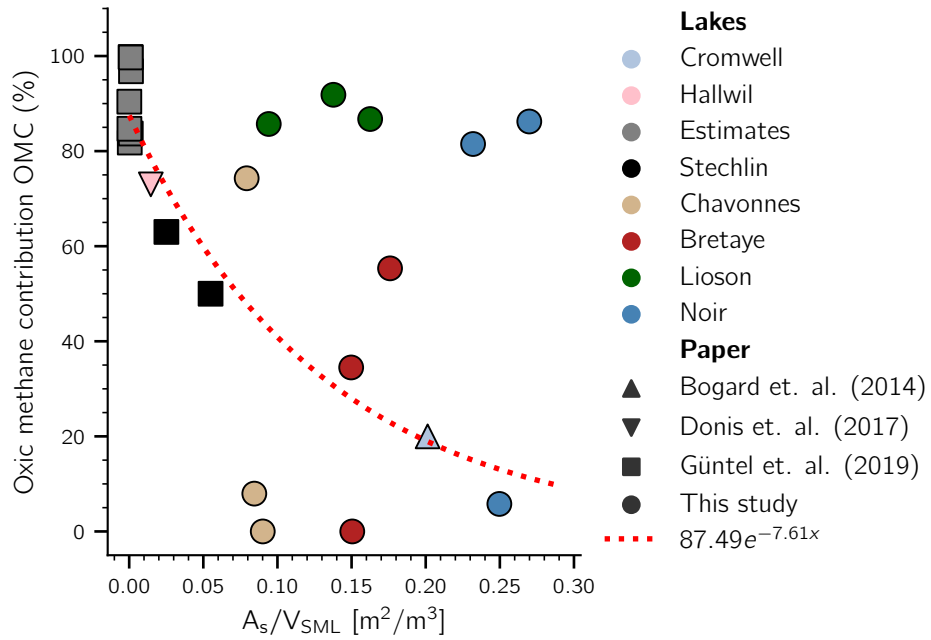


Figure S.A.14.  $P_{net}$  contribution to diffusive versus the ratio between the sediment area ( $A_s$ ) and the epilimnetic volume ( $V_{SML}$ ). The trend line  $y = 87.49e^{-7.61x}$  was proposed by Güntel *et al.* 2019.

---

# Supplementary Information

## Chapter 3

---

César Ordóñez<sup>1</sup>, Alexandrine Massot<sup>1</sup>, Tonya DelSontro<sup>1,2</sup>, Timon Langenegger<sup>1</sup>, and Daniel F. McGinnis<sup>1</sup>

<sup>1</sup>Aquatic Physics Group, Department F.-A. Forel for Environmental and Aquatic Sciences (DEFSE), Faculty of Science, University of Geneva, Uni Carl Vogt, 66 Boulevard Carl-Vogt, 1211 Geneva, Switzerland

<sup>1, 2</sup> Now at Department of Earth and Environmental Sciences, University of Waterloo, Ontario, Canada

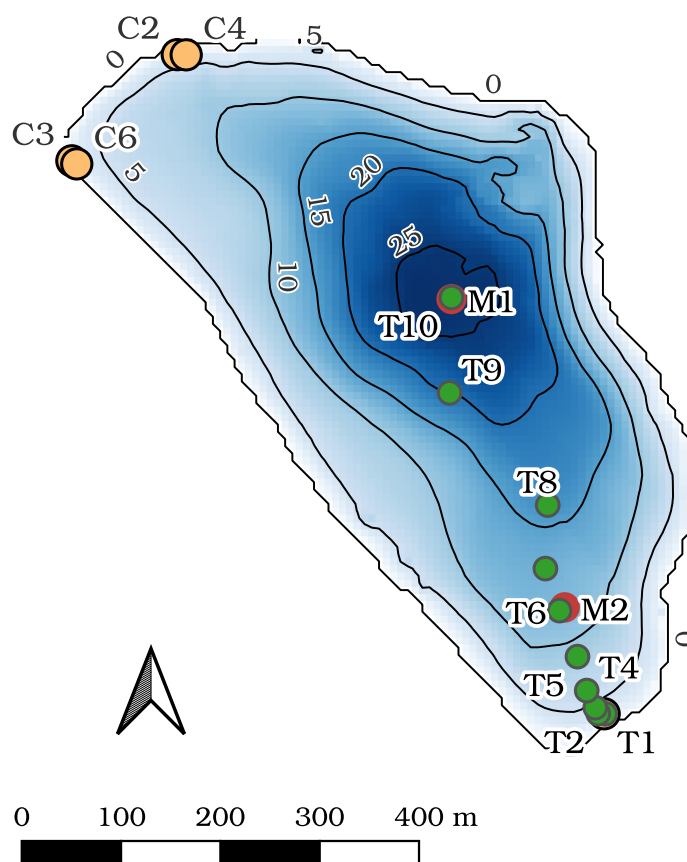


Figure S.B.1. Bathymetry of Soppensee and sampling locations.

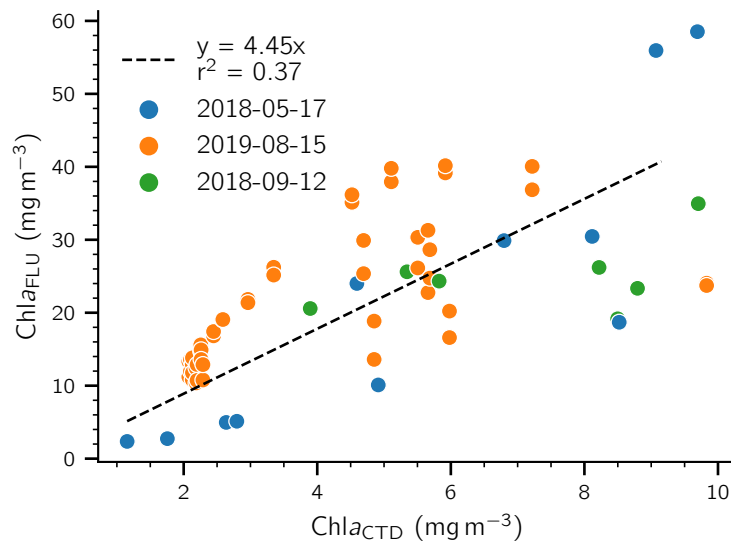


Figure S.B.2. Linear relationship between the chlorophyll-*a* concentration measured by the fluoroprobe ( $\text{Chla}_{\text{FLU}}$ ) and the Seabird SBE ( $\text{Chla}_{\text{CTD}}$ ).

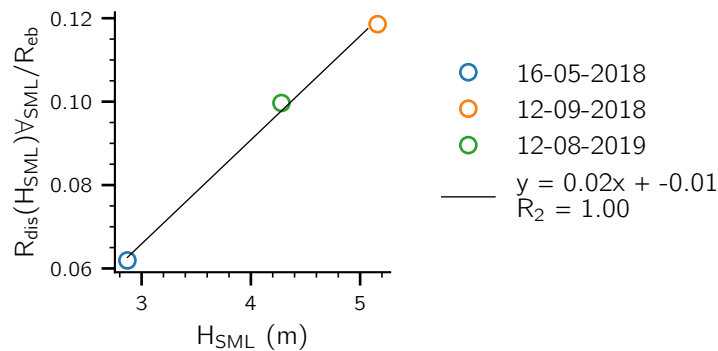


Figure S.B.3. Proportion of total bubble dissolution at the SML of the total ebullition flux versus surface mixed layer depth.

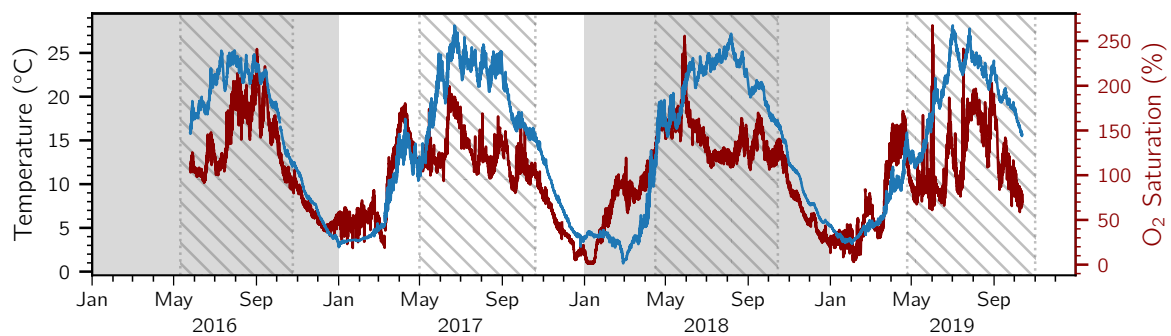


Figure S.B.4. Surface temperature and dissolved oxygen saturation. The shaded areas represent the determined the stratified period for every year.

Table S.B.1. Surface mixed layer depth ( $H_{\text{SML}}$ ), Secchi disk depth, littoral sediment area ( $A_s$ ), planar area at the bottom of the SML ( $A_p$ ) and SML volume ( $V_{\text{SML}}$ ) during the stratified period. The shaded areas represent the determined stratified period for every year.

Dates	$H_{\text{SML}}$ (m)	Secchi depth (m)	Chl <i>a</i> ( $\text{mg m}^{-3}$ )	$A_s$ ( $\text{m}^2$ )	$A_p$ ( $\text{m}^2$ )	$V_{\text{SML}}$ ( $\text{m}^3$ )
25-May-16	3.52			31,891	222,137	854,361
15-Jun-16	3.44			31,079	222,992	836,993
4-Jul-16	3.03			27,044	227,191	746,529
4-Aug-16	4.86	1.92		46,800	206,417	1,131,748
6-Oct-16	5.98	1.57		61,123	191,768	1,344,499
22-May-17	2.93	4.25		26,091	228,167	724,093
12-Jun-17	1.41	0.95	9.25	12,648	240,236	364,807
10-Jul-17	2.90	2.10	2.24	25,808	228,456	717,334
2-Aug-17	3.52	3.50		31,891	222,137	854,361
28-Aug-17	4.00	2.70	1.75	36,976	216,759	957,270
12-Oct-17	6.66	2.40		70,520	182,474	1,465,454
16-May-18	2.87	1.30	8.73	25,478	228,791	709,432
10-Jul-18	3.12	4.50	1.40	27,912	226,296	766,596
12-Sep-18	5.16	2.30	7.11	50,479	202,598	1,190,411
12-Aug-19	4.28	1.79	5.86	40,039	213,519	1,014,792
22-Oct-19	7.48	2.20	4.43	82,371	171,066	1,603,283

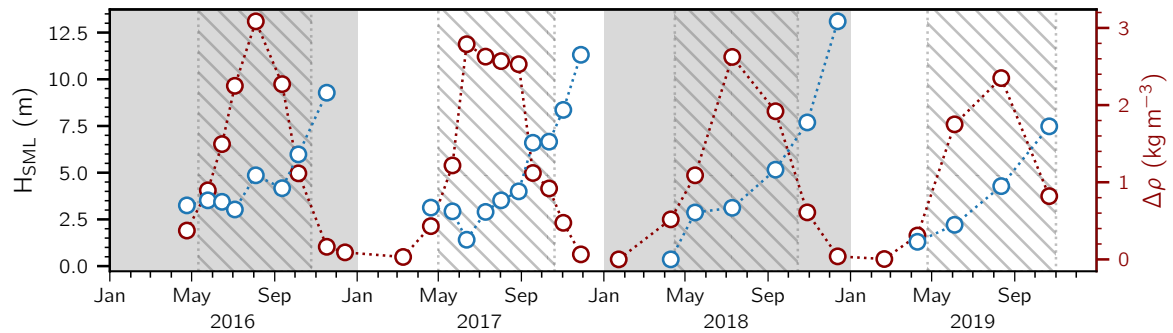


Figure S.B.5. Time series of the surface mixed layer depth ( $H_{\text{SML}}$ ) and the difference of average density between the SML and hypolimnion. The shaded areas represent the determined stratified period for every year.

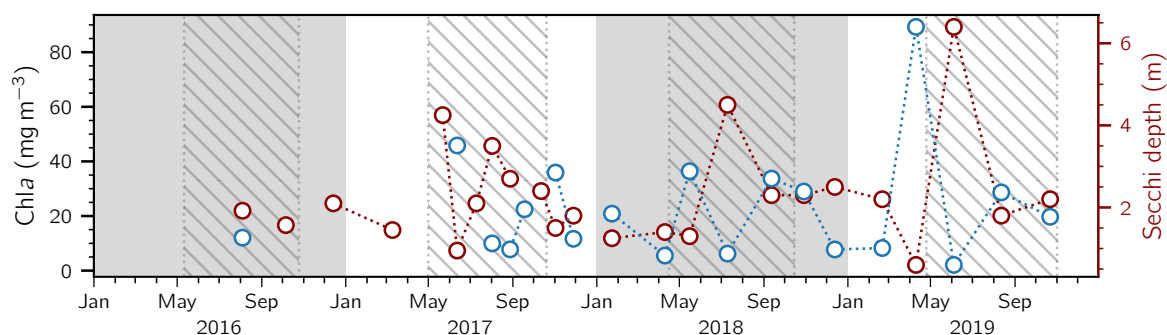


Figure S.B.6. Secchi depths and average chlorophyll-*a* concentrations (Chla) in the SML. The shaded areas represent the determined stratified period for every year.

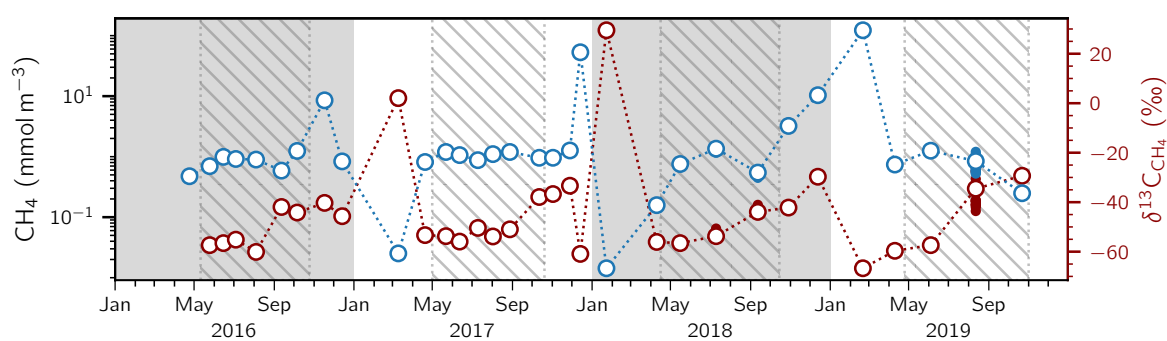


Figure S.B.7. Surface CH<sub>4</sub> concentrations and its isotopic signature ( $\delta^{13}\text{C}_{\text{CH}_4}$ ) from 2016 to 2019. The shaded areas represent the determined stratified period for every year.

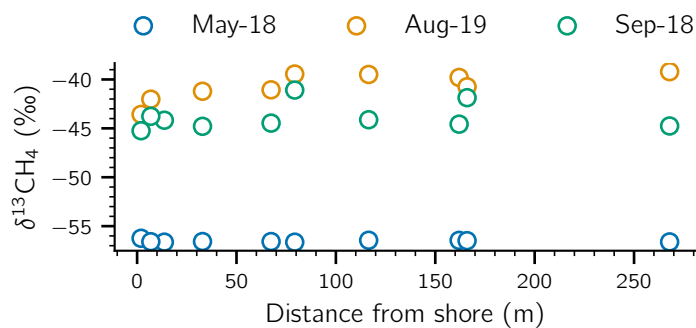


Figure S.B.8. Surface  $\delta^{13}\text{C}_{\text{CH}_4}$  along the transect from shore to center of the lake.

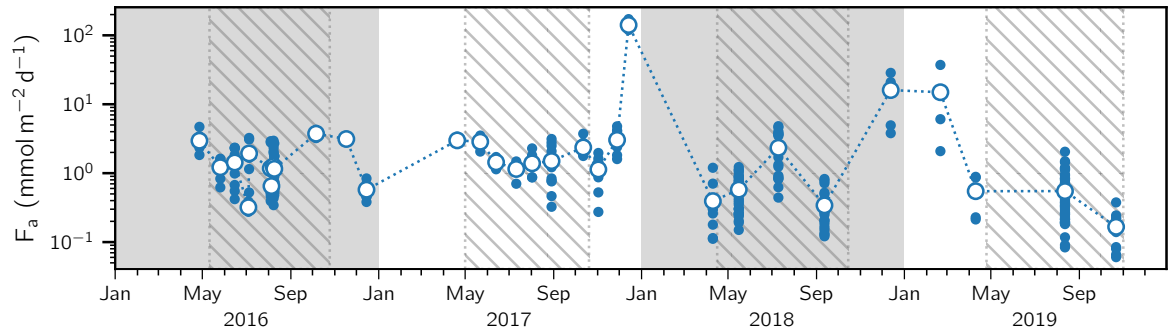


Figure S.B.9. Surface  $\text{CH}_4$  diffusive fluxes ( $F_a$ ) to the atmosphere from 2016 to 2019. The shaded areas represent the determined stratified period for every year.

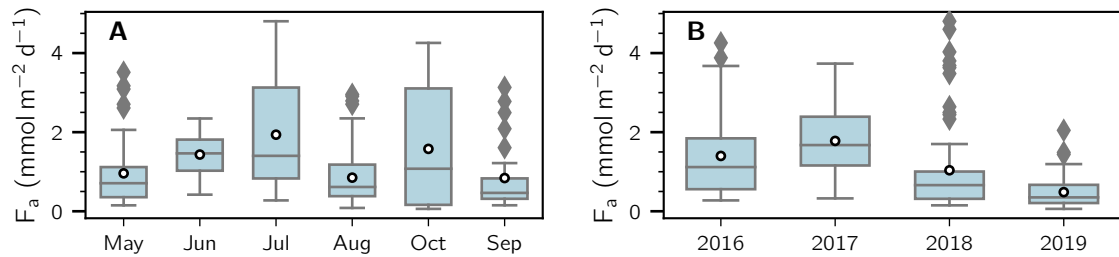


Figure S.B.10. **(A)** Monthly and **(B)** yearly average surface  $\text{CH}_4$  diffusive fluxes to the atmosphere ( $F_a$ ) during the stratified season from 2016 to 2019.

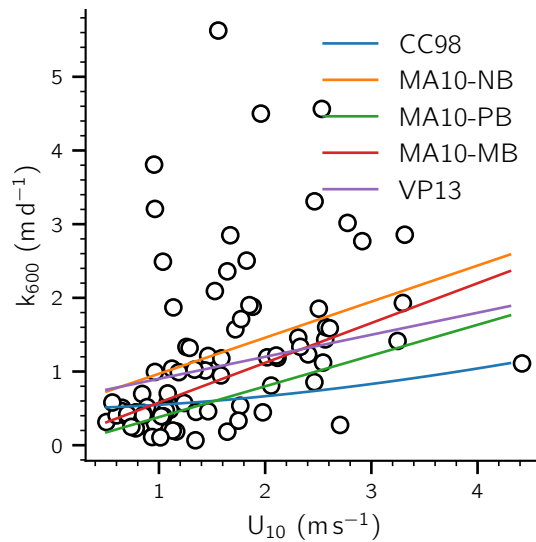


Figure S.B.11. Comparison between chambers based  $k_{600}$  (dots) with different wind based literature parameterization (CC98: Cole & Caraco 1998; MA10-NB, MA10-PB and MA-MB: MacIntyre *et al.* 2010 Negative Buoyancy, Positive Buoyancy and Mixed Model; VP13: Vachon & Prairie 2013).

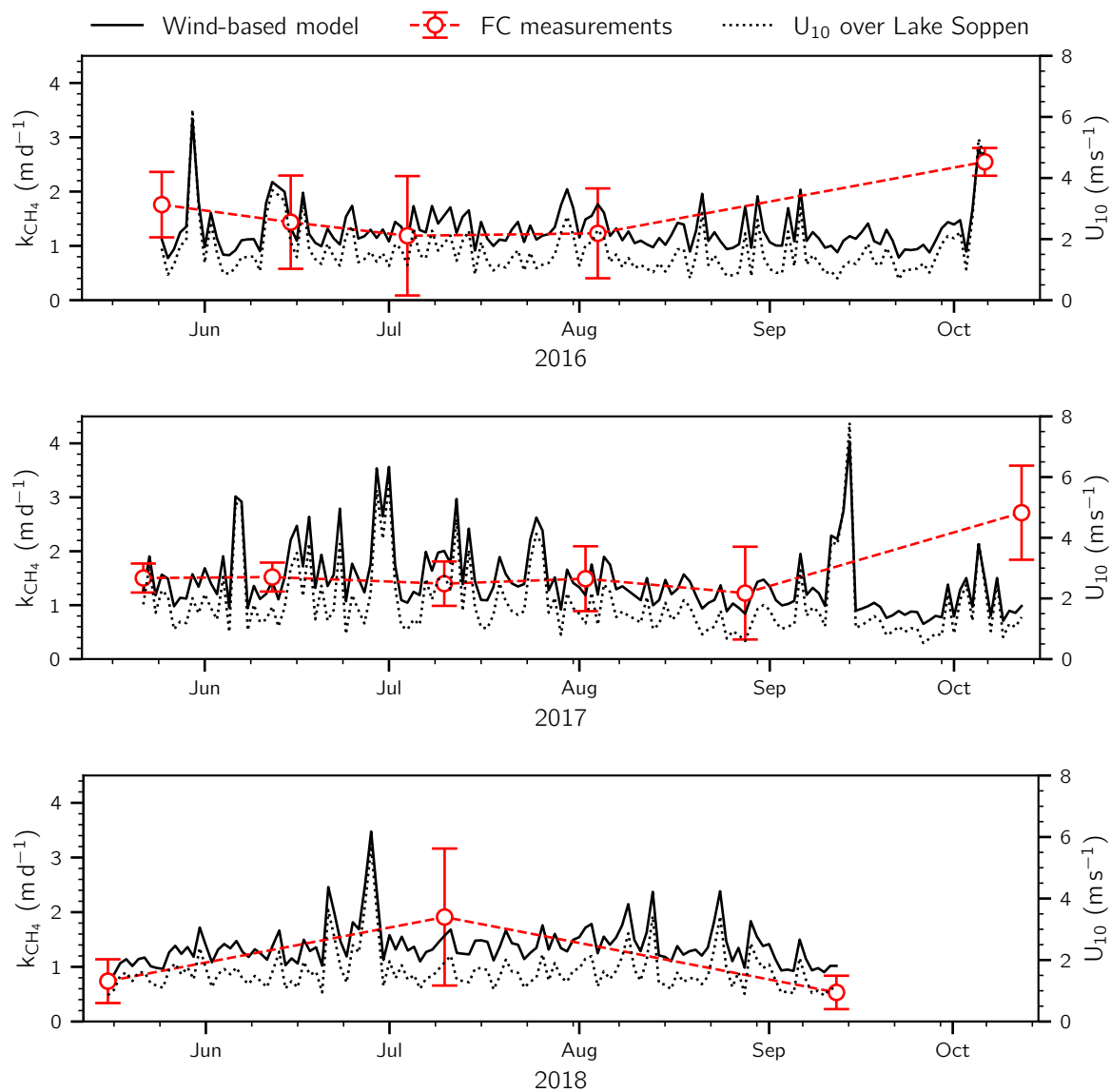


Figure S.B.12. Daily average wind-speed over the lake ( $U_{10}$ , black dotted line) and  $CH_4$  mass transfer coefficient ( $k_{CH_4}$ ) estimated from wind-based model (black line, MacIntyre *et al.* 2010 negative buoyancy) and chamber measurements estimations (red line) for the stratified period for 2016, 2017 and 2018.



Table S.B.2. Root mean square error (RMSE), determination coefficient ( $R^2$ ) and mean normalized bias (MNB) from the comparison between  $k_{600}$  parameterization and chamber-based mass transfer coefficient ( $k_{600,cb}$ ).

Parameterization	$R^2$	RMSE	MNB	Reference
CC98	-0.26	1.59	0.50	Cole & Caraco 1998
MA10-NB	0.14	1.08	0.0	MacIntyre <i>et al.</i> 2010 Negative buoyancy
MA10-PB	-0.18	1.48	0.50	MacIntyre <i>et al.</i> 2010 Positive buoyancy
MA10-MB	0.04	1.21	0.28	MacIntyre <i>et al.</i> 2010 Mixed buoyancy
VP13	0.09	1.15	0.14	Vachon & Prairie 2013

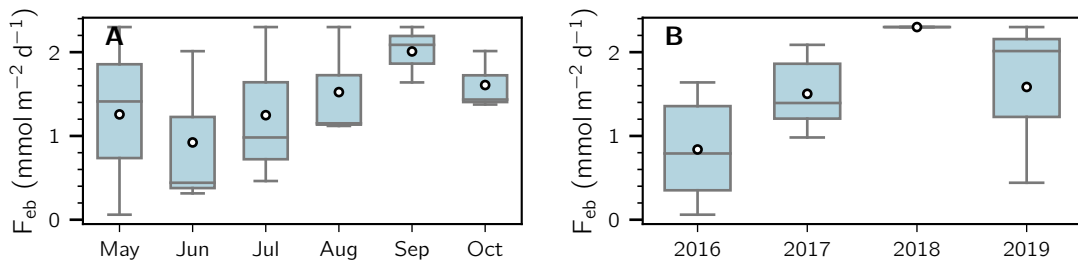


Figure S.B.13. (A) Monthly and (B) yearly average total ebullition flux of  $\text{CH}_4$  ( $F_{\text{ebul}}$ ) during the stratified season from 2016 to 2019.

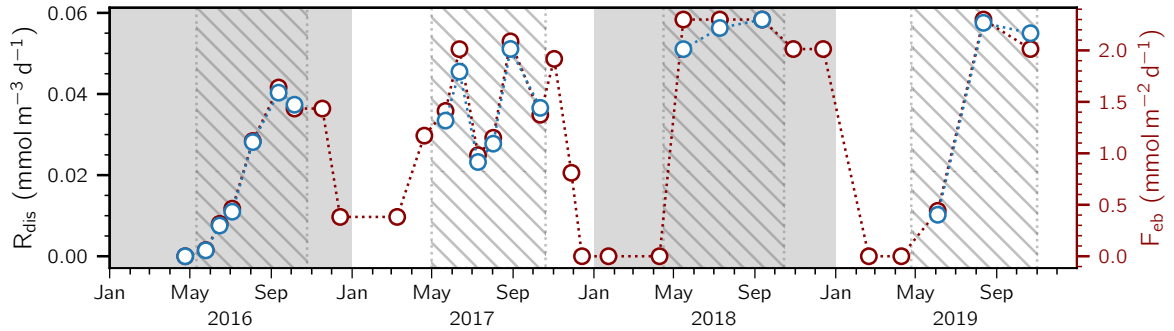


Figure S.B.14. Total ebullition flux ( $F_{\text{eb}}$ ) and bubble  $\text{CH}_4$  dissolution ( $R_{\text{dis}}$ ) in the SML from 2016 to 2019. The shaded areas represent the determined stratified period for every year.

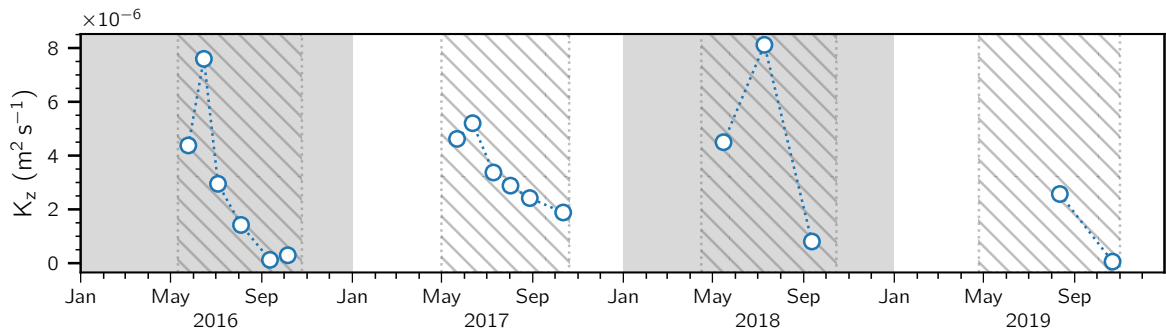


Figure S.B.15. Turbulent diffusion coefficient ( $K_z$ ) just below the bottom of the SML during the stratified period from 2016 to 2019. The shaded areas represent the determined stratified period for every year.

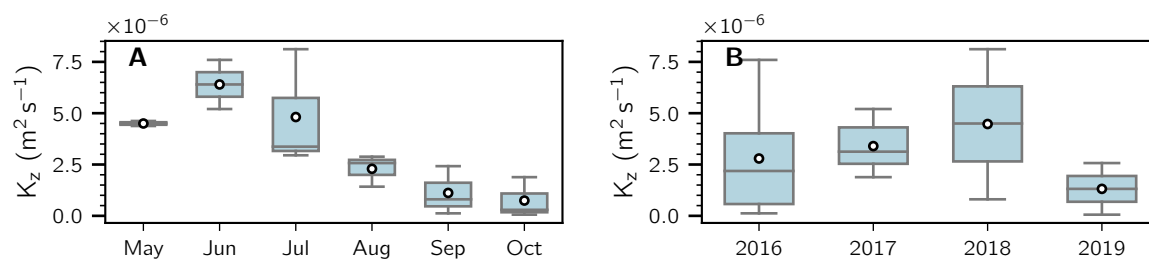


Figure S.B.16. (A) Monthly and (B) yearly average turbulent diffusive coefficient ( $K_z$ ) just below the bottom of the SML during the stratified season from 2016 to 2019.

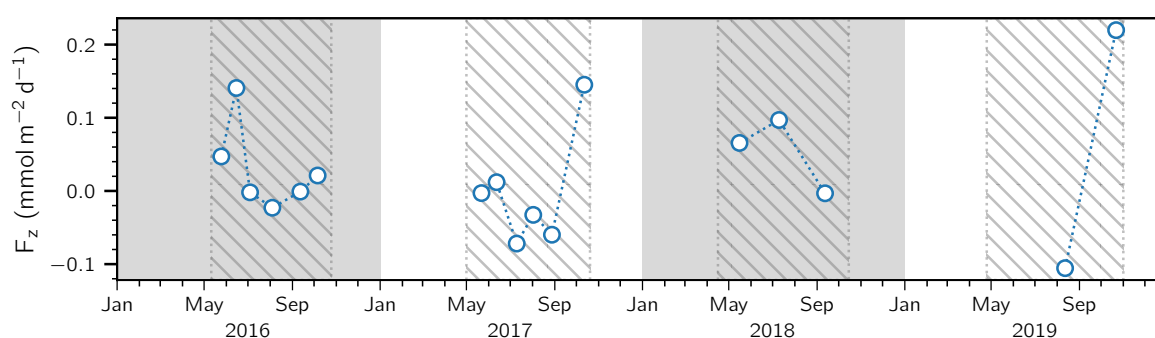


Figure S.B.17. Turbulent diffusive  $\text{CH}_4$  flux ( $F_z$ ) through the bottom of the SML during the stratified period from 2016 to 2019. The shaded areas represent the determined stratified period for every year.

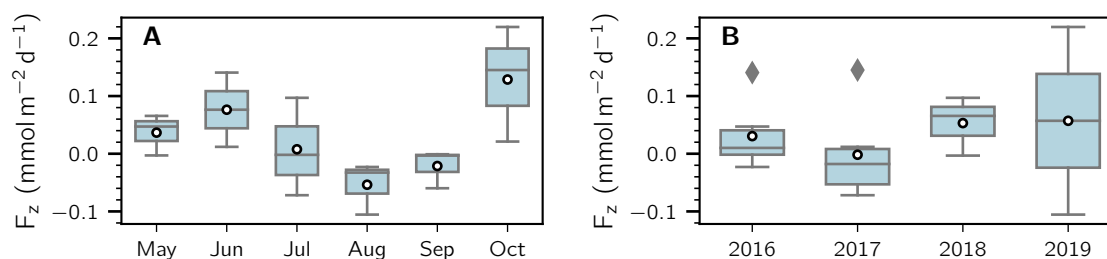


Figure S.B.18. (A) Monthly and (B) yearly average turbulent diffusive  $\text{CH}_4$  flux through the bottom of the SML during the stratified season from 2016 to 2019.

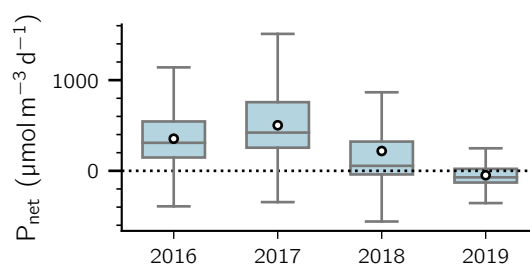


Figure S.B.19. Yearly average  $P_{\text{net}}$  rates in the SML during the stratified season from 2016 to 2019. The number of day averaged are 6, 7, 3 and 2 for 2016, 2017, 2018 and 2019 respectively.

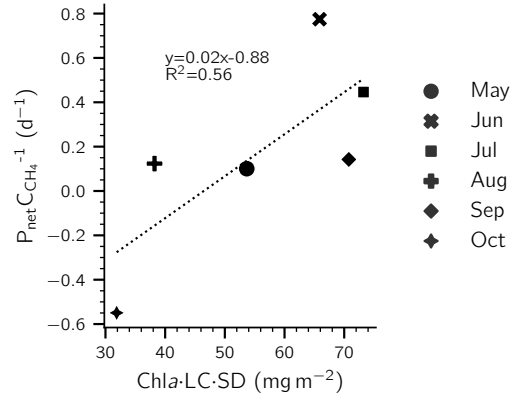


Figure S.B.20. Relation between the ration of  $P_{\text{net}}$  ( $\text{mmol m}^{-3} \text{d}^{-1}$ ) and the surface  $\text{CH}_4$  concentration ( $C_{\text{CH}_4}$ ,  $\text{mmol/m}^3$ ) versus chlorophyll- $a$   $\times$  light climate ( $\text{LC} = 2.5 \frac{\text{SD}}{H_{\text{SML}}}$ , -)  $\times$  Secchi disk depth (SD, m) proposed by Ordóñez *et al.* 2022b. Each point for were calculated as the monthly average during 2016 to 2019.

---

# Supplementary Information

## Chapter 4

---

César Ordóñez<sup>1</sup>, Héloïse Hannart<sup>2</sup>, Femke Hurtak<sup>2</sup>, Julie Seamann-Ricard<sup>1</sup>, Jannine Wetter<sup>3</sup>  
and Daniel F. McGinnis<sup>1</sup>

<sup>1</sup>Aquatic Physics Group, Department F.-A. Forel for Environmental and Aquatic Sciences (DEFSE), Faculty of Science, University of Geneva, Uni Carl Vogt, 66 Boulevard Carl-Vogt, 1211 Geneva, Switzerland

<sup>2</sup>École Polytechnique Fédérale de Lausanne (EPFL), Lausanne, Switzerland

<sup>3</sup>ETH Zürich, Zürich, Switzerland

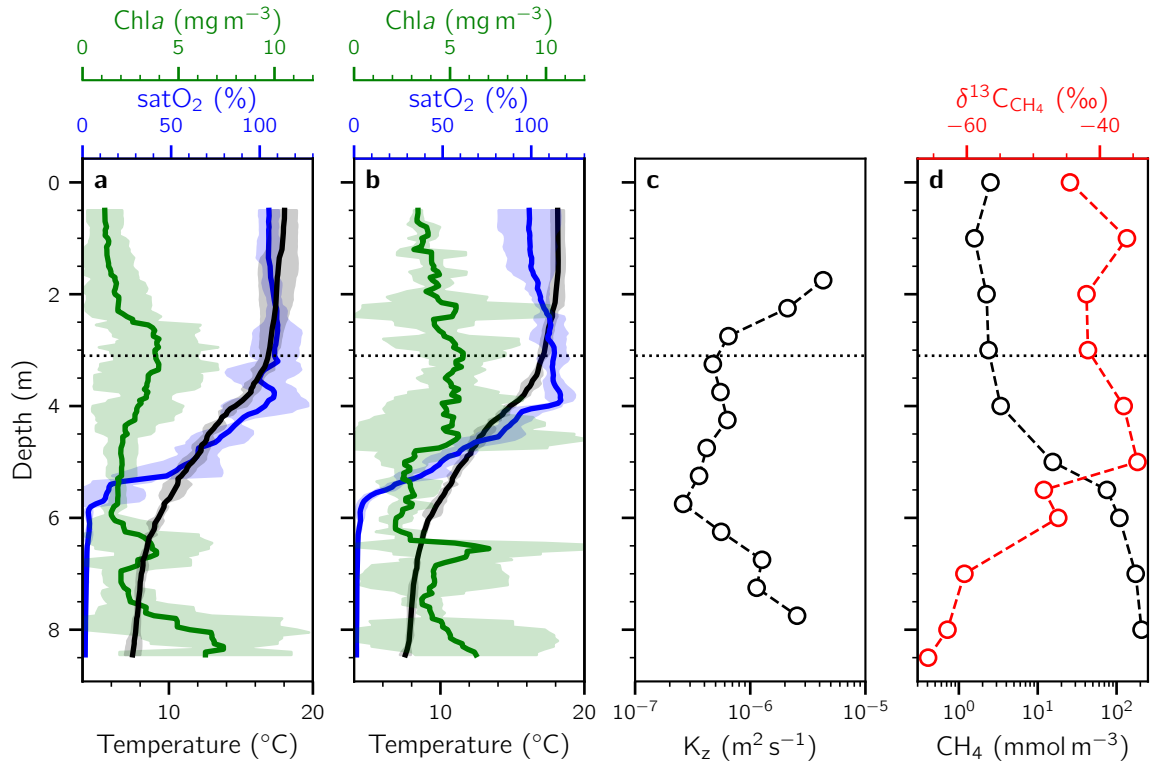


Figure S.C.1. **a** and **b** Water column profile for temperature, chlorophyll-a (Chla) concentration and oxygen saturation (satO<sub>2</sub>) for day (n=3, CTDs conducted at 4:50 PM, 11:30 AM and 2:00 PM) and night (n=3, CTDs conducted at 11:15 PM, 6:10 AM and 6:10 PM) conditions, respectively. **c** Average vertical turbulent diffusive coefficient ( $K_z$ ). **d** Water column profile of CH<sub>4</sub> concentrations and its isotopic signature ( $\delta^{13}\text{C}_{\text{CH}_4}$ ). The dashed line represents the SML depth ( $H_{SML}$ ).

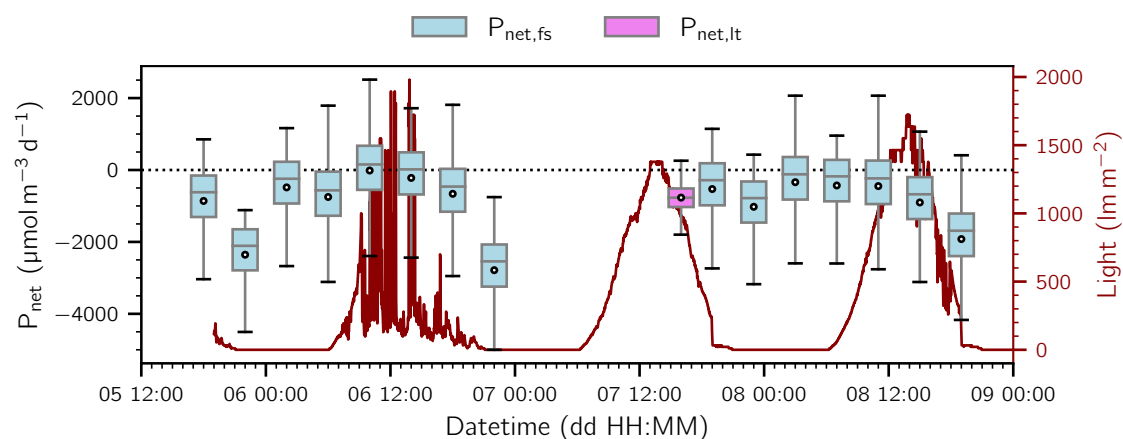


Figure S.C.2.  $P_{\text{net}}$  estimation using the full-scale mass balance ( $P_{\text{net,fs}}$ , light blue box) and the lateral transport model ( $P_{\text{net,lt}}$ , violet box) using  $F_{\text{sed}}=8.3 \text{ mmol/m}^2/\text{d}$ . Each box shows the first and third quartiles with the median (line), whiskers extend to the most extreme data point within 1.5 times the interquartile range from the box. The white dot represents the average of the distribution.

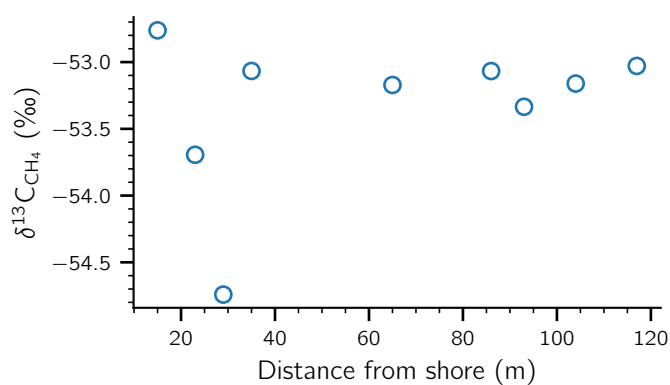


Figure S.C.3. Surface  $\text{CH}_4$  isotopic signature along the transect.

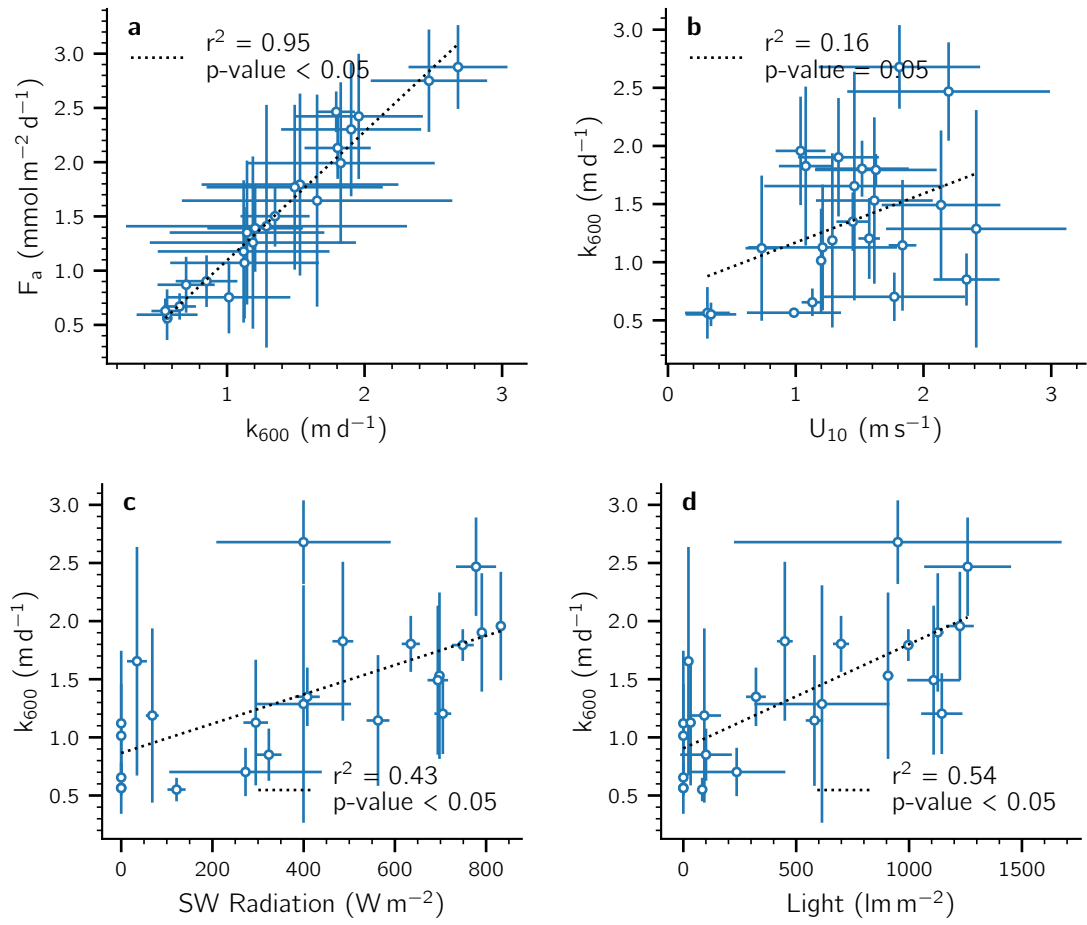


Figure S.C.4. **a** Correlation between the normalized mass transfer coefficient ( $k_{600}$ ) and the diffusive CH<sub>4</sub> emissions ( $F_a$ ). **b** Correlation between  $k_{600}$  versus **b** wind velocity at 10 m ( $U_{10}$ ), **c** short wave solar radiation and **d** light intensity at 4 m deep. The data was averaged at each sampling point and whiskers represent the standard deviation.

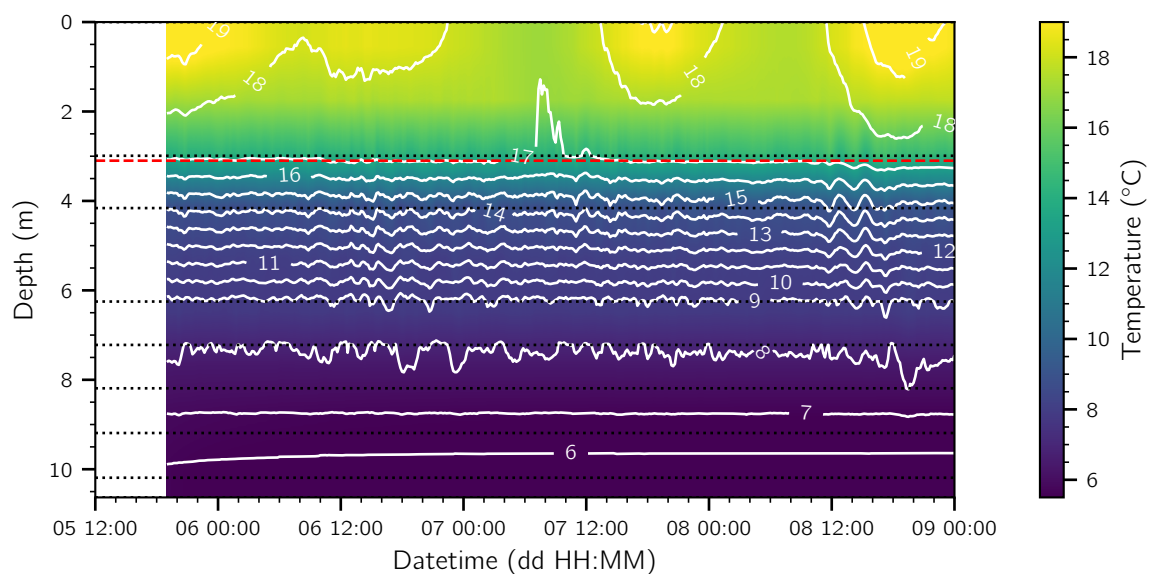


Figure S.C.5. Evolution of the temperature of the water column from 5<sup>th</sup> to 9<sup>th</sup> July 2020 at the deepest point of the lake (M1).

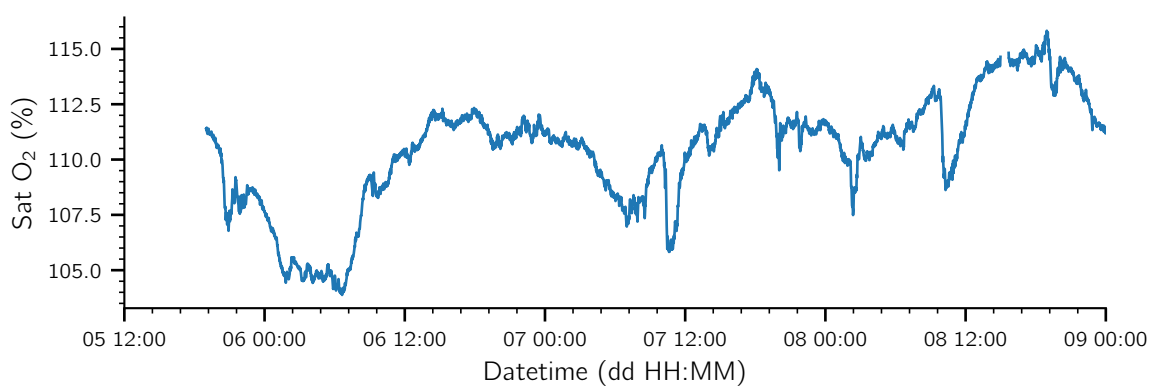


Figure S.C.6. Evolution of surface O<sub>2</sub> saturation at M1.

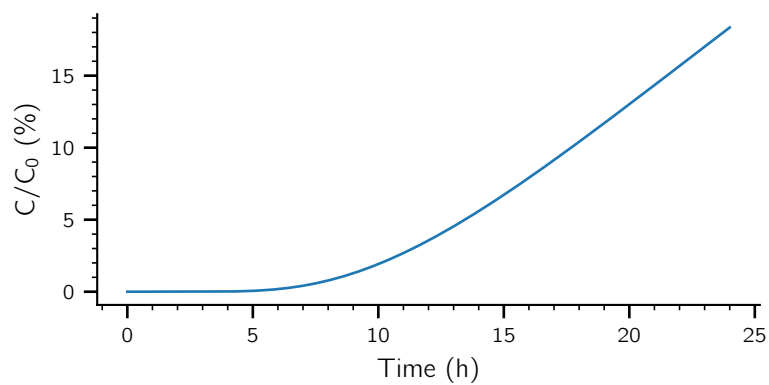


Figure S.C.7. Temporal variation of the percentage of change of the concentration at the center of the lake.



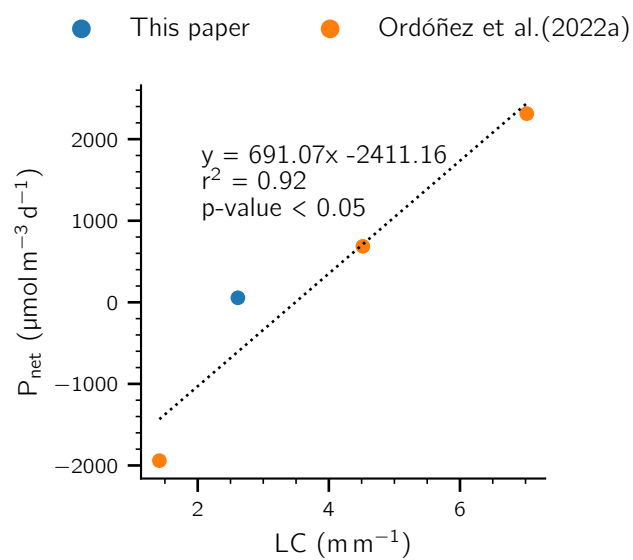


Figure S.C.8. Correlation between average net production rates in the SML ( $P_{\text{net}}$ ) during the day and light climate for the sampling campaigns on July 2020 (this study), June and Sept 2018 and July 2019 (Ordóñez *et al.* 2022b).

---

# Bibliography

1. Adrian, R., O'Reilly, C. M., Zagarese, H., Baines, S. B., Hessen, D. O., Keller, W., Livingstone, D. M., Sommaruga, R., Straile, D., Donk, E. V., Weyhenmeyer, G. A. & Winder, M. Lakes as Sentinels of Climate Change. *Limnology and Oceanography* **54**, 2283–2297. doi:[10.4319/lo.2009.54.6\\_part\\_2.2283](https://doi.org/10.4319/lo.2009.54.6_part_2.2283) (6, part 2 2009).
2. Bastviken, D., Cole, J., Pace, M. & Tranvik, L. Methane Emissions from Lakes: Dependence of Lake Characteristics, Two Regional Assessments, and a Global Estimate. *Global Biogeochemical Cycles* **18**, 1–12. doi:[10.1029/2004GB002238](https://doi.org/10.1029/2004GB002238) (2004).
3. Bastviken, D., Tranvik, L. J., Downing, J. A., Crill, P. M. & Enrich-Prast, A. Freshwater Methane Emissions Offset the Continental Carbon Sink. *Science* **331**, 50–50. doi:[10.1126/science.1196808](https://doi.org/10.1126/science.1196808) (2011).
4. Bastviken, D., Cole, J. J., Pace, M. L. & Van der Bogert, M. C. Fates of Methane from Different Lake Habitats: Connecting Whole-lake Budgets and CH<sub>4</sub> Emissions. *Journal of Geophysical Research: Biogeosciences* **113**. doi:[10.1029/2007JG000608](https://doi.org/10.1029/2007JG000608) (2008).
5. Bastviken, D., Ejlertsson, J. & Tranvik, L. Measurement of Methane Oxidation in Lakes: A Comparison of Methods. *Environmental Science & Technology* **36**, 3354–3361. doi:[10.1021/es010311p](https://doi.org/10.1021/es010311p) (2002).
6. Beaulieu, J. J., DelSontro, T. & Downing, J. A. Eutrophication Will Increase Methane Emissions from Lakes and Impoundments during the 21st Century. *Nature Communications* **10**, 1375. doi:[10.1038/s41467-019-09100-5](https://doi.org/10.1038/s41467-019-09100-5) (1 2019).

7. Bizic, M. Phytoplankton Photosynthesis: An Unexplored Source of Biogenic Methane Emission from Oxic Environments. *Journal of Plankton Research* **43**, 822–830. doi:[10.1093/plankt/fbab069](https://doi.org/10.1093/plankt/fbab069) (2021).
8. Bižić, M., Klintzsch, T., Ionescu, D., Hindiyeh, M. Y., Günthel, M., Muro-Pastor, A. M., Eckert, W., Urich, T., Keppler, F. & Grossart, H.-P. Aquatic and Terrestrial Cyanobacteria Produce Methane. *Science Advances* **6**, eaax5343. doi:[10.1126/sciadv.aax5343](https://doi.org/10.1126/sciadv.aax5343) (2020).
9. Bogard, M. J., del Giorgio, P. A., Boutet, L., Chaves, M. C. G., Prairie, Y. T., Merante, A. & Derry, A. M. Oxic Water Column Methanogenesis as a Major Component of Aquatic CH<sub>4</sub> Fluxes. *Nature communications* **5**, 5350–5350. doi:[10.1038/ncomms6350](https://doi.org/10.1038/ncomms6350) (May 2014).
10. Boudreau, B. P. *Diagenetic Models and Their Implementation: Modelling Transport and Reactions in Aquatic Sediments* (Springer Berlin Heidelberg, Berlin, Heidelberg, 1997).
11. Broecker, W. S. & Peng, T.-H. Gas Exchange Rates between Air and Sea. *Tellus* **26**, 21–35. doi:[10.3402/tellusa.v26i1-2.9733](https://doi.org/10.3402/tellusa.v26i1-2.9733) (1974).
12. Cannone, N., Diolaiuti, G., Guglielmin, M. & Sm, C. Accelerating Climate Change Impacts on Alpine Glacier Forefield Ecosystems in the European Alps. *Ecological Applications* **18**, 637–648 (2008).
13. Cole, J. J., Prairie, Y. T., Caraco, N. F., McDowell, W. H., Tranvik, L. J., Striegl, R. G., Duarte, C. M., Kortelainen, P., Downing, J. A., Middelburg, J. J. & Melack, J. Plumbing the Global Carbon Cycle: Integrating Inland Waters into the Terrestrial Carbon Budget. *Ecosystems* **10**, 171–184. doi:[10.1007/s10021-006-9013-8](https://doi.org/10.1007/s10021-006-9013-8) (2007).
14. Cole, J. J. & Caraco, N. F. Atmospheric Exchange of Carbon Dioxide in a Low-Wind Oligotrophic Lake Measured by the Addition of SF<sub>6</sub>. *Limnology and Oceanography* **43**, 647–656. doi:[10.4319/lo.1998.43.4.0647](https://doi.org/10.4319/lo.1998.43.4.0647) (1998).
15. Conrad, R. Quantification of Methanogenic Pathways Using Stable Carbon Isotopic Signatures: A Review and a Proposal. *Organic Geochemistry* **36**, 739–752. doi:[10.1016/j.orggeochem.2004.09.006](https://doi.org/10.1016/j.orggeochem.2004.09.006) (2005).

16. Conrad, R. The Global Methane Cycle: Recent Advances in Understanding the Microbial Processes Involved. *Environmental Microbiology Reports* **1**, 285–292. doi:[10.1111/j.1758-2229.2009.00038.x](https://doi.org/10.1111/j.1758-2229.2009.00038.x) (2009).
17. Damgaard, L., Revsbech, N. P. & Reichardt, W. Use of an Oxygen-Insensitive Microscale Biosensor for Methane to Measure Methane Concentration Profiles in a Rice Paddy. *Applied and Environmental Microbiology* **64**, 864–870 (1998).
18. DelSontro, T., Beaulieu, J. J. & Downing John A. Greenhouse Gas Emissions from Lakes and Impoundments: Upscaling in the Face of Global Change. *Limnology and Oceanography Letters* **0**. doi:[10.1002/lol2.10073](https://doi.org/10.1002/lol2.10073) (2018).
19. DelSontro, T., del Giorgio, P. A. & Prairie, Y. T. No Longer a Paradox: The Interaction Between Physical Transport and Biological Processes Explains the Spatial Distribution of Surface Water Methane Within and Across Lakes. *Ecosystems* **21**, 1073–1087. doi:[10.1007/s10021-017-0205-1](https://doi.org/10.1007/s10021-017-0205-1) (2018).
20. DelSontro, T., McGinnis, D. F., Sobek, S., Ostrovsky, I. & Wehrli, B. Extreme Methane Emissions from a Swiss Hydropower Reservoir: Contribution from Bubbling Sediments. *Environmental Science & Technology* **44**, 2419–2425 (2010).
21. Donis, D., Flury, S., Stöckli, A., Spangenberg, J. E., Vachon, D. & McGinnis, D. F. Full-Scale Evaluation of Methane Production under Oxic Conditions in a Mesotrophic Lake. *Nature Communications* **8**, 1–11. doi:[10.1038/s41467-017-01648-4](https://doi.org/10.1038/s41467-017-01648-4) (2017).
22. Encinas Fernández, J., Peeters, F. & Hofmann, H. On the Methane Paradox: Transport from Shallow Water Zones Rather than in Situ Methanogenesis Is the Major Source of CH<sub>4</sub> in the Open Surface Water of Lakes. *Journal of Geophysical Research G: Biogeosciences* **121**, 2717–2726. doi:[10.1002/2016JG003586](https://doi.org/10.1002/2016JG003586) (2016).
23. Ernst, L., Steinfeld, B., Barayeu, U., Klintzsch, T., Kurth, M., Grimm, D., Dick, T. P., Rebele, J. G., Bischofs, I. B. & Keppler, F. Methane Formation Driven by Reactive Oxygen Species across All Living Organisms. *Nature*, 1–6. doi:[10.1038/s41586-022-04511-9](https://doi.org/10.1038/s41586-022-04511-9) (2022).
24. Eyring, V., Gillett, N. P., Achutarao, K., Barimalala, R., Barreiro Parrillo, M., Bellouin, N., Cassou, C., Durack, P., Kosaka, Y. & McGregor, S. Human Influence on the

- Climate System: Contribution of Working Group I to the Sixth Assessment Report of the Intergovernmental Panel on Climate Change. *IPCC Sixth Assessment Report* (2021).
25. Flaim, G., Eccel, E., Zeileis, A., Toller, G., Cerasino, L. & Obertegger, U. Effects of Re-Oligotrophication and Climate Change on Lake Thermal Structure. *Freshwater Biology* **61**, 1802–1814. doi:[10.1111/fwb.12819](https://doi.org/10.1111/fwb.12819) (2016).
  26. Forster, P., Storelvmo, T., Armour, K., Collins, W., Dufresne, J.-L., Frame, D., Lunt, D., Mauritsen, T., Palmer, M., Watanabe, M., Wild, M. & Zhang, H. in Masson-Delmotte, V., Zhai, P., Pirani, A., Connors, S. L., Péan, C., Berger, S., Chaud, N., Chen, Y., Goldfarb, L., Gomis, M. I., Huang, M., Leitzell, K., Lonnoy, E., Matthews, J. B. R., Maycock, T. K., Waterfield, T., Yelekçi, O. & Yu, R. *Climate Change 2021: The Physical Science Basis. Contribution of Working Group I to the Sixth Assessment Report of the Intergovernmental Panel on Climate Change* (ed Zhou, B.) (Cambridge University Press, In Press).
  27. Grossart, H.-P., Frindte, K., Dziallas, C., Eckert, W. & Tang, K. W. Microbial Methane Production in Oxygenated Water Column of an Oligotrophic Lake. *Proceedings of the National Academy of Sciences* **108**, 19657–19661. doi:[10.1073/pnas.1110716108](https://doi.org/10.1073/pnas.1110716108) (2011).
  28. Gulev, S. K., Thorne, P. W., Ahn, J., Dentener, F. J., Domingues, C. M., Gong, S. G. D., Kaufman, D. S., Nnamchi, H. C., Rivera, J. & Sathyendranath, S. in *Climate Change 2021: The Physical Science Basis. Contribution of Working Group I to the Sixth Assessment Report of the Intergovernmental Panel on Climate Change* [Masson-Delmotte, V., P. Zhai, A. Pirani, S. L. Connors, C. Péan, S. Breger, N. Caud, Y. Chen, L. Goldfarb, M. I. Gomis, M. Huang, K. Leitzell, E. Lonnoy, J. B. R. Matthews, T. K. Maycock, T. Waterfield, O. Yelekçi, R. Yu and B. Zhou (eds.)] (Cambridge University Press, 2021).
  29. Günthel, M., Donis, D., Kirillin, G., Ionescu, D., Bizic, M., McGinnis, D. F., Grossart, H.-P. & Tang, K. W. Contribution of Oxidic Methane Production to Surface Methane Emission in Lakes and Its Global Importance. *Nature Communications* **10**, 1–10. doi:[10.1038/s41467-019-13320-0](https://doi.org/10.1038/s41467-019-13320-0) (2019).
  30. Günthel, M., Donis, D., Kirillin, G., Ionescu, D., Bizic, M., McGinnis, D. F., Grossart, H.-P. & Tang, K. W. Reply to ‘Oxidic Methanogenesis Is Only a Minor Source of

- Lake-Wide Diffusive CH<sub>4</sub> Emissions from Lakes'. *Nature Communications* **12**, 1205. doi:[10.1038/s41467-021-21216-1](https://doi.org/10.1038/s41467-021-21216-1) (1 2021).
31. Günthel, M., Klawonn, I., Woodhouse, J., Bižić, M., Ionescu, D., Ganzert, L., Kümmel, S., Nijenhuis, I., Zoccarato, L., Grossart, H.-P. & Tang, K. W. Photosynthesis-driven Methane Production in Oxidic Lake Water as an Important Contributor to Methane Emission. *Limnology and Oceanography*, Ino.11557. doi:[10.1002/lno.11557](https://doi.org/10.1002/lno.11557) (2020).
  32. Guo, M., Zhuang, Q., Tan, Z., Shurpali, N., Juutinen, S., Kortelainen, P. & Martikainen, P. J. Rising Methane Emissions from Boreal Lakes Due to Increasing Ice-Free Days. *Environmental Research Letters* **15**, 064008. doi:[10.1088/1748-9326/ab8254](https://doi.org/10.1088/1748-9326/ab8254) (2020).
  33. Hadley, K. R., Paterson, A. M., Stainsby, E. A., Michelutti, N., Yao, H., Rusak, J. A., Ingram, R., McConnell, C. & Smol, J. P. Climate Warming Alters Thermal Stability but Not Stratification Phenology in a Small North-Temperate Lake. *Hydrological Processes* **28**, 6309–6319. doi:[10.1002/hyp.10120](https://doi.org/10.1002/hyp.10120) (2014).
  34. Hardenbroek, M. V., Lotter, A. F., Bastviken, D., Duc, N. T. & Heiri, O. Relationship between  $\delta^{13}\text{C}$  of Chironomid Remains and Methane Flux in Swedish Lakes. *Freshwater Biology* **57**, 166–177. doi:[10.1111/j.1365-2427.2011.02710.x](https://doi.org/10.1111/j.1365-2427.2011.02710.x) (2012).
  35. Harris, C. R. *et al.* Array Programming with NumPy. *Nature* **585**, 357–362. doi:[10.1038/s41586-020-2649-2](https://doi.org/10.1038/s41586-020-2649-2) (2020).
  36. Harrison, J. W., Beecraft, L. & Smith, R. E. H. Implications of Irradiance Exposure and Non-Photochemical Quenching for Multi-Wavelength (Bbe FluoroProbe) Fluorometry. *Journal of Photochemistry and Photobiology B: Biology* **189**, 36–48. doi:[10.1016/j.jphotobiol.2018.09.013](https://doi.org/10.1016/j.jphotobiol.2018.09.013) (2018).
  37. Hartmann, J. F., Günthel, M., Klintzsch, T., Kirillin, G., Grossart, H.-P., Keppler, F. & Isenbeck-Schröter, M. High Spatiotemporal Dynamics of Methane Production and Emission in Oxidic Surface Water. *Environmental Science & Technology* **54**, 1451–1463. doi:[10.1021/acs.est.9b03182](https://doi.org/10.1021/acs.est.9b03182) (2020).
  38. Hartmann, D. L., A. M. G. Klein Tank, M. Rusticucci, L. V. Alexander, S. Brönnimann, Y. Charabi, F. J. Dentener, E. J. Dlugokencky, D. R. Easterling, A. Kaplan, B. J. Soden, P. W. Thorne, M. Wild & P. M. Zhai. in *Climate Change 2013: The Physical Science Basis. Contribution of Working Group I to the Fifth Assessment Report of the*

- Intergovernmental Panel on Climate Change [Stocker, T.F., D. Qin, G.-K. Plattner, M. Tignor, S.K. Allen, J. Boschung, A. Nauels, Y. Xia, V. Bex and P.M. Midgley (Eds.)]. Cambridge University Press (Cambridge, United Kingdom and New York, NY, USA, 2013).*
39. Hilt, S., Grossart, H.-P., McGinnis, D. F. & Keppler, F. Potential Role of Submerged Macrophytes for Oxic Methane Production in Aquatic Ecosystems. *Limnology and Oceanography* (in press) (2022).
  40. Hofmann, H., Federwisch, L. & Peeters, F. Wave-Induced Release of Methane: Littoral Zones as a Source of Methane in Lakes. *Limnology and Oceanography* **55**, 1990–2000. doi:[10.4319/lo.2010.55.5.1990](https://doi.org/10.4319/lo.2010.55.5.1990) (2010).
  41. Huttunen, J. T., Väisänen, T. S., Hellsten, S. K. & Martikainen, P. J. Methane Fluxes at the Sediment–Water Interface in Some Boreal Lakes and Reservoirs. *Boreal Environment Research* **11**, 27–34 (2006).
  42. Imboden, D. M. & Wüest, A. in Lerman, A. & Wüest, A. *Physics and Chemistry of Lakes* (ed Gat, J. R.) 83–138 (Springer-Verlag, 1995).
  43. IPCC. *Summary for Policymakers. In: Climate Change 2021: The Physical Science Basis. Contribution of Working Group I to the Sixth Assessment Report of the Intergovernmental Panel on Climate Change* (Cambridge University Press, 2021).
  44. IPCC. *Climate Change 2022: Mitigation of Climate Change. Contribution of Working Group III to the Sixth Assessment Report of the Intergovernmental Panel on Climate Change* [P.R. Shukla, J. Skea, R. Slade, A. Al Khourdajie, R. van Diemen, D. McCollum, M. Pathak, S. Some, P. Vyas, R. Fradera, M. Belkacemi, A. Hasija, G. Lisboa, S. Luz, J. Malley, (eds.)] (Cambridge University Press, Cambridge, UK and New York, NY, USA, 2022).
  45. Karl, D. M., Beversdorf, L., Björkman, K. M., Church, M. J., Martinez, A. & Delong, E. F. Aerobic Production of Methane in the Sea. *Nature Geoscience* **1**, 473–478. doi:[10.1038/ngeo234](https://doi.org/10.1038/ngeo234) (2008).
  46. Keeling, C. D. The Concentration and Isotopic Abundances of Atmospheric Carbon Dioxide in Rural Areas. *Geochimica et Cosmochimica Acta* **13**, 322–334 (1958).

47. Khatun, S., Iwata, T., Kojima, H., Fukui, M., Aoki, T., Mochizuki, S., Naito, A., Kobayashi, A. & Uzawa, R. Aerobic Methane Production by Planktonic Microbes in Lakes. *Science of The Total Environment* **696**, 133916. doi:[10.1016/j.scitotenv.2019.133916](https://doi.org/10.1016/j.scitotenv.2019.133916) (2019).
48. Khatun, S., Iwata, T., Kojima, H., Ikarashi, Y., Yamanami, K., Imazawa, D., Kenta, T., Shinohara, R. & Saito, H. Linking Stoichiometric Organic Carbon–Nitrogen Relationships to Planktonic Cyanobacteria and Subsurface Methane Maximum in Deep Freshwater Lakes. *Water* **12**, 402. doi:[10.3390/w12020402](https://doi.org/10.3390/w12020402) (2020).
49. King, G. Ecological Aspects of Methane Oxidation, A Key Determinant of Global Methane Dynamics. *Advances in Microbial Ecology* **12**, 431–468. doi:[10.1007/978-1-4684-7609-5\\_9](https://doi.org/10.1007/978-1-4684-7609-5_9) (1992).
50. Klaus, M. & Vachon, D. Challenges of Predicting Gas Transfer Velocity from Wind Measurements over Global Lakes. *Aquatic Sciences* **82**, 53. doi:[10.1007/s00027-020-00729-9](https://doi.org/10.1007/s00027-020-00729-9) (2020).
51. Klintzsch, T., Langer, G., Wieland, A., Geisinger, H., Lenhart, K., Nehrke, G. & Keppler, F. Effects of Temperature and Light on Methane Production of Widespread Marine Phytoplankton. *Journal of Geophysical Research: Biogeosciences* **125**, e2020JG005793. doi:[10.1029/2020JG005793](https://doi.org/10.1029/2020JG005793) (2020).
52. Koschorreck, M., Hentschel, I. & Boehrer, B. Oxygen Ebullition From Lakes. *Geophysical Research Letters* **44**, 1–7. doi:[10.1002/2017GL074591](https://doi.org/10.1002/2017GL074591) (2017).
53. Kreling, J., Bravidor, J., McGinnis, D. F., Koschorreck, M. & Lorke, A. Physical Controls of Oxygen Fluxes at Pelagic and Benthic Oxyclines in a Lake. *Limnology and Oceanography* **59**, 1637–1650. doi:[10.4319/lo.2014.59.5.1637](https://doi.org/10.4319/lo.2014.59.5.1637) (2014).
54. Langenegger, T., Vachon, D., Donis, D. & McGinnis, D. F. What the Bubble Knows: Lake Methane Dynamics Revealed by Sediment Gas Bubble Composition. *Limnology and Oceanography*, 19 (2019).
55. Langenegger, T., Vachon, D., Donis, D. & McGinnis, D. F. Unraveling Lake CH<sub>4</sub> Oxidation Using Modelling of CH<sub>4</sub> Concentration and  $\delta^{13}\text{C}_{\text{CH}_4}$ . *Limnology and Oceanography* (submitted) (2022).



56. Lee, J.-Y., Marotzke, J., Bala, G., Cao, L., Corti, S., Dunne, J. P., Engelbrecht, F., Fischer, E., Fyfe, J. C. & Jones, C. in *Climate Change 2021: The Physical Science Basis. Contribution of Working Group I to the Sixth Assessment Report of the Intergovernmental Panel on Climate Change* [Masson-Delmotte, V., P. Zhai, A. Pirani, S. L. Connors, C. Péan, S. Breger, N. Caud, Y. Chen, L. Goldfarb, M. I. Gomis, M. Huang, K. Leitzell, E. Lonnoy, J. B. R. Matthews, T. K. Maycock, T. Waterfield, O. Yelekçi, R. Yu and B. Zhou (eds.)] (Cambridge University Press, 2021).
57. León-Palmero, E., Contreras-Ruiz, A., Sierra, A., Morales-Baquero, R. & Reche, I. Dissolved CH<sub>4</sub> Coupled to Photosynthetic Picoeukaryotes in Oxic Waters and to Cumulative Chlorophyll *a* in Anoxic Waters of Reservoirs. *Biogeosciences* **17**, 3223–3245. doi:[10.5194/bg-17-3223-2020](https://doi.org/10.5194/bg-17-3223-2020) (2020).
58. Li, W., Dore, J. E., Steigmeyer, A. J., Cho, Y.-J., Kim, O.-S., Liu, Y., Morgan-Kiss, R. M., Skidmore, M. L. & Priscu, J. C. Methane Production in the Oxygenated Water Column of a Perennially Ice-covered Antarctic Lake. *Limnology and Oceanography*. doi:[10.1002/lno.11257](https://doi.org/10.1002/lno.11257) (2019).
59. Li, Y., Fichot, C. G., Geng, L., Scarratt, M. G. & Xie, H. The Contribution of Methane Photoproduction to the Oceanic Methane Paradox. *Geophysical Research Letters* **47**, e2020GL088362. doi:[10.1029/2020GL088362](https://doi.org/10.1029/2020GL088362) (2020).
60. Liikanen, A. & Martikainen, P. J. Effect of Ammonium and Oxygen on Methane and Nitrous Oxide Fluxes across Sediment–Water Interface in a Eutrophic Lake. *Chemosphere* **52**, 1287–1293. doi:[10.1016/S0045-6535\(03\)00224-8](https://doi.org/10.1016/S0045-6535(03)00224-8) (2003).
61. Liikanen, A., Murtoniemi, T., Tanskanen, H., Väisänen, T. & Martikainen, P. J. Effects of Temperature and Oxygenavailability on Greenhouse Gas and Nutrient Dynamics in Sediment of a Eutrophic Mid-Boreal Lake. *Biogeochemistry* **59**, 269–286. doi:[10.1023/A:1016015526712](https://doi.org/10.1023/A:1016015526712) (2002).
62. Lods-Crozet, B. & Reymond, O. Evaluation de l'état écologique de deux lacs sub-alpins suisses (canton de Vaud). *Bulletin of the Vaudoise Society of Natural Sciences* **91**, 157–173 (2008).

63. Lorke, A., Bodmer, P., Noss, C., Alshboul, Z., Koschorreck, M., Bastviken, D., Flury, S., McGinnis, D. F., Maeck, A. & Premke, K. Technical Note: Drifting versus Anchored Flux Chambers for Measuring Greenhouse Gas Emissions from Running Waters. *Biogeosciences* **12**, 7013–7024. doi:[10.5194/bg-12-7013-2015](https://doi.org/10.5194/bg-12-7013-2015) (2015).
64. Lorke, A. & Wüest, A. Probability Density of Displacement and Overturning Length Scales under Diverse Stratification. *Journal of Geophysical Research: Oceans* **107**, 3214. doi:[10.1029/2001JC001154](https://doi.org/10.1029/2001JC001154) (2002).
65. Lotter, A. F. Evidence of Annual Layering in Holocene Sediments of Soppensee, Switzerland. *Aquatic Sciences* **51**, 19–30. doi:[10.1007/BF00877778](https://doi.org/10.1007/BF00877778) (1989).
66. Loulergue, L., Schilt, A., Spahni, R., Masson-Delmotte, V., Blunier, T., Lemieux, B., Barnola, J.-M., Raynaud, D., Stocker, T. F. & Chappellaz, J. Orbital and Millennial-Scale Features of Atmospheric CH<sub>4</sub> over the Past 800,000 Years. *Nature* **453**, 383–386. doi:[10.1038/nature06950](https://doi.org/10.1038/nature06950) (2008).
67. Luxem, K. E., Leavitt, W. D. & Zhang, X. Large Hydrogen Isotope Fractionation Distinguishes Nitrogenase-Derived Methane from Other Methane Sources. *Applied and Environmental Microbiology* **86**. doi:[10.1128/AEM.00849-20](https://doi.org/10.1128/AEM.00849-20) (2020).
68. Mach, V., Blaser, M. B., Claus, P., Chaudhary, P. P. & Rulík, M. Methane Production Potentials, Pathways, and Communities of Methanogens in Vertical Sediment Profiles of River Sitka. *Frontiers in Microbiology* **6**, 1–12. doi:[10.3389/fmicb.2015.00506](https://doi.org/10.3389/fmicb.2015.00506) (MAY 2015).
69. MacIntyre, S. Vertical Mixing in a Shallow, Eutrophic Lake: Possible Consequences for the Light Climate of Phytoplankton. *Limnology and Oceanography* **38**, 798–817. doi:[10.4319/lo.1993.38.4.0798](https://doi.org/10.4319/lo.1993.38.4.0798) (1993).
70. MacIntyre, S., Amaral, J. H. & Melack, J. M. Enhanced Turbulence in the Upper Mixed Layer under Light Winds and Heating: Implications for Gas Fluxes. *Journal of Geophysical Research: Oceans* **n/a**, e2020JC017026. doi:[10.1029/2020JC017026](https://doi.org/10.1029/2020JC017026) (2021).
71. MacIntyre, S., Jonsson, A., Jansson, M., Aberg, J., Turney, D. E. & Miller, S. D. Buoyancy Flux, Turbulence, and the Gas Transfer Coefficient in a Stratified Lake. *Geophysical Research Letters* **37**, 2–6. doi:[10.1029/2010GL044164](https://doi.org/10.1029/2010GL044164) (2010).

72. McGinnis, D. F., Greinert, J., Artemov, Y., Beaubien, S. E. & Wüest, A. Fate of Rising Methane Bubbles in Stratified Waters: How Much Methane Reaches the Atmosphere? *Journal of Geophysical Research: Oceans* **111**, 1–15. doi:[10.1029/2005JC003183](https://doi.org/10.1029/2005JC003183) (2006).
73. McGinnis, D. F., Kirillin, G., Tang, K. W., Flury, S., Bodmer, P., Engelhardt, C., Casper, P. & Grossart, H.-P. Enhancing Surface Methane Fluxes from an Oligotrophic Lake: Exploring the Microbubble Hypothesis. *Environmental Science and Technology* **49**, 873–880. doi:[10.1021/es503385d](https://doi.org/10.1021/es503385d) (2015).
74. Melack, J. M. & Kilham, P. Photosynthetic Rates of Phytoplankton in East African Alkaline, Saline Lakes. *Limnology and Oceanography* **19**, 743–755. doi:[10.4319/lo.1974.19.5.0743](https://doi.org/10.4319/lo.1974.19.5.0743) (1974).
75. Meure, C. M., Etheridge, D., Trudinger, C., Steele, P., Langenfelds, R., van Ommen, T., Smith, A. & Elkins, J. Law Dome CO<sub>2</sub>, CH<sub>4</sub> and N<sub>2</sub>O Ice Core Records Extended to 2000 Years BP. *Geophysical Research Letters* **33**. doi:[10.1029/2006GL026152](https://doi.org/10.1029/2006GL026152) (2006).
76. Morana, C., Bouillon, S., Nolla-Ardèvol, V., Roland, F. A. E., Okello, W., Descy, J.-P., Nankabirwa, A., Nabafu, E., Springael, D. & Borges, A. V. Methane Paradox in Tropical Lakes? Sedimentary Fluxes Rather than Water Column Production in Oxidic Waters Sustain Methanotrophy and Emissions to the Atmosphere. *Biogeosciences Discussions*, 1–20. doi:[10.5194/bg-2020-142](https://doi.org/10.5194/bg-2020-142) (2020).
77. Myhre, G. *et al.* in *Climate Change 2013: The Physical Science Basis. Contribution of Working Group I to the Fifth Assessment Report of the Intergovernmental Panel on Climate Change* (Cambridge University Press, Cambridge, United Kingdom and New York, NY, USA, 2013).
78. Nisbet, E. G. *et al.* Very Strong Atmospheric Methane Growth in the 4 Years 2014–2017: Implications for the Paris Agreement. *Global Biogeochemical Cycles* **33**, 318–342. doi:[10.1029/2018GB006009](https://doi.org/10.1029/2018GB006009) (2019).
79. Nisbet, E. G., Dlugokencky, E. J., Fisher, R. E., France, J. L., Lowry, D., Manning, M. R., Michel, S. E. & Warwick, N. J. Atmospheric Methane and Nitrous Oxide: Challenges Along the Path to Net Zero. *Philosophical Transactions of the Royal Society A: Mathematical, Physical and Engineering Sciences* **379**, 20200457. doi:[10.1098/rsta.2020.0457](https://doi.org/10.1098/rsta.2020.0457) (2021).

80. Nozhevnikova, A. N., Holliger, C., Ammann, A. & Zehnder, A. J. B. Methanogenesis in Sediments from Deep Lakes at Different Temperatures (2–70°C). *Water sciences and technology* **36**, 57–64 (1997).
81. Ordóñez, C., Massot, A., DelSontro, T., Langenegger, T. & McGinnis, D. F. Temporal Dynamic of Oxidic Methane Production in a Hypereutrophic Swiss Lake. *Frontiers in Environmental Science (submitted)* (2022).
82. Ordóñez, C., DelSontro, T., Langenegger, T., Donis, D., Suarez, E. L. & McGinnis, D. F. Towards a Global Scaling of Oxidic Methane Production: Evaluation of the Methane Paradox in Four Swiss Pre-Alpine Lakes. *Nature Communications (submitted)* (2022).
83. Oremland, R. S. Methanogenic Activity in Plankton Samples and Fish Intestines: A Mechanism for in Situ Methanogenesis in Oceanic Surface Waters. *Limnology and Oceanography* **24**, 1136–1141. doi:[10.4319/lo.1979.24.6.1136](https://doi.org/10.4319/lo.1979.24.6.1136) (1979).
84. Oswald, K., Milucka, J., Brand, A., Littmann, S., Wehrli, B., Kuypers, M. M. M. & Schubert, C. J. Light-Dependent Aerobic Methane Oxidation Reduces Methane Emissions from Seasonally Stratified Lakes. *PLoS ONE* **10**, 1–22. doi:[10.1371/journal.pone.0132574](https://doi.org/10.1371/journal.pone.0132574) (2015).
85. Peeters, F., Encinas Fernandez, J. & Hofmann, H. Sediment Fluxes Rather than Oxidic Methanogenesis Explain Diffusive CH<sub>4</sub> Emissions from Lakes and Reservoirs. *Scientific Reports* **9**. doi:[10.1038/s41598-018-36530-w](https://doi.org/10.1038/s41598-018-36530-w) (2019).
86. Peeters, F. & Hofmann, H. Length-Scale Dependence of Horizontal Dispersion in the Surface Water of Lakes. *Limnology and Oceanography* **60**, 1917–1934. doi:[10.1002/lno.10141](https://doi.org/10.1002/lno.10141) (2015).
87. Peeters, F. & Hofmann, H. Oxidic Methanogenesis Is Only a Minor Source of Lake-Wide Diffusive CH<sub>4</sub> Emissions from Lakes. *Nature Communications* **12**, 1206. doi:[10.1038/s41467-021-21215-2](https://doi.org/10.1038/s41467-021-21215-2) (1 2021).
88. Perez-Coronel, E. & Beman, J. M. Biogeochemical and Omic Evidence for Multiple Paradoxical Methane Production Mechanisms in Freshwater Lakes. *bioRxiv*, 2020.07.28.225276. doi:[10.1101/2020.07.28.225276](https://doi.org/10.1101/2020.07.28.225276) (2020).

89. Pighini, S., Ventura, M., Miglietta, F. & Wohlfahrt, G. Dissolved Greenhouse Gas Concentrations in 40 Lakes in the Alpine Area. *Aquatic Sciences* **80**, 32. doi:[10.1007/s00027-018-0583-2](https://doi.org/10.1007/s00027-018-0583-2) (2018).
90. Powell, T. & Jassby, A. The Estimation of Vertical Eddy Diffusivities below the Thermocline in Lakes. *Water Resources Research* **10**, 191–198. doi:[10.1029/WR010i002p00191](https://doi.org/10.1029/WR010i002p00191) (1974).
91. Prairie, Y. T. & del Giorgio, P. A. A New Pathway of Freshwater Methane Emissions and the Putative Importance of Microbubbles. *Inland Waters* **3**, 311–320. doi:[10.5268/IW-3.3.542](https://doi.org/10.5268/IW-3.3.542) (2013).
92. Råman Vinnå, L., Medhaug, I., Schmid, M. & Bouffard, D. The Vulnerability of Lakes to Climate Change along an Altitudinal Gradient. *Communications Earth & Environment* **2**, 1–10. doi:[10.1038/s43247-021-00106-w](https://doi.org/10.1038/s43247-021-00106-w) (1 2021).
93. Read, J. S., Hamilton, D. P., Jones, I. D., Muraoka, K., Winslow, L. A., Kroiss, R., Wu, C. H. & Gaiser, E. Derivation of Lake Mixing and Stratification Indices from High-Resolution Lake Buoy Data. *Environmental Modelling & Software* **26**, 1325–1336. doi:[10.1016/j.envsoft.2011.05.006](https://doi.org/10.1016/j.envsoft.2011.05.006) (2011).
94. Reeburgh, W. S. Oceanic Methane Biogeochemistry. *Chemical Reviews* **107**, 486–513. doi:[10.1021/cr050362v](https://doi.org/10.1021/cr050362v) (2007).
95. Reis, P. C. J., Thottathil, S. D. & Prairie, Y. T. The Role of Methanotrophy in the Microbial Carbon Metabolism of Temperate Lakes. *Nature Communications* **13**, 43. doi:[10.1038/s41467-021-27718-2](https://doi.org/10.1038/s41467-021-27718-2) (1 2022).
96. Repeta, D. J., Ferrón, S., Sosa, O. A., Johnson, C. G., Repeta, L. D., Acker, M., DeLong, E. F. & Karl, D. M. Marine Methane Paradox Explained by Bacterial Degradation of Dissolved Organic Matter. *Nature Geoscience* **9**, 884–887. doi:[10.1038/ngeo2837](https://doi.org/10.1038/ngeo2837) (2016).
97. Rigosi, A., Carey, C. C., Ibelings, B. W. & Brookes, J. D. The Interaction between Climate Warming and Eutrophication to Promote Cyanobacteria Is Dependent on Trophic State and Varies among Taxa. *Limnology and Oceanography* **59**, 99–114. doi:[10.4319/lo.2014.59.1.0099](https://doi.org/10.4319/lo.2014.59.1.0099) (2014).

98. Rinta, P., Bastviken, D., Schilder, J., Van der Hardenbreoek, M., Stotter, T. & Heiri, O. Higher Late Summer Methane Emission from Central than Northern European Lakes. *Journal Limnology* **76**, 52–67. doi:[10.4081/jlimnol.2016.1475](https://doi.org/10.4081/jlimnol.2016.1475) (2017).
99. Rosentreter, J. A., Borges, A. V., Deemer, B. R., Holgerson, M. A., Liu, S., Song, C., Melack, J., Raymond, P. A., Duarte, C. M., Allen, G. H., Olefeldt, D., Poulter, B., Battin, T. I. & Eyre, B. D. Half of Global Methane Emissions Come from Highly Variable Aquatic Ecosystem Sources. *Nature Geoscience*, 1–6. doi:[10.1038/s41561-021-00715-2](https://doi.org/10.1038/s41561-021-00715-2) (2021).
100. Rudd, J. W. M., Furutani, A., Flett, R. J. & Hamilton, R. D. Factors Controlling Methane Oxidation in Shield Lakes: The Role of Nitrogen Fixation and Oxygen Concentration. *Limnology and Oceanography* **21**, 357–364. doi:[10.4319/lo.1976.21.3.0357](https://doi.org/10.4319/lo.1976.21.3.0357) (1976).
101. Sander, R. Compilation of Henry’s Law Constants (Version 4.0) for Water as Solvent. *Atmospheric Chemistry and Physics* **15**, 4399–4981. doi:[10.5194/acp-15-4399-2015](https://doi.org/10.5194/acp-15-4399-2015) (2015).
102. Saunois, M. *et al.* The Global Methane Budget 2000–2017. *Earth System Science Data* **12**, 1561–1623. doi:[10.5194/essd-12-1561-2020](https://doi.org/10.5194/essd-12-1561-2020) (2020).
103. Schmid, M., Ostrovsky, I. & McGinnis, D. F. Role of Gas Ebullition in the Methane Budget of a Deep Subtropical Lake: What Can We Learn from Process-Based Modeling? *Limnology and Oceanography* **62**, 2674–2698. doi:[10.1002/lno.10598](https://doi.org/10.1002/lno.10598) (2017).
104. Schubert, C. J., Lucas, F. S., Durisch-Kaiser, E., Stierli, R., Diem, T., Scheidegger, O., Vazquez, F. & Müller, B. Oxidation and Emission of Methane in a Monomictic Lake (Rotsee, Switzerland). *Aquatic Sciences* **72**, 455–466. doi:[10.1007/s00027-010-0148-5](https://doi.org/10.1007/s00027-010-0148-5) (2010).
105. Schubert, C. J., Diem, T. & Eugster, W. Methane Emissions from a Small Wind Shielded Lake Determined by Eddy Covariance, Flux Chambers, Anchored Funnels, and Boundary Model Calculations: A Comparison. *Environmental Science & Technology* **46**, 4515–4522. doi:[10.1021/es203465x](https://doi.org/10.1021/es203465x) (2012).
106. Seeberg-Elverfeldt, J., Schlüter, M., Feseker, T. & Kölling, M. Rhizon Sampling of Porewaters near the Sediment-Water Interface of Aquatic Systems: Rhizon Porewater

- Sampling. *Limnology and Oceanography: Methods* **3**, 361–371. doi:[10.4319/lom.2005.3.361](https://doi.org/10.4319/lom.2005.3.361) (2005).
107. Sharma, S., Blagrove, K., Filazzola, A., Imrit, M. A. & Franssen, H.-J. H. Forecasting the Permanent Loss of Lake Ice in the Northern Hemisphere Within the 21st Century. *Geophysical Research Letters* **48**, e2020GL091108. doi:[10.1029/2020GL091108](https://doi.org/10.1029/2020GL091108) (2021).
108. Shelley, F., Ings, N., Hildrew, A. G., Trimmer, M. & Grey, J. Bringing Methanotrophy in Rivers out of the Shadows. *Limnology and Oceanography* **62**, 2345–2359. doi:[10.1002/lno.10569](https://doi.org/10.1002/lno.10569) (2017).
109. Soued, C. & Prairie, Y. T. Changing Sources and Processes Sustaining Surface CO<sub>2</sub> and CH<sub>4</sub> Fluxes along a Tropical River to Reservoir System. *Biogeosciences* **18**, 1333–1350. doi:[10.5194/bg-18-1333-2021](https://doi.org/10.5194/bg-18-1333-2021) (2021).
110. Stepanenko, V., Mammarella, I., Ojala, A., Miettinen, H., Lykosov, V. & Vesala, T. LAKE 2.0: A Model for Temperature, Methane, Carbon Dioxide and Oxygen Dynamics in Lakes. *Geoscientific Model Development* **9**, 1977–2006. doi:[10.5194/gmd-9-1977-2016](https://doi.org/10.5194/gmd-9-1977-2016) (2016).
111. Tan, D., Li, Q., Wang, S., Yeager, K. M., Guo, M., Liu, K. & Wang, Y. Diel Variation of CH<sub>4</sub> Emission Fluxes in a Small Artificial Lake: Toward More Accurate Methods of Observation. *Science of The Total Environment* **784**, 147146. doi:[10.1016/j.scitotenv.2021.147146](https://doi.org/10.1016/j.scitotenv.2021.147146) (2021).
112. Tan, Z., Zhuang, Q. & Walter Anthony, K. Modeling Methane Emissions from Arctic Lakes: Model Development and Site-Level Study: Methane Emissions from Arctic Lakes. *Journal of Advances in Modeling Earth Systems* **7**, 459–483. doi:[10.1002/2014MS000344](https://doi.org/10.1002/2014MS000344) (2015).
113. Tang, K. W., McGinnis, D. F., Frindte, K., Brüchert, V. & Grossart, H.-P. Paradox Reconsidered: Methane Oversaturation in Well-Oxygenated Lake Waters. *Limnology and Oceanography* **59**, 275–284. doi:[10.4319/lo.2014.59.1.0275](https://doi.org/10.4319/lo.2014.59.1.0275) (2014).
114. Tang, K. W., McGinnis, D. F., Ionescu, D. & Grossart, H.-P. Methane Production in Oxic Lake Waters Potentially Increases Aquatic Methane Flux to Air. *Environmental Science and Technology Letters* **3**, 227–233. doi:[10.1021/acs.estlett.6b00150](https://doi.org/10.1021/acs.estlett.6b00150) (2016).

115. Thöle, L., Schwörer, C., Colombaroli, D., Gobet, E., Kaltenrieder, P., van Leeuwen, J. & Tinner, W. Reconstruction of Holocene Vegetation Dynamics at Lac de Bretaye, a High-Mountain Lake in the Swiss Alps. *The Holocene* **26**, 380–396. doi:[10.1177/0959683615609746](https://doi.org/10.1177/0959683615609746) (2016).
116. Thompson, R., Kamenik, C. & Schmidt, R. Ultra-Sensitive Alpine Lakes and Climate Change. *Journal of Limnology* **64**, 139–152. doi:[10.4081/jlimnol.2005.139](https://doi.org/10.4081/jlimnol.2005.139) (2 2005).
117. Thorpe, S. A. & Deacon, G. E. R. Turbulence and Mixing in a Scottish Loch. *Philosophical Transactions of the Royal Society of London. Series A, Mathematical and Physical Sciences* **286**, 125–181. doi:[10.1098/rsta.1977.0112](https://doi.org/10.1098/rsta.1977.0112) (1977).
118. Thottathil, S. D., Reis, P. C. J., del Giorgio, P. A. & Prairie, Y. T. The Extent and Regulation of Summer Methane Oxidation in Northern Lakes. *Journal of Geophysical Research: Biogeosciences*. doi:[10.1029/2018JG004464](https://doi.org/10.1029/2018JG004464) (2018).
119. Thottathil, S. D., Reis, P. C. J. & Prairie, Y. T. Methane Oxidation Kinetics in Northern Freshwater Lakes. *Biogeochemistry* **143**, 105–116. doi:[10.1007/s10533-019-00552-x](https://doi.org/10.1007/s10533-019-00552-x) (2019).
120. Tranvik, L. J. *et al.* Lakes and Reservoirs as Regulators of Carbon Cycling and Climate. *Limnology and Oceanography* **54**, 2298–2314. doi:[10.4319/lo.2009.54.6\\_part\\_2.2298](https://doi.org/10.4319/lo.2009.54.6_part_2.2298) (6part2 2009).
121. Turner, A. J., Frankenberg, C. & Kort, E. A. Interpreting Contemporary Trends in Atmospheric Methane. *Proceedings of the National Academy of Sciences* **116**, 2805–2813. doi:[10.1073/pnas.1814297116](https://doi.org/10.1073/pnas.1814297116) (2019).
122. USEPA. *Methods for Chemical Analysis of Water and Wastes* (Methods 370.1, 1983).
123. USEPA. *Methods for the Determination of Inorganic Substances in Environmental Samples* (Methods 365.1 Rev. 2.0, Methods 352.2 Rev. 2.0, 1993).
124. Vachon, D. & Prairie, Y. T. The Ecosystem Size and Shape Dependence of Gas Transfer Velocity versus Wind Speed Relationships in Lakes. *Can. J. Fish. Aquat. Sci.* **70**, 1–8 (2013).



125. Vachon, D., Prairie, Y. T. & Cole, J. J. The Relationship between Near-Surface Turbulence and Gas Transfer Velocity in Freshwater Systems and Its Implications for Floating Chamber Measurements of Gas Exchange. *Limnology and Oceanography* **55**, 1723–1732. doi:[10.4319/lo.2010.55.4.1723](https://doi.org/10.4319/lo.2010.55.4.1723) (2010).
126. Vachon, D., Langenegger, T., Donis, D., Beaubien, S. E. & McGinnis, D. F. Methane Emission Offsets Carbon Dioxide Uptake in a Small Productive Lake. *Limnology and Oceanography Letters* **5**, 384–392. doi:[10.1002/lol2.10161](https://doi.org/10.1002/lol2.10161) (2020).
127. Vachon, D., Langenegger, T., Donis, D. & McGinnis, D. F. Influence of Water Column Stratification and Mixing Patterns on the Fate of Methane Produced in Deep Sediments of a Small Eutrophic Lake. *Limnology and Oceanography*. doi:[10.1002/lno.11172](https://doi.org/10.1002/lno.11172) (2019).
128. Virtanen, P. *et al.* SciPy 1.0: Fundamental Algorithms for Scientific Computing in Python. *Nature Methods* **17**, 261–272. doi:[10.1038/s41592-019-0686-2](https://doi.org/10.1038/s41592-019-0686-2) (2020).
129. Wang, Q., Alowaifeer, A., Kerner, P., Balasubramanian, N., Patterson, A., Christian, W., Tarver, A., Dore, J. E., Hatzenpichler, R., Bothner, B. & McDermott, T. R. Aerobic Bacterial Methane Synthesis. *Proceedings of the National Academy of Sciences* **118**, e2019229118. doi:[10.1073/pnas.2019229118](https://doi.org/10.1073/pnas.2019229118) (2021).
130. Wang, Q., Dore, J. E. & McDermott, T. R. Methylphosphonate Metabolism by *Pseudomonas* Sp. Populations Contributes to the Methane Oversaturation Paradox in an Oxic Freshwater Lake. *Environmental Microbiology* **19**, 2366–2378. doi:[10.1111/1462-2920.13747](https://doi.org/10.1111/1462-2920.13747) (2017).
131. Wanninkhof, R. Relationship between Wind Speed and Gas Exchange over the Ocean. *Journal of Geophysical Research* **97**, 7373. doi:[10.1029/92JC00188](https://doi.org/10.1029/92JC00188) (1992).
132. Wetzel, R. *Limnology, Lake and River Ecosystem* Third (Elsevier Academic Press, 2001).
133. Whiticar, M. J. Carbon and Hydrogen Isotope Systematics of Bacterial Formation and Oxidation of Methane. *Chemical Geology* **161**, 291–314. doi:[10.1016/S0009-2541\(99\)00092-3](https://doi.org/10.1016/S0009-2541(99)00092-3) (1999).
134. Wiesenburg, D. A. & Guinasso, N. L. Equilibrium Solubilities of Methane, Carbon Monoxide, and Hydrogen in Water and Sea Water. *Journal of Chemical & Engineering Data* **24**, 356–360. doi:[10.1021/je60083a006](https://doi.org/10.1021/je60083a006) (1979).

135. Woolway, R. I., Kraemer, B. M., Lenters, J. D., Merchant, C. J., O'Reilly, C. M. & Sharma, S. Global Lake Responses to Climate Change. *Nature Reviews Earth & Environment* **1**, 388–403. doi:[10.1038/s43017-020-0067-5](https://doi.org/10.1038/s43017-020-0067-5) (8 2020).
136. Woolway, R. I. *et al.* Phenological Shifts in Lake Stratification under Climate Change. *Nature Communications* **12**, 2318. doi:[10.1038/s41467-021-22657-4](https://doi.org/10.1038/s41467-021-22657-4) (1 2021).
137. Wüest, A. & Lorke, A. Small-Scale Hydrodynamics in Lakes. *Annual Review of Fluid Mechanics* **35**, 373–412. doi:[10.1146/annurev.fluid.35.101101.161220](https://doi.org/10.1146/annurev.fluid.35.101101.161220) (2003).
138. Xie, H., Li, Y., Zhang, Y. & Geng, L. *CDOM Photodegradation: Implications for the Oceanic Methane Paradox* in *Geophysical Research Abstracts* EGU2019-3396. **21** (2019), 1.
139. Yao, M., Elling, F. J., Jones, C., Nomosatryo, S., Long, C. P., Crowe, S. A., Antoniewicz, M. R., Hinrichs, K.-U. & Maresca, J. A. Heterotrophic Bacteria from an Extremely Phosphate-Poor Lake Have Conditionally Reduced Phosphorus Demand and Utilize Diverse Sources of Phosphorus. *Environmental microbiology* **18**, 656–667. doi:[10.1111/1462-2920.13063](https://doi.org/10.1111/1462-2920.13063) (2016).
140. Yao, M., Henny, C. & Maresca, J. A. Freshwater Bacteria Release Methane as a By-Product of Phosphorus Acquisition. *Applied and Environmental Microbiology* **82**, 6994–7003. doi:[10.1128/AEM.02399-16](https://doi.org/10.1128/AEM.02399-16) (2016).
141. Ye, W.-W., Wang, X.-L., Zhang, X.-H. & Zhang, G.-L. Methane Production in Oxidic Seawater of the Western North Pacific and Its Marginal Seas. *Limnology and Oceanography* **65**, 2352–2365. doi:[10.1002/lno.11457](https://doi.org/10.1002/lno.11457) (2020).
142. Zheng, Y., Harris, D. F., Yu, Z., Fu, Y., Poudel, S., Ledbetter, R. N., Fixen, K. R., Yang, Z.-Y., Boyd, E. S., Lidstrom, M. E., Seefeldt, L. C. & Harwood, C. S. A Pathway for Biological Methane Production Using Bacterial Iron-Only Nitrogenase. *Nature Microbiology* **4**. doi:[10.1038/s41564-017-0091-5](https://doi.org/10.1038/s41564-017-0091-5) (2018).



# César Ordóñez V.

Rue des Caroubiers 2  
1227, Geneva, Switzerland  
 (+41) 78 720 35 82  
 (+41) 22 379 08 46  
 cesar.ordonez@unige.ch  
 ceordonez.github.io  
 ceordonez

## Education

- 2017 - 2022 **Ph.D. in Environmental Science**, *F.-A. Forel for Environmental and Aquatic Science*, University of Geneva, Aquatic Physics Group.  
Thesis: "Oxic Methane Production Dynamics in Lakes". **Ph.D. supervisor: Daniel F. McGinnis**
- 2012 - 2014 **Civil and Environmental Engineering Diploma**, *Faculty of Physical and Mathematical Sciences*, University of Chile.  
Professional Engineer diploma in water resources engineering. Graduated Summa Cum Laude,
- 2008 - 2012 **B.Sc. in Civil and Environmental Engineering**, *Faculty of Physical and Mathematical Sciences*, University of Chile.  
The main focus was on the creation of mathematical skills and the acquisition of basic knowledge in fluid mechanics.

## Working Experience

### Research Experience

- 2015 - 2017 **Research Assistant**, *Center for Climate and Resilience Research (CR)2*, University of Chile.  
The goal of this project is to study the transport of urban pollutants flowing into the Andean Cryosphere.
- 2012 - 2014 **Research Assistant**, *Civil Engineering Dept., Environment and Water Resources Division*, Faculty of Physical and Mathematical Sciences, University of Chile.  
The aim on this project was to characterize physical and biochemical processes in salty lagoons.

### Teaching

- 2021 **Teacher**, *Alpine Env. and Society*, Faculty of Science, University of Geneva.  
This course is part of the Master of Sciences in Environmental Sciences program.
- 2020 **Teaching Assistant**, *Field Course*, Faculty of Science, University of Geneva.  
Greenhouse gases exchange in alpine lakes.
- 2018 **Teaching Assistant**, *Alpine Env. and Society*, Faculty of Science, University of Geneva.  
Greenhouse gases exchange in alpine rivers.

2018 **Teaching Assistant**, *Cadagno Field Course*, Faculty of Science, University of Geneva.

Greenhouse gases exchange and water column characterization in lakes

2012 **Teaching Assistant**, *Fluid Mechanics*, Faculty of Physical and Mathematical Sciences, University of Chile.

*Supervision of students projects*

2019-2020 **Co-advisor**, *Methane fluxes from littoral sediment of a eutrophic swiss lake*, Master thesis, Ms. Aurora Pinto.

2019-2020 **Co-advisor**, *Sources and fate of aerobic methane production: a study on a small eutrophic lake*, Master thesis, Ms. Alexandrine Massot.

## Grants

2021 **Polar Access Fund**, *Arctic Change: Resolving methane and CO<sub>2</sub> concentrations and their fluxes in Baffin Bay*, Swiss Polar Institute, Switzerland.

## Languages

Spanish Native

English Advance

*Proficient reading, writing, and speaking*

## Computer skills

Operative Systems	Windows, Linux	Programming	Java (basic), Bash (basic), Git
Scientific Programming	MATLAB, Python, Scilab, R (basic)	Typography	Microsoft Office, L <sup>A</sup> T <sub>E</sub> X
Aquatic Models	Dyremis (Basic), Caedym (Basic)	Atmospherics Models	WRF
Relevant courses taken	Computing I, Probability and Statistics, Numerical Modeling		

## Publications

### Journal Papers

- [1] A. de la Fuente, C. Ordóñez, and R. Pérez. “Diffusional mass transfer coefficient at the water–sediment interface for wind-induced flow in very shallow lagoons”. In: *Environmental Fluid Mechanics* 15.6 (2015). DOI: 10.1007/s10652-015-9437-9.
- [2] C. Ordóñez, A. de la Fuente, and P. Díaz-Palma. “Modeling the influence of benthic primary production on oxygen transport through the water-sediment interface”. In: *Ecological Modelling* 311 (2015), pp. 1–10. DOI: 10.1016/j.ecolmodel.2015.05.007.
- [3] A. Mazzeo, N. Huneus, C. Ordóñez, A. Orfanos-Cheuquelaf, L. Menut, S. Mailler, M. Valari, H. Denier van der Gon, L. Gallardo, R. Muñoz, R. Donoso, M. Galleguillos, M. Osses, and S. Tolvett. “Impact of residential combustion and

transport emissions on air pollution in Santiago during winter”. In: *Atmospheric Environment* 190 (2018), pp. 195–208. DOI: 10.1016/j.atmosenv.2018.06.043.

- [4] K. W. Tang, S. Flury, D. Vachon, C. Ordóñez, and D. F. McGinnis. “The phantom midge menace: Migratory Chaoborus larvae maintain poor ecosystem state in eutrophic inland waters”. In: *Water Research* 139 (2018), pp. 30–37. DOI: 10.1016/j.watres.2018.03.060.
- [5] N. Huneeus, R. Lapere, A. Mazzeo, C. Ordóñez, N. Donoso, R. Muñoz, and J. A. Rutllant. “Deep winter intrusions of urban black carbon into a canyon near Santiago, Chile: A pathway towards Andean glaciers”. In: *Environmental Pollution* 291 (2021), p. 118124. DOI: 10.1016/j.envpol.2021.118124.
- [6] C. Ordóñez, T. DelSontro, T. Langenegger, D. Donis, E. L. Suarez, and D. F. McGinnis. “Towards a global scaling of oxic methane production: evaluation of the methane paradox in four Swiss pre-alpine lakes”. In: *Nature Communications (submitted)* (2022).

### Conferences

- [1] C. Ordóñez, N. Huneeus, A. Mazzeo, N. Donoso, R. Muñoz, V. Moreno, A. Orfanoz-Cheuquela, L. Gallardo, L. Molina, and A. Vizcarra. “Transport of particle pollution into the Maipo Valley: winter 2015 campaign results”. In: EGU Conference. 2016.
- [2] C. Ordóñez, T. Langenegger, T. DelSontro, S. Flury, K. W. Tang, and D. F. McGinnis. “Multi-lake Survey: hydrodynamics response to climate forcing”. In: PPNW. Solothurn, Switzerland, 2018.
- [3] C. Ordóñez, T. DelSontro, T. Langenegger, D. Donis, A. Massot, A. Pinto, A. Gelbmann, and D. F. McGinnis. “Oxic methane production: filling gaps in the methane lake budget”. In: GLEON 21.5. Online, 2020.
- [4] C. Ordóñez, T. DelSontro, T. Langenegger, D. Donis, A. Massot, A. Pinto, and D. F. McGinnis. “Methane Paradox in pre-alpine lakes evaluated with two mass balance approaches”. In: PPNW 2021 Seminar. 2021.
- [5] C. Ordóñez, T. DelSontro, T. Langenegger, D. Donis, A. Massot, A. Pinto, and D. F. McGinnis. “Methane Paradox in pre-alpine lakes: evaluation of oxic methane production using two mass balance models”. In: ASLO Aquatic Science Meeting. 2021.